UNIVERSITÀ DEGLI STUDI DI PARMA

DOTTORATO DI RICERCA IN
INGEGNERIA INDUSTRIALE

CICLO XXXIV

DYNAMIC MODELING OF EXPLOSION-RESISTANT GLAZED SYSTEMS

Coordinatore:
Chiar.mo Prof. Gianni Royer-Carfagni

Tutore:
Chiar.mo Prof. Gianni Royer-Carfagni

Dottorando: Luca Viviani

Anni Accademici 2018/2019 - 2020/2021

Abstract

This thesis condenses the dynamic modeling of blast resistant glazed façades. After the emergence of terrorism in the early 2000s, the increasing popularity of glass in prestigious buildings has motivated many international standards to provide specific indications for the assessment of windows under explosive scenarios. These norms explain how to conduct experimental tests and how to quickly check the structural resistance of glass components. However, their approach is often based on pure experience and difficult to extend in other situations. For the present work, a theoretical point of view is assumed. The problem is approached at different levels, in order to cover all the principal aspects to consider during the design phase.

The blast loading action, deriving from an explosion, can effectively be interpreted via Friedlander equation (a semi-empirical model). It presents a time dependent exponential form, which is composed of a compression phase and a subsequent suction phase. The pressure time history depends on few parameters, whose calibration has to be performed accordingly (empirical relations, experiments, technical literature, etc.). A uniformly distributed pressure over the surface of glazed panels is assumed and, on the basis of blast impulse, different modes of vibrations can be excited. As related problem, glazed surfaces are often required to withstand also against soft-body impacts. New regulations provides for testing procedures, where these impulsive actions are concentrated on a small area, which dynamically changes according to the deformed shape of impacting body. The pendulum test is first analyzed with a simple approach based upon an equivalent linear and nonlinear 2-DoF system. The time history analysis is complemented with energetic considerations that, with reasonable assumptions, can directly provide the maximum stress in the panel through an equivalent static load. Moreover, a finite element tool has been developed, which uses nonlinear unilateral beam elements available in a commercial software for structural analysis. The comparison between the predictions of the proposed methods with that obtained from experiments and other advanced software, indicates the accuracy of this engineering approach and its range of applicability.

For applications involving impulsive loads, laminated glass is usually employed so that an equivalent ductility is achieved and the risk related to the projection of fragments is reduced. These sandwich composites are made of glass plies, which are

coupled by the cohesive action of polymeric interlayers. To this purpose, suitable structural models are introduced and numerically tested for both beams and plates. Fractional calculus (differential equations involving fractional derivatives) is adopted to describe the viscoelasticity at the level of the interlayer. As a main advantage, only two parameters are needed to define the relaxation function for commercial polymers. The solution of equilibrium equations is obtained *à la* Galerkin and their time integration is performed by means of Grünwald-Letnikov method. The comparison with the classical method, relying on an expansion in Prony series of the relaxation law, highlights the simplifications obtainable with fractional approach.

Since glass is a brittle material, there are few possibilities to significantly improve its resistance against impulsive loads. Therefore, one can employ dissipative devices to interpose between panels and back structure: the energy released by the load is partially absorbed by sacrificial (crushing) elements, consequently glass is unloaded. This is theoretically demonstrated with reference to a paradigmatic problem, in which a glass pane is connected to a load-bearing structure through a dissipative unit. The unit is composed of a movable piston in unilateral contact, on its two opposite sides, with shock absorbers capable of plastic deformation, which are activated respectively during the compression and suction phase of blast load. The nonlinear dynamic equations are solved by a customized algorithm, which considers the possible impacts of the piston at the end of its stroke. Through a parametric analysis, criteria are proposed for the optimal design of such dissipative unit. The proposed technical solution is compared with a linear viscous dashpot, which is not as efficient as the previous one in limiting the effects of the first compression phase, but it can considerably reduce subsequent oscillations. A hybrid device, where viscous dampers and crushing components are integrated in parallel, seems to represent the best compromise.

From an engineering perspective, it is important to asses the load-bearing capacity of the whole glazing system instead of the sole panels. As guide for structural design, a simple analytical model is proposed, so that a synthetic, but comprehensive, view of the phenomenon is permitted. The dynamic interaction among the blast load, the ensemble of panels and the load-bearing structure is studied in a paradigmatic lumped element model. The rear structure is represented by a pretensioned cable connected in series with a spring element; while each glass panel is reduced to a nonlinear oscillator via to Rayleigh's method. The model allows to tune the inertia and the stiffness of the back structure. Generally, a compliant back structure allows an optimal absorption of energy and, consequently, preserve the panels.

Contents

Chapter 1

Introduction

1.1 Bomb-blast resisting glazed façades

After the September 11th, international community has had to face the problem of assessing the risk for people and property to be target of explosions in the vicinity of public/private buildings. Until then, apart from military applications, this issue had been mainly considered for industrial buildings located close to storage areas for detonating fluids (like natural gas and hydrocarbons). Generally, industrial buildings are constituted by massive structures in steel or reinforced concrete, for which adequate countermeasures could be taken without any concern in terms of visual impact. The new challenge, dictated by the threat of terroristic attack, is instead represented by prestigious buildings, where large glazed surfaces are often employed. The use of glass is becoming popular thanks to its unique aesthetic properties, but glazed panels are naturally unsuitable to withstand impulsive actions because of their intrinsic brittleness. As examples, we recall the attacks which took place in Jakarta against Australian Embassy and in Olso government quarter (Fig. 1.1): broken windows show the disruptive effects on glass caused by bomb cars exploded close to the buildings. Therefore, it is necessary to evaluate the effects of blast waves impacting on them.

In order to meet this demand, codes and safety standards provide general guidelines for structural design. More specifically, in 1991 the U.S. Departments of the Army, Navy and Air Force licensed a tri-service manual [1] to define the effects of explosions and assess the consequent ultimate resistance capacity of facilities. Norms like EN 12600 [2] and GSA-TS01-2003 [3] prescribe experimental procedures to test glass panes against impulsive loads (impacts, etc.). The most employed testing methods are conducted by means of shock tube apparatus, and they are ruled by standards like EN 13123 [4, 5] and EN 13124 [6, 7]. In Europe, ISO 16933 [8] and ISO 16934 [9] have provided since 2007 a procedure to determine the air-blast

(a)

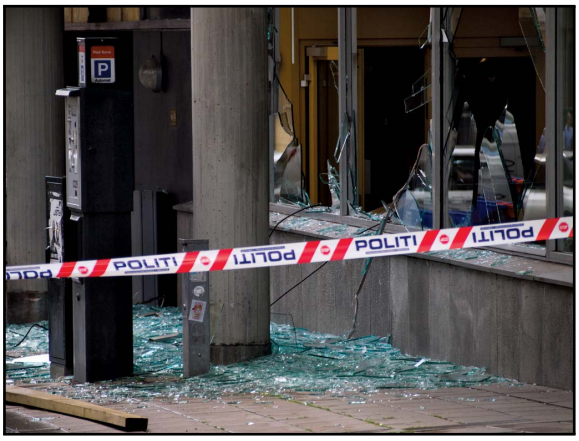

(b)

Figure 1.1. Effects on glazed façades of a terrorist attack. (a) Australian Embassy bombing in Jakarta, 2004 (photo from devpolicy.org). (b) Broken windows photographed in Oslo government quarter during 2011 Norway attacks (photo from britannica.com)

resistance of glazing, introducing models for vehicle and satchel bombs to classify glazing performance within a broad range of blast parameters. A review of technical literature about glazed façades under extreme loading scenarios (seismic events, wind or blast loads) can be found in [10, 11], with particular emphasis on design methods and current research trends. In practice, a bomb blast resisting façade shall be designed at *three levels*: 1) glass panes, 2) supporting devices and 3) rear load-bearing structure.

The first level is focused on mechanical properties of glass, in terms of fracture resistance and ductility. Laminated glass is recommended, because the interposition

of a viscous polymeric interlayer between glass plies[1] allows to achieve an increased ductility in pre- and post-breakage phases. The interlayer produces a shear coupling action between the plies [12], so that the bending stiffness of the laminate is intermediate between two borderlines cases: *layered limit* (lower-bound), with free-sliding plies; *monolithic limit* (upper-bound), where no sliding between plies occurs (the flexural inertia is represented by the entire cross section of glass). In the post-breakage phase, glass shards remain attached to the polymer and the ensemble maintains a certain bending capacity [13]. To this respect, we recall the work of Pelfrene et al. [14], who studied the post-breakage behavior of laminated glass on the basis of standard laboratory tests ruled by EN 13541 [15]. We mention also the work Hooper et al. [16], who conducted many full scale blast tests on laminated glass panels to develop an innovative finite element model suitable for bomb blast applications.

The second level of structural design concerns the supporting devices. Special mechanical connectors can be installed at the interface between the building structure and the glazed façade, with the goal of dissipating the energy transmitted by a blast load. Amadio and Bedon made an extensive research about this topic. They designed innovative viscoelastic spider connectors employable in glass curtain wall [17], as well as dissipative devices (formed by metallic plates with an interposed polymeric layer) to be installed at the pane corners [18]. Alternatively, when pretensioned cables are used as load-bearing structures, a frictional mechanism can be applied at the top (bottom) of the main cables to enhance dissipation [19].

The third level refers to the global behavior of façades, and not just to the dynamics of single panels. The state of stress in glass can be consistently reduced by tuning the inertia and the stiffness of rear structure [20, 21]. Preliminary investigations have shown that cable-supported façades perform much better than mullion and transom façades, because of their compliance. As also attested by Schlaich et al. [22], they can adsorb much of the energy transmitted by impulsive loads (explosions, wind gusts, seismic events, etc.). For example, a cable-stayed façade was designed by Sobek for the International O'Hare Airport (Chicago) in order to fulfill blast mitigation requirements [23]. Active controls can possibly be employed [24] but, to the best of our knowledge, this is not a common engineering application.

1.2 Objectives

As global objective, we want to study and optimize glazed façades that are required to resist against impulsive loads. An analytical approach has been adopted, in order

[1] They are usually bonded by the polymeric interlayers with a process at high temperature and pressure in autoclave.

to extend on a scientific basis what is written in international norms and known in engineering practice. Our attention is focused on the three paradigmatic elements composing a façade subjected to blast loading: glass panels, supporting devices and rear structure. More specifically, the principal scopes of such research can be listed as follows:

- Synthesizing what prescribed by norms and latest scientific literature about blast loading calculation. The load time history is usually determined via empirical models. However, it is important to understand what are the physical motivations of such models as well as their limitations.

- Modeling the pendulum test through an analytical approach. Impacts are the most common impulsive loads, consequently it is often required to assess the glass resistance through specific commercial software and/or laboratory tests. With the purpose to provide a quick and practical alternative, a lumped element model is investigated.

- Understanding the role of polymeric interlayers in laminated glass subjected to short duration loads. Viscoelastic properties of polymers directly affect the dynamic response of sandwich panels. Fractional calculus seems to be an analytical approach very suitable to model the relaxation/creep function of viscoelastic materials, especially if compared with Prony series (the classic approach). To this purpose, the computational advantages of this method needs to be assessed.

- Proposing a new type of dissipative device for glazed panels, which is able to efficiently absorb the energy transmitted by a blast load. There are some examples in the literature that consider viscous dampers or sacrificial components for these applications; anyway, it is not known what is the optimal mixing of such mechanisms.

- Analyzing the beneficial effects related to a proper load-bearing structure in a blast loading scenario. It is intuitive to conclude that a compliant rear structure absorbs a greater amount of energy than a stiffer one, because of its compliance. Therefore, stiffness and inertia need to be calibrated for the global structural design.

1.3 Outline

This thesis is divided in six chapters and one appendix. The arguments are exposed in the following order:

Chapter 2 - The modeling of impulsive actions

The impulsive loading actions includes explosions and impacts. The blast loads are usually obtained through experimental procedures or empirical models. To this purpose, Friedlander model is illustrated: a simple exponential relation, defined by few empirical parameters, which gives the pressure time history. International norms are presented, so that it is possible to relate what they prescribe with the scientific background. Since glass panels are frequently required to resist under the action of impacting bodies, the pendulum test is analytically reproduced by means of a paradigmatic lumped element model. A commercial finite element software takes the results of this model as input. Further comparisons reveals the good agreement with experimental tests and the wide range of applicability of such an analytical tool.

Chapter 3 - Laminated glass modeled via fractional calculus

A structural model for laminated glass is introduced, where both beams and plates are considered. The viscoelastic behavior of the interlayer is modeled by means of relaxation functions, whose time dependence is interpreted via fractional calculus. Several numerical experiments are conducted under impulsive loads; the results are contextually discussed.

Chapter 4 - The advantages of dissipative supporting devices

Since glass is a brittle material, dissipative devices can effectively be employed in façades with a high risk of explosive events. An innovative device, based on crushing components (shock absorbers), is proposed and analyzed. Its optimization is performed though specific parametric analyses. Moreover, its efficacy has been compared with that of a classic viscous damper.

Chapter 5 - The role of rear load-bearing structure

A lumped element model about a cable-supported façade is proposed. A global perspective is assumed, inasmuch the entire façade is called to withstand against a possible blast loading action deriving from an explosion. The attention is focused on the rear structure, that is optimized in terms of inertia and stiffness.

Chapter 6 - Conclusions

This chapter is dedicated to discuss the previous analyses. The contents are summarized and the main results are highlighted. Some further developments are briefly suggested.

Chapter A - Fractional calculus in viscoelasticity

Fractional derivatives can be proficiently used to fit data following a power law dependence. The Caputo's fractional derivative is recalled; then, its numerical formulation is expressed through Grünwald-Letnikov operators.

Chapter 2

The modeling of impulsive actions

The set of impulsive loading actions, that glazed panels are usually called to withstand, includes I. explosions and II. impacts.

I. The deleterious effects produced by an explosion are related to the propagating pressure wave and the accidental projection of fragments. Hereafter, we deal about the first aspect by investigating how to model the loading pressure with respect to a stationary target (a glazed façade or a panel). In particular, some empirical relations, useful for engineering design, are introduced; then, the principal testing methods are listed in agreement with international norms, and finally the influence of loading phases is highlighted.

II. For safety barriers and full-height façades, glass shall possess a sufficient capacity when it is subjected to accidental impacts of humans and avoid brittle failure. Generally, this type of loading action is not distributed on the total surface of the panel, but it is concentrated on a small area. The dynamic problem is highly nonlinear, because the impactor presents a not negligible deformability so that the contact area changes during the interaction with panel. This is a free-boundary problem which is empirically approached with the standardized soft-body test [2]. The modeling of such testing procedure will be discussed in the second part of this chapter.

2.1 The blast load

2.1.1 Friedlander equation

A *shock wave* (or alternatively *blast wave*) can be defined as a thin region of rapid state variation across which there is a flow of matter and all the fluid properties (pressure, velocity, density, etc.) are discontinuous [25]. For our goals, the shock

wave is supposed to be formed after an explosive chemical reaction[1], where the gasses produced present a temperature higher than the atmosphere. As consequence, gasses expand outward while pressure and density at their center drop. The wave so formed consists in a sudden pressure discontinuity, that is followed by a rapid decay with subsequent fluctuations under the atmospheric pressure, as schematically represented in Fig. 2.1.

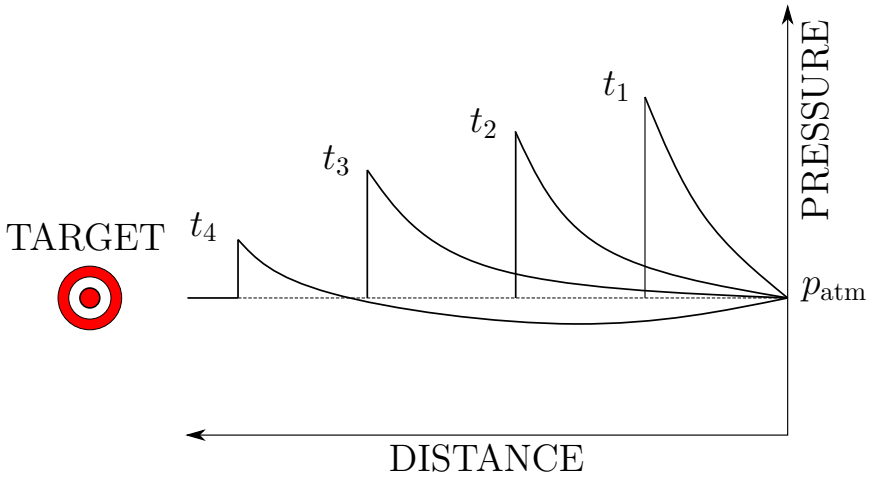

Figure 2.1. Pressure-distance curves represented in subsequent instants after an explosion, with $0 < t_1 < t_2 < t_3 < t_4$ [26].

The shock front can be idealized as a surface, with zero thickness, moving away from the explosive charge through a medium. Balance equations must conserve mass, momentum, energy and entropy for a control volume that isolates the shock front. When atmospheric pressure ($p_{\text{atm}} = 101.3\,\text{kPa}$) is negligible in comparison with that behind the front, it is possible to assume the time evolution of an explosion as self-similar inasmuch its geometry is preserved. Therefore, one can use dimensional analysis theory to find an approximated solution in terms of field variables (pressure, velocity, density, etc.) as demonstrated by Sedov [27] and Taylor [28, 29]. However this analytical treatment is not suitable for us, because it requires initial hypotheses acceptable only for very intense explosions, such that of atomic bombs. Instead, we consider situations where weak explosions (hand-carried satchel bombs or, at most, vehicle bombs) occur far from the target. A common situation is represented in Fig. 2.2.

[1]The burning process of explosives involves a fuel (whose molecules contain atoms of carbon, hydrogen, nitrogen, sulfur, and oxygen) that oxidized through an exothermic reaction. This process can be classified as a deflagration or a detonation. In the first case the speed of combustion is less than the speed of sound in fuel material, while in the second case is greater. Only the supersonic propagation (detonation) causes the formation of shock waves.

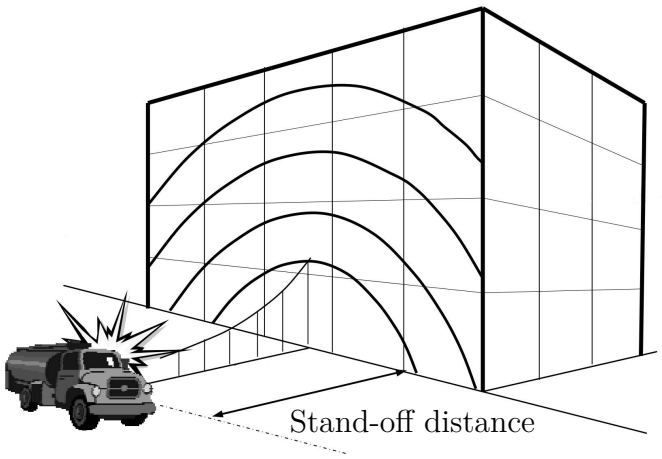

Figure 2.2. Schematic representation of blast loads on building caused by a vehicle bomb attack [30].

In the technical literature, there are quick and practical expressions which can be adopted to preliminarily design architectural glazing when geometries, as well as other conditions, have not been yet fully defined. Subsequently, we decide to interpret the time dependent pressure, acting on a stationary target, by using *Friedlander equation*. It presents an exponential wave form reading

$$p(t) = p_{\text{atm}} + p_0\left(1 - \frac{t}{T_d}\right)e^{-\frac{\beta}{T_d}t}, \tag{2.1}$$

where p_{atm} indicates the atmospheric pressure, p_0 is the peak overpressure, β is the decay parameter and T_d is the time compression duration[2]. The shape function distinguishes two phases: the first is referred to as the *compression phase* $p(t) > p_{\text{atm}}$, while the subsequent is denoted as *suction phase* $p(t) < p_{\text{atm}}$. This loading action is plotted in Fig. 2.3 (continuous line), where $t = 0$ represents the instant at which the blast collision occurs in correspondence of the target. Note that the difference between the negative peak pressure and the atmospheric pressure is indicated as $\Delta p^{\min}$.

All the parameters can be deduced from empirical relations depending on the scaled distance

[2]The original formulation proposed by Friedlander [31] did not account for atmospheric pressure. The expression (2.1) introduces the term p_{atm} because it is useful in further thermodynamic considerations. Obviously, the net load acting on a façade/window (located on Earth) includes only the overpressure contribution.

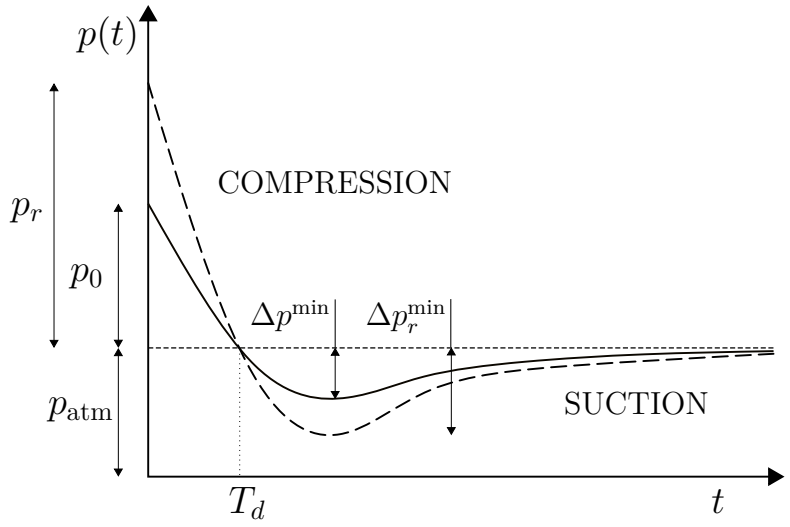

Figure 2.3. Time dependent force per unit area interpreted according to Friedlander equation (continuous line) and its reflected impulse (dashed line).

$$Z = \frac{R}{W_{\mathrm{TNT}}^{1/3}}\,, \tag{2.2}$$

where R denotes the distance between blast site and target, while W represents the mass of charge expressed in trinitrotoluene (TNT) kilograms [32]. If an explosive charge is characterized by W_{exp} as mass and H_{exp} as heat of detonation, the equivalent amount of TNT (in terms of released energy) reads

$$W_{\mathrm{TNT}} = W_{\mathrm{exp}} \frac{H_{\mathrm{exp}}}{H_{\mathrm{TNT}}}, \tag{2.3}$$

with $H_{\mathrm{TNT}} = 4.1 \div 4.55\,\mathrm{MJ/kg}$ (TNT heat of denotation). The scaled distance is useful to compare different explosions in terms of magnitude: the lower it is, the stronger will be its disruptive effect. Two blast events, respectively characterized by $(R_1,\, W_{\mathrm{TNT},1})$ and $(R_2,\, W_{\mathrm{TNT},2})$, are considered equivalent if

$$\frac{R_1}{R_2} = \left(\frac{W_{\mathrm{TNT},1}}{W_{\mathrm{TNT},2}}\right)^{1/3}. \tag{2.4}$$

For example, an explosion originated by 100 Kg of TNT and placed at 68 m from the target, is assumed to produce the same effects of another one originated by 10 Kg of TNT and located 32 m from the target.

Brode [33] was the first to use the scaled distance as the sole parameter to quantify the initial peak overpressure for a perfectly spherical charge in absence of obstacles. Further studies have been performed by scientists to provide more precise

expressions on the basis of experimental data. Some of the most popular relations, suitable for a spherical free-air blast, were proposed by Kinney and Graham [26]. Their popularity is due to an optimal agreement with experimental results provided by Kingery and Bulmash [34] over a broad range of scaled distances. Here, only the expressions relative to the compression phase are reported:

- peak overpressure (the unit of measure depends on p_{atm})

$$p_0 = p_{\mathrm{atm}} \cdot \frac{808\left[1+\left(\frac{Z}{4.5}\right)^2\right]}{\sqrt{\left[1+\left(\frac{Z}{0.048}\right)^2\right]}\cdot\sqrt{\left[1+\left(\frac{Z}{0.32}\right)^2\right]}\cdot\sqrt{\left[1+\left(\frac{Z}{1.35}\right)^2\right]}}\,; \quad (2.5)$$

- time positive duration

$$T_d = W_{\mathrm{TNT}}^{1/3} \cdot \frac{980\left[1+\left(\frac{Z}{0.54}\right)^{10}\right]}{\left[1+\left(\frac{Z}{0.02}\right)^3\right]\cdot\left[1+\left(\frac{Z}{0.74}\right)^6\right]\cdot\sqrt{\left[1+\left(\frac{Z}{6.9}\right)^2\right]}} \quad [\mathrm{ms}]; \quad (2.6)$$

- positive impulse

$$i^+ = W_{\mathrm{TNT}}^{1/3} \cdot \frac{6.7\cdot\sqrt{1+\left(\frac{Z}{0.23}\right)^4}}{Z^2\cdot\sqrt[3]{1+\left(\frac{Z}{1.55}\right)^3}} \quad [\mathrm{kPa{\cdot}ms}]. \quad (2.7)$$

These expressions are plotted in Fig. 2.4, as functions of Z for $W_{\mathrm{TNT}} = 1\,\mathrm{kg}$. Naturally, if the scaled distance Z increases, the compression phase becomes less relevant in terms of peak pressure and positive impulse.
Once the positive impulse i^+ is known, it is possible to mathematically deduce the decay coefficient β by integrating Friedlander relation over the time and solving the nonlinear equation

$$i^+ = \int_0^{T_d} p_0\left(1-\frac{t}{T_d}\right)e^{-\frac{\beta}{T_d}t}\,dt = p_0 T_d\left[\frac{1}{\beta}-\frac{1}{\beta^2}(1-e^{-\beta})\right]. \quad (2.8)$$

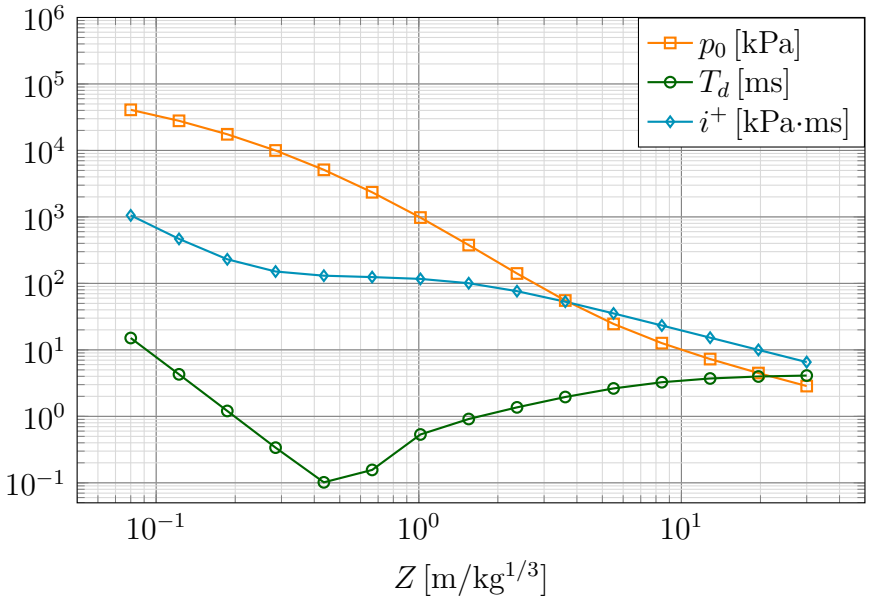

Figure 2.4. Blast parameters depending on scaled distance Z, calculated through the empirical relations proposed by Kinney and Graham [26].

Karlos et al. [35] highlighted that the time positive duration is usually affected by the greatest uncertainty. Therefore, they proposed to estimate the decay coefficient by means of one empirical relation[3] and subsequently calculate T_d by integrating Friedlander equation over the time. Alternatively, Goel et al. [36] suggest to adopt the simpler relation

$$\beta = 1.5Z^{-0.38} \quad 0.1 \leq Z \leq 30. \tag{2.9}$$

which was provided by Teich and Gebbeken [37].

2.1.2 Reflection

When gas particles collide against a surface along their travel, they bounce back obstructing the motion of other incoming particles and causing a local increase of pressure. This process is denoted as *reflection* and it is manly affected by the angle of incidence α, which is subtended between the propagating direction of blast impulse and the impinging surface. The worst condition occurs when the blast wave perpendicularly invests a plane surface ($\alpha = 0°$); while oblique surfaces ($\alpha \gg 0°$)

[3]Karlos et al. [35] fitted Kingery–Bulmash data [34] evaluating the decay coefficient θ through almost twenty numerical coefficients included in one polynomial expression.

mitigate the magnitude of reflected pressure. Reflection phenomena have to be analytically considered in Friedlander equation. This can be done by means of two different coefficients [37]: one for the positive phase c_r^+ and one for the negative phase c_r^-. For an infinite plane perpendicularly invested by a blast impulse and by assuming $\gamma = 1.4$ as constant value of heat capacity ratio, it is possible to state

$$c_r^+ = \frac{p_r}{p_0} = \frac{8p_{\text{so}} + 6p_{\text{atm}}}{p_{\text{so}} + 6p_{\text{atm}}}\,, \tag{2.10}$$

where p_r indicates the reflected overpressure and $p_{\text{so}} = p_{\text{atm}} + p_0$. For what concerns the coefficient suitable for the negative phase, Teich and Gebbeken [37] proposed the expression

$$c_r^- = \frac{\Delta p_r^{\min}}{\Delta p^{\min}} = \frac{1.9Z - 0.45}{Z} \quad Z > 0.5, \tag{2.11}$$

where $\Delta p_r^{\min}$ indicates the difference between the negative reflected peak pressure and the atmospheric pressure. With reference to Fig. 2.3, the reflected curve (dashed line) is easily calculated by using both coefficients[4]

$$q(t) = \begin{cases} p_{\text{atm}} + c_r^+ p_0 \left(1 - \dfrac{t}{T_d}\right) e^{-\frac{\beta}{T_d}t} & t \le T_d \\ \\ p_{\text{atm}} + c_r^- p_0 \left(1 - \dfrac{t}{T_d}\right) e^{-\frac{\beta}{T_d}t} & t > T_d \end{cases}. \tag{2.12}$$

The pressure experienced by a generic point, belonging to a vertical surface, is influenced by normal reflection so that the initial peak p_0 increases up to p_r. However, it is possible that the shock front was previously reflected and amplified by other surfaces, such as the ground. In this thesis, only unconfined explosions are taken into account, which can be classified on the basis of relative position between charge and target structure. The role played by the ground is implicitly considered in all the cases listed below [1]:

a **Free-air burst** The detonation occurs in free air; the consequent blast wave does not interact with obstacles (absence of reflections) during its travel and it is not subjected to any amplification because of ground.

b **Air burst** The explosion occurs in air, but it prior invests the ground forming an oblique reflection or alternatively a *Mach stem*.

[4]Possibly, the coefficient relative to the positive phase can be used also for negative phase, on the safe side.

c **Surface burst** The charge detonates at the level of ground; thus the explosion propagates hemispherically and the energy released is concentrated in half the volume.

The same explosion could be identified by all previous categories with respect to three targets placed at different distances: the closest would be subjected to a free-air burst, while the farther would experience a surface burst.

Free-air bursts are probably the most rare situations during a terrorist attack and they are the simplest to model: there are no reflection phenomena due to the ground and many experimental results are directly available from the literature.

For what concerns *air bursts*, the shock front is reflected by the terrain before hitting the structure. Predicting the correct dynamic evolution would require sophisticated numerical simulations; however there are approximated solutions suitable for engineering scopes. When the angle of incidence α is lower than a value depending on front velocity (usually $\alpha \leq 40° \div 45°$), the shock wave is obliquely reflected by ground. In this case, balance equations (or pre-existing tables/graphs based on experimental activity) allow us to characterize the reflected front in terms of peak overpressure and velocity. On the contrary, if the angle of incidence overpasses the limit value (usually for $\alpha \geq 40° \div 45°$), Mach stem is created. It is a new vertical front whose height is delimited by ground level and triple point trajectory (i.e., intersection between incident wave and reflected wave). Its pressure distribution is uniform, and the magnitude depends on the incident wave's angle as well as the shock velocity [26]. This process is schematically represented in Fig. 2.5(a).

The most common type of terrorist attack can be classified as a *surface burst*, inasmuch the height of charge is consistently less than the distance from the target ($H \ll R$). For example, this situation could be verified when a truck full of explosive detonates in front of a building. The presence of the ground forces the explosion to concentrate all the energy into a hemisphere, almost doubling the peak overpressure. The load can be assumed as uniform over the frontal wall of the building, as schematically drawn in Fig. 2.5(b).
There are formulations specifically obtained for hemispherical explosions, like that by Newmark and Hansen [39], that is

$$p_0 = 6784\frac{W}{R^3} + 93\sqrt{\frac{W}{R^3}}\,, \tag{2.13}$$

where the peak overpressure p_0 is expressed in bars and the weight of charge is in tons ($1\,\text{ton} = 1000\,\text{kg}$). Unfortunately, also the most corroborated empirical relations are usually deduced from intense bursts and they do not cover a broad interval of scaled distances; consequently they risk to be not sufficiently precise for conventional explosives located far from targets. For this reason, analytical relations like (2.5)-(2.7) are reputed to be the most suitable. Since they are deduced

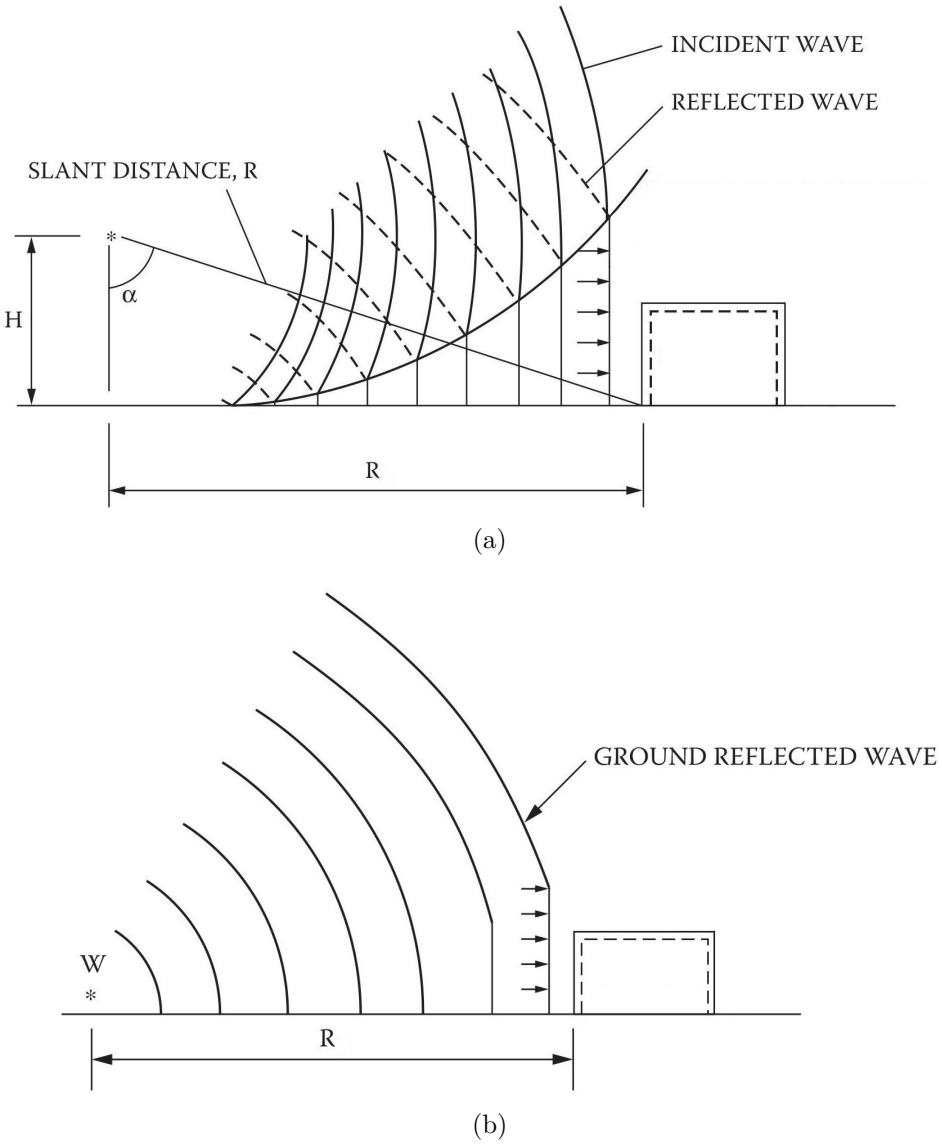

Figure 2.5. Explosion environment [1, 38]: (a) air burst; (b) surface burst.

for spherical explosions, the weight of charge has to be multiplied by a coefficient, generally 1.7-1.8 [32], in order to account for the presence of the ground.

As a further loading contribution related to an explosion, it should be considered also the pressure due to the impact of wind, commonly denoted as drag pressure $p_{\text{drag}}(t)$. Its value mainly depends on wind velocity behind the shock front and the target geometry. Its expression can be estimated as [26]

$$p_{\text{drag}}(t) = \frac{1}{2} C_D \rho_a u(t)^2 \tag{2.14}$$

where C_D is the drag coefficient[5] (for a plane vertical surface $C_D \approx 1$), ρ_a is the air density and $u(t)$ is the wind velocity. The drag pressure tends to last longer than the impulse related to the blast wave, but it generally presents a lower magnitude. Because of the difficulty to predict the time history of wind velocity, this contribution is often neglected.

2.1.3 International norms and testing methods

Norms and testing methods are needed to provide basic recommendations about the structural design of glazing systems subjected to explosive events. Firstly, it is necessary to define a blast load that a façade (or alternatively a window) is called to withstand, on the basis of what level of risk is considered acceptable. Then, a validation can be conducted by choosing *i*) *full-scale arena blast tests* or by employing *ii*) a shock wave simulator, commonly known as *shock tube*.

In 1991 the U.S. Departments of the Army, Navy and Air Force licensed a tri-service manual [1] to define the effects of explosions and assess the resistance capacity of facilities. More recently, the GSA-TS01-2003 [3] prescribed experimental procedures to test glass panes against explosions; it categorizes hazard levels and it further suggests software tools in order to predict glazing response.

In Europe, since 2007, norms such as ISO 16933:2007 [8] and ISO 16934:2007 [9] have provided standard procedures to test and classify glazing performance against explosive loads. The norm ISO 16933:2007 [8] rules full scale arena blast tests: it provides one hazard rating for glazing (see Tab. 2.1) and it classifies blast loads in terms of reflected pressure peak as well as positive impulse (see Tab. 2.2). For example, if a glazed façade is tested with a level 3 vehicle bomb type (80 kPa, 380 kPa·ms) and consequent damages are classified within level C in current hazard rating, one can use the code EXV25(C) to asses its blast resistance. For the sake of completeness, the norm ISO 16934:2007 [8] adopts the same approach to deal with the alternative testing procedure based on shock tube facility.

In more recent years, the Joint Research Centre (JRC) published several technical reports in order to give a comprehensive overview about the effects of explosions on structures. Karlos and Solomos [40] suggest an engineering approach for blast loading calculation on the basis of the most popular scientific literature. Moreover, they furnish some practical examples useful to understand how to estimate this type

[5]The drag coefficient is the ratio between two energy items. One corresponds to the energy required to overcome the drag forces at some definite velocity (numerator); the other corresponds to the kinetic energy associated with that velocity (denominator).

of loads. Also the report [41] broadly discusses on blast resistance of buildings and glazed façades. In particular, it clarifies how to calculate a shock wave loading action; it describes the material modeling of glass; it lists the principal testing methods; it shows how to conduct finite element analyses.

Hazard rating	**Hazard rating description**	**Definition**
A	No break	The glazing is observed not to fracture and there is no visible damage to the glazing system.
B	No hazard	The glazing is observed to fracture but the inner, rear face leaf is fully retained in the facility test frame or glazing system frame with no breach and no material is lost from the interior surface. Outer leaves from the attack face may be sacrificed and may fall or be projected out.
C	Minimal hazard	The glazing is observed to fracture. Outer leaves from the attack face may be sacrificed and may fall or be projected out. The inner, rear face leaf shall be substantially retained, with the total length of tears plus the total length of pullout from the edge of the frame less than 50 % of the glazing sight perimeter. Also, there are no more than three rateable perforations or indents anywhere in the witness panel and any fragments on the floor between 1 m and 3 m from the interior face of the specimen have a sum total united dimension of 250 mm or less. Glazing dust and slivers are not accounted for in the hazard rating. If by design intent there is more than 50 % pullout but the glazing remains firmly anchored by purpose-designed fittings, a rating of C (minimal hazard) may be awarded, provided that the other fragment limitations are met. The survival condition and anchoring provisions shall be described in the test report.
D	Very low hazard	The glazing is observed to fracture and significant parts are located no further than 1 m behind the original location of the rear face. Parts be projected any distance from the attack face towards the blast source. Also, there are no more than three rateable perforations or indents anywhere in the witness panel, and any fragments on the floor between 1 m and 3 m from the interior face of the specimen have a sum total united dimension of 250 mm or less. Glazing dust and slivers are not accounted for in the rating.

E	Low hazard	The glazing is observed to fracture, and glazing fragments or the whole of the glazing fall between 1 m and 3 m behind the interior face of the specimen and not more than 0,5 m above the floor at the vertical witness panel. Also, there are 10 or fewer rateable perforations in the area of the vertical witness panel higher than 0,5 m above the floor and none of the perforations penetrate more than 12 mm.
F	High hazard	Glazing is observed to fracture and there are more than 10 rateable perforations in the area of the vertical witness panel higher than 0,5 m above the floor, or there are one or more perforations in the same witness panel area with fragment penetration more than 12 mm.

Table 2.1: Hazard rating criteria for arena tests [8].

Classification code	**Mean peak air-blast pressure [kPa]**	**Mean compression phase impulse [kPa· ms]**	**Classification code**	**Mean peak air-blast pressure [kPa]**	**Mean compression phase impulse [kPa· ms]**
EXV45(X)	30	180	SB1(X)	70	150
EXV33(X)	50	250	SB2(X)	110	200
EXV25(X)	80	380	SB3(X)	250	300
EXV19(X)	140	600	SB4(X)	800	500
EXV15(X)	250	850	SB5(X)	700	700
EXV12(X)	450	1200	SB6(X)	1600	1000
EXV10(X)	800	1600	SB7(X)	2800	1500

Table 2.2. Classification criteria for vehicle bombs (on left) and for hand-carried satchel bombs (on right) [8].

A typical experimental set up, used for an open arena blast test, is shown in Fig. 2.6. The targets are disposed along a circular trajectory, while the charge is placed at the center. Glazing are fixed to cubicle and robust back structures made of steel, whose design is imposed by standard to not affect the dynamic behavior of samples. The test requires a planar ground surface and the absence of any obstacle along the shock wave propagation, avoiding reflection or turbulence phenomena. In

Fig. 2.6(a) we represent an explosive charge which lies on a frangible support. This is needed to "fictitiously" reproduce the situation of a bomb carried by a vehicle: the consequent shock front is supposed to be vertical. The measurement of the pressure time history is performed by pressure gauges fixed on different blocks made of concrete, that prevent spurious vibrations. All the blocks must respect specific limitations in terms of distances and angles with samples, as reported in Fig. 2.6(b). The different size of blocks, as well as their geometrical proportions, possibly lead to several errors. For this reason, further calculations could be necessary to fix them.

(a)

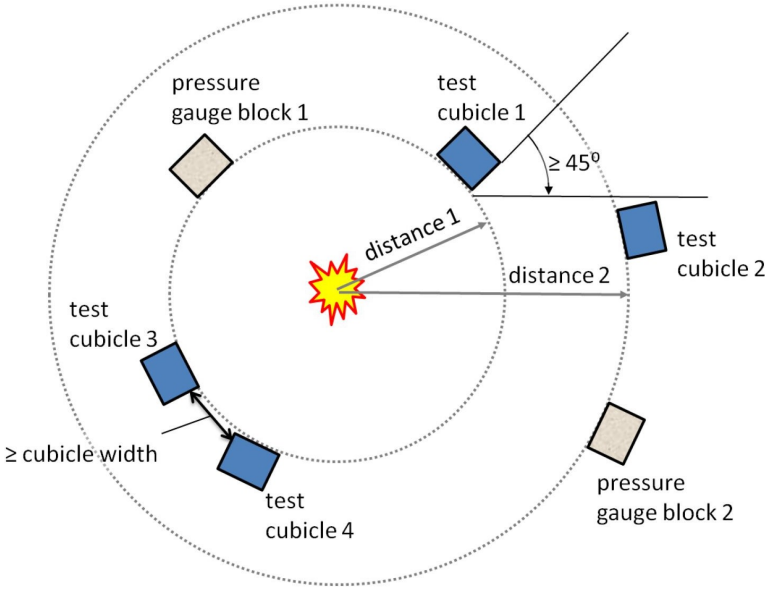

(b)

Figure 2.6. Open arena set-up used to test blast resisting glazing [41]. (a) Explosive charge in front of windows. (b) Schematic representation.

Alternatively, one can conduct experimental activity on glass plates by using a

shock tube (see Fig. 2.7). It can generate the proper shock wave by means of an explosive charge or, more simply, by means of compressed gas.

The first solution requires a tubular chamber characterized by a constant cross-section, inside which an explosion occurs. Once the explosive detonates, the shock front propagates along the tube forming a planar wave due to reflection phenomena against the internal surface. If the shock tube is opened at the end, overpressure drops and subsequent air-flow fluctuations produce the negative phase, interpreted by Friedlander equation.

If the blast impulse is originated by compressed gas, the shock tube is composed by two chambers separated by a steel diaphragm. They are filled with the same gas at different pressures and, sometimes, there is a variable cross-section to favor the expansion of gas. The shock front is created after the diaphragm rupture, which makes the compression wave travel toward the chamber with lower pressure. Inside the chambers, there are several reflection phenomena that must be managed by employing, for example, controllable valves. The time dependent pressure assumes a wave form similar to that of Friedlander equation and there exist numerical models to predict it on the basis of shock tube performances [42]. For further explanations we suggest to read the report [41]; a comparison of the existing blast tests can be found in [43].

2.1.4 The effects of negative phase

The suction phase of a generic blast load is usually neglected by standards inherent to glazing and windows. In fact, it is common to assume as linear the compression phase, in order to perform a synthetic characterization through the peak overpressure and the positive impulse. Here, the limitations of this approach are analyzed, by highlighting the importance of the negative phase for a correct dynamic response.

Consider a glass panel loaded with a uniform distributed pressure over its surface. The time dependent pressure is classified as EXV25 in accordance with norm ISO 16933:2007 [8]. The net action can be interpreted via Friedlander equation, where the reflected peak pressure and the positive impulse are set as $p_r = 80\,\text{kPa}$ and $i_r^+ = 380\,\text{kPa·ms}$. Since this category of arena test must be performed with 100 kg of TNT, we suppose $W_{\text{TNT}} = (1.7 \cdot 100)\,\text{kg}$ as equivalent mass of charge, by implicitly accounting for a surface burst. Once the scaled distance is calculated as

$$Z = \frac{R}{W_{\text{TNT}}^{1/3}} = \frac{25}{(1.71 \cdot 100)^{1/3}} = 4.51\,\text{kg/m}^{1/3}, \tag{2.15}$$

it is possible to use relations (2.5)-(3.32) and obtain the initial peak overpressure $p_0 = 35.40\,\text{kPa}$, as well as the time positive duration $T_d = 12.7 \cdot 10^{-3}\,\text{s}$. For what concerns the decay coefficient, we can solve the nonlinear equation

(a)

(b)

Figure 2.7. Shock tube facility denoted as "BlastStar" at Fraunhofer Ernst Mach Institute: (a) Complete shock tube. (b) Glazed panel fractured by an impulsive wave loading.

$$i_r^+ = \int_0^{T_d} p_r \left(1 - \frac{t}{T_d}\right) e^{-\frac{\beta}{T_d}t}\, dt = p_r T_d \left[\frac{1}{\beta} - \frac{1}{\beta^2}(1 - e^{-\beta})\right] \tag{2.16}$$

from which $\beta = 0.95$ is deduced. Possibly, one can first calculate the decay coefficient (2.9) and then deduce the time positive duration. The results are similar and, in absence of direct experimental evidence, both of procedures are assumed to be analogous. The negative reflection coefficient depends on scaled distance (2.11),

and it results $c_r^- = 1.80$. In conclusion, the loading pressure curve is obtained with relation (2.12). In the engineering practice, a simplified expression is often used: the compression phase can be approximated with a triangular law and by neglecting the subsequent suction phase. A new time positive duration $\tilde{T}_d = 9.5 \cdot 10^{-3}$ s is needed to equate the reflected positive impulses. So, for the case at hand, the linearized pressure function reads

$$q_{\text{lin}}(t) = \begin{cases} p_r \left(1 - \dfrac{t}{\tilde{T}_d}\right) & t \leq \tilde{T}_d \\ 0 & t > \tilde{T}_d \end{cases} . \tag{2.17}$$

Both of time histories are represented in Fig. 2.8.

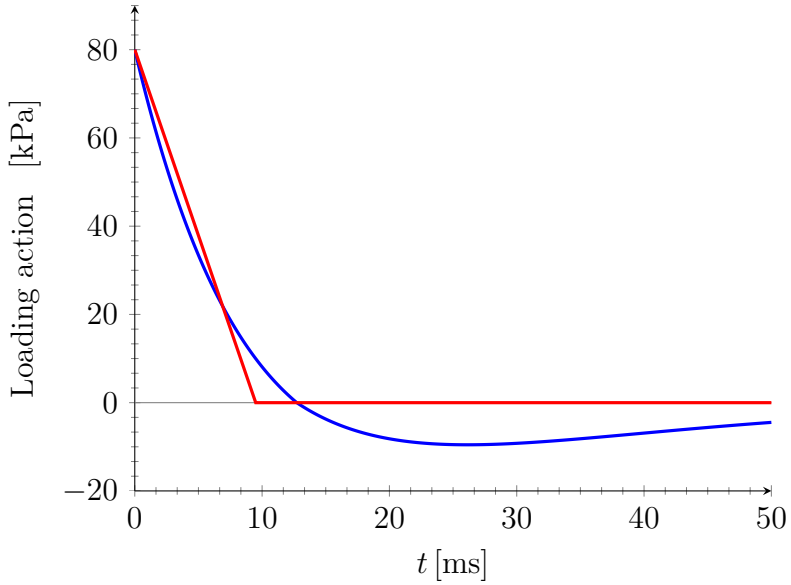

Figure 2.8. Time dependent pressure consequent to a reflected blast wave on plane surface: Friedlander relation (blue) and its linearized form (red).

The linear impulse is reputed to be on the safe side, because suction phase ideally counteracts the previous compression phase. However, this is not necessarily true for a glazed panel subjected to an impulsive loading action, inasmuch the negative phase can activate different vibration modes. Wei and Dharani [44] performed numerical analyses on laminated glazing subjected to blast loading. They discover that mid-span deflections associated to the negative phase could be as much as twice those caused by the positive phase. To this purpose, Teich and Gebbeken [37] elaborated a demarcation criteria for linear oscillating systems. Roughly, if inequality $T_d/T < 0.55e^{0.026Z}$ subsists, the underpressure phase increases the maximum deflection. As an alternative approach, one can formulate considerations based on the frequency

domain. Take a simply supported squared glass plate, with size $a \times b \times s = 2 \times 2 \times 0.01\,\mathrm{m}^3$, Young's modulus $E_g = 70 \cdot 10^9\,\mathrm{Pa}$, Poisson's ratio $\nu = 0.22$ and mass per unit area $\mu = (2500 \cdot s)\,\mathrm{kg/m}^2$. According to Kirchhoff-Love plate theory [45], the modal frequencies can be calculated as

$$f_{mn} = \frac{\pi}{2}\left(\frac{m^2}{a^2} + \frac{n^2}{b^2}\right)\sqrt{\frac{E_g s^3}{12(1-\nu^2)\mu}}, \tag{2.18}$$

where m and n are the mode numbers. Now, observe the graph in Fig. 3.6, which reports the Fourier transforms inherent to Friedlander's load and its linear approximation (previously introduced).

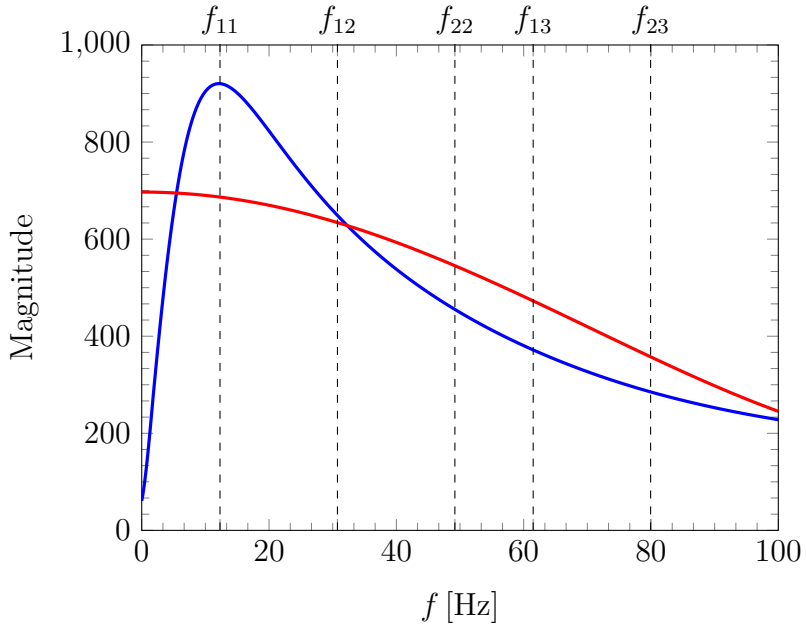

Figure 2.9. Magnitude–frequency diagram corresponding to the Fourier transforms of Friedlander equation (blue) its linearized form (red).

In the same figure, we represent also the first modal frequencies relative to the glass panel (f_{11}, f_{12}, f_{22}, f_{13}, f_{23}), that intersect at different heights the functions. For the frequency f_{11}, the Friedlander's load presents a peak much higher than the maximum level reached by the triangular impulse. This means that when linear approximation is used, frequency f_{11} is badly quantified within the dynamic response, while higher modal frequencies risk to be overestimated. These discrepancies can diminish or increase according to the blast parameters adopted (the decay coefficient above all). Correctly estimating the first frequency contribution is of paramount importance, because the associated modal shape is supposed to be dominant and

to maximize the work of loading pressure. For a quick comparison, different modal shapes are indicated in Fig. 2.10, from which it is evident how higher modes result to be less critical for the state of stress characterizing a plate.

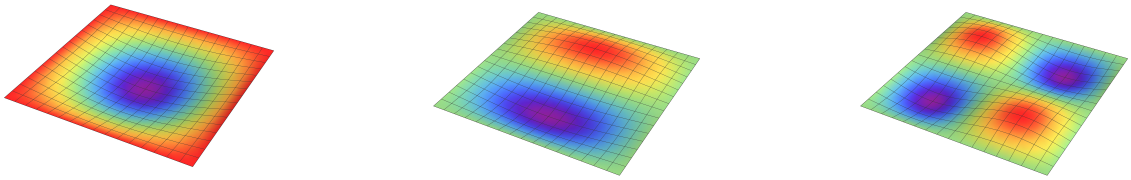

(a) $f_{11} = 12.30\,\text{Hz}$ (b) $f_{12} = 30.75\,\text{Hz}$ (c) $f_{22} = 59.03\,\text{Hz}$

Figure 2.10. First modes of vibration for a simply supported $2 \times 2\,\text{m}^2$ square glass plate with thickness $s = 10\,\text{mm}$, and corresponding natural frequencies.

Teich et al. [46] studied the role of negative phase about a loaded cable-net façade, whose dynamic behavior is geometrically nonlinear. Although there is not a pronounced influence, for low level blast threats (such as ISO EXV45), the negative phase often determines the maximum absolute deflection. Rigby et al. [47] summarize existing methods to calculate negative phase action; they provide numerical examples showing the importance of its correct calculation.

In conclusion, the complete impulse provides a more precise and safe indication about what is the load experienced by a glazed panel during an explosion. Hence it will be used in the following chapters.

2.2 The pendulum test on glazed surfaces

Norms like the EN 12600 [2] have defined a standardized soft-body test, consisting in a twin pneumatic tyre of mass $50 \pm 0.1\,\text{kg}$, of the same type used for automotive applications and inflated with a nominal internal pressure of $3.5 \pm 0.2\,\text{bar}$, hanging from a rope so to form a pendulum. In the position at rest the rope is vertical and the tyres just touch the glass panel. The impact test is done by dropping the pendulum from a certain height and by verifying that the glass does not break or, if it breaks, the fragments are not harmful. To fulfill this second requirement, glass should be either tempered[6], so that it breaks into little smooth pieces, or laminated

[6]In tempered glass, heating and rapid cooling induces a beneficial eigenstress. When glass is broken, the stored strain energy is suddenly released and the glass breaks in little pieces, whose size depends upon the level of tempering.

with polymeric interlayers[7], that retain the shards thanks to the polymer-to-glass adhesion.

The technical procedure TRAV [48], followed by other recent normative proposals [49], regulates the use of glass panes for various applications, especially barriers and façades, distinguished for the type of fixing devices (pointwise or continuous). There has been considerable theoretical research on this subject in the last twenty years [50, 51, 52, 53, 54] but, despite this, the procedure to assess the glass capacity remains essentially experimental. This implies some difficulties. First of all, the procedure has a cost for the experiments. Secondly, in the case of a complex underlying load-bearing structure, it is difficult to simulate in-lab, on a reduced-scale mock-up, the real boundary conditions of the plate by connecting it to a frame via springs and, possibly, dashpots. If the test is done on the real structure it is very unpleasant, if the result is negative, to re-design and substitute the glazing once it has been already installed. Therefore, there is a motivated need for a predictive theoretical tool able to reproduce, analytically and/or numerically, the results of the impact pendulum test.

Noteworthy theoretical and experimental work has been conducted in the area of contact dynamics in the past decades, to define consistent models for low-speed impacts. The most used is the "contact force" approach, where the contact action is defined as a function of time. It is then possible to use standard finite element (FE) software to analyze, in the equivalent static regime, the state of stress in the glass panel and, hence, predict failure, modulo the assessment of the effective value of the glass strength under impulsive (short duration) actions [55]. In the "compliant contact force model", the contact force between two objects is explicitly defined as a continuous function of the local deformation and its rate. Since the pioneering work by Hertz [56], many authors have developed the normal force in the context of quasi-static contact analysis of elastic bodies. The nonlinear viscoelastic contact force model by Hunt and Crossley [57] has been experimentally validated [58] and it is now currently used in multibody dynamics. Models of this kind usually assume that the deformation of the impinging bodies can be modeled with a nonlinear contact spring, so that the problem can be reduced to a two degree of freedom (2-DoF) system, composed of rigid masses joined by non-linear springs and viscoelastic elements.

However, the soft-body impact test on glazed surfaces is quite peculiar for a number of reasons. First of all, the glass panel is a slender plate whose (nonlinear) vibrations may interact with the impacting body. A computational technique for modeling impacts on laminated panels, while considering the glass breakage phase,

[7]Laminated glass is a sandwich structure where glass plies are permanently coupled with polymeric interlayers with a process at high temperature and pressure in autoclave.

was implemented in [59] by using an explicit FE solver. A simplified numerical model based upon the Rayleigh-Ritz method, employing the Ritz vectors associated with the deformation under fundamental static load cases, was proposed in [60], but nonlinear geometric (membrane) effects in the glass were not considered appropriately. A simplified model for easy engineering verification was presented in [53] by using equivalent static loads derived from a 2-DoF model, and compared with more sophisticated numerical methods of analysis. More important, one should recall that the impactor, in order to reproduce the consistency of a human body, is made with commercial pneumatic tyres, whose mechanical properties are uncertain. The procedure proposed in [54] to characterize the soft impact in terms of total impulse, duration and maximum acceleration, has indicated a wide dispersion of results, also when using the same testing equipment. The careful experimental measurements of [61] have demonstrated that the energy loss during the impact is produced during the contact stage due to the deformation of the tyres and the glass plate, a finding that indicates the crucial role of damping for the coupled system.

More in general, since impactor is much softer than glass, the contact area can substantially vary during the impact, on the contrary to what happens with rigid impactors or projectiles [62]. This results in a free-boundary problem, where the size and form of the contact area needed to be determined. Indeed this effect is of paramount importance, because the form and the size of the region on which the contact force is distributed can considerably affect the state of stress in a plate [63]. Schneider et al. [51] performed a series of tests with the standardized impacting pendulum, by defining a model in which the stiffness of the tyre is schematized as a simple linear spring, and carefully considering the evolution in time of the imprint. By assuming that the tyre pressure does not vary during the impact, they proposed a FE model of the impactor as a set of volume elements implemented in `ANSYS`, which simulates a homothetic enlarging imprint of elliptical shape as the contact force increases. This model was simplified in the problem of a concentrated mass (the tyre) connected to a plate (the glass panel) through a spring, and the role of aforementioned solid model was to proportionate the contact area. To our knowledge, a similar-in-type analysis is the base for an element available in the library of the software `SJ Mepla`, commonly used nowadays for structural glass design. However, the explanatory documentation for `SJ Mepla` [64] does not mention specifically what types of elements are used in the numerical simulations; moreover, no dissipation is considered by the software and the possibility of multiple impacts due to the bouncing of the pendulum is ruled out. What is more, `SJ Mepla` allows to consider only one glass panel, either isolated or framed, so that the deformability of the rear load-bearing structure can only be simulated through elastic constrains.

In order to develop a rational and practical engineering design method, it is important to propose ready-to-use analytical models, which allow to understand which are the effects and their real importance. On the other hand, it would be

useful to define a FE contact model that could be implemented in a wide range of commercial software for structural analysis. A software of this kind is usually based upon the assembly of beams, which are the elements of most practical use. More sophisticated multi-purpose software, like `ABAQUS` or `ANSYS`, can handle unilateral contacts using ad hoc elements, albeit at the price of a noteworthy computational effort, but such softwares are not commonly available in design companies and, in any case, their use within complex framed structures is time consuming in the input procedure.

Here, through a simplification *à la* Rayleigh that permits to consider an effective equivalent stiffness and inertia for a glass panel, we start with a simplified analysis where the problem of the impacting pendulum is reduced to a 2-DoF damped system. Apart from the nonlinearities consequent to the assumed *unilateral* contact of the springs, this model has been already used by many authors [53, 54], but it is used here to recognize explicitly that there are cases of practical importance for which the inertia of plate can be neglected. In cases of this kind, the problem can be solved with energetic considerations, accounting for the geometric nonlinearities of the plate [63] in a very rapid and ready-to-use way. A simple analytical test is then proposed to recognize which are the cases for which such an energetic method is accurate. As a second step, we develop a contact FE model, consisting of nonlinear beam elements, and we implement it in the commercial software `Straus7`, commonly used for structural analysis. Comparisons with the experiments recorded in [65] and results obtainable with `SJ Mepla` and `ABAQUS`, confirm the accuracy of the proposed FE tool, whose greatest advantage is that it can be interfaced with complex structural models, as illustrated in paradigmatic examples. Although only monolithic glass plates have been considered here, by using the concept of effective thickness [66], all the presented methods could in principle be used also for laminated glass, possibly accounting for the post-glass breakage phase [67, 68]. The content follows [69].

2.2.1 The 2-DoF lumped element model

The dynamic problem of an impacting twin-tyre pendulum [2] is first schematized with the simplest 2-DoF system. The model is similar to that proposed in [51, 53], but it differs from that because we consider unilateral contact and dissipation, whose importance has been evidenced in [61]. This model is here used to recognize the importance of the various contributions which govern the phenomenon in terms of inertia, damping and elasticity.

In the linear case, the dynamic response of the glass panel can be reduced to that of a harmonic oscillator with Rayleigh's method [70]. We consider the glass

as a plate, simply supported on the four sides[8], and we place the origin of our reference system at one of its corners, with axes parallel to the borders. The out-of-plane displacement field $w(x, y, t)$ is defined through the shape function $\psi(x, y) = \sin(\pi x/a)\sin(\pi y/b)$, which respects the boundary conditions of the plate, in the form

$$w(x, y, t) = \psi(x, y)\delta_p(t), \tag{2.19}$$

where $\delta_p(t)$ is the displacement at the center of panel. The selected shape function is in agreement with the first vibration mode of the plate, but it rules out the higher modes. The forthcoming comparisons with FE analyses confirm that the approximation made in (2.19) can provide good results, but this may be consequent to the fact that, in all the considered cases, the impact occurs in the central area of plate. We expect that when the impact is eccentric, also higher modes of vibration may become involved and, therefore, the simple 2-DoF approach should be considered with care.

For what concerns the inertial properties, if ρ is the mass per unit volume and $a \times b \times s$ the dimensions of panel, the effective mass m_p reads

$$m_p = \rho s \int_0^a \int_0^b \psi(x, y)^2 \, dxdy. \tag{2.20}$$

By denoting with E_g the Young's modulus, ν the Poisson's ratio of glass and $D = E_g s^3/12(1-\nu^2)$ the flexural rigidity of the plate, the effective stiffness k_p takes the form

$$k_p = D \int_0^a \int_0^b \left[\frac{\partial^2 \psi(x,y)}{\partial x^2} + \frac{\partial^2 \psi(x,y)}{\partial y^2} \right]^2 - 2(1-\nu) \left[\frac{\partial^2 \psi(x,y)}{\partial x^2} \frac{\partial^2 \psi(x,y)}{\partial y^2} - \left(\frac{\partial^2 \psi(x,y)}{\partial x \partial y} \right)^2 \right] dxdy. \tag{2.21}$$

The impacting tyres are schematized as a simple pendulum hinged at the top with a rope of length r. The mass of the tyres $m_t = 50\,\text{kg}$ is set according to standards [2]. The deformability of the tyres during impact is modeled with a spring of stiffness $k_t = 400\,\text{kN/m}$ as in [51].

[8]The way in which the plate is supported at its borders strongly influences the actual dynamic response. For this reason, the standard [2] carefully specifies how to clamp the panel along its perimeter. The geometry of the clamping frame is prescribed as well as the presence of specific rubber strips on the edges of the panel to increase adherence. The inner part of the clamping frame shall be rigidly connected to the experimental apparatus, in such a way that it can withstand the transmitted forces with negligible displacements.

As shown in Fig. 2.11, the Lagrangian coordinate adopted to describe the motion of pendulum is the angle $\theta_t(t)$, that the stretched rope forms with the vertical direction. In general, we will suppose that the first impact occurs at $t = 0$, which corresponds to the initial condition $\theta_t(0) = 0$. Experience suggests that, after the first impact, the displacement of the plate $\delta_p(t)$, and also the corresponding displacement of the tyre $\delta_t(t)$, are small with respect to r. Consequently, for $t \geq 0$ one can assume that $\theta_t \ll 1$, so $\sin\theta_t(t) \cong \theta_t(t)$, and $\delta_t(t) \cong r\theta_t(t)$. This implies that the vertical component of tyres displacement is neglected. If h is the drop height and g indicates the gravitational acceleration, the second initial condition can be found by equating the potential energy with the kinetic energy, i.e., $m_t g h = \frac{1}{2} m_t \dot{\delta}_t(0)^2$ which provides $\dot{\theta}_t(0) = \sqrt{2gh}/r$.

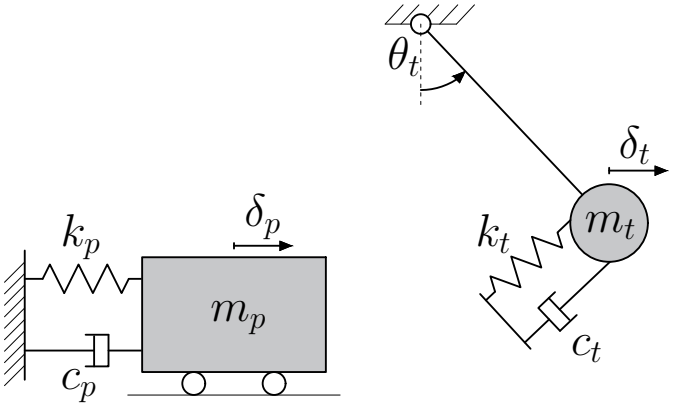

Figure 2.11. Simplified 2-DoF system. The panel is schematized as a harmonic oscillator with effective mass m_p, stiffness k_p, damping coefficient c_p and degree of freedom $\delta_p(t)$. The impacting twin-tyre is a simple pendulum with mass m_t and length r, with added stiffness k_t, damping coefficient c_t and degree of freedom $\delta_t = r\sin\theta_t(t) \simeq r\,\theta_t(t)$.

The 2-DoF system has been studied in both the damped and the undamped configuration, where the viscous dampers are located as in Fig. 2.11. The damping coefficient for the tyre pendulum system c_t is assumed within the range 5-10% of the critical damping value $c_{ct} = 2m_t\sqrt{g/r}$. For what concerns the damping coefficient for the panel c_p, this is assumed to be 0.1-5% of the critical value $c_{cp} = 2\sqrt{m_p k_p}$. Two systems of equations are used to solve the impact problem, one for the coupled and the other for the uncoupled system. According to the sign convention adopted, the *coupled* system is characterized by the condition $\delta_p(t) - \delta_t(t) \geq 0$ (the tyres remain attached to the glass plate) and the motion is obtained by solving a system of two differential equation, whose initial conditions are $\delta_p(0) = \dot{\delta}_p(0) = \theta_t(0) = 0$ and $\dot{\theta}_t(0) = \sqrt{2gh}/r$. The equations of motion take the classical form

$$m_p\ddot{\delta}_p + c_p\dot{\delta}_p + c_t(\dot{\delta}_p - r\dot{\theta}_t) + k_p\delta_p + k_t(\delta_p - r\theta_t) = 0, \tag{2.22a}$$

$$m_t r\ddot{\theta}_t + c_t(r\dot{\theta}_t - \dot{\delta}_p) + k_t(r\theta_t - \delta_p) = 0\,. \tag{2.22b}$$

The *uncoupled* problem is associated with the event $\delta_p(t) - \delta_t(t) \leq 0$, when the pendulum detaches from the panel. Now the governing equations are that of a harmonic oscillator for the glass panel, i.e., $m_p\ddot{\delta}_p + c_p\dot{\delta}_p + k_p\delta_p = 0$, and that of a simple pendulum for the tyre, i.e., $\ddot{\theta}_t r + g\theta_t = 0$. The complete motion is found by solving one of the system of equations according to the condition $\delta_p(t) - \delta_t(t) \geq 0$ or $\delta_p(t) - \delta_t(t) \leq 0$.

The results from this simple approach are compared with the findings of the experimental campaign of [65], for a panel of size $a = 876\,\text{mm}$, $b = 1938\,\text{mm}$ and $s = 10\,\text{mm}$, impacted at the center by a soft-body with a drop height $h = 450\,\text{mm}$. We set $r = b$ and, for what concerns the glass, we take $E_g = 70000\,\text{MPa}$, $\nu = 0.22$ and $\rho = 2500\,\text{kg/m}^3$. We consider both undamped and damped systems, by assuming for the latter case $c_p = 0.05\,c_{cp}$ and $c_t = 0.1\,c_{ct}$.

Fig. 2.12(a) compares the accelerations of tyres $\ddot{\delta}_{t,d}(t)$ and $\ddot{\delta}_{t,nd}(t)$, obtained with the *damped* and the *undamped* model respectively, with the experimental results $\ddot{\delta}_{t,e}(t)$ [65]. The corresponding values for the acceleration at the central point of glass panel[9], i.e., $\ddot{\delta}_{p,d}(t)$, $\ddot{\delta}_{p,nd}(t)$ and $\ddot{\delta}_{p,e}(t)$, are shown in Fig. 2.12(b). Remarkably, despite the simplicity of the approach, the shape of the graphs is in qualitative agreement with the experiments. The corresponding errors are summarized in Table 2.3, from which it is clear that the damped model fits the experiments better than the undamped model. The instant in which the tyre detaches from the panel is clearly recognizable from the graphs at $t \simeq 0.04 \div 0.05\,\text{s}$.

	Experimental data	Damped 2-DoF model	Undamped 2-DoF model	Error in damped model [%]	Error in undamped model [%]
$\ddot{\delta}_t(t)\,[\text{m/s}^2]$	196.40	216.63	228.21	10.30	16.20
$\varepsilon_x \cdot 10^3$	1.61	1.80	1.83	11.80	13.66
$\varepsilon_y \cdot 10^3$	1.10	1.12	1.15	1.82	4.55

Table 2.3. Pendulum test with drop height $h = 450\,\text{mm}$ on $876 \times 1938 \times 10\,\text{mm}^3$ glass panels. Comparison of maximum tyre acceleration $\ddot{\delta}_t(t)$ and maximum strains ε_x and ε_y at panel center, from the experimental data of [65] and the analytical results obtained from the modified Rayleigh's approach.

[9]In the tests of [65], the accelerometer is not exactly placed at the center of glass panel; hence, we have re-scaled the experimental results according to the shape function $\psi(x, y)$.

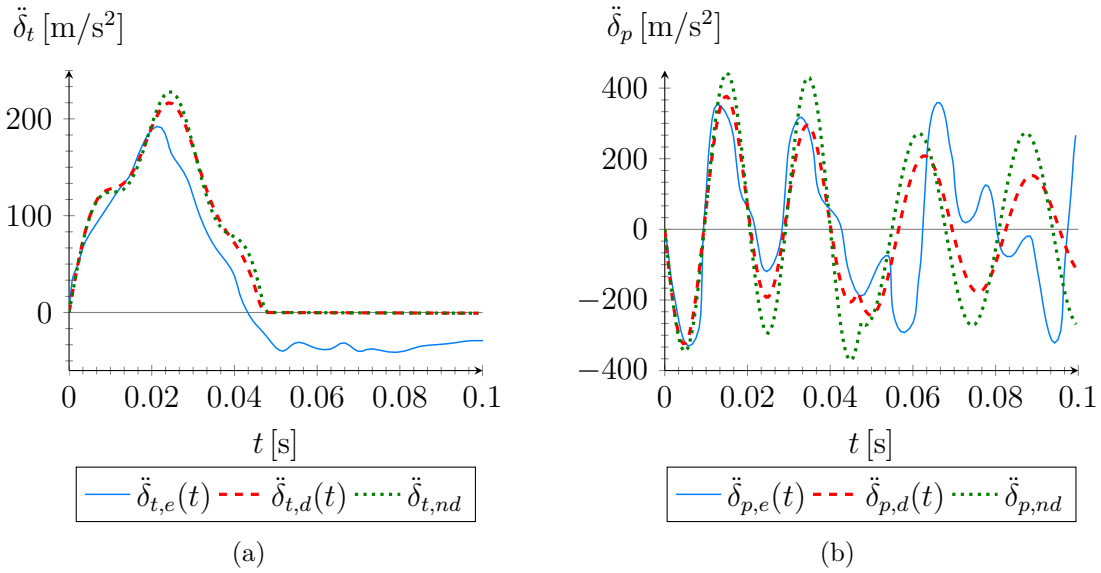

Figure 2.12. Pendulum test with drop height $h = 450\,\text{mm}$ on $876 \times 1938 \times 10\,\text{mm}^3$ glass panels. (a) Acceleration of the tyre experimentally measured $\ddot{\delta}_{t,e}(t)$ and calculated with the damped $\ddot{\delta}_{t,d}(t)$ and undamped models $\ddot{\delta}_{t,nd}(t)$. (b) Corresponding values for the accelerations at the panel center $\ddot{\delta}_{p,e}(t)$, $\ddot{\delta}_{p,d}(t)$ and $\ddot{\delta}_{p,nd}(t)$.

Rayleigh's method is in general accurate for displacements but not for stresses. This is because the actual local curvature of the deformed surface, from which the state of stress depends, may be not accurately catched by the assumed shape function because of the load concentrated on the contact surface. To overcome this difficulty, we propose a "post-processing calculation", here referred to as the *modified Rayleigh's approach*. By assuming that the gross time dependent displacement in both tyres and panel are well estimated through Rayleigh's method, we can determine the maximum contact force through the properties of tyres, here modeled by the stiffness k_t and the damping c_t. From this, it is possible to directly calculate the state of stress in glass by smearing such force on the imprint area. The glass panel is also subjected to the inertial forces, which depend upon the acceleration of the corresponding points of the plate. We assume that such forces can be estimated through the second derivative of the out-of-plane displacement (2.19) with respect to time, established through Rayleigh's approach. The actual deformation will differ from the aforementioned estimation essentially because of the load concentrated on the imprint; but, the greatest difference are certainly in terms of local curvature, which affects the state of stress, and not in terms of absolute displacement, which is associated with the inertial forces. In conclusion, we consider the plate loaded by the contact forces transmitted by tyres and inertial forces, calculated as indicated

before. The corresponding state of stress can be determined either analytically, in series expansions, or numerically.

It is convenient, for the forthcoming considerations to distinguish, in the displacement field of the panel, the parts associated with the inertial forces and the contact forces. Observe that such fields are not those obtained with the shape function used in the Rayleigh's method, although they are determined a posteriori by using the results of such method.

The inertial contribution $w_i(x, y, t)$ can be directly computed [71] and it reads

$$w_i(x, y, t) = \frac{-\rho s \ddot{\delta}_p(t)}{\pi^4 D \left(\frac{1}{a^2} + \frac{1}{b^2}\right)^2} \sin\left(\frac{\pi x}{a}\right) \sin\left(\frac{\pi y}{b}\right). \tag{2.23}$$

For what concerns the contribution of the contact forces, here called $w_f(x, y, t)$, we assume that it can be approximately calculated by considering the pressure of tyres p exerted on a time dependent square of area $A(t)$. The centroid of this area has coordinates $(\xi, \eta) = (a/2, b/2)$ and it is delimitated by four edges, of size $u(t) = \sqrt{A(t)}$, parallel to the borders. The spring force $F_k(t)$ from the impactor, the force transmitted by the damper $F_c(t)$ and the tyres print $A(t)$, assuming a constant tyres pressure $p = 3.5\,\text{bar}$, can be calculated as

$$F_k(t) = [\delta_p(t) - \delta_t(t)]k_t, \tag{2.24a}$$
$$F_c(t) = [\dot{\delta}_p(t) - \dot{\delta}_t(t)]c_t, \tag{2.24b}$$
$$A(t) = [F_k(t) + F_c(t)]/p. \tag{2.24c}$$

Hence, the corresponding displacement field is estimated by summing up the leading terms of the series [71]

$$w_f(x, y, t) = \frac{1}{\pi^4 D} \sum_{m=1}^{\infty} \sum_{n=1}^{\infty} \frac{a_{mn}}{\left(\frac{m^2}{a^2} + \frac{n^2}{b^2}\right)^2} \cdot \sin\left(\frac{m\pi x}{a}\right) \sin\left(\frac{n\pi y}{b}\right), \tag{2.25}$$

where

$$a_{mn} = \frac{16p}{\pi^2 mn} \sin\left(\frac{m\pi\xi}{a}\right) \sin\left(\frac{n\pi\eta}{b}\right) \cdot \sin\left(\frac{m\pi u(t)}{2a}\right) \sin\left(\frac{n\pi u(t)}{2b}\right). \tag{2.26}$$

Therefore, the (post-processed) displacement field of the panel $w_p(x, y, t)$ results to be

$$w_p(x, y, t) = w_i(x, y, t) + w_f(x, y, t), \tag{2.27}$$

from which the strains on the plate surface read

$$\varepsilon_x = \frac{s}{2}\frac{\partial w_p^2(x, y, t)}{\partial x^2}, \tag{2.28a}$$

$$\varepsilon_y = \frac{s}{2}\frac{\partial w_p^2(x, y, t)}{\partial y^2}. \tag{2.28b}$$

The strains at the center of panel, obtained from the undamped ($\varepsilon_{x,nd}$ and $\varepsilon_{y,nd}$) and the damped model ($\varepsilon_{x,d}$ and $\varepsilon_{y,d}$), are compared in Fig. 2.13 with the experimental measures of Pacios et al. [65] ($\varepsilon_{x,e}$ and $\varepsilon_{y,e}$). The peak of the curves is reached approximately at the same time and the shape is qualitatively similar. The differences between the peak values are recorded in Table 2.3. The very simple analytical model seems accurate enough, especially when damping is considered[10]. The errors in terms of strains are of the order of 10%, but it should be observed that this is a *linear* analysis, which neglects second order geometric effects in the plate (membrane stress). We will show in the sequel how the second order effects can be taken into account to improve the accuracy. In any case, if the strains were directly calculated by using the out-of-plane displacement (2.19), i.e., without using the *modified* Rayleigh's approach, the errors would be higher than 30%.

The level of approximation that can be obtained by using the simple 2-DoF approach may not appear particularly high, but one should also consider that the testing apparatus itself carries a noteworthy degree of uncertainty[11]. Hence, one cannot expect to reproduce, with the utmost accuracy, the results of experimental tests by using a simple numerical model, where all the variables that govern the complex dynamic response are combined into one parameter k_t. This represents the equivalent stiffness of the twin-tyre pendulum and, implicitly, can also take into account, albeit partially, the compliance of the plate supports. We have performed a sensitivity analysis for the parameter k_t, which represents the only variable quantity. The mass of the impactor, as well as the mechanical properties of the plate, should be assumed to be deterministic, because they are affected by a much lower level

[10]These experiments consider monolithic glass only, but we infer that the viscoelasticity of the polymeric interlayer may render the damping effect even more important in the case of laminated glass, as indicated by other studies [52, 72, 73].

[11]The tyres mentioned in [2] are commercial tyres, not any more under production, so that laboratories sometimes are forced to use other types of tyres. Moreover, the stiffness of rubber varies with aging and temperature. In addition, the vibrations may be strongly affected if the clamping frame of the glass plate is not rigidly connected to a fixed support.

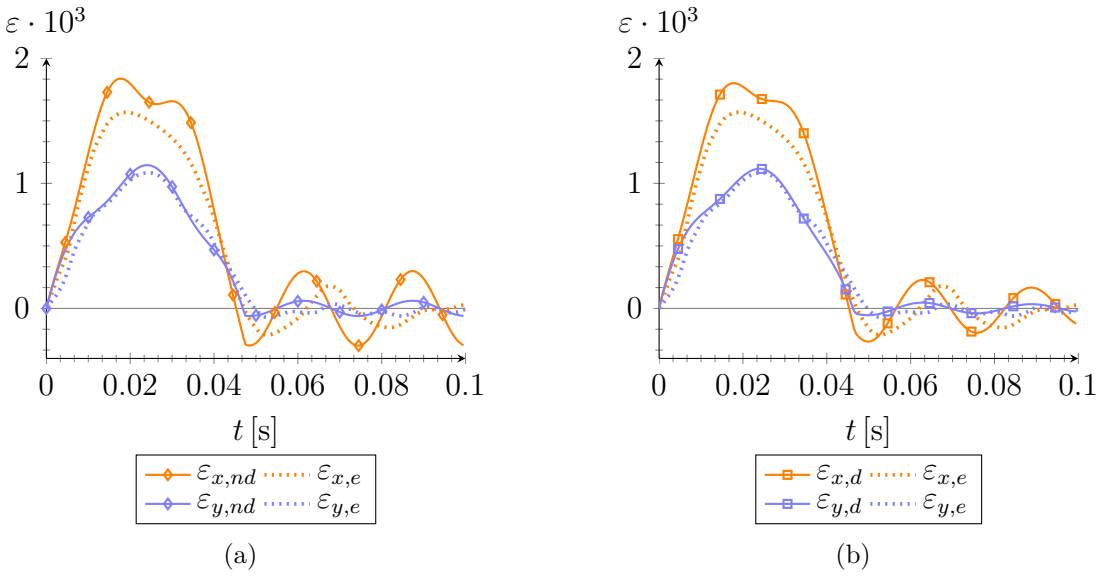

Figure 2.13. Pendulum test with drop height $h = 450\,\text{mm}$ on $876 \times 1938 \times 10\,\text{mm}^3$ glass panel. Experimentally-measured strains at the panel center ($\varepsilon_{x,e}$ and $\varepsilon_{y,e}$) compared with the predictions from (a) the undamped model ($\varepsilon_{x,nd}$ and $\varepsilon_{y,nd}$) and (b) the damped model ($\varepsilon_{x,d}$ and $\varepsilon_{y,d}$).

of uncertainty. From this analysis, it is clear that the acceleration and the strains increase as k_t becomes higher with respect to the considered value $k_t = 400\,\text{kN/m}$, whereas a lower value allows to better estimate the strains, in particular the maximum value of ε_x, but not the accelerations. In general, by using $k_t = 400\,\text{kN/m}$, as indicated in [51], a good compromise is achieved.

2.2.2 Energetic approach

We present an energetic approach that implies considerable simplifications at the price of neglecting some contributions during the analysis. In particular, we will show that when the inertia of panel is negligible, a straightforward calculation allows to accurately determine the state of stress taking into account second order effects.

Energetic approach with nonlinear analysis

The analysis through the modified Rayleigh's approach of Section 2.2.1 permits to distinguish the contribution in terms of strain associated with the inertial forces ($\varepsilon_{x,i}$, $\varepsilon_{y,i}$) and the contact forces from the tyres print ($\varepsilon_{x,f}$, $\varepsilon_{y,f}$). The corresponding values from the damped model are separately plotted in Fig. 2.14 together with their sum (ε_x, ε_y). What should be noticed is that the peak values are determined

by the sole part due to the contact force, being the inertial contribution of secondary importance. Indeed, the effective mass of the panel (2.20) is quite small, because in a simply supported plate the displacement in proximity of the constrained edges is limited.

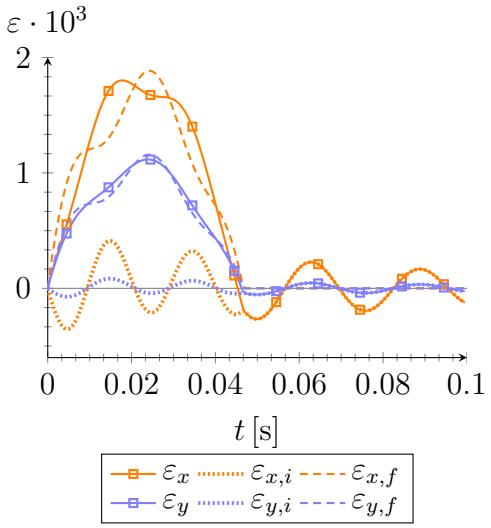

Figure 2.14. Decomposition of the strains (ε_x, ε_y) in the part due to the inertia of the panel ($\varepsilon_{x,i}$, $\varepsilon_{y,i}$) and those associated with the contact forces from the tyre print ($\varepsilon_{x,f}$, $\varepsilon_{y,f}$).

The analysis of the 2-DoF system of Fig. 2.11 can be greatly simplified in the limit $m_p \to 0$. The resulting scheme is reported in Fig. 2.15, composed by the single mass of tyres m_t, the stiffness of panel k_p and the stiffness of the impacting body k_t. The advantage of this schematization is that one can readily consider second order bending effects in the plate through a nonlinear spring k_p, as it will be shown later on.

In problems of this type, the intrinsic damping of the glass plate is not expected to play a decisive role in terms of peak values for stress and deflections, immediately after the impact, since the impulsive character of the impinging action is such that intrinsic viscous forces have not enough time to dissipate energy. However, when considering the successive oscillations, the intrinsic viscosity of the glass plate should be taken into account in addition to the viscosity of the tyres and of plate supports. It has been discussed by Amabili [74, 75, 76] for the case of plates made of steel that the intrinsic damping may have a nonlinear character, which becomes dominant for sufficiently large amplitudes. In particular, experiments [74] have shown as the damping coefficient may be more than six times larger than that corresponding to infinitesimal vibrations when the amplitude is about twice the thickness of the plate. Therefore, in order to reproduce the response in the long term after the impact,

further experimental activity is required to assess the intrinsic damping coefficient of glass and its possible nonlinear dependence upon the vibration amplitude, but this is not the scope of the present work.

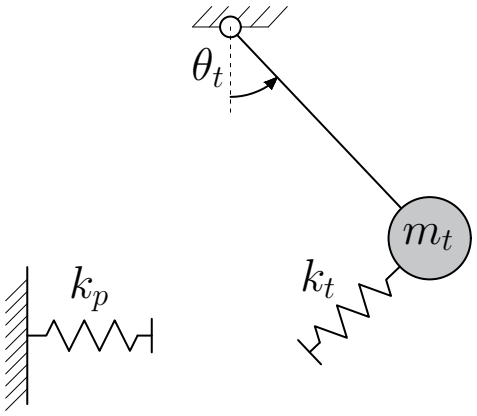

Figure 2.15. The dynamic system obtained by neglecting the inertia of the plate, composed by the tyres mass m_t, the plate stiffness k_p and the tyres stiffness k_t.

The effective value of k_p may be estimated analytically but, more rapidly, by using a standard FE geometric nonlinear analysis. It is important to observe that, by considering average dimensions of plates and the tyres pressure $p = 3.5$ bar, the resulting stiffness k_p does not depend on the tyres print area $A(t)$. To illustrate, consider again the $876 \times 1938 \times 10\,\mathrm{mm}^3$ simply supported plate. Fig. 2.16 shows the displacement at the center of panel as a function of the applied force F, either concentrated in one point or distributed on a square area of size $100 \times 100\,\mathrm{mm}^2$ (as obtained with the FE code `Straus7` in a linear or geometric nonlinear analysis). Although it is well known that results are very different in terms of stress (under a concentrated force the stress grows unboundedly in a plate), the maximum displacement is identical in practice. In fact, as already mentioned in Section 2.2.1, the deformations are quite different in terms of local curvature, but not in terms of global displacement. Therefore, the effective stiffness k_p can be directly calculated with a numerical experiment, considering a plate under a concentrated force, irrespectively of the imprint area on which the contact force is distributed.

Once the response of the nonlinear spring k_p has been estimated through its force vs displacement constitutive law $F(\delta)$, the model of Fig. 2.15 can be used to get the correct dynamic response in terms of displacement. In particular, the maximum force transmitted to the panel can be calculated from energy balance, since the maximum value of the strain energy, in both k_p and k_t, is certainly reached when the mass m_t is at rest, i.e. the kinetic energy is null. Hence, one can write

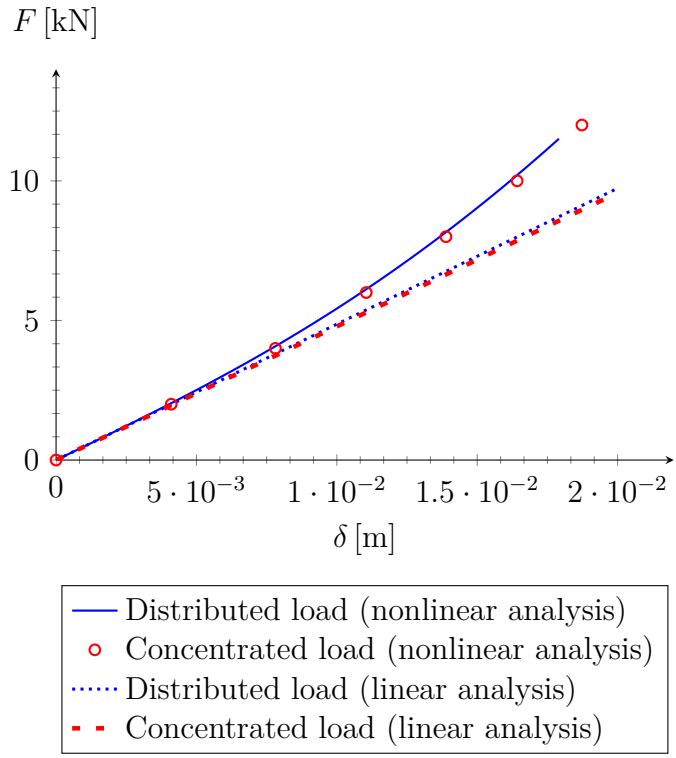

Figure 2.16. Simply supported glass panel $876 \times 1938 \times 10\,\mathrm{mm}^3$ under the force F, either concentrated at he center or distributed on a $100 \times 100\,\mathrm{mm}^2$ square area. Linear and geometric nonlinear analysis.

$$m_t g h = \int_0^{\delta^*} F(\delta)\, d\delta + \frac{1}{2k_t}[F(\delta^*)]^2, \tag{2.29}$$

where δ^* denotes the maximum displacement of the nonlinear spring k_p. The second term indicates the strain energy stored in the tyres, here modeled with a linear spring k_t, but of course one could consider nonlinear effects also in this contribution. From (2.29) one can find the value of δ^* and, consequently, the contact force $F(\delta^*)$. In order to determine the state of stress in the panel, one calculates[12] the print area $A(\delta^*) = F(\delta^*)/p$ by setting $p = 3.5\,\mathrm{bar}$ and then performs, a posteriori, a standard FE analysis to obtain the state of stress. In conclusion, one considers the model of Fig. 2.15 to calculate the displacement, and post-processes the data to obtain the state of stress.

[12]The inflation pressure may slightly vary during the impact, but its variation is a second order quantity and it is certainly negligible if the tyre is compliant. This is a general assumption reported in textbooks on transportation technology [77].

For the same case of Section 2.2.1, with $m_t = 50\,\text{kg}$, $k_t = 400\,\text{kN/m}$ and the constitutive law $F(\delta)$ derived from Fig. 2.16, we achieve the results summarized in Table 2.4. Here, we also show the values obtained in a nonlinear dynamic analysis with the software `SJ Mepla`. The maximum errors for the stresses σ_x and σ_y, as well as the maximum displacement δ_p, remain within the order of 3%.

	Energetic Approach: nonlinear analysis	`SJ Mepla`: dynamic nonlinear analysis	Error [%]
δ_p [m]	0.0171	0.0176	2.84
σ_x [MPa]	134.7	131.1	2.75
σ_y [MPa]	104.9	105.0	0.01

Table 2.4. Pendulum test with drop height $h = 450\,\text{mm}$ on $876 \times 1938 \times 10\,\text{mm}^3$ glass panels. Maximum stresses σ_x, σ_y and displacement δ_p. Results from the nonlinear energetic balance and from `SJ Mepla` dynamic nonlinear analysis.

Energetic approach with linear analysis

The energetic approach simplifies in the linear case to reach formulas in closed form, whose main advantage is that they can be readily implemented and solved. By doing so, the energetic balance (2.29) reads

$$m_t g h = \frac{1}{2} F \delta_p(F) + \frac{1}{2}\frac{F^2}{k_t}\,, \tag{2.30}$$

where

$$\delta_p(F) = \frac{4F}{\pi^4 abD} \sum_{m=1}^{\infty}\sum_{n=1}^{\infty} \frac{1}{\left(\dfrac{m^2}{a^2} + \dfrac{n^2}{b^2}\right)^2} \tag{2.31}$$

is the displacement at the plate center due to a concentrated force F here applied. If we substitute the relation (2.31) in the equivalence (2.30), we obtain

$$F = \sqrt{2 m_t g h} \cdot \left[\frac{1}{k_t} + \frac{4}{\pi^4 abD} \sum_{m=1}^{\infty}\sum_{n=1}^{\infty} \left(\frac{m^2}{a^2} + \frac{n^2}{b^2}\right)^{-2}\right]^{-1/2}. \tag{2.32}$$

Once the applied force is known, it is possible to calculate the print area $A = F/p$, which is supposed to be a square of side $u = \sqrt{A}$ as before (other forms

can be similarly considered). Then, we can calculate a posteriori the displacement field of the plate thanks to the relations (2.25)-(2.26) and, through the constitutive equations for the glass plate, we evaluate the maximum stress in terms of σ_x and σ_y at the center.

The results obtainable with this approach are again checked for the simply supported panel $876 \times 1938 \times 10\,\text{mm}^3$. Table 2.5 shows a comparison with those derived from a FE linear static analysis where, once the impacting force (2.32) is calculated, the solution is found via `Straus7` by smearing F on a square of side $u = \sqrt{A}$. In the same table we also report the results obtained with a dynamic linear analysis in `SJ Mepla`. The errors remain very limited in all the comparisons, confirming the accuracy of the method. In general, the energetic approach in the linear analysis does not require any FE modeling, and it can be easily implemented in elementary computational tools (like an `Excel` worksheet) to provide ready-to-use results. The differences between the nonlinear and the linear approaches can be appreciated from the comparison between Table 2.4 and Table 2.5. Obviously the linear approach, by neglecting the effects of the membrane stresses in the plate, provides conservative results.

	Energetic Approach: linear analysis	FE: linear static analysis	`SJ Mepla`: dynamic linear analysis	Error - Energetic (linear) vs FE [%]	Error - Energetic (linear) vs `SJ Mepla` [%]
$\delta_p(t)$ [m]	0.0196	0.0196	0.0205	0.00	4.59
σ_x [MPa]	146.6	146.2	142.8	0.27	2.66
σ_y [MPa]	113.0	112.0	109.4	0.89	3.29

Table 2.5. Pendulum test with drop height $h = 450\,\text{mm}$ on $876 \times 1938 \times 10\,\text{mm}^3$ glass panels. Maximum stresses σ_x, σ_y and out-of-plane displacement δ_p. Comparison between the linear energetic approach and numerical results obtained via `Straus7` and `SJ Mepla`.

2.2.3 Case study

The software `SJ Mepla` allows to calculate the dynamic response of isolated glass units under impact loading, both in the linear and in nonlinear case, but considering one single plate represents a limitation. In order to analyze complex real structures [78], we propose a contact model that can be implemented in most of commercial codes for structural analysis.

The contact box tool

The main problem consists in modeling the tyres and consequently modifying in time their contact area. The twin-tyre pendulum is modeled as a point with mass $m_t = 50\,\text{kg}$, attached to a pendulum, with drop height h, which impacts the glass plate with velocity $\sqrt{2gh}$ at time $t = 0\,\text{s}$. The mass is attached to a hanging wire of length r, that can be reproduced with a beam element hinged at the top or, equivalently, by connecting the mass m_t to a spring of stiffness $k = m_t g/r$, which equals the restoring force of the pendulum under the hypothesis of small oscillations. If just the first impact needs to be considered, one can set $k = 0$.

According to the scheme of Fig. 2.17, the mass m_t is connected to the spring of stiffness $k = m_t g/r$, on one side, and to the spring $k_t = 400\,\text{kN/m}$ [51], on the other side, which simulates the intrinsic stiffness of the tyres. The spring k_t is in turn attached to a system referred to as the "contact box", consisting of a mass free rigid plane further connected to the glass plate by a system of beam elements. The function of the contact box is to transmit a constant pressure p on the glass panel by acting on an elliptically shaped region, which homothetically increases as the resultant of the contact force increases, and vice versa.

As indicated in Fig. 2.17(c), the glass panel is meshed with rectangular shell elements and, for the case at hand, the maximum contact zone is assumed to be $200 \times 200\,\text{mm}^2$, corresponding to the area where the contact box is located. Within the contact box, each node of the plate is connected with the specular point on the rigid plate through two beams placed in series, one referred to as the "gap-beam" and the other one as the "connection-beam". The connection-beam is fixed at one end to the node on the glass plate, whereas the other end is joined to the gap-beam, which is linked to the specular point on the rigid plane. The two beams have, in total, a height of 2 mm in order to minimize the interference with the deformation of the plate. The gap-beam provides a unilateral contact because its axial stiffness is null (inactive element) if the relative displacement of its ends (considered positive if it corresponds to elongation) is not lower than $-\delta_{\text{gap}}$ (where δ_{gap} is the gap); it becomes infinite otherwise (active element). The gap varies from beam to beam according to the paraboloid surface shown in Fig. 2.17(a) so that, as the rigid plane is pushed against the glass panel, the active gap-beams lay within an elliptical region, evidenced in red colour in Fig. 2.17(b).

Obviously, each connection-beam becomes active if and only if the gap-beam to which it is connected is active. The connection-beams are rigid-plastic, i.e. they transmit a constant axial force, which is set equal to pA_i, where $p = 3.5\,\text{bar}$ and A_i is its area of influence on the plate. Three types of connection-beams are used in the model at hand, corresponding to 3 different influence areas of $2500\,\text{mm}^2$, $1250\,\text{mm}^2$ and $625\,\text{mm}^2$, according to the size of the mesh used for the plate at the connection point. In conclusion, the system composed by gap and connection-beam in series

works only under compression, when the tyres push the plate beyond the gap δ_{gap}; otherwise it does not offer any constraint and, when all the elements within the contact box are inactive, the mass m_t is detached from the plate. The restoring force of the pendulum is modeled through the spring of stiffness $k = m_t g/r$, which connects m_t to a fixed point: this allows for the possibility of multiple bumps. It is also possible, with no complication, to insert a damping element to consider dissipation effects, but this is not done here.

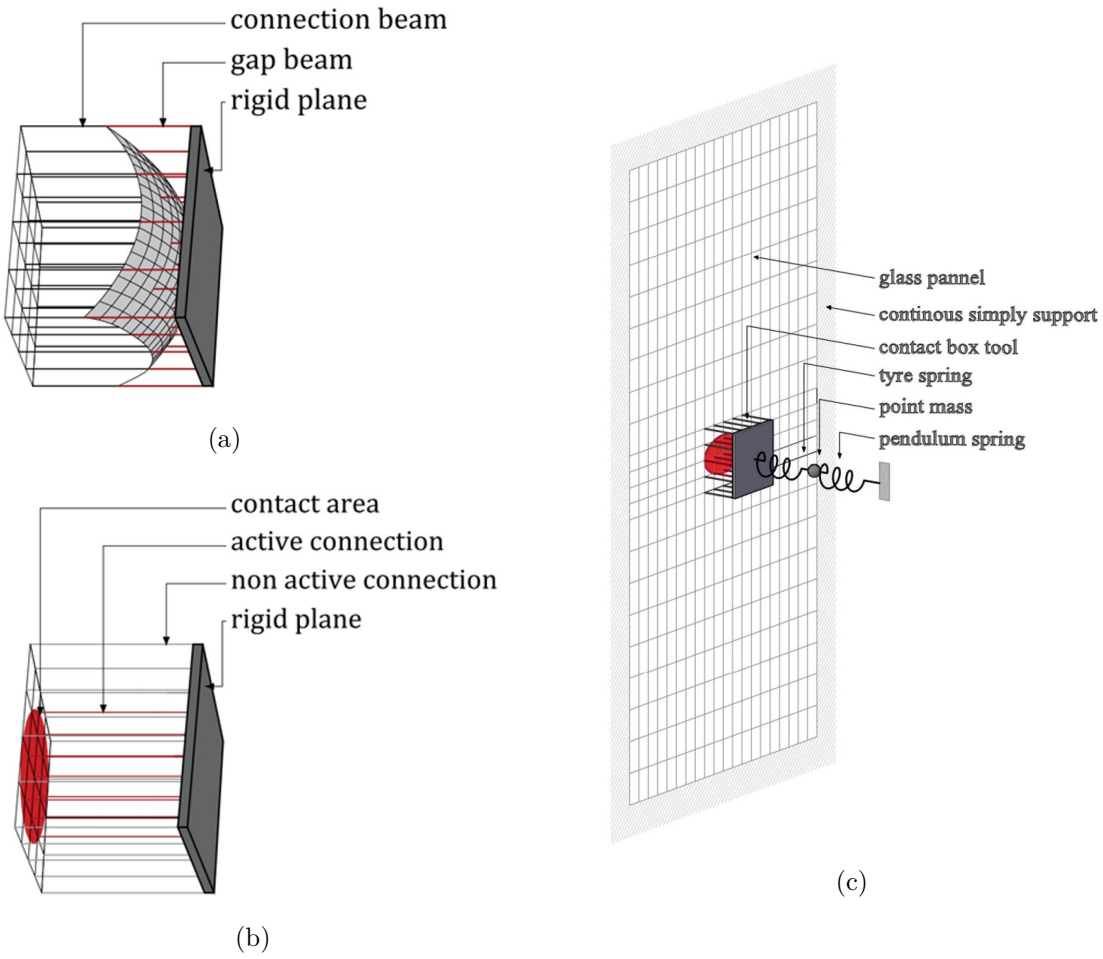

Figure 2.17. Schematics of the contact box. (a) Section of the paraboloid profile for the gaps δ_{gap}. (b) Representation of the connecting beams with the resulting elliptical contact print area that collects the active elements. (c) Assembly of the contact box with the glass plate and the mass of tyres m_t via the spring k_t. On the other side, the mass m_t is connected through the spring $k = m_t g/r$ to a fixed point.

All the elements of the contact box are available in the library of commercial

software for structural analysis including `Straus7`, here used for this analysis. This tool represents an advancement with respect to the `SJ Mepla` software that, to the best of our knowledge, does not consider dissipation and takes into account only the first impact between the pendulum and the panel, ruling out multiple bumps. More important, now it is possible to consider a whole complex structure and apply the contact box at those elements where the impact test needs to be simulated.

Examples of applicability

The standards DIN 18008-4 [78] and TRAV [48] prescribe to verify the compliance of glass with different impacting energy, defined by the drop height h for the structural categories A, B and C, as indicated in Table 2.6. The linearly supported glazing or point fixed glazing are classified in category A; the glass barriers fixed below, where the singles panes are linked by a continuous handrail, are in category B; the linearly supported glazing or point fixed glazing on which it is not required to carry any horizontal imposed loads at the fixed height, are in category C.

	Category A	Category B	Category C
Drop height h [mm]	900	700	450

Table 2.6. Drop height required for soft body impact test for various categories according to DIN 18008-4 [78] and TRAV [48].

As an example, we consider a structural glazing in category A. The tyres with drop height $h = 900\,\text{mm}$, corresponding to an initial velocity $v_t = 4202.14\,\text{mm/s}$, impact in the middle of a monolithic glass plate simply supported on the four edges. In Table 2.7, the values of maximum stress $\sigma_{\max}$ and maximum displacement $\delta_{\max}$ are recorded for panels of different size, as calculated with the transient nonlinear dynamic solver implemented in `Straus7` by using the contact box tool. These are compared with the results provided by the nonlinear dynamic analysis executed on `SJ Mepla`. The differences are in general very small, and can be attributed to the different-in-type numerical solvers, as well as to the different mesh generated by the programs.

It is interesting to apply, for the same cases, the nonlinear energetic approach of Section 2.2.2. An analysis similar to that used for the graph in Fig. 2.16 indicates how the overall stiffness of glass panels is independent of the imprint contact area. In Table 2.7 we also record the results obtained with the energetic approach, which show a good agreement with the previous ones at least for the $1000 \times 2000 \times 10\,\text{mm}^3$ and the $900 \times 3100 \times 12\,\text{mm}^3$ panels, but overestimate both stress and displacement for the largest panel.

Panel size [m^3]	σ_{max} [MPa] SJ Mepla: non-linear dynamic analysis	δ_{max} [mm] SJ Mepla: non-linear dynamic analysis	σ_{max} [MPa] FE model: contact box	δ_{max} [mm] FE model: contact box	σ_{max} [MPa] Energetic Approach: non-linear analysis	δ_{max} [mm] Energetic Approach: non-linear analysis	σ_{max} [MPa] ABAQUS	δ_{max} [mm] ABAQUS
$1 \times 2 \times 0.01$	160.77	28.29	156.27	27.91	155.44	25.70	163.47	26.86
$0.9 \times 3.1 \times 0.012$	146.48	17.73	144.46	17.45	138.20	18.03	152.00	19.00
$2.7 \times 5.2 \times 0.01$	108.88	48.53	110.34	47.43	121.57	65.50	105.01	52.04

Table 2.7. Monolithic glass panels of different size, simply support on the four edges, impacted at the center by a pendulum with drop height 900 mm. Comparison in terms of maximum stress σ_{max} and displacement δ_{max} of the results obtained with the contact-box tool implemented in Straus7 (nonlinear dynamic analysis), with SJ Mepla (nonlinear dynamic analysis), with the energetic non-linear approach and with ABAQUS.

For the sake of comparison, the same glass panels were modeled with ABAQUS and the corresponding results are added in Table 2.7. Basically, ABAQUS can apply two approaches to model the contact interaction: the penalty method or the kinematic contact formulation. The first method is hard to use for the considered problem because, under strong geometric nonlinearities, the penalty functional may become non-convex in type, as theoretically discussed in [79]. The kinematic contact formulation, used here, achieves compliance with the contact conditions thanks to a predictor/corrector method.

The impactor can be modeled at different levels of complexity. Pelfrene et al. [80] attempted to reproduce the exact shape of the tyres and the presence of the inflating gas in ABAQUS, whereas Schneider and Schula [81] considered in Ansys a homogenous solid body with comparable properties. Indeed, as illustrated in Section 2.2.2, the kinetic energy of the impactor is converted into strain energy associated with the inflexion of glass plate and the deformation of the impactor itself, besides the dissipated part that is usually a second order quantity[13], or can be neglected on the safe side. Since the actual distribution of the contact forces has a limited effect on the deflection of glass plate, as demonstrated in Fig. 2.16, the deflection is determined by the equivalent *stiffness of the impactor*, which is modeled by the spring k_t in the simplified approach of Section 2.2.1. On the other hand, the imprint area and the distribution of contact forces, which are governed by the *shape of the impactor*, have an effect on the distribution of stress in the plate.

Here, the impactor has been modeled by following the approach of [81]. Having

[13]During a real test, the dissipated energy can be estimated through the difference between the initial drop height and height reached by the impactor after the first contact.

in mind the engineering practice in which the contact area between a tyre and the road pavement is assumed to be circular [77] (despite the toroidal shape of tyre), the impactor has been modeled as represented in Fig. 2.18. It is composed of a soft quasi-hemispherical portion, connected on the flat part to a disk made of a stiff material, which simulates the steel mass on which the tyres are mounted, both modeled with four-node tetrahedral elastic elements. The radius of curvature and the elastic properties of the portion that will be in contact with the plate have been chosen in order to reproduce the expected size of the imprint area and the expected strain energy stored in the tyres consequent to the impact. On one hand, the more compliant the material and the higher the radius of curvature, the larger is the contact area. This affects the maximum principal tensile stress in the plate, but numerical experiments have shown that the variation is noteworthy only if the impactor is either very hard or very soft: for reasonable choices of the elastic parameters, the difference is mild. On the other hand, since a compliant body stores more energy than an almost rigid body, the deflection of plate, which is only mildly influenced by the size and shape of the impact surface, decreases as the stiffness of the impactor body is decreased. Our conclusion is that the parameters that govern the dynamic response of the plate are the stiffness of impactor and, to a less extent, its shape. In the end, good results were obtained by assigning the geometry represented in Fig. 2.18(a) by using $E = 185 \cdot 10^3\,\mathrm{Pa}$ as Young's modulus and $\nu = 0.49$ as Poisson's ratio in the neo-Hookean characterization of finite elasticity. The corresponding FE model is indicated in Fig. 2.18(b).

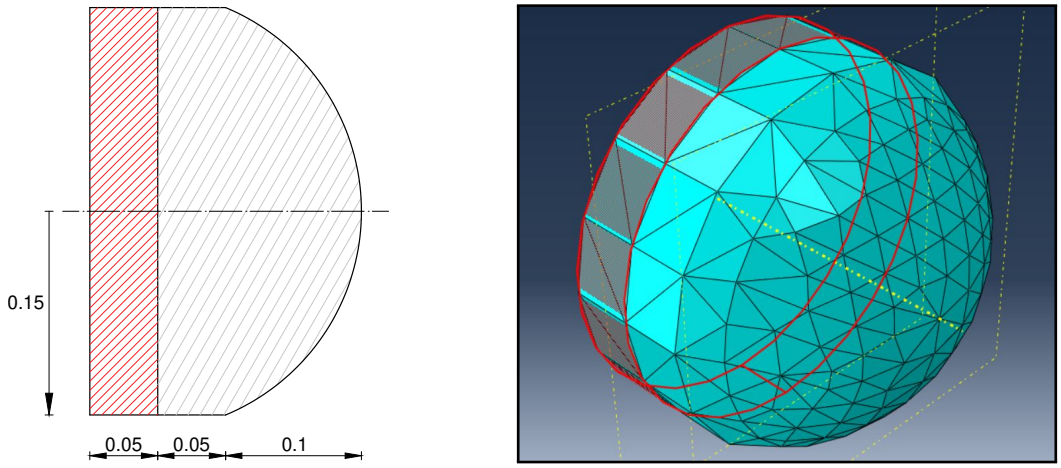

(a) (b)

Figure 2.18. Model of the impactor implemented in ABAQUS: (a) Section (measures in meters); (b) FE model as shown in ABAQUS viewer.

The glass panel has been modeled with four-node shell elements with a finer

mesh in proximity of impact area. During the motion, the impactor is constrained to move along a line in the out-of-plane direction. At the initial instant $t = 0\,\mathrm{s}$, the impactor is just about to get in touch with the plate at the assigned velocity, which has been directly calculated from the imposed drop height. The FE assembly is represented in Fig. 2.19.

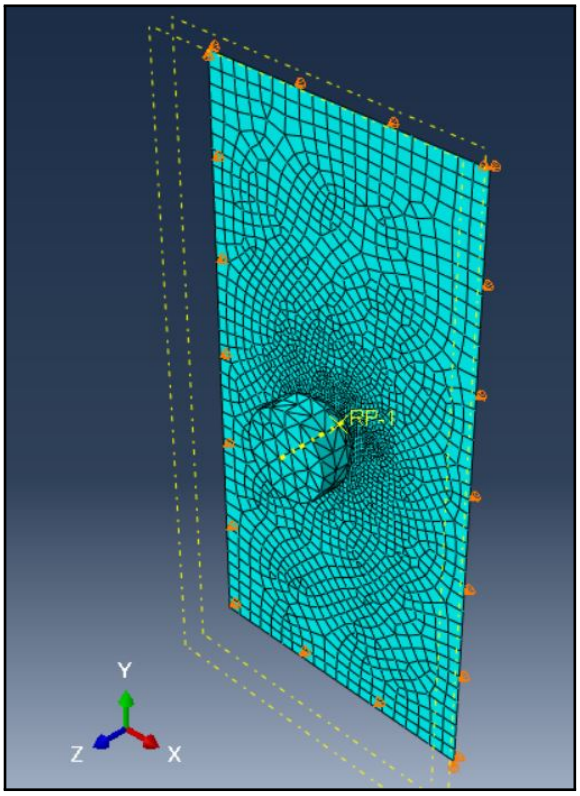

Figure 2.19. FE model of the assembly of impactor and glass plate, as shown in ABAQUS viewer.

Two images from the ABAQUS output fields are shown in Fig. 2.20. The deformed configuration of the impactor, indicated in Fig. 2.20(a), provides a qualitative appreciation of the contact process, which has been assumed to be frictionless. The great distortion of the mesh may generate numerical problems for the solver: the results of simulation need to be checked with care, for example by controlling that the contact pressure and the size of contact area are the same for both the impactor and the plate. Meshes of various size needed to be considered before reaching a compromise between accuracy and computing time.

Various problems of numerical convergence were encountered during the simulations, which discouraged us from attempting a more complex modeling like that of [80]. Nevertheless, despite all the simplifications in the ABAQUS model, the results

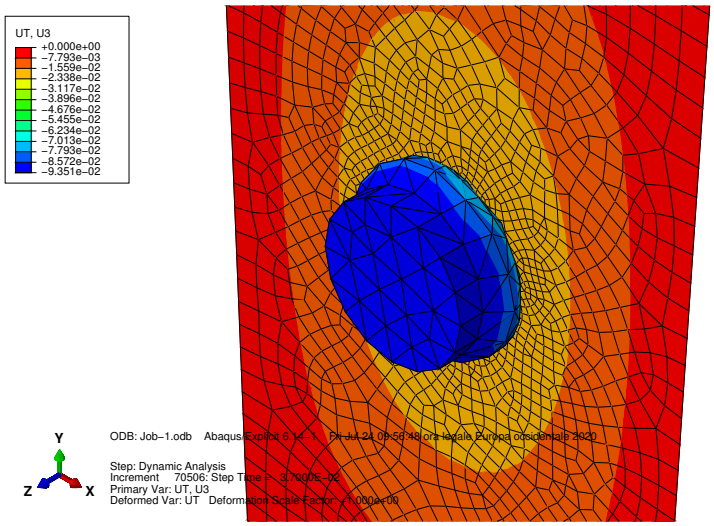

(a)

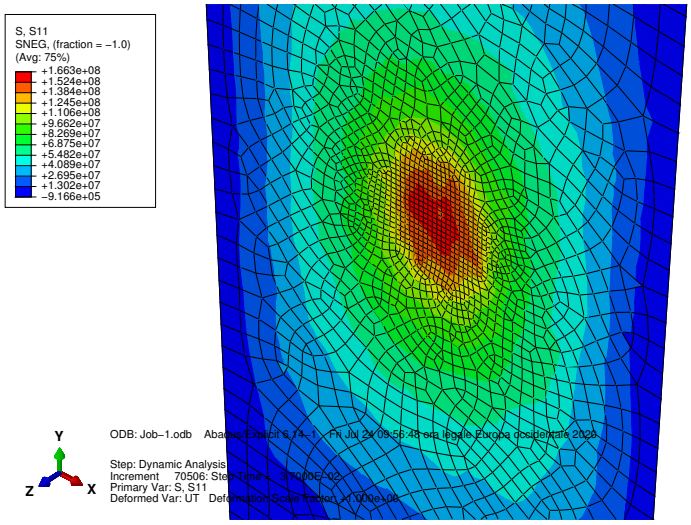

(b)

Figure 2.20. FE simulation of the soft-body impact on a glass plate continuously supported at the edges. (a) Deformed shape of the impactor and the plate at the instant of maximum deflection (displacement expressed in meter); (b) Plot of the maximum tensile component on the glass plate at the same instant (stress expressed in Pascal).

summarized in Table 2.7 show a good agreement with those obtained with the proposed contact box tool, as well as with `SJ Mepla`, which is considered a reference software for this type of analysis. However, it should be mentioned that the computing time with an i7 processor for an analysis with the contact box tool is of the

order of a few minutes, whereas in ABAQUS it may take a few days to reach similar results when using the aforementioned model. At this stage, we cannot estimate what is the computation time to obtain accurate results if a complex model like that of [80] is used instead.

For a further comparison, Table 2.8 records the results obtained with the modified Rayleigh's method for the 2-DoF system described in Section 2.2.1. It is interesting to observe the effective mass of glass pane m_p, calculated as per (2.20): this is much less than the impacting mass $m_t = 50\,\text{kg}$ for the first two panels, but it is almost twice of that for the largest panel. Therefore, it is not surprising that the nonlinear energetic approach, which neglects the inertial contribution, overestimates stress and displacement for this latter case. Of course, in the modified Rayleigh's approach the geometric nonlinearity cannot be taken into account. If we compare the results with those of Table 2.7, we observe that stress and displacement are quite different, especially for the first and third panel, where the aspect ratio is the highest. Indeed, when the deformation of panel is far from being cylindrical, membrane effects become important.

Panel size [m]	$\sigma_{\max}$ [MPa] SJ Mepla: linear dynamic analysis	$\delta_{\max}$ [mm] SJ Mepla: linear dynamic analysis	$\sigma_{\max}$ [MPa] Modified Rayleigh's method	$\delta_{\max}$ [mm] Modified Rayleigh's method	m_p [kg]
$1 \times 2 \times 0.01$	197.64	37.72	203.53	35.10	12.50
$0.9 \times 3.1 \times 0.012$	153.85	19.92	163.28	16.70	20.93
$2.7 \times 5.2 \times 0.01$	122.77	87.75	146.10	112.94	86.08

Table 2.8. Monolithic glass panels of different size, simply supported on the four edges, impacted at the center by a pendulum with drop height 900 mm. Comparison in terms of maximum stress $\sigma_{\max}$ and displacement $\delta_{\max}$ of results obtained with SJ Mepla (linear dynamic analysis) and the 2-DoF analysis with Rayleigh's method.

The examples just considered indicate that an energetic nonlinear analysis provides values on the safe side and the approximation is good only when the participating mass is much less than the mass of panel. Therefore, to check the accuracy of this ready-to-use analysis, one should preliminary calculate the effective mass by using (2.20), or its counterpart when the boundary conditions of the plate are different, and control that this is substantially less than the impacting mass m_t.

In any case, although the SJ Mepla software can examine the effects of three different impact points as defined by DIN 18008-4 [78], the analysis is limited to one panel with various boundary conditions. To illustrate the use of the contact box tool in the analysis of complex structures as a whole, we consider the case study

represented in Fig. 2.21(a), which refers to a single cable supported façade.
The vertical supporting cables, of length $L = 7.48\,\text{m}$ and cross sectional area $A = 1.54\,\text{cm}^2$, are fixed at the ends and pre-tensioned until reaching an axial load $N = 15.9\,\text{kN}$ to increase their stiffness. The façade is composed of 20 glass units, dividing the surface in columns of width 1.75 m, 1,79 m, 1.79 m, 1.79 m and 1.75 m, and rows of height 2.38 m, 1.9 m, 1.3 m, 1.9 m (from bottom to top). Each column of glass units is supported by two cables placed in proximity of the borders, so that the whole façade is supported by 10 cables. The glass units are fixed to the cables by special point fixing devices, of the type described in [82, 83], which provide in general a constraint statically equivalent to hinges at the four vertices, with the two constraints at the panel top vertices allowing the relative displacement between panel and cable in the direction of the cable to permit thermal movements. Any two adjacent point-fixings on neighbouring panels, laying on adjacent cables, are also linked together at each vertex to create a continuous load-bearing structure. The fixation points are evidenced with marked dots in Fig. 2.21(a). A similar design has been used for one of the façades in the shopping mall Montefiore Conad in Cesena, Italy [84]. We suppose that an accessible floor is present approximately at mid-height of the façade, so that it makes sense to consider a soft body impact, with a drop height $h = 0.9\,\text{m}$, in the central panel. This is indicated in Fig. 2.21(b), which also shows the mesh that is used for the numerical simulation. Each glass panel, supposed of monolithic glass with thickness $s = 16\,\text{mm}$, is modeled with shell elements, and the mesh is refined where the contact box is applied. The nonlinear transient dynamic analysis, executed in `Straus7`, provides the maximum out-of-plane displacement field represented in Fig. 2.21(c), as well as the maximum tensile stress in glass, shown in Fig. 2.21(d). The maximum displacement of the cables and the corresponding maximal axial force are indicated in Fig. 2.21(e) and Fig. 2.21(f), respectively. Of course the software can provide the whole time history for stress and displacement, but this picture refers to the instant where the peak stress is reached in the panel.

It may be of interest, again, to compare the results just obtained with those coming from the nonlinear energetic approach of Section 2.2.2. In this case, the nonlinear stiffness of the panel, including the effect of the rear supporting structure, is calculated with a FE model by applying an increasing concentrated force at the impact point: also in this case the area of the imprint does not provide significant variations in terms of calculated displacements. The state of stress is calculated a posteriori as indicated above. By observing the results collected in Table 2.9, one can notice that the energetic approach overestimates of about 60% the maximum displacement: this is because this method does not consider the inertia contribution, which can be substantial since the whole façade, supported by cables, is involved in the motion. The same conclusion holds for the maximum tensile stress, for which the energetic approach provides values approximately 50% higher than the `Straus7`

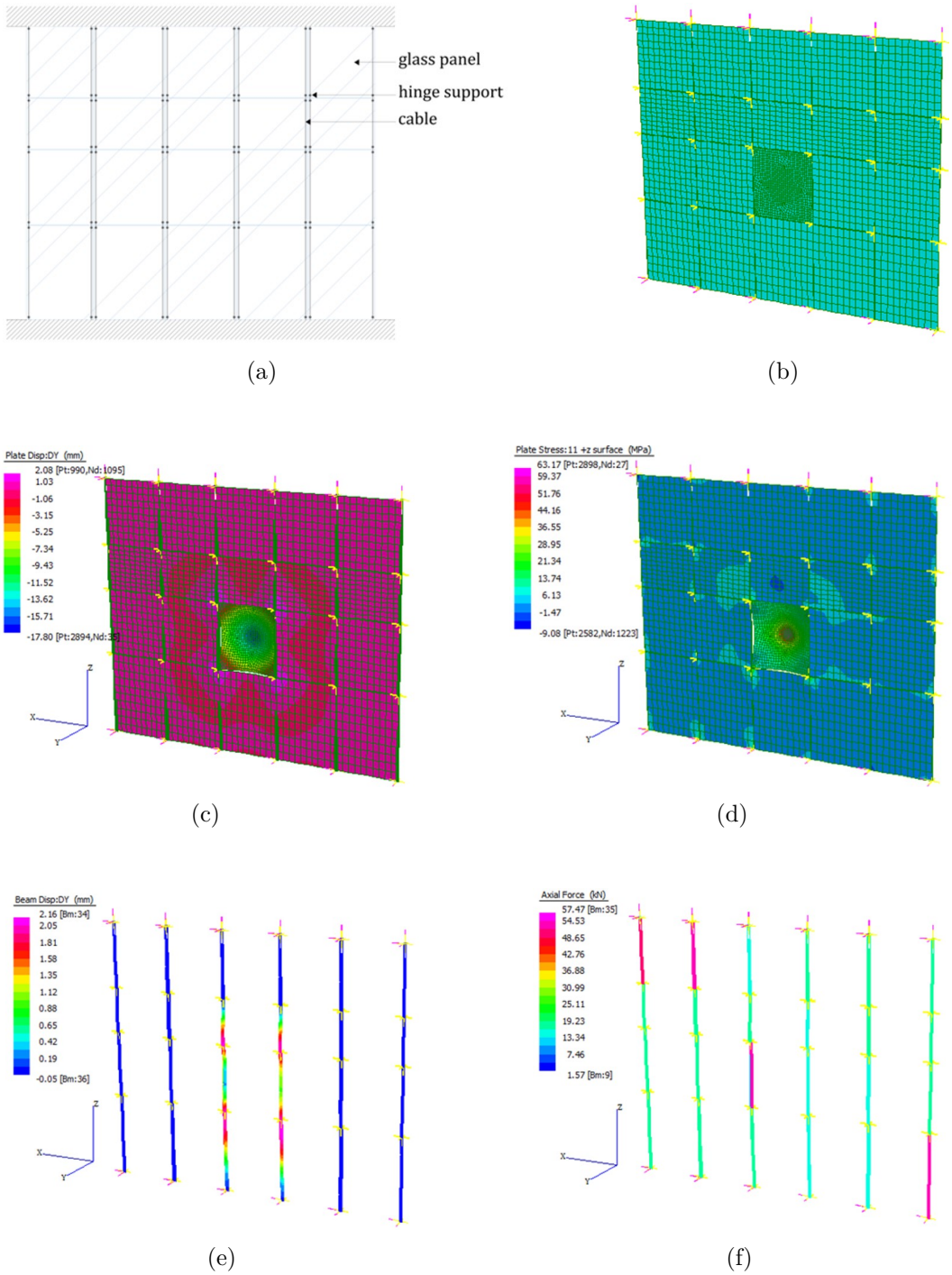

Figure 2.21. Nonlinear transient dynamic analysis executed in `Straus7` for a single cable supported façade. (a) Layout. (b) FE model with indication of the panel under impact test. (c) Maximum out-of-plane displacement of the façade. (d) Maximum tensile stress in glass. (e) Displacement of the supporting cables. (f) Tensile stress in the supporting cable.

analysis. Although the energetic approach is always on the safe side, the approximation is certainly not accurate.

$\sigma_{\max}$ [MPa] FE model: contact box	$\delta_{\max}$ [mm] FE model: contact box	$\sigma_{\max}$ [MPa] Energetic Approach: nonlinear analysis	$\delta_{\max}$ [mm] Energetic Approach: nonlinear analysis
63.2	40.6	91.7	66.1

Table 2.9. The energetic approach applied with the nonlinear transient dynamic analysis on `Straus7` by using the contact box on the whole façade structure.

This example shows the potentiality of the proposed contact box tool in analyzing the structure as a whole, providing a more comprehensive view of the impact test, whose effect may not be well estimated if the analysis is limited to one single panel.

Chapter 3

Laminated glass modeled via fractional calculus

Glazed panels constitute the first level at which a bomb blast resisting façade, or façade amenable to resist an impact, can be designed. In common architectural applications, laminated glass is adopted with the purpose to reach an equivalent ductility/load-bearing capacity in pre- and post-breakage phases. In practice, two (or more) glass plies are bonded together thanks to thin polymeric layers: after a high temperature process in autoclave, polymerization reactions produce a cohesive coupling which makes the "sandwich" sound. The stiffness of such composite is intermediate between two borderline cases: *layered limit*, with free-sliding plies; *monolithic limit*, where no sliding occurs between the plies. This happens because of the polymer's viscoealstic behavior, whose role needs to be modeled and assessed in structural theories for laminated glass.

A mathematical approach, alternative to the classical formulation of linear viscoelasticity, defines the constitutive laws in terms of differential equations involving fractional derivatives of order α, with $0 < \alpha < 1$. In this way, relaxation and creep functions are interpreted by means of power-laws rather than a series of exponentials (i.e., Prony series). As a main advantage, only two experimental parameters are necessary for the calibration of constitutive model.

This chapter is based on the sandwich beam model proposed in [85], that analyzes how viscoelastic polymers affects the dynamic response of laminated beams subjected to quasi-static loads. After a brief introduction about the experimental characterization of viscoelastic polymers, an analytical model for three-layered beams is introduced and tested under impulsive loading conditions (the inertial contribution is not negligible). Subsequently, through the same approach, an analytical model for sandwich plates is proposed and tested.

3.1 The viscoelastic properties of interlayers

The adhesive interlayers that bond the glass plies are usually made of viscoelastic polymeric materials, exhibiting relaxation and creep behavior. It is very important to determine their viscoelastic properties inasmuch they strongly affect the mechanical response of laminated glass especially under short-duration actions. Such properties can be measured by experimental procedures, which are classified in two main categories: static tests and dynamic tests. For what concerns *static tests*, the strain rate (or alternatively the stress rate) is zero or moderate at most. During a relaxation test, the strain remains constant over the time and the stress is read as output in the form of relaxation curve; on the contrary, creep tests are performed by imposing a constant stress in order to measure the time history in terms of strain (creep curve). A *dynamic test* provides for a time dependent external action (e.g., a sinusoidal load) defined by means of magnitude and frequency. These tests are carried out with dynamic mechanical analysers (DMA), which work in strain control or stress control. Further details about the experimental procedures can be in found in [86, 87].

In the bi-logarithmic stress-time plane, a typical relaxation curve $R(t)$ is characterized by two pseudo-linear branches connected by a transition curve, where the stress suddenly decreases to an almost constant value. The time domain can be very wide but, since a generic blast load presents a duration of the order $T_d \sim 0.01\,\mathrm{s}$, for most commercial materials used as interlayers only the left hand side branch of such curve is of importance. For practical reasons (inertia of the testing machine, feasibility), the observation period is limited to an interval varying from a minimum of a few seconds to a maximum of a few weeks. This period is "theoretically" extended by using the Time-Temperature Superposition (TTS) principle: a temperature variation produces a modification of the time scale during which the effects of viscosity become visible. The model proposed by William, Landel and Ferry (WLF) [88] is one of the most famous. It determines the time shift $\log(a_{\mathcal{T}})$ as a function of the current temperature $\mathcal{T}$ and a reference temperature $\mathcal{T}_0$, in the form

$$\log(a_{\mathcal{T}}) = \frac{-C_1(\mathcal{T} - \mathcal{T}_0)}{C_2 + (\mathcal{T} - \mathcal{T}_0)}\,, \tag{3.1}$$

where C_1 and C_2 are constants to be experimentally calibrated. According to the TTS principle, $R(t)|_{\mathcal{T}} = R(t/a_{\mathcal{T}})|_{\mathcal{T}_0}$; hence, in the plane $\log(R)$-$\log(t)$, the graph associated with $\mathcal{T}_0$ is shifted of the quantity $-\log(a_{\mathcal{T}})$ with respect to that corresponding to $\mathcal{T}$. Several tests can be performed within the same reference time interval at different temperatures, so that the curves are then shifted to find other branches of the relaxation curve at the reference temperature $\mathcal{T}_0$. This procedure can be conceptualized as in Fig. 3.1: the curve obtained at $\mathcal{T}_I < \mathcal{T}_0$ ($\mathcal{T}_{II} > \mathcal{T}_0$) is left-shifted (right-shifted) in the bi-logarithmic stress-time plane.

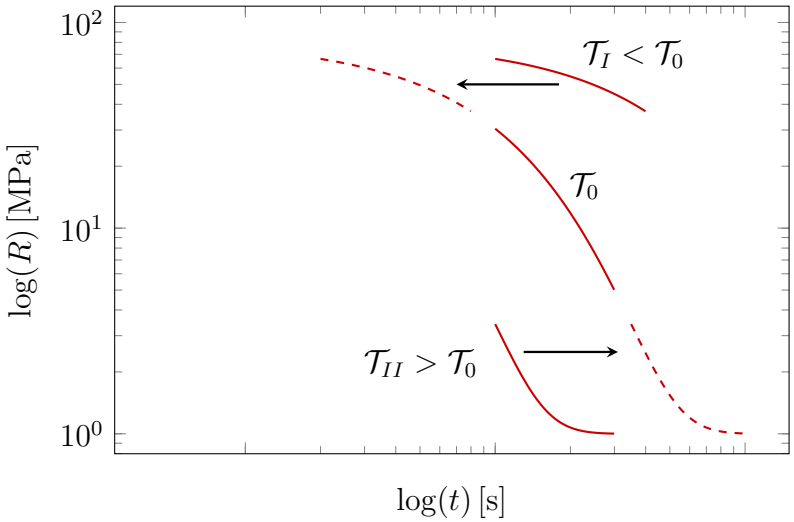

Figure 3.1. Time-Temperature Superposition (TTS) principle used to obtain the relaxation function $R = R_{\mathcal{T}_0}(t)$ at the reference temperature $\mathcal{T}_0$, by shifting the experimental curves (continuous line) obtained at the temperatures $\mathcal{T}_I < \mathcal{T}_0$ and $\mathcal{T}_{II} > \mathcal{T}_0$.

There are many types of polymers used in glazing applications, with different in type responses, for which the transition zone is located at different temporal scales. Our purpose is to determine the behavior of laminated glass under blast loads, whose characteristic time scale is represented by the duration T_d in Friedlander equation (see Chapter 2), of the order 10^{-2} s. Therefore, it is certainly sufficient to consider only the left hand side branch in the time domain, where the relaxation curve $R(t)$ can be well approximated by a power law corresponding to a straight line in the bi-logarithmic plane (see Fig. 3.2). This property is of paramount importance, because it allows to extrapolate $R(t)$, obtained from static tests, towards the very small time scales required to accurately model the effects of a blast wave.

Dynamic tests could be used to directly estimate the viscoelastic properties for times of the order of 10^{-4} s, but these are usually performed on the bare polymeric material. This fact may produce noteworthy uncertainties, because the bonding process of the glass plies to the polymeric interlayers, conducted at high temperature and pressure in autoclave, may significantly modify the mechanical characteristics of the pristine polymer. Static relaxation tests can be performed on laminated glass packages [89], but it is impossible to directly observe the response at such short times due to the limitation of experimental set-up. Therefore, the assumption of a power law trend results to be the natural way in which the measurements on time scales of the order 10^0 s can be extrapolated to the branch of interest on the left hand side of the relaxation curve.

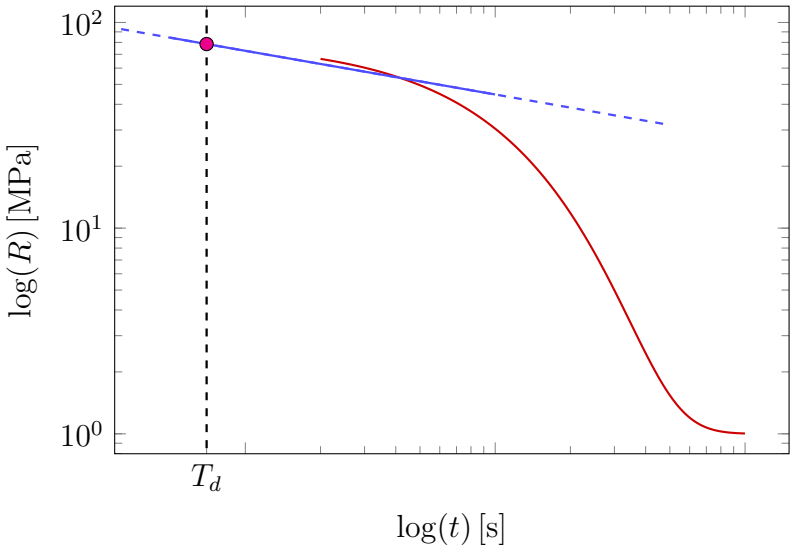

Figure 3.2. Qualitative plot of a typical relaxation function $R(t)$. The first branch is fitted by a power law (straight line), which allows to analytically extrapolate the values at time-scales of the same order of the blast duration T_d.

Said this, in order to illustrate the potentialities of the fractional modeling, reference is made to the careful experimental campaign conducted by Biolzi et al. [89] on laminated glass joints with different interlayers. Fig. 3.3 shows a few relaxation functions obtained by interpolating the measured points in quasi-static tests, distinguished by markers of different shape. For different environmental temperatures, the graphs indicate the response before the transition branch of three polymeric films commonly used in glazing applications: polyvinyl butyral (PVB), ionoplast SentryGlas (SG) and high performance plasticized PVB (commercially known as DG41 and denoted as DG). While by considering $T_d = 0.01\,\mathrm{s}$ as the representative duration of loading action, the domain of interest is evidenced by the rectangle drawn in the same picture. The extrapolation from the experimental measures is represented by the dashed branches of the lines.

According to the fractional characterization of viscoelasticity, recalled in the Appendix A, an expression of the type (A.7) interprets a power law dependence of the relaxation curve $R(t)$ [MPa] on the time t [s], i.e.,

$$R(t) = \frac{C_\alpha}{\Gamma(1-\alpha)} t^{-\alpha}\,, \tag{3.2}$$

where $\Gamma(\cdot)$ is Euler's Gamma function and C_α is hence measured in [MPa s^α]. The coefficients α and C_α, corresponding to the materials considered in Fig. 3.3, are collected in Table 3.1. In particular, the exponent α is provided by the slope of relaxation function in bi-logarithmic plane, while C_α can be obtained from its intercept

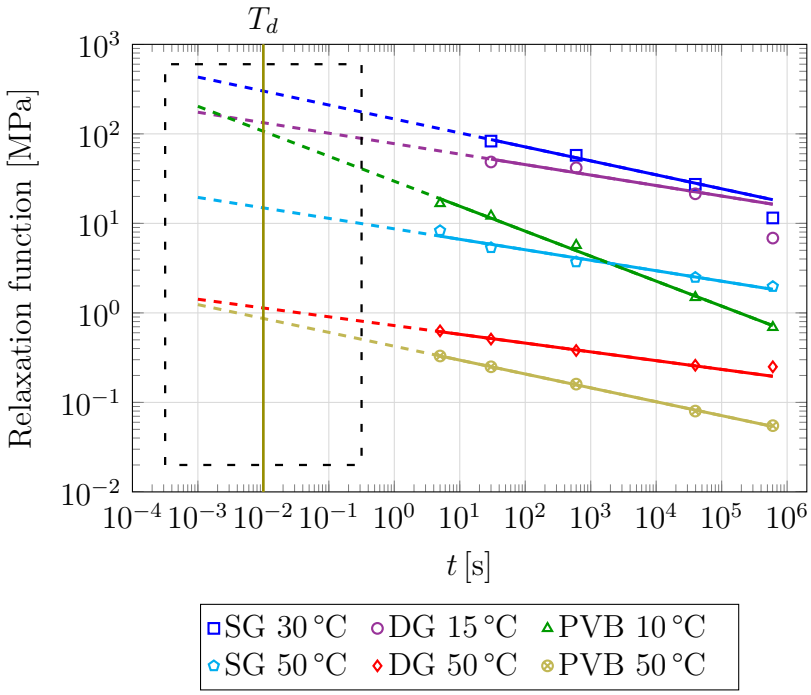

Figure 3.3. Relaxation function for three polymeric interlayers (SG, DG, PVB) at various temperatures, obtained from the experimental campaign of Biolzi et al. [89]. Interpolation with a power law (linear trend in the bi-log plane) to the times of interest for the applications to blast loadings.

with the vertical line $t = 10^0$ s.

Material	Temperature [°C]	α	$C_\alpha/\Gamma(1-\alpha)$ [MPa s$^\alpha$]	C_α [MPa s$^\alpha$]
SG	30	0.156	146.665	164.008
SG	50	0.117	8.690	9.409
DG	15	0.117	77.709	84.138
DG	50	0.098	0.722	0.770
PVB	10	0.279	29.566	37.431
PVB	50	0.155	0.424	0.474

Table 3.1. Fractional viscoelastic parameters α and C_α for three polymeric interlayers (SG, DG, PVB) at various temperatures, calibrated from the experimental campaign of Biolzi et al. [89].

It should be mentioned that the most traditional approach consists in expanding the relaxation function in Prony series, i.e.,

$$R(t) = R_0 + \sum_{i=1}^{N} R_i e^{-t/\theta_i} \,. \tag{3.3}$$

This corresponds to a generalized Wiechert model, composed by one elastic spring in parallel with N spring-dashpot Maxwell elements. Hence, R_0 represents the long term modulus associated with the spring, whereas the terms R_i and θ_i, for $i = 1 \dots N$, indicate the relaxation moduli and the relaxation times corresponding to the i^{th} Maxwell element in the series.

This procedure, however, is not natural, because it attempts to interpolate a power law with exponentials. To illustrate, Fig. 3.4 reports what obtained in the bi-logarithmic representation with $N = 1, 2, 3$ exponentials, with reference to the PVB at 50 °C. The power law corresponds to a straight line, whereas the Prony series provides a "wiggly" approximation. Consequently, at least 10-15 terms (corresponding to 21-31 parameters) are usually recommended to obtain a reasonable result. On the other hand, a fractional viscoelastic characterization only requires the calibration of the two parameters α and C_α in (3.2), which can be easily and directly determined with a graphical construction.

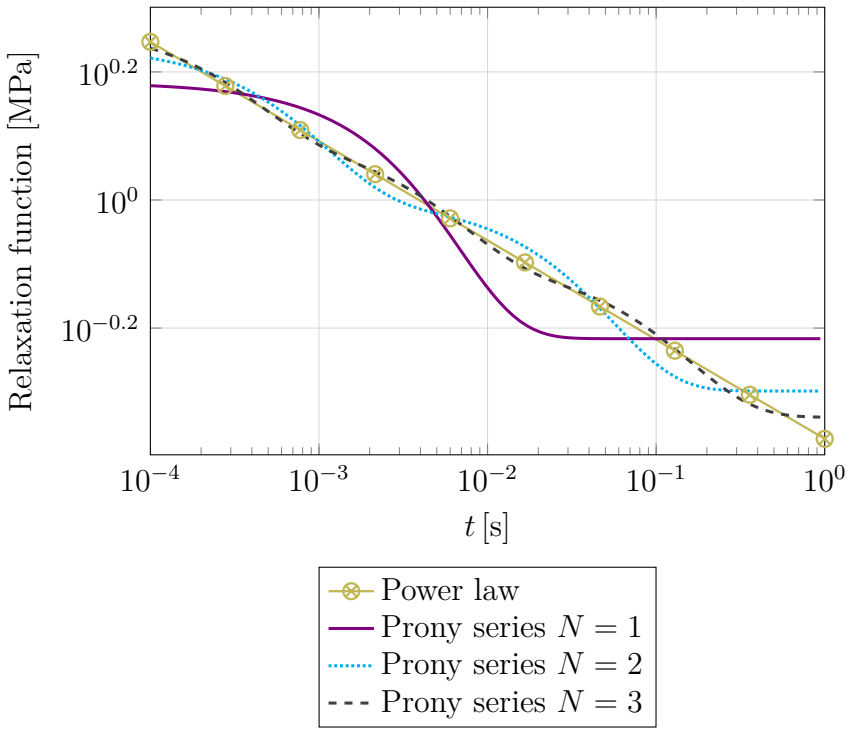

Figure 3.4. Interpolation of the power law relaxation function for PVB at 50°C with Prony series with 1, 2 and 3 exponential terms.

3.2 Laminated glass beams

The dynamic equilibrium of a laminated glass beam is now considered. After recalling the Friedlander equation, that serves to represent the pressure time history transmitted by a blast load, a mechanical model for a sandwich beam is introduced. Then, some numerical experiments are conducted and discussed.

3.2.1 The blast load

A blast wave is supposed to induce a vertical uniformly distributed force per unit area $p(t)$ on the exposed surface, which can be interpreted via Friedlander equation in the form

$$p(t) = p_r\left(1 - \frac{t}{T_d}\right)e^{-\beta\frac{t}{T_d}}. \tag{3.4}$$

For the case considered in the following, $\beta = 0.8$ is the decay parameter, $T_d = 0.01\,\mathrm{s}$ is the time positive duration and $p_r = 30\,\mathrm{kN/m^2}$ is the initial pressure peak. Such parameters approximately correspond to a category proposed by the standard[1] ISO 16933 [8]. The qualitative graph of such a relationship is represented in Fig. 3.5(a).

This action can be ideally divided into two stages: the positive (compression) phase for $t \leq T_d$ and the negative (suction) phase for $t > T_d$. Although the positive period is the most emphasized by standards and norms, the failure of glazing usually happens during the negative one [90, 44, 47, 91]. In fact, rebounding failure may occur due to the combined effect of the elastic recovery force and the negative blast wave. Moreover, under certain conditions, higher vibration modes of glass components can be activated and become relevant.

From a pure technical point of view, which concerns the numerical solution of the governing equations related to a vibrating system, it should be observed that there is a strong discontinuity at $t = 0$. Since such irregularity can compromise the numerical approach, in this section it will be convenient to ideally decompose the action into the sum of a step (Heaviside) function $p_r\mathcal{H}(t)$ and the remaining contribution, which thus results to be continuous at the origin. Furthermore, it is useful to distinguish, within the second one, the continuous part of the compression phase from the suction (negative) phase. The three contributions are evidenced in the graphs of Fig. 3.5(b). The reason for this decomposition is that the response to a step function can be analytically regularized, whereas the continuous contributions can be numerically approximated. By summing up the step function with the continuous part of the

[1]The standard ISO 16933 [8] rules full-arena blast tests, providing a hazard rating for glazing and classifying a blast load in terms of pressure peak as well as positive impulse. The blast parameters used in this article correspond to a vehicle bomb type classified as EXV 45 (X).

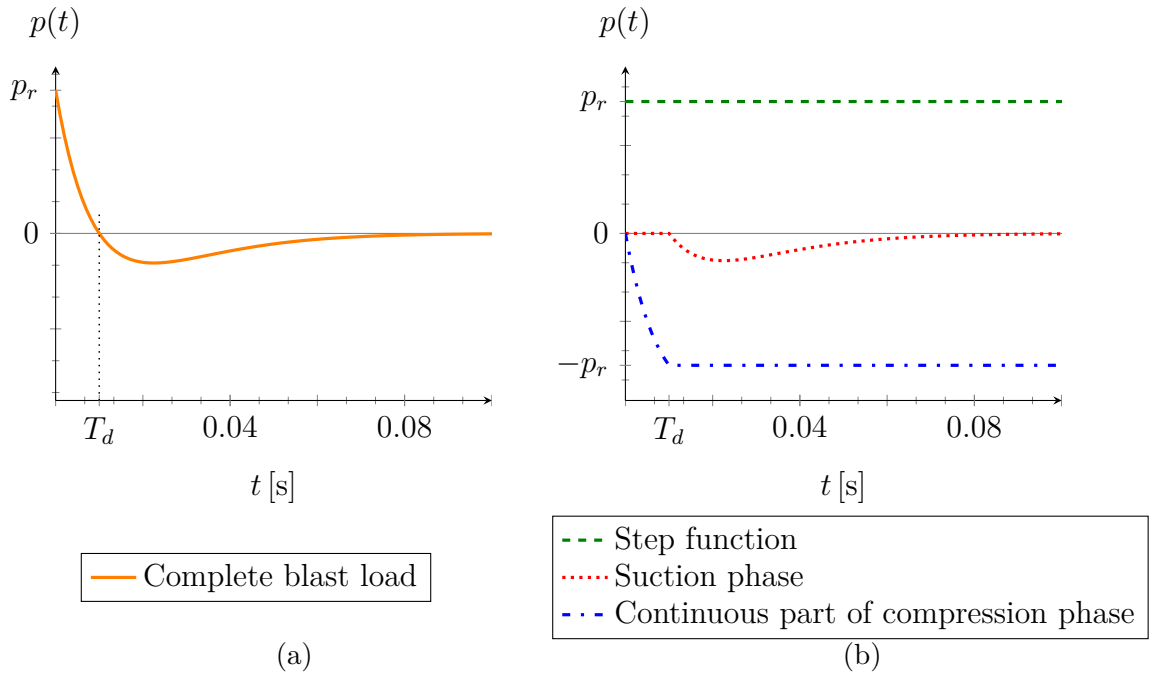

Figure 3.5. Time dependent force per unit area consequent to a blast action: a) complete impulse intepreted via Friedlander relation and b) and its decomposition into the step impulse (green dashed line), the continuous part of the compression phase (blue dashed line) and the suction phase (red dashed line).

compression phase, one obtains the complete compression phase, which should be separated from the suction phase in order to better recognize the influence of the two on the vibrating system.

Since this study is limited to 1-D models for laminated glass, we consider as a representative example a simply supported beam composed by two plies with Young's modulus $E_g = 70\,\text{GPa}$ for glass, of length L, width $b = 1\,\text{m}$ and thickness $h = 0.1\,\text{m}$ (cross-sectional area $A = b \cdot h$), so that the mass per unit length of the whole beam, neglecting the mass of interlayer, is $\mu = (2500 \cdot 2A[\text{m}^2])\,\text{kg/m}$. The plies are coupled by a polymeric interlayer of thickness $r\,h$, with $r = 0.228$. The modal frequencies of the beam read [70]

$$f_n = \frac{\pi^2 n^2}{L^2}\sqrt{\frac{E_g I_x}{\mu}}, \tag{3.5}$$

where n is the mode number and I_x is the effective moment of inertia with respect to centroidal neutral x-axis. Depending on the stiffness of polymeric interlayer, I_x shall fall within the two limits usually referred to as *layered* (I_ℓ) and *monolithic* (I_m). In the layered limit the two plies can freely slide one another: hence, $I_\ell = 2(bh^3/12)$.

On the opposite, the monolithic limit accounts for perfectly coupled plies, so that $I_m = 2(bh^3/12) + (1+r)^2 h^2 A/2$.

In Fig. 3.6, the magnitude-frequency diagram obtained from the Fourier transform of the Friedlander impulse is depicted. In the same figure, we report (black dashed lines) the modal frequencies for $n = 1$ of the laminated beam with $L = 4\,\mathrm{m}$ at the layered limit ($f_{1,\ell}^{L=4\,\mathrm{m}} = 9.42\,\mathrm{Hz}$) and at the monolithic limit ($f_{1,m}^{L=4\,\mathrm{m}} = 22.15\,\mathrm{Hz}$). Since the real frequency associated with the first mode is certainly between the two aforementioned limits, this shall correspond to a point close to the peak: the first vibration mode is prone to be triggered. The frequencies associated with higher vibration modes are shifted to the right hand side of the diagram ($f_{n,\ell}^{L=4\,\mathrm{m}} = n^2 f_{1,\ell}^{L=4\,\mathrm{m}}$ and $f_{n,m}^{L=4\,\mathrm{m}} = n^2 f_{1,m}^{L=4\,\mathrm{m}}$), and might also be involved in the vibrations, although with less intensity depending on I_x. The same graphs also reports the case of a beam for which $L = 2\,\mathrm{m}$. Due to the fact that the length is one half of the previous case, it states that $f_{1,\ell}^{L=2\,\mathrm{m}} = f_{2,\ell}^{L=4\,\mathrm{m}} = 37.69\,\mathrm{Hz}$ and $f_{1,m}^{L=2\,\mathrm{m}} = f_{2,m}^{L=4\,\mathrm{m}} = 88.58\,\mathrm{Hz}$. The contribution of the highest vibrations modes corresponds to the extreme left hand side branch of the diagram.

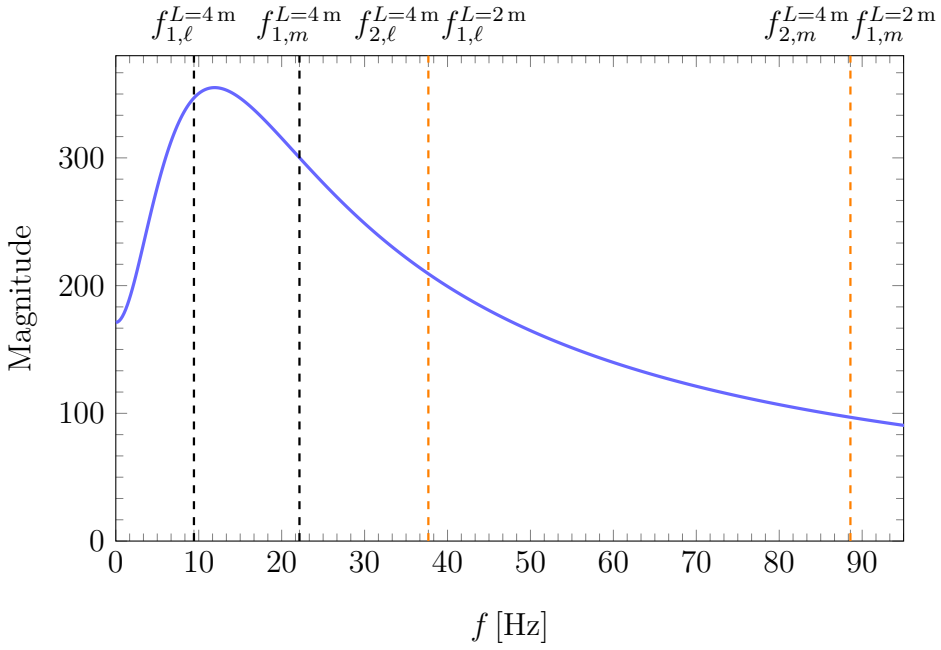

Figure 3.6. Magnitude–frequency diagram corresponding to the Fourier transform of Friedlander impulse. The modal frequencies for $n = 1$ and $n = 2$ at the layered/monolithic limits are reported for a beam of length $L = 4\,\mathrm{m}$ (black dashed lines) and for a beam of length $L = 2\,\mathrm{m}$ (orange dashed lines for $n = 1$).

Indeed, one of the parameters that affects the most the overall deformation of the structure is the characteristic duration of the blast impulse, which is usually

associated with the parameter T_d in Friedlanded equation. To illustrate, consider the beam as an equivalent harmonic oscillator of stiffness k^* and mass m^*, which is subjected to a triangular-shaped load of maximum value F_0 and duration T_0. Three different-in-type scenarios can be distinguished in the dynamic response [38, 92]: the *impulsive* regime, the *dynamic* regime and the *quasi-static* regime. The impulsive regime takes place when the load duration is small with respect to the fundamental vibration period of the structure, in practice when $T_0\sqrt{k^*/m^*} < 0.4$, so that its effect is to impart a momentum letting the mass freely oscillate afterwards: the corresponding maximum displacement is of the order of $u_{\max} \simeq \mathcal{I}/\sqrt{k^* m^*}$, where $\mathcal{I} = \frac{1}{2}F_0 T_0$ is the impulse (for $T_0\sqrt{k^*/m^*} = 0.4$ one has $u_{\max} = F_0/k^*$ [38]). On the other hand, the quasi-static regime is for loads with longer duration, for which $T_0\sqrt{k^*/m^*} > 40$: now the inertial forces do not contribute significantly and the maximum load is suddenly applied ($u_{\max} \simeq 2F_0/k^*$ for $T_0\sqrt{k^*/m^*} \to \infty$). The dynamic regime is a trade-off between the aforementioned scenarios: in this case, $u_{\max}$ specifically depends on the load time history. In conclusion, the deformation and stress of structural components invested by the blast load strongly depend upon their dynamic properties.

For the beam considered before, we can assume that $\sqrt{k^*/m^*}$ lays between the limits $2\pi f^L_{1,\ell}$ and $2\pi f^L_{1,m}$. Thus, one has $0.59 < T_d\sqrt{k^*/m^*} < 1.39$ for $L = 4\,\mathrm{m}$ and $2.37 < T_d\sqrt{k^*/m^*} < 5.56$ for $L = 2\,\mathrm{m}$. Both conditions correspond to the dynamic regime, but the longer beam is closer to the impulsive regime if compared with the shorter one. In general, in a well-designed glazing the quasi-static regime can be hardly attained because it would correspond to an element too much compliant, which cannot meet the requirements in terms of serviceability limit states under wind or barrier loads, as prescribed by standards.

3.2.2 Governing equations for a simply supported sandwich beam

The analytical treatment of the problem follows the same arguments proposed in [85] for the static case only, to which the reader is referred for a more detailed presentation. The governing equations are briefly recalled and extended to the dynamical case.

The laminated glass beam, of mass per unit length μ, is composed of two glass plies of length L, width b, thickness h (cross-sectional area $A = b \cdot h$). These are coupled by a viscoelastic polymeric interlayer of thickness $r\,h$, with $r \ll 1$. The beam is subjected to forces per unit length $q(z,t)$. As indicated in Fig. 3.7, this load can be considered, with respect to the horizontal middle plane of the laminate, as the sum of the antisymmetric part, consisting of $q(z,t)/2$ with concurring directions

acting on each one of the plies and producing the bending of the beam, and the symmetric part, where the loads $q(z,t)/2$ have opposite direction. The symmetric part is inessential for the bending of the beam if one assumes, as customarily, that the variation of the interlayer thickness consequent to its transverse axial deformation is negligible. Hence, only the antisymmetric case needs to be analyzed.

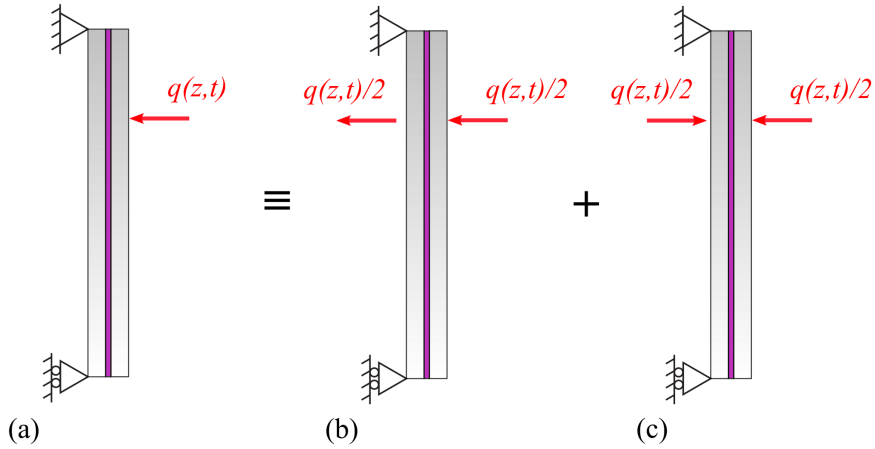

Figure 3.7. (a) Model problem of a simply supported laminated beam composed of two linear-elastic external plies bonded by a viscoelastic interlayer. Decomposition of the transverse applied load $q(z,t)$ in (b) antisymmetric and (c) symmetric components with respect to the horizontal middle plane.

Let $N(z,t)$, $V(z,t)$ and $M(z,t)$ respectively denote the axial force, the shear force and bending moment acting on the extrados ply of the laminated glass beam, as indicated in Fig. 3.8. The shear stress $\tau_{yz}(z,t)$ in the interlayer, supposed homogeneous in the thickness, produces in this element an action equipollent to axial forces $n(z,t)$ per unit length of the form $b\tau_{yz}(z,t)$ and moments $m(z,t)$ per unit length equal to $\dfrac{1}{2}(1+r)hb\tau_{yz}(z,t)$, as per Fig. 3.8.
Therefore, for this element, the equations of dynamic equilibrium read

$$\frac{\partial N(z,t)}{\partial z} = -n(z,t) = -b\tau_{yz}(z,t), \tag{3.6a}$$

$$\frac{\partial V(z,t)}{\partial z} = \frac{1}{2}q(z,t) - \frac{1}{2}\mu\frac{\partial^2 v}{\partial t^2}, \tag{3.6b}$$

$$\frac{\partial M(z,t)}{\partial z} = V(z,t) - m(z,t) = V(z,t) - \frac{(1+r)hb}{2}\tau_{yz}(z,t). \tag{3.6c}$$

The displacements of representative points, referred to the axially deformed glass ply, are shown in Fig. 3.9. Denote with $w_C(z,t)$ the axial displacement of the centroidal

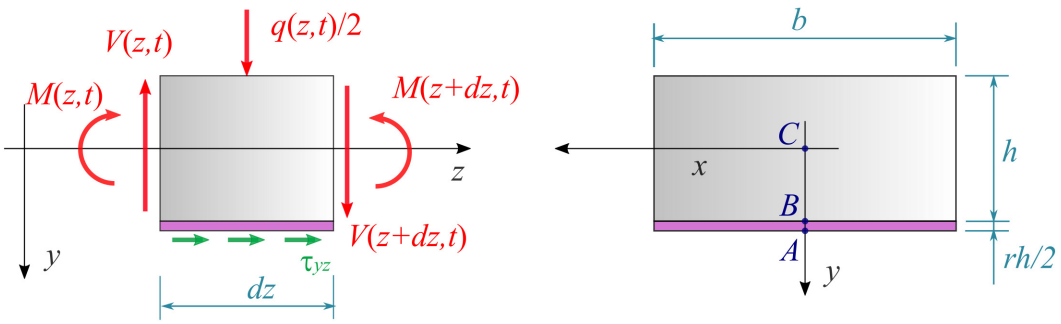

Figure 3.8. Free body diagram of the extrados ply of the laminated glass beam.

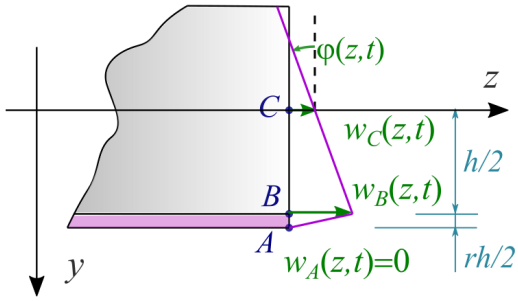

Figure 3.9. Displacement field at representative points of the interlayer when the axial deformation of the glass beam is considered.

points of the upper ply, and make the usual assumptions that the rotations $\varphi(z,t)$ are small, i.e.,

$$\frac{\partial v(z,t)}{\partial z} = -\varphi(z,t). \tag{3.7}$$

The constitutive equations for the beam are of the type

$$\frac{\partial w_C(z,t)}{\partial z} = \frac{N(z,t)}{EA}, \tag{3.8a}$$

$$\frac{\partial^2 v(z,t)}{\partial z^2} = -\frac{M(z,t)}{EI}. \tag{3.8b}$$

On the other hand, the constitutive equation for viscoelastic interlayer takes the form

$$\tau_{yz}(z,t) = C_\alpha \, {}_0^C\mathcal{D}_t^\alpha[\gamma_{yz}(z,\cdot)](t), \tag{3.9}$$

where ${}^{C}_{0}\mathcal{D}^{\alpha}_{t}[\gamma_{yz}(z,\cdot)](t)$ is the Caputo's fractional derivative with respect to t of order α of the shear strain $\gamma(z,t)$, as defined in (A.9). After differentiation, one finds

$$\frac{\partial^2 w_C(z,t)}{\partial z^2} = -\frac{n(z,t)}{EA} = -\frac{b\tau_{yz}(z,t)}{EA}, \tag{3.10a}$$

$$\frac{\partial^3 v(z,t)}{\partial z^3} = -\frac{1}{EI}\left(V(z,t) - \frac{(1+r)hb}{2}\tau_{yz}(z,t)\right) \tag{3.10b}$$

$$\frac{\partial^4 v(z,t)}{\partial z^4} = -\frac{1}{EI}\left(-\frac{1}{2}q(z,t) + \frac{1}{2}\mu\frac{\partial^2 v(z,t)}{\partial t^2} - \frac{(1+r)hb}{2}\frac{\partial \tau_{yz}(z,t)}{\partial z}\right) \tag{3.10c}$$

At this point, it is important to relate $w_C(z,t)$ with the displacement $w_B(z,t)$ of the corresponding point of the intradox of the ply, through the geometric relation

$$w_B(z,t) = w_C(z,t) + \frac{h}{2}\varphi(z,t)\,. \tag{3.11}$$

Differentiation with respect to z provides

$$\frac{\partial w_B(z,t)}{\partial z} = \frac{N(z,t)}{EA} + \frac{hM(z,t)}{2EI}\,. \tag{3.12}$$

But the shearing of the polymer is related with the rotation of the beam and $w_B(z,t)$ through the condition

$$\gamma_{yz} = -\frac{2}{rh}w_B(z,t) - \varphi(z,t) = -\left[\frac{2}{rh}w_C(z,t) + \frac{1+r}{r}\varphi(z,t)\right]. \tag{3.13}$$

From (3.8a) and (3.10a), under the constitutive assumption (3.9), one finds

$$\frac{\partial N(z,t)}{\partial z} = \frac{b}{r}C_\alpha\, {}^{C}_{0}\mathcal{D}^{\alpha}_{t}\left[\frac{2}{h}w_C(z,\cdot) + (1+r)\varphi(z,\cdot)\right](t) \tag{3.14}$$

In conclusion, after a few calculations, the fractional differential equations which governs the problem in terms of vertical displacement $v(z,t)$ and axial force $N(z,t)$ result to be

$$\frac{\partial^4 v(z,t)}{\partial z^4} + \frac{(1+r)h}{2EI}\frac{\partial^2 N(z,t)}{\partial z^2} = \frac{1}{2EI}\left[q(z,t) - \mu\frac{\partial^2 v(z,t)}{\partial t^2}\right] \tag{3.15a}$$

$$\frac{\partial^2 N(z,t)}{\partial z^2} - \frac{2b}{rhEA}C_\alpha\, {}^{C}_{0}\mathcal{D}^{\alpha}_{t}[N(z,\cdot)](t) = -\frac{(1+r)b}{r}C_\alpha\, {}^{C}_{0}\mathcal{D}^{\alpha}_{t}\left[\frac{\partial^2 v(z,\cdot)}{\partial z^2}\right](t). \tag{3.15b}$$

For what concerns the spatial variable z, four boundary conditions are needed in terms of $v(z,t)$ and two conditions in terms of $N(z,t)$. In particular, we set the following:

$$v(0,t) = 0 \qquad v(L,t) = 0\,; \tag{3.16a}$$

$$\left.\frac{\partial^2 v(z,t)}{\partial z^2}\right|_{z=0} = 0 \qquad \left.\frac{\partial^2 v(z,t)}{\partial z^2}\right|_{z=L} = 0\,; \tag{3.16b}$$

$$N(0,t) = 0 \qquad N(L,t) = 0. \tag{3.16c}$$

To these, the initial conditions

$$v(z,t) = 0\,, \quad \frac{\partial v(z,t)}{\partial t} = 0\,, \quad \text{for } z \in (0,L) \text{ and } t \leq 0\,, \tag{3.17}$$

have to be added. From (3.15b), one directly obtains $N(z,t) = 0$ for $z \in (0,L)$ and $t \leq 0$.

The equations (3.15a)-(3.15b) can be solved by using an approach *à la* Galerkin. The vertical displacement $v(z,t)$, the axial force $N(z,t)$ and the external load $q(z,t)$ are expressed through Fourier sine series as

$$v(z,t) = \sum_{k=1}^{N} v_k(t) \sin\left(\frac{k\pi z}{L}\right), \tag{3.18a}$$

$$N(z,t) = \sum_{k=1}^{N} N_k(t) \sin\left(\frac{k\pi z}{L}\right), \tag{3.18b}$$

$$q(z,t) = \sum_{k=1}^{N} q_k(t) \sin\left(\frac{k\pi z}{L}\right). \tag{3.18c}$$

These expressions satisfy the boundary conditions (3.16) and, by substituting them in (3.15a), one can define the k^{th} time dependent component of the axial tensile force through

$$N_k(t) = \frac{L^2}{k^2\pi^2}\frac{\mu}{h(1+r)}\frac{\partial^2 v_k(t)}{\partial t^2} + \frac{k^2\pi^2}{L^2}\frac{2EI}{h(1+r)}v_k(t) - \frac{L^2}{k^2\pi^2}\frac{1}{h(1+r)}q_k(t)\,. \tag{3.19}$$

Further substituting (3.19) in (3.15b), one fractional differential equation is obtained in the form

$$
\begin{aligned}
&- \frac{L^2}{k^2\pi^2}\frac{C_\alpha b}{r}\frac{2\mu}{h^2(1+r)EA}\,{}_0^C\mathcal{D}_t^{2+\alpha}[v_k(\cdot)](t) - \frac{\mu}{h(1+r)}\frac{\partial^2 v_k(t)}{\partial t^2} \\
&\qquad - \frac{k^2\pi^2}{L^2}\frac{C_\alpha b}{r}\left[\frac{4I}{h^2(1+r)A} + (1+r)\right]{}_0^C\mathcal{D}_t^{\alpha}[v_k(\cdot)](t) \\
&\qquad\qquad - \frac{k^4\pi^4}{L^4}\frac{2EI}{h(1+r)}v_k(t) \\
&\qquad = -\frac{L^2}{k^2\pi^2}\frac{C_\alpha b}{r}\frac{2}{h^2(1+r)EA}\,{}_0^C\mathcal{D}_t^{\alpha}[q_k(\cdot)](t) - \frac{1}{h(1+r)}q_k(t)\,, \quad (3.20)
\end{aligned}
$$

where $v_k(t)$ is the unknown function, corresponding to the k^{th} time dependent component of vertical displacement.

Equation (3.20) could be directly solved via a step-by-step integration by expressing all the derivatives through the Grünwald-Letnikov numerical formulation, recalled in Appendix A. Rigorously speaking, this method can be used when the applied action is a regular function of time t, but the blast load interpreted by Friedlander equation (3.4) presents a strong initial discontinuity at $t = 0$. The indistinct application of the numerical method involves an implicit regularization of the datum, which requires a very small integration step for its approximation. This may lead to an excessive computational effort. In order to overcome this problem, one possibility consists in integrating both sides of (3.20) up to the order $2+\alpha$ which, from a practical point of view, is equivalent to applying the Riemann-Liouville fractional integral (A.4) of order $2 + \alpha$. Since the system is at rest for $t \leq 0$ as per (3.17), recalling (A.4) and the equality (A.10), one obtains

$$
\begin{aligned}
&- \frac{L^2}{k^2\pi^2}\frac{C_\alpha b}{r}\frac{2\mu}{h^2(1+r)EA}v_k(t) - \frac{\mu}{h(1+r)}\,{}_0\mathcal{I}_t^{\alpha}[v_k(\cdot)](t) \\
&\qquad - \frac{k^2\pi^2}{L^2}\frac{C_\alpha b}{r}\left[\frac{4I}{h^2(1+r)A} + (1+r)\right]{}_0\mathcal{I}_t^{2}[v_k(\cdot)](t) \\
&\qquad\qquad - \frac{k^4\pi^4}{L^4}\frac{2EI}{h(1+r)}\,{}_0\mathcal{I}_t^{2+\alpha}[v_k(\cdot)](t) \\
&\qquad = -\frac{L^2}{k^2\pi^2}\frac{C_\alpha b}{r}\frac{2}{h^2(1+r)EA}\,{}_0\mathcal{I}_t^{2}[q_k(\cdot)](t) - \frac{1}{h(1+r)}\,{}_0\mathcal{I}_t^{2+\alpha}[q_k(\cdot)](t)\,. \quad (3.21)
\end{aligned}
$$

This equation is advantageous because both ${}_0\mathcal{I}_t^{2}[q_k(\cdot)](t)$ and ${}_0\mathcal{I}_t^{2+\alpha}[q_k(\cdot)](t)$ are C^1 functions. This result also highlights the great versatility of the fractional viscoelastic characterization, which formally allows a straightforward integration of the equations. Now, it is convenient to define the following two functions, related to the load, i.e.,

$$Q(z,t) = {}_0\mathcal{I}_t^2[q(z,\cdot)](t) = \frac{1}{\Gamma(2)}\int_0^t (t-\bar{t})\, q(z,\bar{t})\, d\bar{t}\,, \tag{3.22a}$$

$$P(z,t) = {}_0\mathcal{I}_t^{2+\alpha}[q(z,\cdot)](t) = \frac{1}{\Gamma(2+\alpha)}\int_0^t (t-\bar{t})^{\alpha+1}\, q(z,\bar{t})\, d\bar{t}\,, \tag{3.22b}$$

which are smooth even if $q(z,t)$ is not. In practice, they represent a regularized version of the applied load for which we consider their Fourier sine series

$$Q(z,t) = \sum_{k=1}^{N} Q_k(t)\sin\left(\frac{k\pi z}{L}\right), \tag{3.23a}$$

$$P(z,t) = \sum_{k=1}^{N} P_k(t)\sin\left(\frac{k\pi z}{L}\right). \tag{3.23b}$$

By subdividing the time interval under investigation $[0,\, T]$ in s subintervals of amplitude $\Delta t = t_j - t_{j-1}$ with $j = 1 \dots s$, define the vectors

$$\mathbf{Q}_{k,s} = [Q_k(t_1)\; Q_k(t_2)\; \dots\; Q_k(t_s)]\,, \tag{3.24a}$$

$$\mathbf{P}_{k,s} = [P_k(t_1)\; P_k(t_2)\; \dots\; P_k(t_s)], \tag{3.24b}$$

which are referred to the k^{th} component of Fourier sine series (3.23). By using the Grünwald-Letnikov approach, recalled in the Appendix, equation (3.21) can be written in matrix form as

$$\begin{aligned} -\frac{L^2}{k^2\pi^2}\frac{C_\alpha b}{r}\frac{2\mu}{h^2(1+r)EA}\mathbf{I}_s\mathbf{v}_{k,s} - \frac{\mu}{h(1+r)}\mathbf{A}_s^{(-\alpha)}\mathbf{v}_{k,s} \\ - \frac{k^2\pi^2}{L^2}\frac{C_\alpha b}{r}\left[\frac{4I}{h^2(1+r)A} + (1+r)\right]\mathbf{A}_s^{(-2)}\mathbf{v}_{k,s} \\ - \frac{k^4\pi^4}{L^4}\frac{2EI}{h(1+r)})\mathbf{A}_s^{(-2-\alpha)}\mathbf{v}_{k,s} \\ = -\frac{L^2}{k^2\pi^2}\frac{C_\alpha b}{r}\frac{2}{h^2(1+r)EA}\mathbf{I}_s\mathbf{Q}_{k,s} - \frac{1}{h(1+r)}\mathbf{I}_s\mathbf{P}_{k,s}\,, \end{aligned} \tag{3.25}$$

where $\mathbf{I}_s$ is the $s \times s$ identity matrix and $\mathbf{A}_s^{(\xi)}$, with $\xi = -\alpha;\, -2;\, -2-\alpha$, is the $s \times s$ lower band strip matrix

$$\mathbf{A}_s^{(\xi)} = \frac{1}{\Delta t^\xi}\begin{bmatrix} \omega_1(\xi) & & & \\ \omega_2(\xi) & \omega_1(\xi) & & \\ \vdots & \ddots & \ddots & \\ \omega_s(\xi) & \dots & \omega_2(\xi) & \omega_1(\xi) \end{bmatrix}, \tag{3.26}$$

with $\omega_1 = 1$, $\omega_2 = -\xi$, ..., $\omega_{\xi+1} = \dfrac{j-\xi-1}{j}\omega_j(\xi)$. From (3.25) the time history $\mathbf{v}_{k,s}^T = [v_{k,1}(t_1)\ v_{k,2}(t_2)\ \dots\ v_{k,s}(t_s)]$ can be calculated via step-by-step integration. The complete displacement field, in terms of vertical displacement $v(z,t)$, is found when the coefficients $v_k(t)$ of the Fourier sine series (3.18a) is known.

3.2.3 Numerical Experiments

As representative examples, we consider the same cases already introduced in Section 3.2.1, corresponding to simply supported laminated glass beams, with two glass plies sandwiching a polymeric interlayer, with length either $L = 2\,\mathrm{m}$ or $L = 4\,\mathrm{m}$. With reference to Fig. 3.8, for each ply we set $b = 1\,\mathrm{m}$ and $h = 0.1\,\mathrm{m}$, $A = b\,h$, Young's modulus $E_g = 70\,\mathrm{GPa}$. The mass per unit length of each ply is $(2500 \cdot A[\mathrm{m}^2])\,\mathrm{kg/m}$, whereas the mass of interlayer is supposed negligible. The thickness of the interlayer is $r\,h = 2.28\,\mathrm{mm}$, with $r = 0.228$, so it results from the assembly of six polymeric sheets of 0.38 mm, representing the commercial thickness of the single sheet. The beams are subjected to the effect of the blast wave, modelled as a time varying pressure $p(t)$ given by Friedlander equation (3.4), with the same parameters considered in Section 3.2.1. Hence, the transversal load per unit length acting on the beam is $q(z,t) = \hat{q}(t) = b\,p(t)$. In the following numerical experiments, equations (3.19) and (3.21) have been solved for the first 20 terms (10 terms not-null) of the Fourier sine series (3.18a) and (3.18b).

Monolithic and Layered limit

Solutions are presented in terms of transverse displacement $v(z,t)$ and axial force $N(z,t)$, both evaluated at $z = L/2$.

The monolithic limit accounts for glass plies perfectly coupled by the interlayer, and therefore corresponds to the case $C_\alpha \to \infty$. For the case $L = 2\,\mathrm{m}$, the results are represented in Fig. 3.10, where the complete solution (20 terms) is juxtaposed with the contributions corresponding to first non-null terms of the Fourier expansion $k = 1$ and $k = 3$. It should be observed that the term corresponding to the first vibration mode ($k = 1$) is dominant. The third mode ($k = 3$) is involved only at the beginning, but it rapidly fades. Since there is no dissipation from the interlayer, this means that the corresponding energy is in practice transferred to the first vibration mode.

Higher vibration modes become important for the longer beam with $L = 4\,\mathrm{m}$, for which the counterpart of Fig. 3.10 is represented by Fig. 3.11. Observe, in particular, that the third vibration mode ($k = 3$) considerably affects the axial force. This increases the peaks that correspond to the first mode ($k = 1$): a noteworthy error would have been made if the Fourier expansion had been limited to the first term.

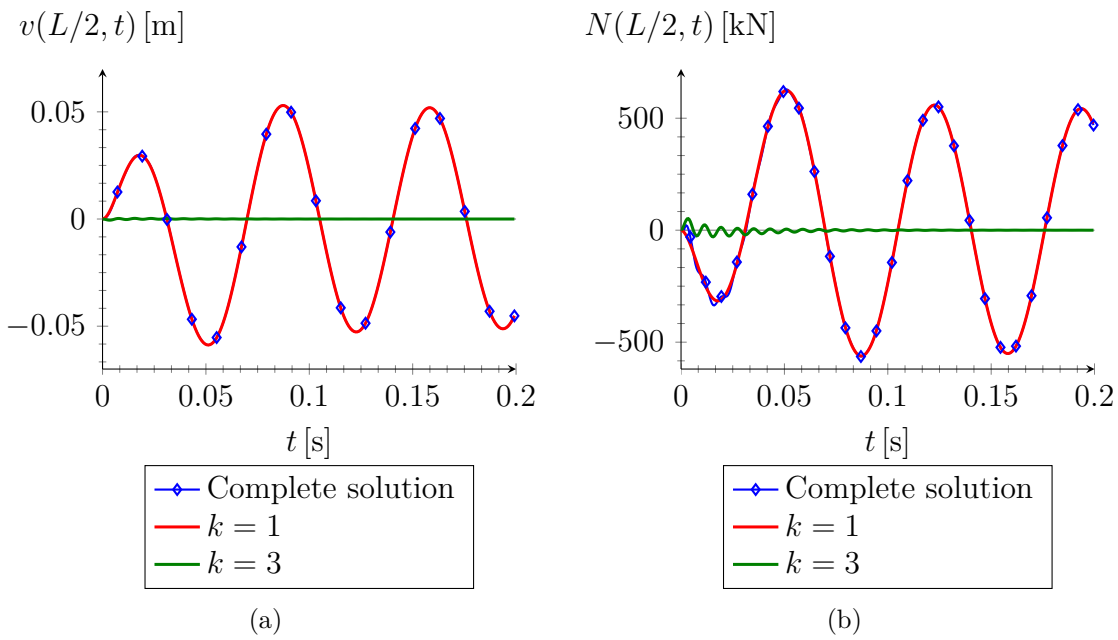

Figure 3.10. Monolithic limit, corresponding to the case $C_\alpha \to \infty$, for $L = 2\,\mathrm{m}$. (a) Transverse displacement $v(L/2,t)$ and (b) axial force $N(L/2,t)$, and contributions from the first ($k = 1$) and third ($k = 3$) vibration modes (numerical results obtained with a time-step $\Delta t = 10^{-4}\,\mathrm{s}$).

It is interesting to consider separately the contribution from the compression (positive) and suction (negative) phases of the blast wave, as indicated in Fig. 3.5. The graphs in Fig. 3.12 show this decomposition for the displacement $v(L/2,t)$ for either the cases $L = 2\,\mathrm{m}$ or $L = 4\,\mathrm{m}$. Observe that the maximum peak, in absolute terms, is attained at the second extremal point of the graphs, and this cannot be obtained by considering the compression phase only, as (unfortunately) it is customary in the engineering practice. In fact, the rebounding action caused by the elastic recovery force is increased by the suction phase of load; hence, the maximum displacement is negative, in accordance with the negative phase direction. In the ideal monolithic limit there is no dissipation, but we expect that, in a real case, the free oscillations consequent to this peak are damped by the viscosity of the interlayer. Hence, the most critical condition for the glass should in general be in correspondence of the second extremal point, in correspondence of the suction phase of the blast load[2].

The layered limit accounts for freely-sliding glass plies and can be obtained by

[2]Experiments have provided evidence that when a laminated glazing is broken by a blast wave, the interlayer with the adherent shards is projected outwards, rather than inwards.

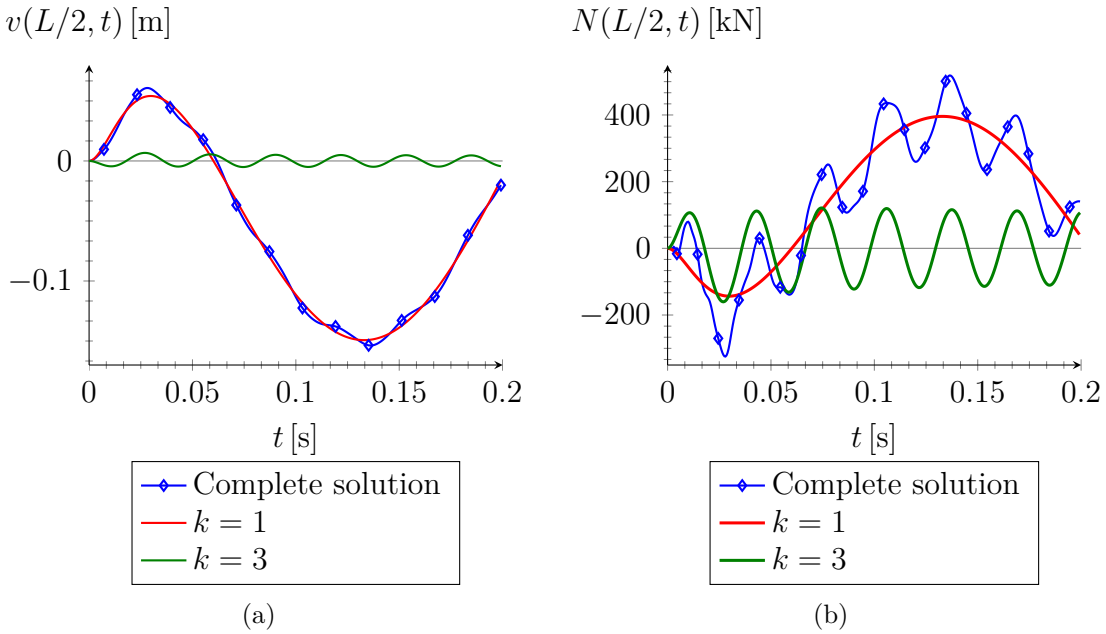

Figure 3.11. Monolithic limit, corresponding to the case $C_\alpha \to \infty$, for $L = 4\,\mathrm{m}$. (a) Transverse displacement $v(L/2,t)$ and (b) axial force $N(L/2,t)$, and contributions from the first ($k = 1$) and third ($k = 3$) vibration modes (numerical results obtained with a time step $\Delta t = 10^{-4}\,\mathrm{s}$).

setting $\alpha = 0$ and $C_\alpha = 0$. Obviously, the normal force in the plies is null. For $L = 2\,\mathrm{m}$ and $L = 4\,\mathrm{m}$, Fig. 3.13 shows the complete solution for $v(L/2,t)$ together with the contribution from the first ($k = 1$) and third ($k = 3$) vibration modes. As for the monolithic limit, the third mode mostly comes into play in the longer beam, although it remains of limited importance. The displacements are higher than in the monolithic limit due to the absence of any coupling effect by interlayer.

Convergence analysis

The fractional differential equations (3.20) are difficult to solve, because the applied load is strongly discontinuous in time at $t = 0$. Hence, the datum has been regularized by integrating with respect to time, in order to provide the expressions (3.21). This procedure is straightforward if one considers, as schematically indicated in Fig. 3.5(b), the decomposition of the blast wave pressure into the sum of a step (Heaviside) function, which carries the discontinuity and the remaining contribution (continuous at the origin). In fact, the Riemann Liouville fractional integrals appearing in (3.21) can be analytically solved when operating on a step function; the contribution associated with the continuous part of the applied load shall be

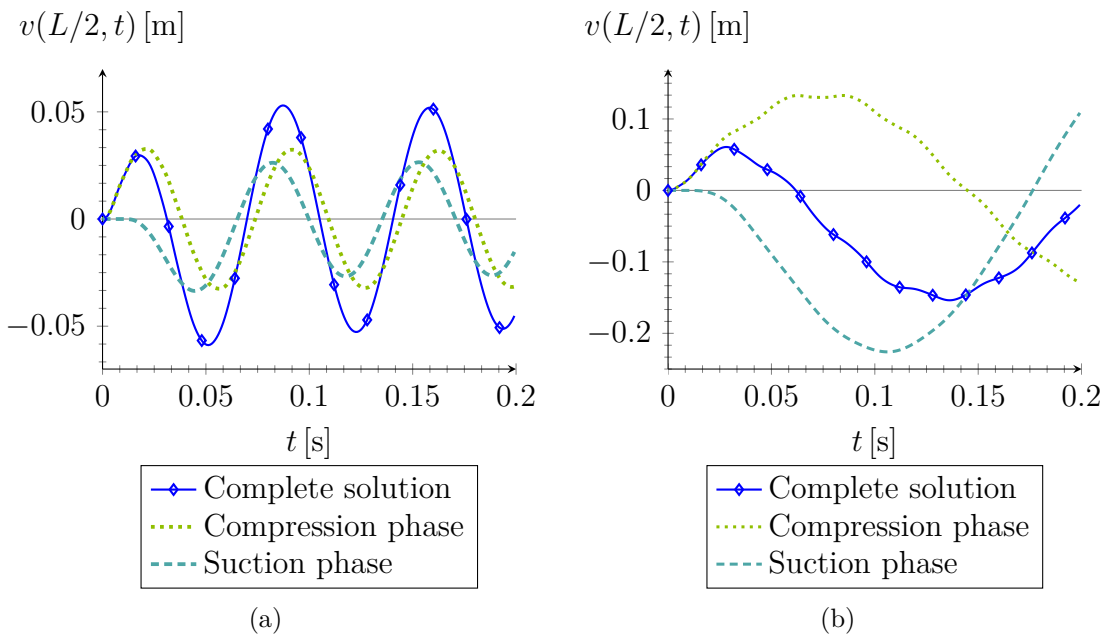

Figure 3.12. Monolithic limit corresponding to the case $C_\alpha \to \infty$. Transverse displacement $v(L/2,t)$ for (a) $L = 2\,\mathrm{m}$ and (b) $L = 4\,\mathrm{m}$, in which the contributions from the compression and suction phases are distinguished.

evaluated numerically. This is a mixed numerical-analytical method of solution, which by-passes the difficulties associated with the irregularity of the applied load. As purpose, the convergence of the Grünwald-Letnikov numerical scheme is discussed with respect to the time step Δt, when this is applied either to the equations (3.21), or tout-court to (3.20), hereafter respectively referred to as the *fractional integral equations* and the *fractional differential equations*. In this second case, we expect a much slower convergence because the numerical algorithm operates on a discontinuous function, which therefore requires an extremely reduced time step to be represented with accuracy. The fractional integral equations (3.25) are solved with a step-by-step integration for every k^{th} component, finding the array of values $v_{k,1}(t_1)\ v_{k,2}(t_2)\ \ldots\ v_{k,s}(t_s)$. We consider the first 20 terms of the Fourier sine series (10 non-null terms), by considering the sum (3.18a) with $N = 20$. The fractional differential equations (3.20), can be handled and solved in a similar way.

In the following examples, the interlayer is made of PVB operating at 50 °C, of the same type considered in [89], for which the constitutive fractional viscoelastic parameters are $\alpha = 0.155$ and $C_\alpha = 0.474\,\mathrm{MPa\ s}^\alpha$, as indicated in Table 3.1. The convergence of solution in terms of transverse displacement and axial force is studied while changing the integration time step Δt.

Consider first the fractional integral equations (3.21). The time histories for

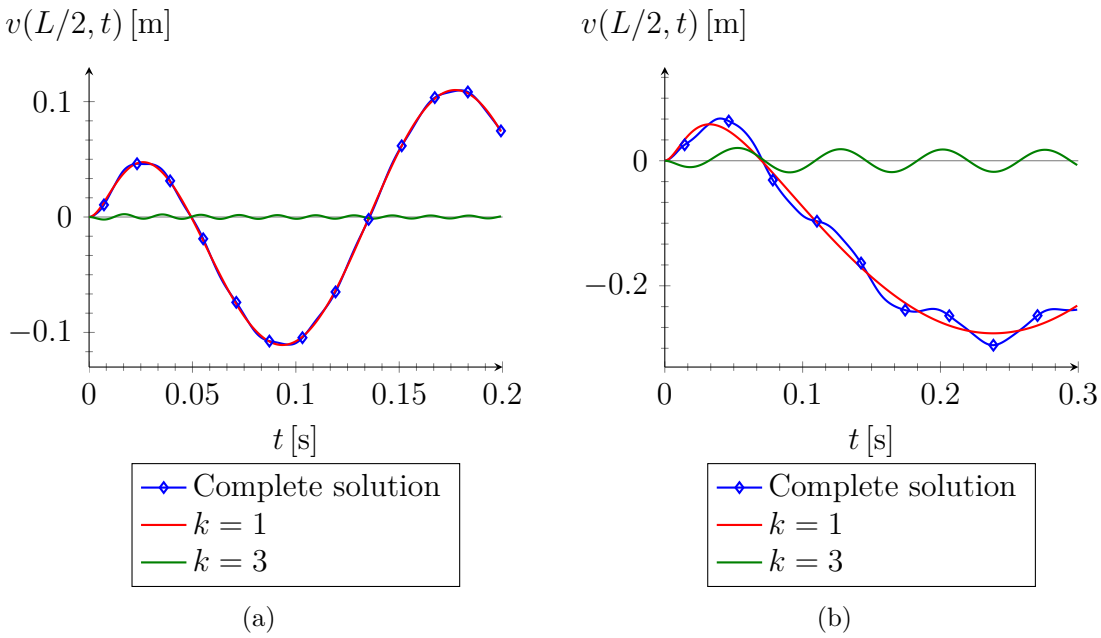

Figure 3.13. Layered limit corresponding to $\alpha = 0$ and $C_\alpha = 0$. Transverse displacement $v(L/2,t)$ evaluated for (a) $L = 2\,\mathrm{m}$ and (b) $L = 4\,\mathrm{m}$, and contributions from the first ($k = 1$) and third ($k = 3$) vibration modes (numerical results obtained with a time-step $\Delta t = 10^{-4}\,\mathrm{s}$).

the transverse displacement $v(L/2,t)$ and the axial force $N(L/2,t)$, obtained with different values of Δt, are represented in Fig. 3.14 for a beam with length $L = 2\,\mathrm{m}$. The graphs tend to overlap when the time step is of the order of $\Delta t = 10^{-3}\,\mathrm{s}$; using larger values the solution is not accurate.
The comparison with the solution obtainable via the fractional differential equations (3.20) can be better appreciated by reducing the time interval of observation to 0.05 s, which corresponds to a smaller neighborhood of the point of load discontinuity, in correspondence of the positive peak. Figs. 3.15(a) and 3.15(b) respectively show the transverse displacement $v(L/2,t)$ obtained either with (3.20) or (3.21). As expected, the fractional differential formulation (3.20) provides a much slower convergence with respect to the integral equations (3.21). The roughest time step $\Delta t = 5 \cdot 10^{-3}\,\mathrm{s}$ does not provide a sufficient precision in the first case, but it is quite accurate in the second case.

The greater accuracy of the integral formulation is even more appreciable in terms of axial forces in the glass plies. Being obtained through the relation (3.19) once the transverse displacement is known, the axial force $N(z,t)$ is strongly affected by any error in $v(z,t)$ because second-order derivative $\partial^2 v(z,t)/\partial t^2$ is involved. Fig. 3.16 compares the differential and integrated forms of the equations in terms of the value

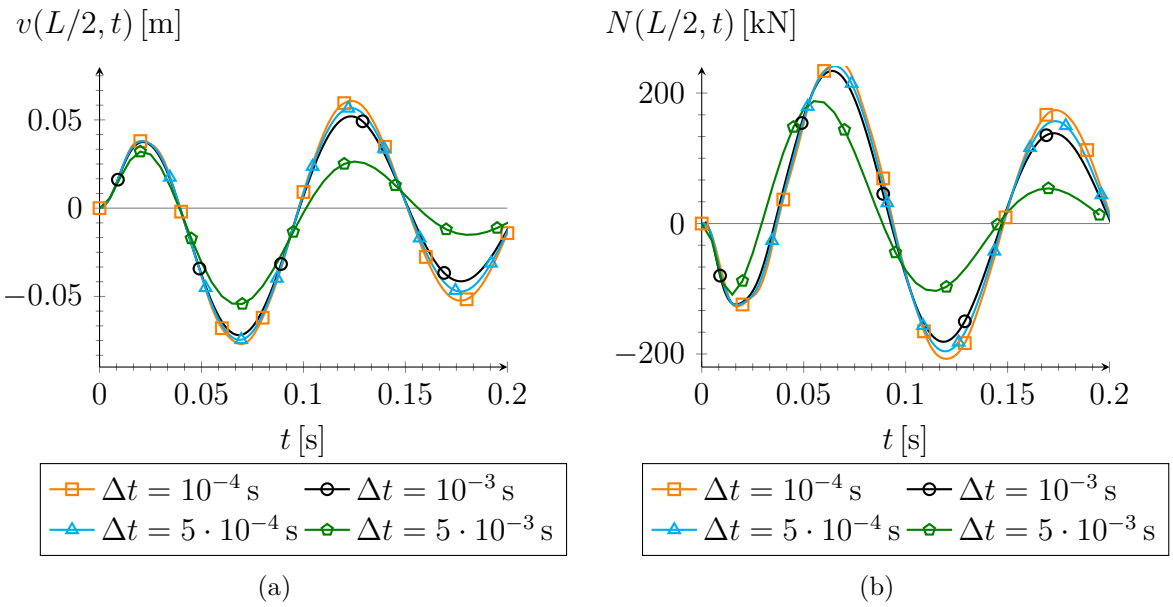

Figure 3.14. Convergence analysis for the fractional integrated equations (3.21) for a laminated beam with $L = 2\,\text{m}$ for various time steps Δt. (a) Transverse displacement $v(L/2,t)$ and (b) axial force $N(L/2,t)$ at midspan.

at midspan $N(L/2,t)$. Observe that the numerical approximation of the fractional differential equations (3.20) misses the solution - in particular the initial condition $N(L/2{,}0)$ is not satisfied - unless a very small time step, of the order of $\Delta t = 10^{-4}\,\text{s}$, is used. On the other hand, the fractional integral equations (3.21) provide much better results, because all solutions satisfy the initial condition $N(L/2{,}0)$ and they well overlap.

Various types of commercial polymeric interlayers

Now, we analyze the dynamic response of a beam laminated with different commercial polymeric interlayers, at various temperatures. The viscoelastic parameters are indicated in Table 3.1 and correspond to the materials tested in [89], for which the measured relaxation functions have been extrapolated to smaller times under the assumption of a power law trend, as schematically indicated in Fig. 3.3.

For a beam with $L = 2\,\text{m}$, the time dependent responses in terms of $v(L/2,t)$ and $N(L/2,t)$ are represented in Fig. 3.17, where also the monolithic limit, previously calculated in Section 3.2.3, is juxtaposed for the sake of comparison. The coefficient α does not sensibly vary from one material to the other, being the main difference in terms of the parameter C_α, which consequently measures the "stiffness" of the interlayer and its capacity in terms of shear coupling. Of course, the stiffer the

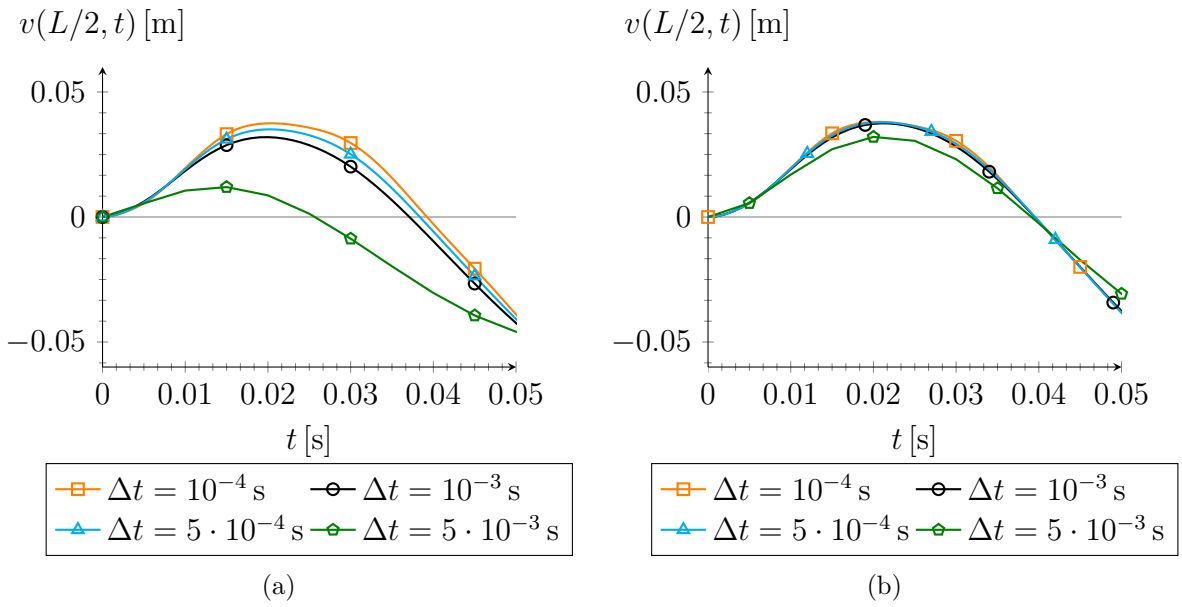

Figure 3.15. Convergence analysis for a laminated beam with $L = 2\,\mathrm{m}$ in terms of transverse displacement $v(L/2,t)$. Results from (a) the fractional differential equations (3.20) and (b) the fractional integrated equations (3.21) for various time steps Δt.

polymer, the smaller the amplitude and the higher the frequencies of oscillations. The shear coupling is responsible of the onset of the axial forces in the glass plies, which consequently diminish the more compliant the polymer is. The DG polymer at 15 °C, which presents the greatest coefficient $C_\alpha = 84.138\,\mathrm{MPa\ s}^\alpha$, imparts to the laminated beam a response close to the monolithic limit. The PVB at 50 °C provides for higher deformations and, consequently, the oscillations present a frequency lower than in the other cases. Here, the coupling action between plies is weak because of the low the coefficient $C_\alpha = 0.474\,\mathrm{MPa\ s}^\alpha$: this is confirmed by the limited axial force that is transmitted to the plies. The SG interlayer at 50 °C represents an intermediate case.

The counterpart of this figure for the case $L = 4\,\mathrm{m}$ is represented in Fig. 3.18. The same conclusions hold, even if now the contribution of the third vibration mode provides secondary oscillations that superimpose on first vibration mode. Also in this case, the PVB at 50 °C provides the weakest shear coupling (oscillations at low frequency and limited axial force), wheareas the DG at 15 °C approaches the monolithic limit.

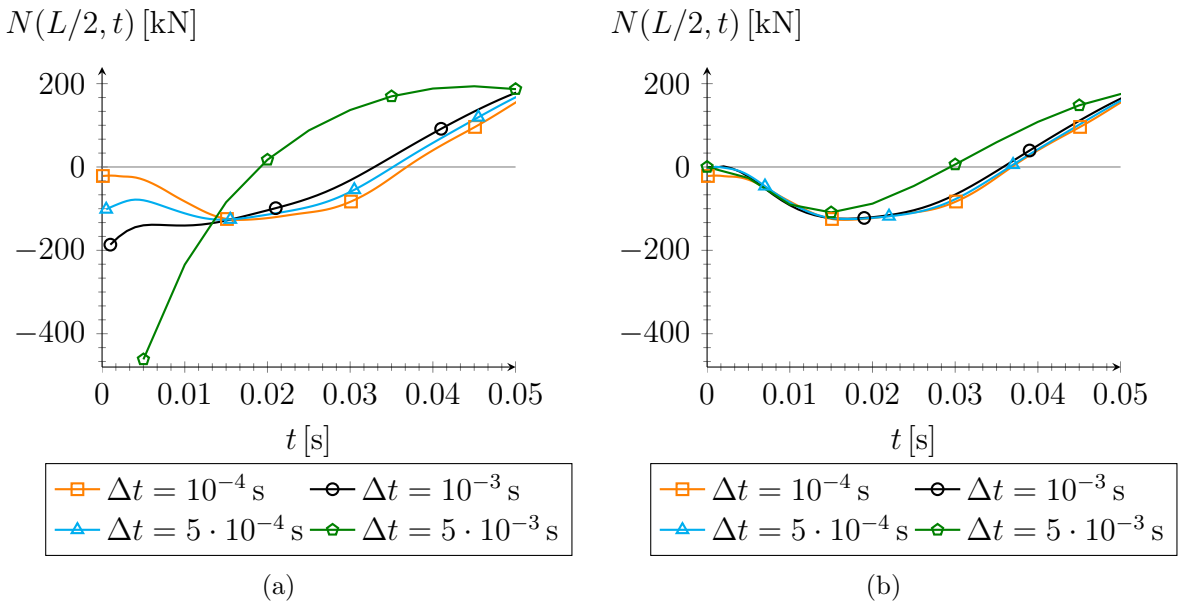

Figure 3.16. Convergence analysis for a laminated beam with $L = 2\,\text{m}$ in terms of axial force at midspan of the plies $N(L/2,t)$. Results from (a) the fractional differential equations (3.20) and (b) the fractional integrated equations (3.21) for various time steps Δt.

Parametric Analysis

The fractional viscoelastic characterization of polymeric interlayers relies upon the coefficient α, as well as on the modulus C_α, which is usually measured in MPa s^α, a somehow unusual unit of measure for an engineer. The physical meaning of such parameters can be clarified by recalling that the relaxation function takes the form of type $R(t) = [C_\alpha/\Gamma(1-\alpha)] \cdot t^{-\alpha}$, with R [MPa], t [s] and C_α [MPa s^α]. This corresponds to a straight line in the bi-logarithmic plane $\log(R)$-$\log(t)$, for which $-\alpha$ is the slope, while $C_\alpha/\Gamma(1-\alpha)$ represents the intersection at $t = 10^0$ s.

In order to better recognize the role of viscous parameters, a parametric analysis is performed where the values of α and C_α are *ideally* varied with reference to their graphical interpretation. The considered case is that of a beam with length $L = 2\,\text{m}$ and viscoelastic properties of PVB at 50 °C, with $\alpha = 0.155$ and $C_\alpha/\Gamma(1-\alpha) = 0.424\,\text{MPa s}^\alpha$ (see Table 3.1), which corresponds to the solid line in the bi-logarithmic plane of Fig. 3.19. By keeping fixed the value of the intercept point A with the line $t = 10^0$ s and by varying α, one obtains a pencil of lines which correspond to $C_\alpha = \Gamma(1-\alpha) \cdot 0.424\,\text{MPa s}^\alpha$.

The responses of a beam laminated with the polymers represented by this pencil of lines, for varying α, are plotted in Fig. 3.20 in terms of $v(L/2,t)$ and $N(L/2,t)$.

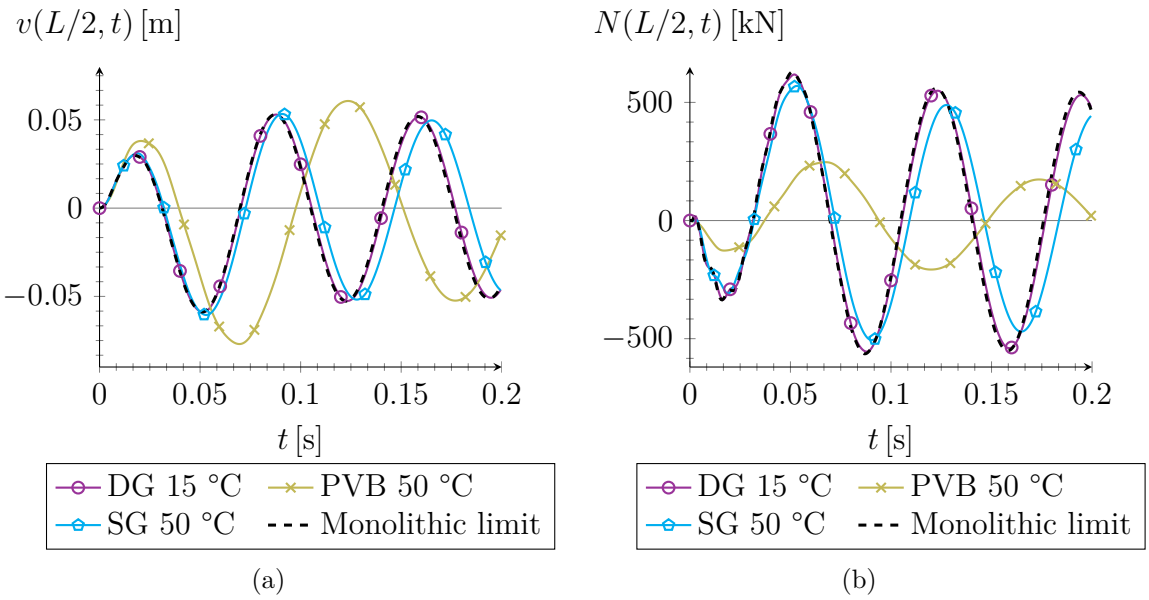

Figure 3.17. Response of a beam with length $L = 2\,\mathrm{m}$ laminated with various types of commercial polymeric interlayers. (a) Transverse displacement $v(L/2,t)$ and (b) axial force $N(L/2,t)$.

The limit cases are represented by the horizontal line with $\alpha = 0$ and the line inclined of -45 °corresponding to $\alpha = 1$. As expected, the role of the slope α is very important because it strongly affects the maximum deflection and the maximum axial force to which the beam is subjected. When $\alpha = 1$ the beam is the stiffest and the shear coupling between plies is maximized; on the other, setting $\alpha = 0$ leads to a decrease of axial force and consequently to a maximization of the deflections. We conjecture that the reason for this is that the beam is somehow sensitive to the values of the relaxation function for times of the order of the characteristic duration of the applied action which, for the case at hand, is approximately $t = 10^{-2}\,\mathrm{s}$. Indeed, it is clear from Fig. 3.19 that such values decrease with the slope of the representative lines in the bi-logarithmic plots.

If we take the pivot point B on $t = 10^{-2}\,\mathrm{s}$ to define a new pencil of lines, we can repeat almost the same procedure. Now, changing α causes an unavoidable variation of C_α. The solutions provided are almost overlapped, as shown in Fig. 3.21, because of two main reasons: the relaxation functions assume quite similar values for times of the order of T_d (characteristic duration of the applied action), and the coefficients C_α are great enough to almost reach the monolithic limit.

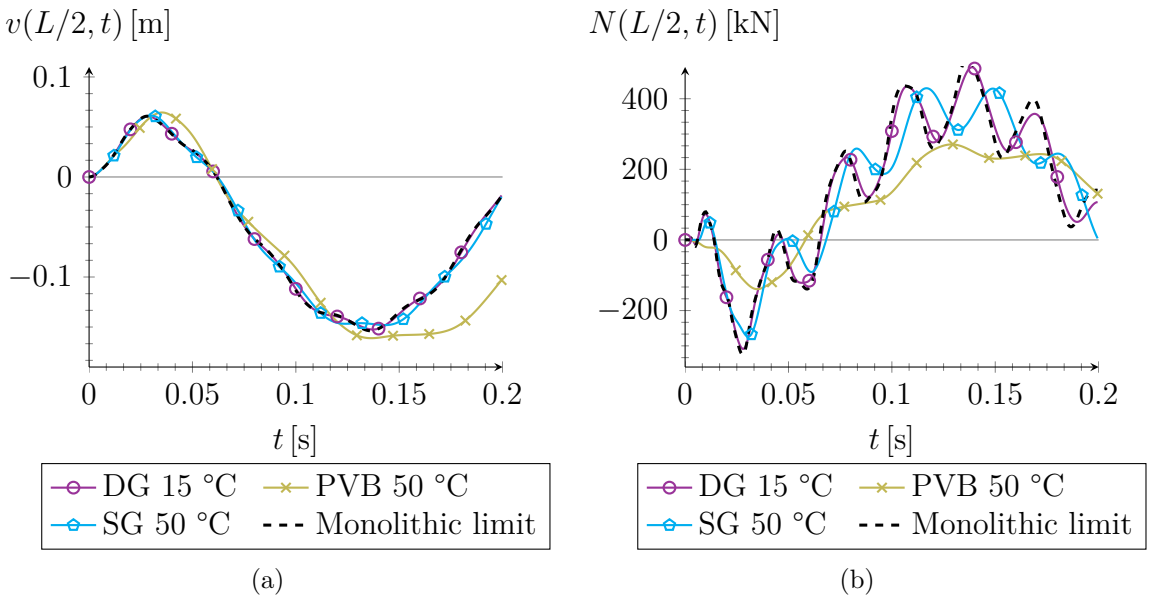

Figure 3.18. Response of a beam with length $L = 4\,\mathrm{m}$ laminated with various types of commercial polymeric interlayers. (a) Transverse displacement $v(L/2,t)$ and (b) axial force $N(L/2,t)$.

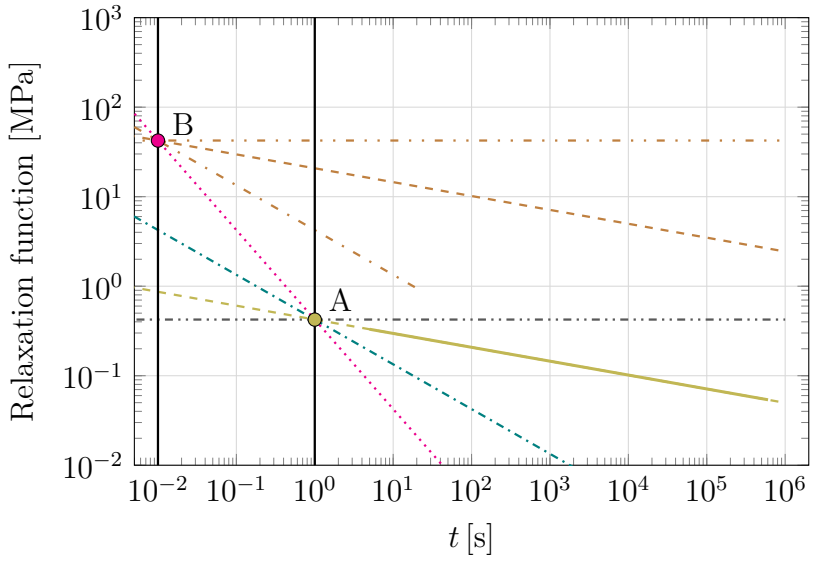

Figure 3.19. Bi-logarithmic plot of the relaxation functions used for the parametric analyses. The case of PVB at 50 °C is plotted with solid line.

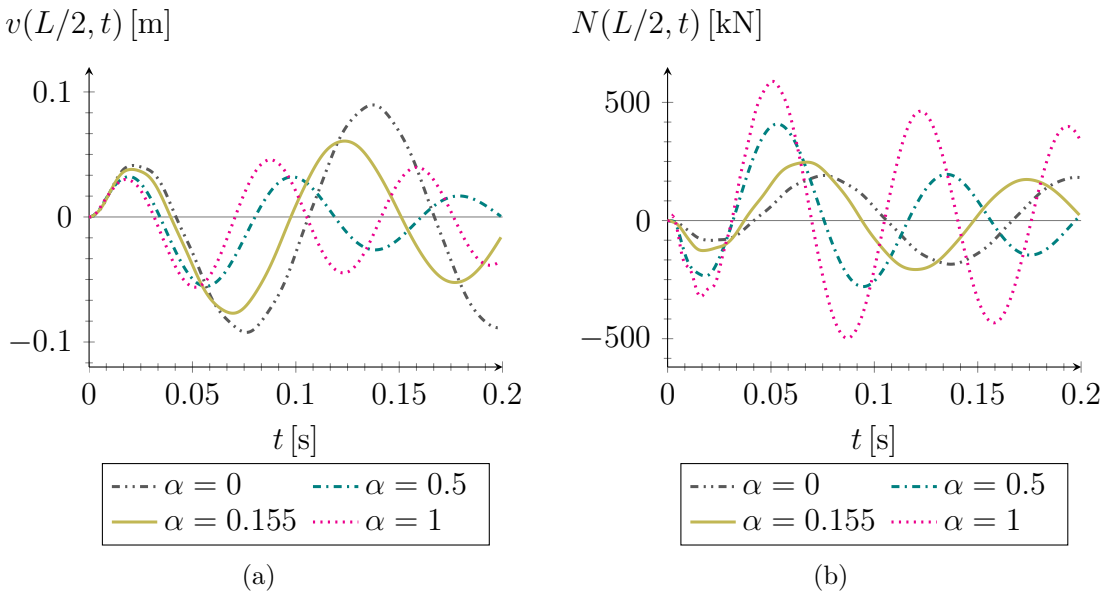

Figure 3.20. Parametric analyses for a beam with length $L = 2\,\mathrm{m}$, laminated with the polymers corresponding to the pencil of lines passing through the point A in Fig. 3.19. (a) Transverse displacements $v(L/2,t)$ and (b) axial force $N(L/2,t)$ at midspan.

3.2.4 The approach via Prony series

Since it is customary to interpret the relaxation function of a viscoelastic material through an expansion in Prony series, it is useful to compare the results of Section 3.2.3 with those obtainable with this characterization.

Governing equations

For the same simply supported beam considered in Sections 3.2.3, with the same notation of Section 3.2.2, we now specialize the governing equations to the Prony series. The balance equation (3.15a), written in terms of the vertical displacement $v(z,t)$, remains valid, but it is necessary to reformulate the constitutive relation describing the shear coupling through the interlayer. The shear strain $\gamma_{yz}(z,t)$ is assumed to be linear in the thickness. Hence, Boltzmann's superposition principle allows to write the shear stress in the general form

$$\tau_{yz}(z,t) = R(0)\gamma_{yz}(z,t) - \int_0^t \frac{\partial R(t-\bar{t})}{\partial \bar{t}} \gamma_{yz}(z,\bar{t})\, d\bar{t}\,, \tag{3.27}$$

where $R(t) = R_0 + \sum_{i=1}^{N} R_i e^{-t/\theta_i}$ denotes the relaxation function expressed via Prony series. From (3.8a) and (3.10a) one finds the dynamic equilibrium equation relative

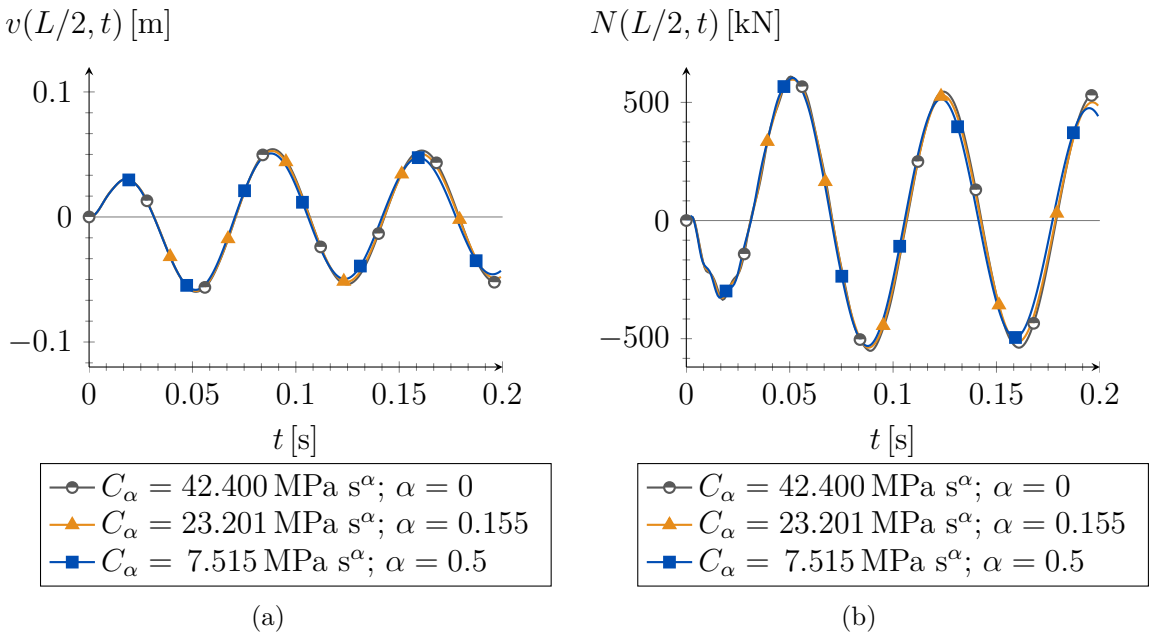

Figure 3.21. Parametric analyses. Transverse displacement $v(z,t)$ associated to various C_α and α, so that their relaxation functions all intersect the pivot point (magenta) in Fig. 3.19. They are evaluated in $z = L/2$, with $L = 2\,\mathrm{m}$.

to the axial force. After a few calculations, one obtains the counterpart of (3.15b) as an integro-differential equation of the form

$$\frac{\partial^2 N(z,t)}{\partial z^2} = -bR(0)\left[-\frac{2}{rh}\frac{N(z,t)}{EA} + \frac{1+r}{r}\frac{\partial^2 v(z,t)}{\partial z^2}\right] + b\int_0^t \frac{\partial R(t-\bar{t})}{\partial \bar{t}}\left[-\frac{2}{rh}\frac{N(z,\bar{t})}{EA} + \frac{1+r}{r}\frac{\partial^2 v(z,\bar{t})}{\partial z^2}\right] d\bar{t}\,. \quad (3.28)$$

Equations (3.15a) and (3.28) govern the dynamic equilibrium of the laminated beam when associated with the boundary (3.16) and the initial conditions (3.17). These can also be solved with an approach *à la* Galerkin. The vertical displacement $v(z,t)$, the axial force $N(z,t)$ and the external load $q(z,t)$ are expressed in Fourier sine series (3.18), and substituted into (3.15a) and (3.28). From (3.15a), one readily obtains the k^{th} component of the axial tensile force, as per (3.19). Further substituting (3.19) in (3.28), one finally finds the integro-differential equation

$$
\begin{aligned}
-\left(R(0)\frac{2b}{rhEA}+\frac{k\pi^2}{L^2}\right)\left(\frac{L^2}{k^2\pi^2}\frac{\mu}{h(1+r)}\frac{\partial^2 v_k(t)}{\partial t^2}+\frac{k^2\pi^2}{L^2}\frac{2EI}{h(1+r)}v_k(t)\right.\\
\left.-\frac{L^2}{k^2\pi^2}\frac{1}{h(1+r)}q_k(t)\right)=R(0)\frac{k^2\pi^2}{L^2}\frac{b(1+r)}{r}v_k(t)-\int_0^t\frac{\partial R(t-\bar{t})}{\partial\bar{t}}\left[\frac{2b}{rhEA}\right.\\
\times\left(\frac{L^2}{k^2\pi^2}\frac{\mu}{h(1+r)}\frac{\partial^2 v_k(\bar{t})}{\partial\bar{t}^2}+\frac{k^2\pi^2}{L^2}\frac{2EI}{h(1+r)}v_k(\bar{t})-\frac{L^2}{k^2\pi^2}\frac{1}{h(1+r)}q_k(\bar{t})\right)\\
\left.+\frac{k^2\pi^2}{L^2}\frac{b(1+r)}{r}v_k(\bar{t})\right]d\bar{t}. \quad (3.29)
\end{aligned}
$$

With a step-by-step integration, by using the finite difference approach, the function $v_k(t)$ can be numerically determined.

Comparison

In order to compare the results obtainable via the Prony series approach with those corresponding to fractional treatment by means of power laws, consider the same beam analyzed in Section 3.2.3 of length $L = 2\,\mathrm{m}$, laminated with a PVB working at an environmental temperature of 50 °C. The representative points of the relaxation function, measured in [89], can be well interpreted by a power law, whose parameters are recorded in Table 3.1. This function has been extrapolated on the left hand side to the time scale of interest, of the order of $10^{-4}\,\mathrm{s}$, as the continuation of the linear trend in the bi-log plot, depicted in Fig. 3.3.

Indeed, the power law represents our benchmark reference trend: the Prony series is the sum of exponential terms, whose coefficients need to be calibrated in order to fit this datum. Certainly, a large number of parameters is necessary to achieve a good precision. Since we are interested in the short-term response under the short-duration blast wave, we set in (3.3) $R_0 = 0$ and we calibrate the coefficients R_i and θ_i, $i = 1 \dots N$, for either $N = 5$ or $N = 10$. Fig. 3.22 shows the results as bi-log plots: the line corresponding to the power law has been best fitted by the series of exponential functions using the command `FindFit` in `Mathematica`, which uses the Levenberg–Marquardt algorithm. The interpolations are focused on diverse intervals, corresponding to $t \in (10^{-4},10^{-2})$ for $N = 5$, and to $t \in (10^{-4},10^{0})$ for $N = 10$. Observe that outside such intervals, the Prony series diverges from the power law trend.

The corresponding response under the blast wave, in terms of displacement $v(L/2,t)$ and axial force $N(L/2,t)$ at midspan are reported in Fig. 3.23. In all the considered cases, solutions have been obtained by using a time step $\Delta t = 10^{-4}\,\mathrm{s}$. All graphs perfectly overlap at least up to the first peak, for times of the order $5 \cdot 10^{-2}\,s$. This is the time interval for which the interpolation with both $N = 5$

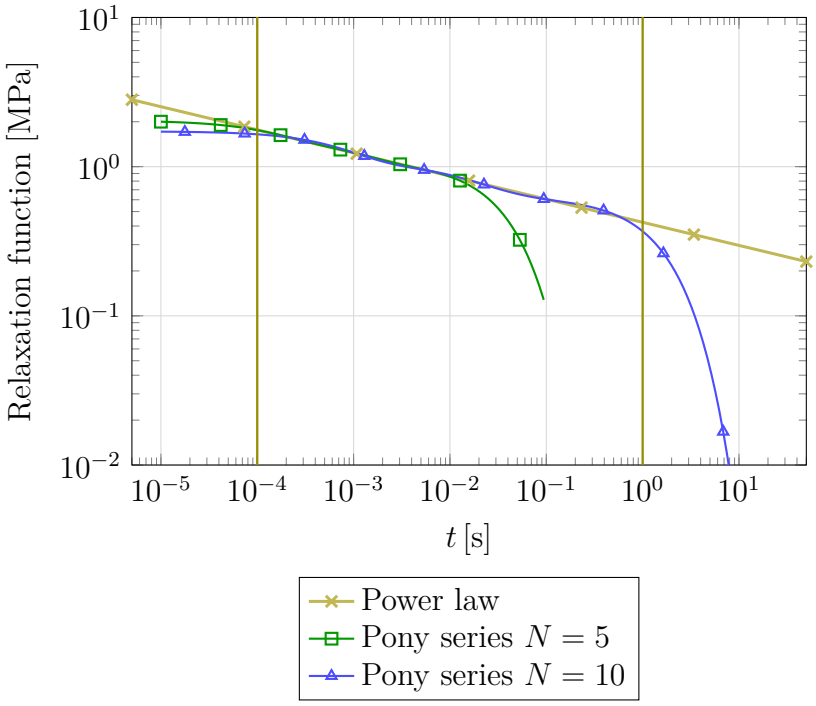

Figure 3.22. Relaxation functions corresponding to PVB at 50 °C, expressed by means of a power law (yellow) and Prony series with either $N = 10$ (light blue) or $N = 5$ (green) terms.

and $N = 10$ almost overlap with the power law. However, for longer times, the solution for $N = 5$ diverges from the others, because now the Prony interpolation is not accurate, as it is clear from Fig. 3.22. In this case, at least $N = 10$ terms are needed to obtain results that square with the output from the fractional model. In any case, if the interval of observation was prolonged beyond 10^0 s, where also the Prony interpolation with $N = 10$ terms diverges, one would notice a difference with respect to the trend obtained with the fractional approach. However, for such long times the dissipation has already smoothen out the oscillations provoked by the blast wave.

This example highlights the difficulties while using Prony series to interpolate a relaxation function that exhibits a power law trend, even if for the case at hand the applied action has a short duration and, hence, the relaxation function needs to be well interpolated only in a very restricted time interval. Results are not accurate outside the strict interval in which the corresponding curves overlap; consequently, in the worked example, $N = 10$ terms in the Prony series are necessary to obtain an optimal accordance. However, a noteworthy effort is needed to calibrate the 20 coefficients that determine the series (10 terms R_i and 10 terms θ_i), instead of just two parameters that define the power-law (C_α and α). It should also be mentioned

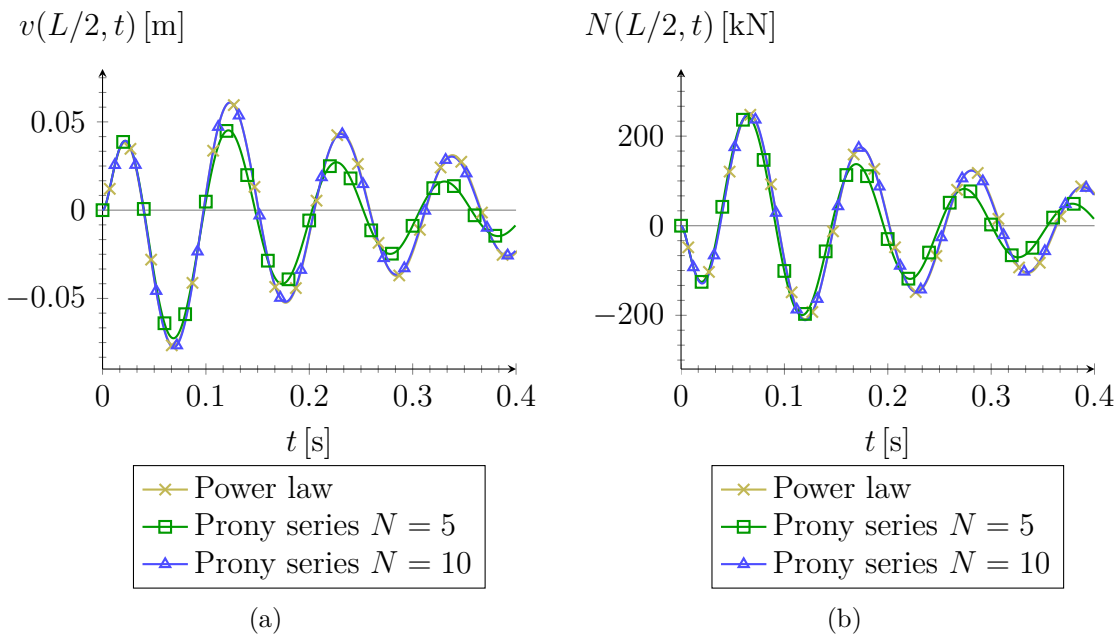

Figure 3.23. Laminated beam with $L = 2\,\mathrm{m}$, laminated with a PVB interlayer at 50 °C. Results in terms of (a) transverse displacement $v(L/2,t)$ and (b) axial force $N(L/2,t)$ at midspan, obtained with the fractional characterization of the power law (yellow) and its interpolation with a Prony series with either $N = 5$ (blue) or $N = 10$ (green) terms, indicated in Fig. 3.22.

that when the time dependent response is investigated during a very short time period, it is difficult to interpolate the relaxation function with exponential terms because the coefficients θ_i become very large, and this may cause overflow errors because the output is close to the machine precision. This inconvenience is bypassed while using the fractional characterization of viscoelastic response.

3.3 Laminated glass plates

As natural extension of laminated glass beams, we propose an analytical model for simply supported sandwich plates. The viscoelastic behavior of interlayer is described through fractional calculus; the glass plies are assumed to be Kirchhoff-Love plates, and the impulsive load follows Friedlander equation. Finally, some numerical experiments are conducted in order to highlight the resulting state of stress.

3.3.1 The blast load

The blast load needs to be changed in order to better highlight the dynamic response of plate. The glass panel is loaded with a time dependent force per unit area, which is uniformly distributed on its surface and acts along the out-of-plane direction. The time history of such load is assumed to be analogous to that classified as EXV25[3], in accordance with norm ISO 16933:2007 [8]. This loading action can be interpreted via Friedlander equation

$$p(t) = p_r\left(1 - \frac{t}{T_d}\right)e^{-\beta\frac{t}{T_d}}\,, \tag{3.30}$$

where p_r is the peak overpressure, T_d is the time positive duration and β is the decay coefficient. The norm ISO 16933:2007 just imposes the peak overpressure $p_r = 80\,\text{kPa}$ and the positive impulse $i_r^+ = 380\,\text{kPa·ms}$. In order to obtain all the rest of parameters, $W_{\text{TNT}} = (1.7 \cdot 100)\,\text{kg}$ is taken as equivalent mass of charge[4], so that the scaled distance results

$$Z = \frac{R}{W_{\text{TNT}}^{1/3}} = \frac{25}{(1.71 \cdot 100)^{1/3}} = 4.51\,\text{kg/m}^{1/3}\,. \tag{3.31}$$

It is possible to take an empirical formula based on Z variable from literature, and get the time positive duration. The relation proposed by Kinney and Graham [26] is adopted because of its optimal agreement with experimental results provided by Kingery and Bulmash [34]. Therefore, it reads

$$T_d = W_{\text{TNT}}^{1/3} \cdot \frac{980\left[1 + \left(\dfrac{Z}{0.54}\right)^{10}\right]}{\left[1 + \left(\dfrac{Z}{0.02}\right)^{3}\right] \cdot \left[1 + \left(\dfrac{Z}{0.74}\right)^{6}\right] \cdot \sqrt{\left[1 + \left(\dfrac{Z}{6.9}\right)^{2}\right]}} = 12.7\ \text{ms}; \tag{3.32}$$

From the nonlinear equation

$$i_r^+ = \int_0^{T_d} p_r\left(1 - \frac{t}{T_d}\right)e^{-\frac{\beta}{T_d}t}\,dt = p_r T_d\left[\frac{1}{\beta} - \frac{1}{\beta^2}(1 - e^{-\beta})\right], \tag{3.33}$$

the decay coefficient $\beta = 0.95$ is automatically deduced.

---

[3]This blast load refers to an open arena full-scale test, which is performed by placing the target (i.e. glass panel) on a rigid frame at $R = 25\,\text{m}$ from the detonating charge. The energy released corresponds to 100 kg of TNT.

[4]The coefficient 1.7 is needed to consider the ground reflection (surface burst): the energy is concentrated inside a hemispherical volume and it consequently results almost doubled.

3.3.2 Governing equations for a simply supported sandwich plate

The laminated glass panel is formed by two elastic glass plies, sandwiching a thin viscoelastic interlayer. After having presented the mechanical model for the composite plate, the governing equations are extended to take into account the presence of a compliant back structure, which supports the plate.

3.3.3 Governing equations for a simply supported plate

The schematic representation of the composite plate is that of Fig. 3.24(a). This is a three-layer plate composed by two thick elastic plies (layers "1" and "2") sandwiching one thin viscoelastic core (layer "0"). We introduce a reference frame with the (x, y) axes located in-plane, as indicated in the Figure, and one z axis for each layer such that the mid-surface corresponds to $z = 0$. The external plies are Kirchhoff-Love plates; the core is too compliant to provide axial/bending stiffness, but it produces the shear coupling of the layers that are bonded through it, under the assumption that there is no sliding at the interfaces.
The thickness of the external plies is denoted by h_i with $i = 1{,}2$, so that the distance between the mid-planes reads

$$\bar{h} = h_0 + \frac{h_1 + h_2}{2}\,, \tag{3.34}$$

where h_0 represents the thickness of polymeric core. With reference to Figs. 3.24(b)-3.24(c), the interlayer "0" undergoes *shear strains*, which depend on the in-plane displacements $u_i = u_i(x, y, t)$ and $v_i = v_i(x, y, t)$ of the external layers, for $i = 1{,}2$, as well as the out-of-plane displacement $w = w(x, y, t)$, which is the same for both layers. In particular, pure geometric considerations indicate that, within the hypothesis of infinitesimal deformations, the engineering shear strain components $\gamma_{x,0}$ and $\gamma_{y,0}$, considered independent of the variable z due to thinness of the interlayer, take the form

$$\gamma_{x,0} = \gamma_{x,0}(x, y, t) = \frac{u_{2,0} - u_{1,0}}{h_0} + \frac{\partial w}{\partial x} = \frac{u_2 - u_1}{h_0} + \frac{\bar{h}}{h_0}\frac{\partial w}{\partial x}\,, \tag{3.35a}$$

$$\gamma_{y,0} = \gamma_{y,0}(x, y, t) = \frac{v_{2,0} - v_{1,0}}{h_0} + \frac{\partial w}{\partial y} = \frac{v_2 - v_1}{h_0} + \frac{\bar{h}}{h_0}\frac{\partial w}{\partial y}\,. \tag{3.35b}$$

For a constitutive model based on fractional calculus, recalled in the Appendix, the shear forces per unit length $Q_{x,0}$ and $Q_{y,0}$ depend on the shear stresses $\tau_{xz,0} = \tau_{xz,0}(x, y, t)$ and $\tau_{yz,0} = \tau_{yz,0}(x, y, t)$ reading

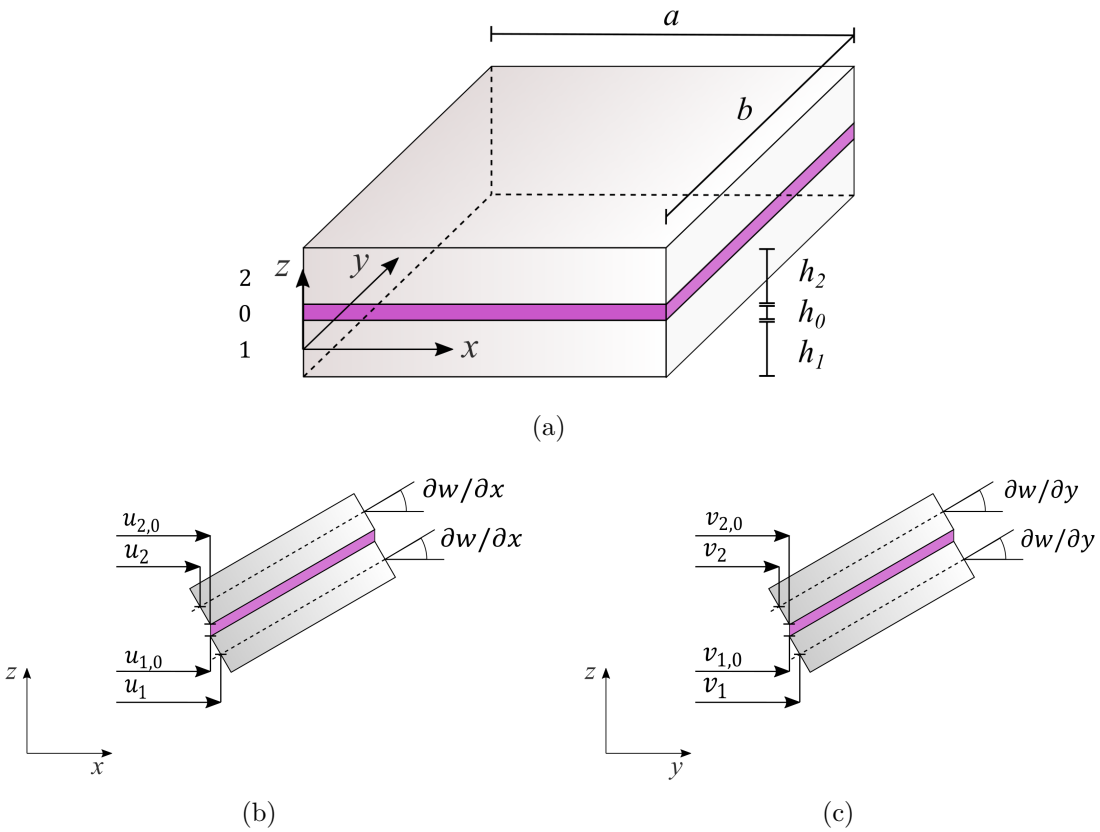

Figure 3.24. Schematic representation of a three-layered sandwich plate. (a) Initial configuration. (b) Deformed configuration on the plane x-z. (c) Deformed configuration on the plane y-z.

$$Q_{x,0} = Q_{x,0}(x,y,t) = \int_{-h_0/2}^{h_0/2} \tau_{xz,0}\, dz = C_\alpha\, {}_0^C\mathcal{D}_t^\alpha \left[u_2 - u_1 + \bar{h}\frac{\partial w}{\partial x} \right](t)\,, \tag{3.36a}$$

$$Q_{y,0} = Q_{y,0}(x,y,t) = \int_{-h_0/2}^{h_0/2} \tau_{yz,0}\, dz = C_\alpha\, {}_0^C\mathcal{D}_t^\alpha \left[v_2 - v_1 + \bar{h}\frac{\partial w}{\partial y} \right](t)\,, \tag{3.36b}$$

where C_α is a dimensional coefficient and α is the order of Caputo's fractional derivative (see Appendix A).

The strain components in the layers "1" and "2"($\varepsilon_{x,i}$, $\varepsilon_{y,i}$, $\varepsilon_{xy,i}$, for $i = 1,2$), are listed as follows

$$\varepsilon_{x,i} = \varepsilon_{x,i}(x,y,z,t) = \frac{\partial u_i}{\partial x} - z\frac{\partial^2 w}{\partial x^2}\,; \tag{3.37a}$$

$$\varepsilon_{y,i} = \varepsilon_{y,i}(x,y,z,t) = \frac{\partial v_i}{\partial y} - z\frac{\partial^2 w}{\partial y^2}\,; \tag{3.37b}$$

$$\varepsilon_{xy,i} = \varepsilon_{xy,i}(x,y,z,t) = \frac{\partial u_i}{\partial y} + \frac{\partial v_i}{\partial x} - 2z\frac{\partial^2 w}{\partial x \partial y}\,. \tag{3.37c}$$

The related stresses can be obtained from the corresponding constitutive relations. Denoting with E_i the Young's modulus and with ν_i the Poisson's ratio of the i^{th} layer, for $i = 1{,}2$, the in-plane forces per unit length can be written as

$$N_{x,i} = N_{x,i}(x,y,t) = \int_{-h_i/2}^{h_i/2} \sigma_{x,i}\, dz = \frac{E_i h_i}{1-\nu_i^2}\left(\frac{\partial u_i}{\partial x} + \nu_i \frac{\partial v_i}{\partial y}\right), \tag{3.38a}$$

$$N_{y,i} = N_{y,i}(x,y,t) = \int_{-h_i/2}^{h_i/2} \sigma_{y,i}\, dz = \frac{E_i h_i}{1-\nu_i^2}\left(\frac{\partial v_i}{\partial y} + \nu_i \frac{\partial u_i}{\partial x}\right), \tag{3.38b}$$

$$N_{xy,i} = N_{xy,i}(x,y,t) = \int_{-h_i/2}^{h_i/2} \sigma_{xy,i}\, dz = \frac{E_i h_i}{2(1+\nu_i)}\left(\frac{\partial u_i}{\partial y} + \frac{\partial v_i}{\partial x}\right); \tag{3.38c}$$

while the bending moments per unit length are

$$M_{x,i} = M_{x,i}(x,y,t) = \int_{-h_i/2}^{h_i/2} \sigma_{x,i} z\, dz = -\frac{E_i h_i^3}{12(1-\nu_i^2)}\left(\frac{\partial^2 w}{\partial x^2} + \nu_i \frac{\partial^2 w}{\partial y^2}\right), \tag{3.39a}$$

$$M_{y,i} = M_{y,i}(x,y,t) = \int_{-h_i/2}^{h_i/2} \sigma_{x,i} z\, dz = -\frac{E_i h_i^3}{12(1-\nu_i^2)}\left(\frac{\partial^2 w}{\partial y^2} + \nu_i \frac{\partial^2 w}{\partial x^2}\right), \tag{3.39b}$$

$$M_{xy,i} = M_{xy,i}(x,y,t) = \int_{-h_i/2}^{h_i/2} \sigma_{xy,i} z\, dz = -\frac{E_i h_i^3}{12(1+\nu_i)}\left(\frac{\partial^2 w}{\partial x \partial y}\right). \tag{3.39c}$$

The governing equations can be deduced from Hamilton's principle, i.e.,

$$\int_{t_1}^{t_2} [\delta(\mathcal{K} - \mathcal{U}) + \delta\mathcal{W}_{\text{nc}} + \delta\mathcal{W}_{\text{ext}}]\, dt = 0\,, \tag{3.40}$$

where $\mathcal{K}$ represents the kinetic energy of the sandwich plate, $\mathcal{U}$ is the elastic energy, $\mathcal{W}_{\text{nc}}$ is the work made by the non-conservative forces and $\mathcal{W}_{\text{ext}}$ is the work of the external load.

By neglecting the kinetic energy associated to in-plane trajectories, one finds

$$\mathcal{K} = \frac{1}{2}\mu \int_A \dot{w}^2\, dA\,, \tag{3.41}$$

where $\mu = \rho_0 h_0 + \rho_1 h_1 + \rho_2 h_2$ is global mass per unit area, having denoted with ρ_j, $j = 0,1,2$ the densities of the corresponding layers.

The elastic energy presents two contributions, respectively related to the in-plane and bending deformations of the external plies only. Therefore, it reads

$$\begin{aligned}\mathcal{U} = \frac{1}{2}\int_A \sum_{i=1,2}\Bigg[N_{x,i}\frac{\partial u_i}{\partial x} + N_{y,i}\frac{\partial v_i}{\partial y} + N_{xy,i}\left(\frac{\partial u_i}{\partial y} + \frac{\partial v_i}{\partial x}\right) \\ + M_{x,i}\frac{\partial^2 w}{\partial x^2} + M_{y,i}\frac{\partial^2 w}{\partial y^2} + 2M_{xy,i}\frac{\partial^2 w}{\partial x \partial y}\Bigg] dA\,.\end{aligned} \tag{3.42}$$

The non-conservative work is due to the viscous core, whose action is

$$\delta\mathcal{W}_{\text{nc}} = \int_A [Q_{x,0}, \delta\gamma_{x,0} + Q_{y,0}\,\delta\gamma_{y,0}]\, dA\,. \tag{3.43}$$

Since the plate is loaded by a uniformly distributed force per unit area $p(t)$, the work performed by the external forces results

$$\delta\mathcal{W}_{\text{ext}} = p\int_A \delta w\, dA\,. \tag{3.44}$$

In the considered case study, for simplicity both external plies are monoliths made of the same material (Young's modulus $E_1 = E_2 \equiv E_g$ and Poisson's ratio $\nu_1 = \nu_2 \equiv \nu$), and with the same thickness ($h_1 = h_2 \equiv h$). Their dimensions are thus indicated as $a \times b \times h$. Due to the geometric and load symmetry, $u_1 = -u_2$ and $v_1 = -v_2$. Hence, having defined $\Delta u = u_2 - u_1$ and $\Delta v = v_2 - v_1$, the problem is described by the three equilibrium equations

$$\begin{aligned}\mu\frac{\partial^2 w(x,y,t)}{\partial t^2} + \frac{E_g h^3}{6(1-\nu^2)}\left(\frac{\partial^4 w(x,y,t)}{\partial x^4} + 2\frac{\partial^4 w(x,y,t)}{\partial x^2 \partial y^2} + \frac{\partial^4 w(x,y,t)}{\partial y^4}\right) \\ = \frac{\bar{h}}{h_0} C_\alpha\, {}_0^C\mathcal{D}_t^\alpha\left[\frac{\partial \Delta u(x,y,\cdot)}{\partial x} + \bar{h}\frac{\partial^2 w(x,y,\cdot)}{\partial x^2}\right](t) \\ + \frac{\bar{h}}{h_0} C_\alpha\, {}_0^C\mathcal{D}_t^\alpha\left[\frac{\partial \Delta v(x,y,\cdot)}{\partial y} + \bar{h}\frac{\partial^2 w(x,y,\cdot)}{\partial y^2}\right](t) + p(t)\,,\end{aligned} \tag{3.45a}$$

$$\begin{aligned}\frac{E_g h}{1-\nu^2}\left[\frac{\partial^2 \Delta u(x,y,t)}{\partial x^2} + \frac{1}{2}(1-\nu)\frac{\partial^2 \Delta u(x,y,t)}{\partial y^2} + \frac{1}{2}(1+\nu)\frac{\partial^2 \Delta v(x,y,t)}{\partial x \partial y}\right] \\ = \frac{2}{h_0} C_\alpha\, {}_0^C\mathcal{D}_t^\alpha\left[\Delta u(x,y,\cdot) + \bar{h}\frac{\partial w(x,y,\cdot)}{\partial x}\right](t)\,,\end{aligned} \tag{3.45b}$$

$$\frac{E_g h}{1-\nu^2}\left[\frac{\partial^2 \Delta v(x,y,t)}{\partial y^2}+\frac{1}{2}(1-\nu)\frac{\partial^2 \Delta v(x,y,t)}{\partial x^2}+\frac{1}{2}(1+\nu)\frac{\partial^2 \Delta u(x,y,t)}{\partial x \partial y}\right] = \frac{2}{h_0}C_\alpha \, {}_0^C\mathcal{D}_t^\alpha\left[\Delta v(x,y,\cdot)+\bar{h}\frac{\partial w(x,y,\cdot)}{\partial y}\right](t)\,. \quad (3.45c)$$

It is clear that the first equation represents the out-of-plane equilibrium, whereas the remaining two indicate the equilibrium in the x and y direction, respectively.

Hamilton's principle also provide the boundary conditions, which can synthetically stated in variational form as

$$\begin{aligned}
&-\int_{\partial\Omega}\sum_{i=1,2}\left[N_{x,i}n_x\delta u_i+N_{y,i}n_y\delta v_i+N_{xy,i}(n_y\delta u_i+n_x\delta v_i)\right]d\ell \\
&\quad-\int_{\partial\Omega}\sum_{i=1,2}\left[M_{x,i}n_x\frac{\partial\delta w}{\partial x}+M_{y,i}n_y\frac{\partial\delta w}{\partial y}+M_{xy}\left(n_y\frac{\partial\delta w}{\partial x}+n_x\frac{\partial\delta w}{\partial y}\right)\right]d\ell \\
&\quad+\int_{\partial\Omega}\sum_{i=1,2}\left[\frac{\partial M_{x,i}}{\partial x}n_x+\frac{\partial M_{y,i}}{\partial y}n_y+\frac{\partial M_{xy}}{\partial y}n_x+\frac{\partial M_{xy}}{\partial x}n_y\right]\delta w\,d\ell \\
&\quad-\int_{\partial\Omega}\frac{\bar{h}}{h_0}\left(Q_{x,0}n_x+Q_{y,0}n_y\right)\delta w\,d\ell=0 \quad (3.46)
\end{aligned}$$

In order to solve the set of equilibrium equations for a *simply supported plate*, the unknown variables and the loading action are expressed in double Fourier sine series, in the form

$$w(x,y,t)=\sum_{m=1}^{M}\sum_{n=1}^{N}w_{mn}(t)\sin\left(\frac{m\pi x}{a}\right)\sin\left(\frac{n\pi y}{b}\right), \quad (3.47a)$$

$$\Delta u(x,y,t)=\sum_{m=1}^{M}\sum_{n=1}^{N}\Delta u_{mn}(t)\cos\left(\frac{m\pi x}{a}\right)\sin\left(\frac{n\pi y}{b}\right), \quad (3.47b)$$

$$\Delta v(x,y,t)=\sum_{m=1}^{M}\sum_{n=1}^{N}\Delta v_{mn}(t)\sin\left(\frac{m\pi x}{a}\right)\cos\left(\frac{n\pi y}{b}\right), \quad (3.47c)$$

$$p(x,y,t)=\sum_{m=1}^{M}\sum_{n=1}^{N}p_{mn}(t)\sin\left(\frac{m\pi x}{a}\right)\sin\left(\frac{n\pi y}{b}\right). \quad (3.47d)$$

This choice automatically fulfills the boundary conditions for a simply supported plate with in-plane free edges. By substituting them in the system (3.45), the equations relative to the m-n components become

$$\mu\frac{\partial^2 w_{mn}(t)}{\partial t^2}+\frac{E_g h^3}{6(1-\nu^2)}\left(\frac{\pi^4 m^4}{a^4}w_{mn}(t)+\frac{2\pi^4 m^2 n^2}{a^2 b^2}w_{mn}(t)+\frac{\pi^4 n^4}{b^4}w_{mn}(t)\right)$$
$$=\frac{\bar{h}}{h_0}C_\alpha\,{}_0^C\mathcal{D}_t^\alpha\left[-\frac{\pi m}{a}\Delta u_{mn}(\cdot)-\bar{h}\frac{\pi^2 m^2}{a^2}w_{mn}(\cdot)\right](t)$$
$$+\frac{\bar{h}}{h_0}C_\alpha\,{}_0^C\mathcal{D}_t^\alpha\left[-\frac{\pi n}{b}\Delta v_{mn}(\cdot)-\bar{h}\frac{\pi^2 n^2}{b^2}w_{mn}(\cdot)\right](t)+p_{mn}(t) \quad (3.48a)$$

$$\frac{E_g h}{1-\nu^2}\left[-\frac{\pi^2 m^2}{a^2}\Delta u_{mn}(t)-\frac{\pi^2 n^2}{2b^2}(1-\nu)\Delta u_{mn}(t)-\frac{\pi^2 mn}{2ab}(1+\nu)\Delta v_{mn}(t)\right]$$
$$=\frac{2}{h_0}C_\alpha\,{}_0^C\mathcal{D}_t^\alpha\left[\Delta u_{mn}(\cdot)+\bar{h}\frac{\pi m}{a}w_{mn}(\cdot)\right](t) \quad (3.48b)$$

$$\frac{E_g h}{1-\nu^2}\left[-\frac{\pi^2 n^2}{b^2}\Delta v_{mn}(t)-\frac{\pi^2 m^2}{2a^2}(1-\nu)\Delta v_{mn}(t)-\frac{\pi^2 mn}{2ab}(1+\nu)\Delta u_{mn}(t)\right]$$
$$=\frac{2}{h_0}C_\alpha\,{}_0^C\mathcal{D}_t^\alpha\left[\Delta v_{mn}(\cdot)+\bar{h}\frac{\pi n}{b}w_{mn}(\cdot)\right](t)\,. \quad (3.48c)$$

This problem regards only the time dependent functions $w_{mn}(t)$, $\Delta u_{mn}(t)$ and $\Delta v_{mn}(t)$, with initial conditions $w_{mn}(t)=\Delta u_{mn}(t)=\Delta v_{mn}(t)=0$ for $t<0$.

The system (3.48) can be numerically solved by approximating the fractional derivatives via the Grünwald-Letnikov approach, referred to in the Appendix. Let the time interval of interest $[0,T]$ be divided in s subintervals, whose amplitude is $\Delta t=t_{j+1}-t_j$ with $1\le j\le s-1$. Then, preliminary calculate the $s\times s$ matrices

$$\mathbf{A}^{(\xi)}=\frac{1}{\Delta t^\xi}\begin{bmatrix}\omega_1(\xi) & & & \\ \omega_2(\xi) & \omega_1(\xi) & & \\ \vdots & \ddots & \ddots & \\ \omega_s(\xi) & \dots & \omega_2(\xi) & \omega_1(\xi)\end{bmatrix}=\begin{bmatrix}A_{11}^{(\xi)} & & & \\ A_{21}^{(\xi)} & A_{22}^{(\xi)} & & \\ \vdots & \ddots & \ddots & \\ A_{s1}^{(\xi)} & \dots & \dots & A_{ss}^{(\xi)}\end{bmatrix} \quad (3.49)$$

with $\omega_1=1$, $\omega_2=-\xi$, …, $\omega_{\xi+1}=\dfrac{j-\xi-1}{j}\omega_j(\xi)$. If we express $f(t)|_{t=t_j}=f_j$ as the value of the generic function $f(t)$ at $t=t_j$, the discrete approximation of the system (3.48) becomes

$$\mu \sum_{g=1}^{j+1} A_{j+1,g}^{(2)} w_{mn,g} + \frac{E_g h^3}{6(1-\nu^2)} \left(\frac{\pi^4 m^4}{a^4} + \frac{2\pi^4 m^2 n^2}{a^2 b^2} + \frac{\pi^4 n^4}{b^4} \right) w_{mn,j}$$
$$= \frac{\bar{h}}{h_0} C_\alpha \left[-\frac{\pi m}{a} \sum_{g=1}^{j} A_{j,g}^{(\alpha)} \Delta u_{mn,g} - \bar{h} \frac{\pi^2 m^2}{a^2} \sum_{g=1}^{j} A_{j,g}^{(\alpha)} w_{mn,g} \right]$$
$$+ \frac{\bar{h}}{h_0} C_\alpha \left[-\frac{\pi n}{b} \sum_{g=1}^{j} A_{j,g}^{(\alpha)} \Delta v_{mn,g} - \bar{h} \frac{\pi^2 n^2}{b^2} \sum_{g=1}^{j} A_{j,g}^{(\alpha)} w_{mn,g} \right] + p_{mn,j} \,, \quad (3.50a)$$

$$\frac{E_g h}{1-\nu^2} \left[-\frac{\pi^2 m^2}{a^2} \Delta u_{mn,j} - \frac{\pi^2 n^2}{2b^2} (1-\nu) \Delta u_{mn,j} - \frac{\pi^2 mn}{2ab} (1+\nu) \Delta v_{mn,j} \right]$$
$$= \frac{2}{h_0} C_\alpha \left[\sum_{g=1}^{j} A_{j,g}^{(\alpha)} \Delta u_{mn,g} + \bar{h} \frac{\pi m}{a} \sum_{g=1}^{j} A_{j,g}^{(\alpha)} w_{mn,g} \right] , \quad (3.50b)$$

$$\frac{E_g h}{1-\nu^2} \left[-\frac{\pi^2 n^2}{b^2} \Delta v_{mn,j} - \frac{\pi^2 m^2}{2a^2} (1-\nu) \Delta v_{mn,j} - \frac{\pi^2 mn}{2ab} (1+\nu) \Delta u_{mn,j} \right]$$
$$= \frac{2}{h_0} C_\alpha \left[\sum_{g=1}^{j} A_{j,g}^{(\alpha)} \Delta v_{mn,g} + \bar{h} \frac{\pi n}{b} \sum_{g=1}^{j} A_{j,g}^{(\alpha)} w_{mn,g} \right] . \quad (3.50c)$$

This is an algebraic system, from which the unknown values $w_{mn,j+1}$, $\Delta u_{mn,j}$ and $\Delta v_{mn,j}$ can be obtained as a function of the corresponding values at the previous steps, starting from null initial conditions. The complete solution, related to the m-n mode, is given by

$$\mathbf{w}_{mn,s}^T = [w_{mn,1}(t_1)\ w_{mn,2}(t_2)\ \dots\ w_{mn,s}(t_s)] \,,$$

$$\mathbf{\Delta u}_{mn,s}^T = [\Delta u_{mn,1}(t_1)\ \Delta u_{mn,2}(t_2)\ \dots\ \Delta u_{mn,s}(t_s)] \,,$$

$$\mathbf{\Delta v}_{mn,s}^T = [\Delta v_{mn,1}(t_1)\ \Delta v_{mn,2}(t_2)\ \dots\ \Delta v_{mn,s}(t_s)] \,.$$

Schematic of the rear supporting structure

In practical applications, the panel is connected to a load-bearing back structure, whose deformation cannot be neglected in general. In particular cases, the compliance of the load-bearing structure can be tailored designed, in order to tune the

dynamic response of the system and absorb/dissipate at least part of the energy from the blast wave, safeguarding the integrity of the panel.

We now consider the mechanical system schematically represented in Fig. 3.25, where the back structure is modeled via a lumped oscillating mass m_r, connected to the ground by means of the spring k_r in parallel with the dashpot c_r. Four kinematic variables describe the deformation in this configuration: the translation of the back structure $\tilde{w}(t)$; the out-of-plane displacement of panel $w(x, y, t)$ and the in-plane relative displacements between the external layers $\Delta u(x, y, t)$ and $\Delta v(x, y, t)$ (reference frame as in Fig. 3.24(a)).

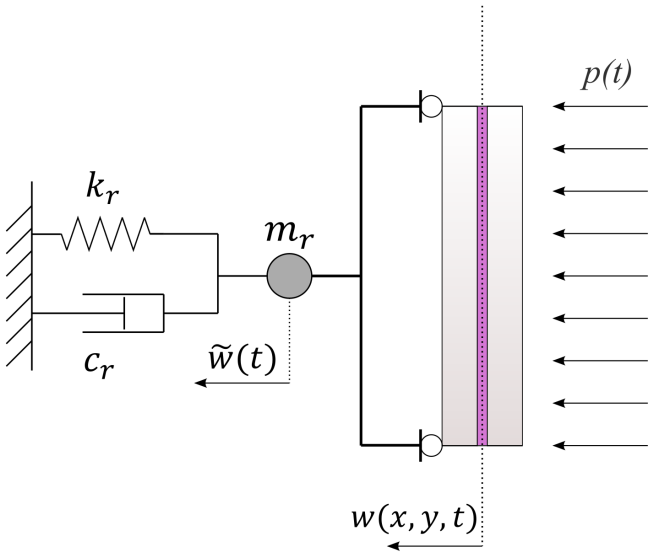

Figure 3.25. Lumped element model representing the load-bearing back structure that supports the laminated panel.

The set of equilibrium equations is deduced again from Hamilton's principle (3.40). The kinetic energy $\mathcal{K}$ of (3.41) has to be complemented with the contribution of the mass m_r and shall consider that the absolute out-of-plane displacement of any point (x, y) of the plate is now $w(x, y, t) + \tilde{w}(t)$. The elastic energy $\mathcal{U}$ takes the same form (3.42), to which the part associated with k_r has to be added. The dissipation from the non-conservative forces is again given by (3.43) plus the contribution from c_r. In the work of external forces (3.44), one has now to consider $w(x, y, t) + \tilde{w}(t)$ in place of $w(x, y, t)$.

There are now four partial differential equations, that are respectively associated with each kinematic variable. The motion of the supporting back structure is governed by the equivalence

$$m_r\frac{\partial^2\tilde{w}(t)}{\partial t^2}+\mu\int_A\left[\frac{\partial^2 w(x,x,t)}{\partial t^2}+\frac{\partial^2\tilde{w}(t)}{\partial t^2}\right]dA+c_r\frac{\partial\tilde{w}(t)}{\partial t}+k_r\tilde{w}(t)=\int_A p(t)\,dA\,. \quad (3.51)$$

For what concerns the out-of-plane equilibrium, this reads

$$\begin{aligned}\mu&\left(\frac{\partial^2 w(x,y,t)}{\partial t^2}+\frac{\partial^2\tilde{w}(t)}{\partial t^2}\right)\\&+\frac{E_g h^3}{6(1-\nu^2)}\left(\frac{\partial^4 w(x,y,t)}{\partial x^4}+2\frac{\partial^4 w(x,y,t)}{\partial x^2\partial y^2}+\frac{\partial^4 w(x,y,t)}{\partial y^4}\right)\\&=\frac{\bar{h}}{h_0}C_\alpha\,{}_0^C\mathcal{D}_t^\alpha\left[\frac{\partial\Delta u(x,y,\cdot)}{\partial x}+\bar{h}\frac{\partial^2 w(x,y,\cdot)}{\partial x^2}\right](t)\\&\quad+\frac{\bar{h}}{h_0}C_\alpha\,{}_0^C\mathcal{D}_t^\alpha\left[\frac{\partial\Delta v(x,y,\cdot)}{\partial y}+\bar{h}\frac{\partial^2 w(x,y,\cdot)}{\partial y^2}\right](t)+p(t)\,. \quad (3.52)\end{aligned}$$

The in-plane equilibrium of the panel is still governed by (3.45b)-(3.45c).

This set of equations can be solved by substituting the unknown functions with their double Fourier sine series (3.47) and by applying the Grünwald-Letnikov integration scheme over the time. Since the translation $\tilde{w}(t)$ does not depend on the spatial coordinates (x,y,z), it is necessary to preliminary integrate the equation (3.52) over the area of panel, so that it becomes

$$\begin{aligned}\mu&\left(\Xi_{mn}\frac{\partial^2 w_{mn}(t)}{\partial t^2}+\Theta_{mn}\frac{\partial^2\tilde{w}(t)}{\partial t^2}\right)\\&+\frac{\Xi_{mn}E_g h^3}{6(1-\nu^2)}\left(\frac{\pi^4m^4}{a^4}w_{mn}(t)+\frac{2\pi^4m^2n^2}{a^2b^2}w_{mn}(t)+\frac{\pi^4n^4}{b^4}w_{mn}(t)\right)\\&=\Xi_{mn}\left\{\frac{\bar{h}}{h_0}C_\alpha\,{}_0^C\mathcal{D}_t^\alpha\left[-\frac{\pi m}{a}\Delta u_{mn}(\cdot)-\bar{h}\frac{\pi^2m^2}{a^2}w_{mn}(\cdot)\right](t)\right.\\&\quad\left.+\frac{\bar{h}}{h_0}C_\alpha\,{}_0^C\mathcal{D}_t^\alpha\left[-\frac{\pi n}{b}\Delta v_{mn}(\cdot)-\bar{h}\frac{\pi^2n^2}{b^2}w_{mn}(\cdot)\right](t)+p_{mn}(t)\right\}, \quad (3.53)\end{aligned}$$

where we have set

$$\Theta_{mn}=\int_A\sin\left(\frac{m\pi x}{a}\right)\sin\left(\frac{n\pi y}{b}\right)dA, \quad (3.54a)$$

$$\Xi_{mn}=\int_A\sin^2\left(\frac{m\pi x}{a}\right)\sin^2\left(\frac{n\pi y}{b}\right)dA\,. \quad (3.54b)$$

From the subset equations (3.53) and (3.48b)-(3.48c), each mode $w_{mn}(t)$ can be found as a function of $\tilde{w}(t)$. The modes $w_{mn}(t)$ are calculated in cascade at each time step and, by substituting them in the equation (3.51), one finds

$$m_r \frac{\partial^2 \tilde{w}(t)}{\partial t^2} + \mu \int_A \left[\frac{\partial^2 w_{mn}(t)}{\partial t^2} \sum_{m=1}^{M} \sum_{n=1}^{N} \sin\left(\frac{m\pi x}{a}\right) \sin\left(\frac{n\pi y}{b}\right) + \frac{\partial^2 \tilde{w}(t)}{\partial t^2} \right] dA + c_r \frac{\partial \tilde{w}(t)}{\partial t} + k_r \tilde{w}(t) = \int_A p(t)\, dA\,, \quad (3.55)$$

where now $\tilde{w}(t)$ is the sole variable.

3.3.4 Numerical experiments

The case study is represented by the simply supported sandwich plate introduced in Section 3.3.3. Both plies are assumed to be made of glass with Young's modulus $E_g = 70{\cdot}10^9$ Pa, Poisson's ratio $\nu = 0.25$ and density $\rho = 2500\,\mathrm{kg/m^3}$. By referring to Fig. 3.24, their dimensions are set as $a \times b \times h_i = 1 \times 1 \times 0.01\mathrm{m}^3$, with $i = 1{,}2$. Three different interlayers are investigated: PVB at 50 °C ($\alpha = 0.155$, $C_\alpha = 0.474\,\mathrm{MPa\ s^\alpha}$); SG at 50 °C ($\alpha = 0.117$, $C_\alpha = 9.409\,\mathrm{MPa\ s^\alpha}$) and DG at 15 °C ($\alpha = 0.117$, $C_\alpha = 84.138\,\mathrm{MPa\ s^\alpha}$). The thickness of the interlayer $h_0 = 2.28\,\mathrm{mm}$ as well its density $\rho_0 = 1000\,\mathrm{kg/m^3}$ are taken as constants. We recall that the laminated plate is subjected to the load per unit area (3.30). In the following numerical experiments, also the case concerning a compliant rear structure is analyzed.

Dynamic response of a simply supported plate

In the Fourier expansions (3.47), the asymmetric modes are null because the problem is symmetric: we first attempt at considering modes $m = 1{,}3$ and $n = 1{,}3$ only. Fig. 3.26 reports the displacement components $w_{mn}(t)$ as a function of time for PVB at 50 °C. It is clear that first mode $w_{11}(t)$ is dominant, while the second modes $w_{13}(t) \equiv w_{31}(t)$ provide for oscillations of amplitude two orders of magnitude smaller. The graph of mode $w_{33}(t)$ is not reported because of negligible amplitude. This example confirms that a truncation to the third order in the Fourier expansion does not cause appreciable loss of precision. The same conclusion is expected to be valid also for the other interlayers, which are stiffer than PVB at 50 °C.

The state of stress in the glass is measured by the component σ_{xx}, evaluated on the external surface of the internal ply (the one not directly invested by the pressure wave), in correspondence of the center $(x, y) = (a/2, b/2)$. The corresponding time history is plotted in Fig. 3.27 for PVB at 50 °C, which is juxtaposed to the graphs corresponding to the layered limit (free sliding plies, $C_\alpha = 0\,\mathrm{MPa\ s^\alpha}$) and monolithic

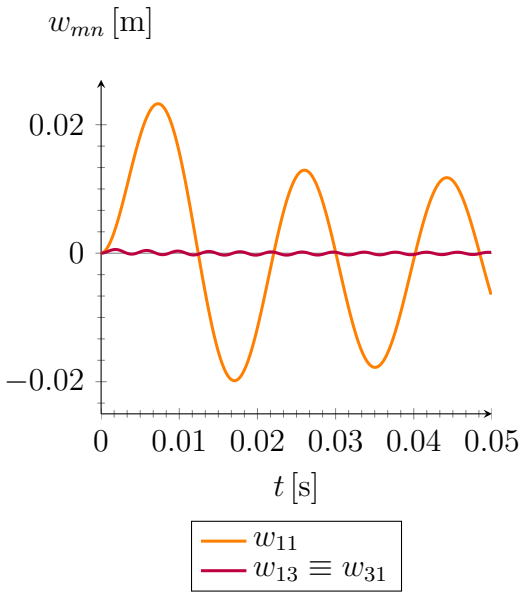

Figure 3.26. Modes of vibration $w_{mn}(t)$ plotted as a function of time for an interlayer of PVB at 50 °C.

limit (rigid shear coupling of the plies, $C_\alpha \to \infty$ MPa s$^\alpha$). The Figure shows this interlayer provides results close to the layered limit: therefore the stress is due to the bending contribution. The maximum tensile peak is approximately 140 MPa; the compression peak is of the same order.

Remarkably, observe that there is a slight compression at the center of plate, occurring during the very first instants ($\sim 10^{-3}$ s). This is the most evident at the layered limit, for which it is approximately 10 MPa, while it decreases as the shear coupling of the glass plies increases, being minimal at the monolithic limit. The initial compression is due to the counter-inflection of panel in a neighborhood of its center. This is the most compliant region of the plate, which is consequently the most restrained by the effect of the inertia when it is impacted by the blast wave. Indeed, at the beginning of the deformation process, the bending shape of the plate is of the type represented in Fig. 3.28, where the change of curvature is evident. In general, the entity of the counter-inflection does not appear relevant for the structural integrity of the panel. However, for representative values of the key parameters (thickness of the glass plies, initial peak pressure), the dynamic response may be such that the bending failure does not start in correspondence of the center, but at the borders of the panel [91].

Observe that, since the stress distribution is linear through the thickness, the maximum and minimum values are certainly located on the surfaces of each plies. In Fig. 3.29(a), the four points A, B, C and D are schematically indicated in

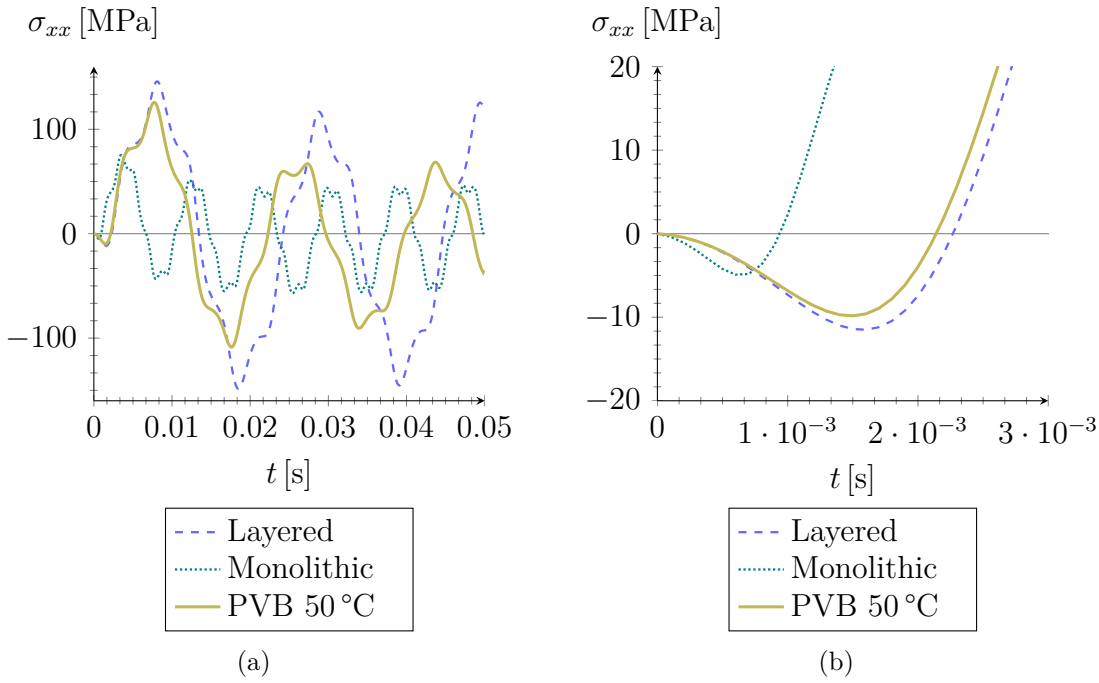

Figure 3.27. Time history of the stress component σ_{xx} evaluated at the center of the internal glass ply. (a) Extended time interval ($0 - 5 \cdot 10^{-2}$ s); (b) detail of the first instants ($0 - 3 \cdot 10^{-3}$ s).

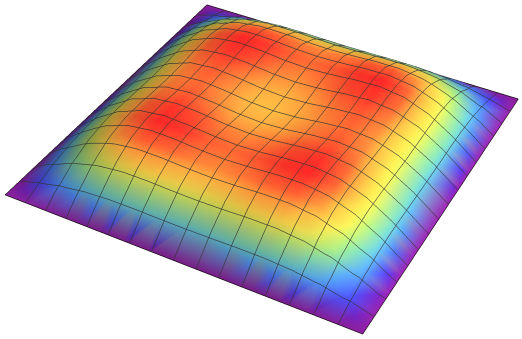

Figure 3.28. Qualitative deformed shape of the sandwich panel when it has just been impacted by the blast wave.

correspondence of the centers of the four surfaces of the glass plies; for PVB at 50 °C as interlayer, the corresponding σ_{xx} is represented as a function of time in Fig. 3.29(b). The external points A and D are those subjected to the highest stresses in absolute value, because here the bending and membrane contribution sum up. On the contrary, the membrane contribution is opposite to the bending contributions in correspondence of the internal points B and D. At the layered limit, where the

membrane stress is null, the stress at the external points shall be opposite to that at the internal points. Hence, the graphs of Fig. 3.29(b) indicate that the interlayer of PVB at 50 °C provides a condition close to the layered limit.

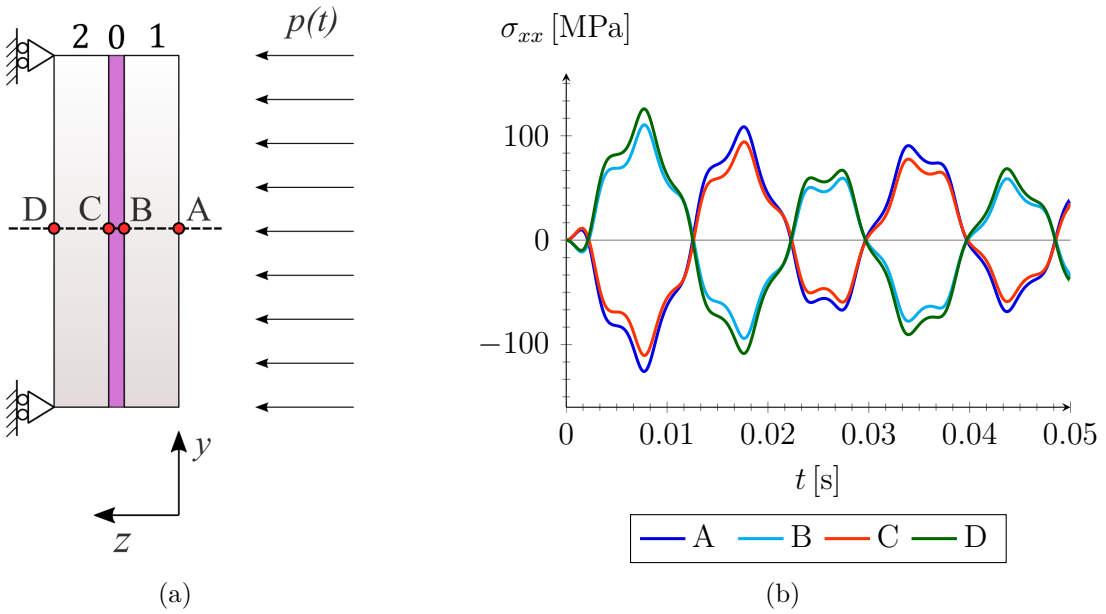

Figure 3.29. Stress component σ_{xx}, evaluated at the centers of the four surfaces of the glass plies, with PVB at 50 °C as interlayer. (a) Schematic representation of the loaded sandwich plate and indication of the measuring points. (b) Stress-time graphs.

In Fig. 3.30, we show the time histories of σ_{xx}, evaluated at point D of Fig. 3.29(a) (center of the external surface of the second ply), when the interlayer is of the type SG at 50 °C or DG at 15 °C. It is evident that now the response is closer to the monolithic limit, because C_α is higher than for PVB at 50 °C and the interlayer is stiffer. Both solutions provide for stress peaks of the same order. The main difference is represented by the frequency of oscillation: the higher is C_α, the higher the frequency is. For DG at 15 °C as interlayer, the solution in practice overlaps with the monolithic limit.

The contour plot in Fig. 3.31(a) represents the qualitative shear stress distribution over the plate characterizing the interlayer. The maximum values are located at midpoints of the edges; while the minimum values (shear stress null) are located at corners and center. With reference to point $(x, y) = (0, b/2)$, the shear stress time history is plotted in Fig. 3.31(b). The interlayer DG at 15 °C presents the highest viscoelastic coefficient C_α, therefore it provides for the highest stress peak. Otherwise, by considering PVB at 50 °C (C_α very low), the stress peak is approximately reduced of one order of magnitude. There is not a proportional relation between C_α

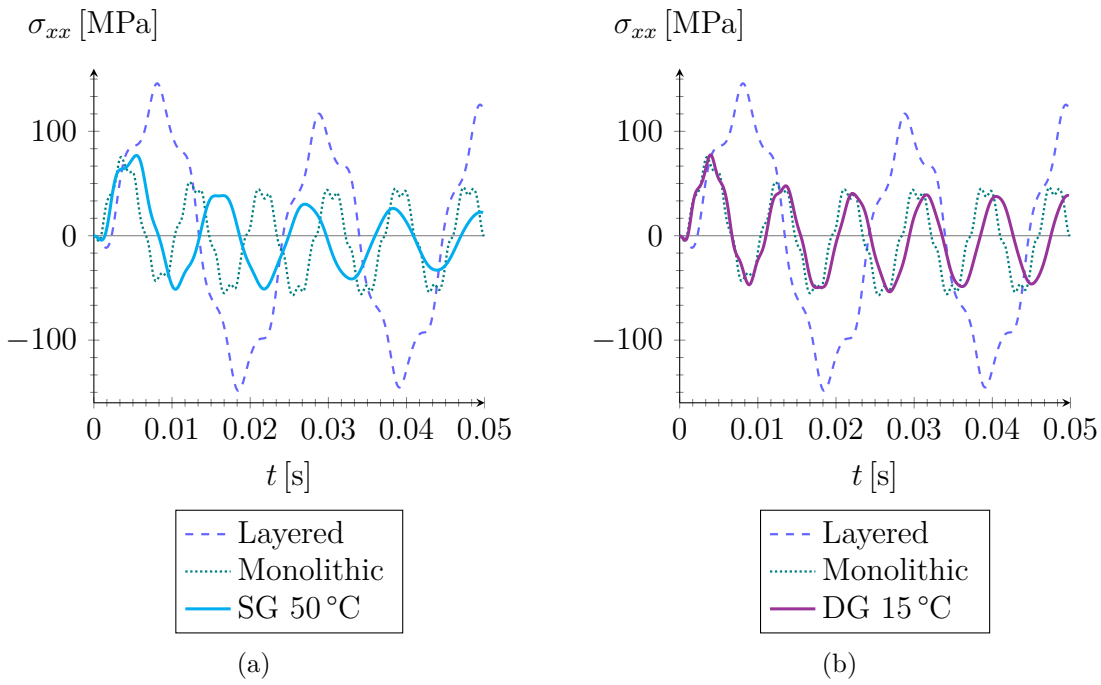

Figure 3.30. Stress component σ_{xx} related to the 2nd ply, in correspondence of $(x, y, z) = (a/2, b/2, h/2)$. (a) SG at 50 °C (b) DG at 15 °C

and the magnitude of maximum shear; anyway, if the interlayer is stiffer, an higher peak in terms of shear stress is expected.

In order to understand what is the contribution due to the hereditary memory of viscoelasticity for the interlayer, it is interesting to compare the previous results in terms of the stress σ_{xx} in the glass, with numerical experiments for perfectly elastic interlayers. Recall that all the relaxation functions are assumed to be power laws that fit the experimental data provided by Biolzi et al. [89]. In the bi-logarithmic plots of Fig. 3.32, these are represented by inclined straight lines, which interpolate the experimental points, highlighted with circles. An equivalence with an elastic material (quasi-elastic approximation [44, 93]), can be done by considering for it the shear modulus in the relaxation curve that corresponds to the characteristic duration of the loading action. Therefore, the elastic behavior of each interlayer is determined by drawing a horizontal line, corresponding to $\alpha = 0$, which intersects the relaxation function at $t = T_d$, where $T_d = 1.27 \cdot 10^{-2}$ s is the time duration of the positive blast pressure, as per Friedlander equation (3.30). In conclusion, the elastic limit is denoted by setting $R(t) = \hat{C}_0$ that, for the cases at hand, takes the value: $\hat{C}_0 = 0.835$ MPa for PVB at 50 °C; $\hat{C}_0 = 14.484$ MPa for SG at 50 °C; $\hat{C}_0 = 129.516$ MPa for DG at 15 °C.

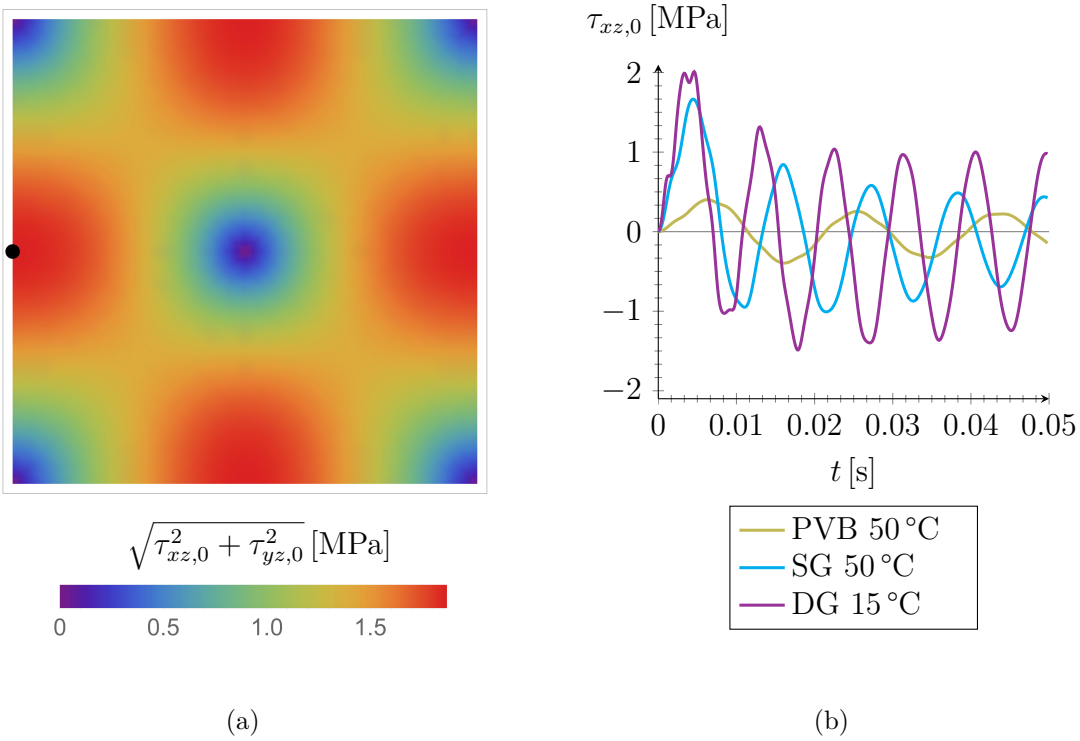

(a) (b)

Figure 3.31. Shear stress in the interlayer. (a) Contour plot. (b) Stress $\tau_{xz,0}$, calculated in correspondence of the midpoint of the edge (black dot), as a function of time.

The results to be compared are reported in Fig. 3.33 for the three considered interlayers. In all the cases, there is a good superimposition between viscoelastic and elastic cases for what concerns the first peak. When considering the response in a broader time interval, the difference is minimal with DG at 15 °C, the stiffest of all, inasmuch the monolithic limit is attained. PVB at 50 °C and SG at 50 °C provide a similar response: the dissipation provided by the viscous component decreases the magnitude of the successive peaks and slightly increases the frequency of oscillations. If PVB at 50 °C is used as interlayer, the sandwich is more compliant; hence, there are less oscillations within the considered time interval if compared with the other materials.

Effects of the supporting structure

With reference to the simple model of Fig. 3.25, proposed in Section 3.3.3, the influence of the supporting back structure is now investigated. In particular, the following three cases are distinguished for the sake of comparison.

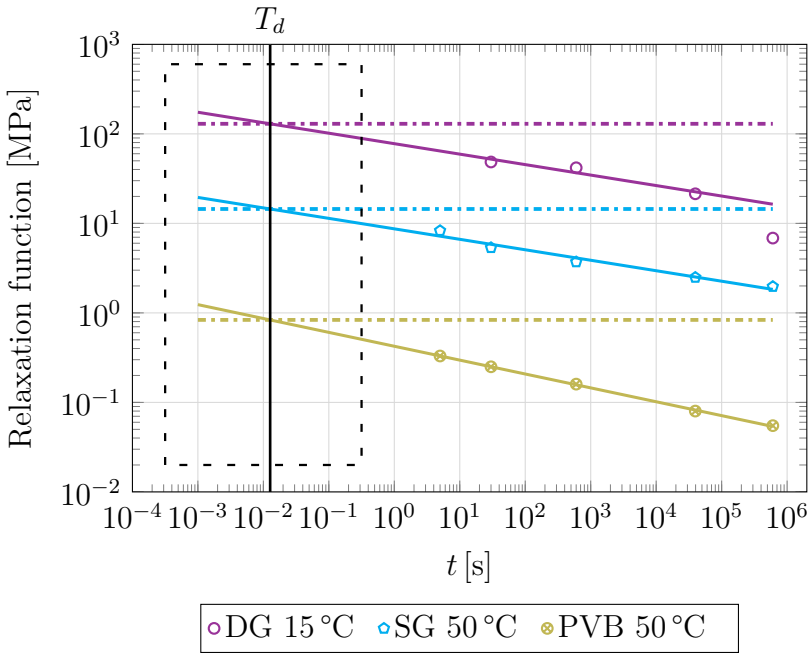

Figure 3.32. Relaxation functions plotted for the interlayers considered in [89]. Extrapolation with a power law (continuous lines in the bi-logarithmic scale) and elastic approximation (horizontal dash-dotted lines), by considering the secant shear modulus at $t = T_d = 1.27 \cdot 10^{-2}$ s, for PVB at 50 °C, SG at 50 °C and DG at 15 °C.

1. **Rigid structure.** This is the limit case $k_r \to \infty$, providing for a rigidly-borne panel. The blast wave totally transfers its energy to the panel, which responds through its deformation.

2. **Simply supported beam.** The glass panel can be fixed to a frame composed of transoms and mullions. We assume an equivalent simply supported beam, whose cross-sectional inertia is $I = 42\,930 \cdot 10^{-8}\,\mathrm{m}^4$ with mass per unit length $\bar{m}_b = 79.4\,\mathrm{kg/m}$ (standard profile IPE A 500 UNI 5398). By setting $E_s = 210\,\mathrm{GPa}$ for steel, the spring stiffness in the model is set to be $k_r = 48 E_s I / L^3 = 67.614 \cdot 10^3\,\mathrm{N/m}$ where $L = 4\,\mathrm{m}$. Assuming the shape function $\Upsilon(x) = 4(x/L)(x/L - 1)$ for its deformation, the effective lumped mass results to be $m_r = \bar{m}_b \int_0^L \Upsilon(x)^2\,dx \simeq 169.387\,\mathrm{kg}$.

3. **Pre-tensioned cable.** A back structure made of multiple cables exhibits the maximum compliance, which enhances its capacity to absorb energy from an impulsive load. We set $N_0 = 300\,\mathrm{kN}$ as the tensile force in a cable of length $L = 4\,\mathrm{m}$, so that $k_r = 2N_0/(L/2) = 150\,\mathrm{kN/m}$. In order to consider the weight of the fixing devices besides the self-weight of the cable, the considered mass is $m_r = 50\,\mathrm{kg}$, but ballast may be artfully added if advantageous.

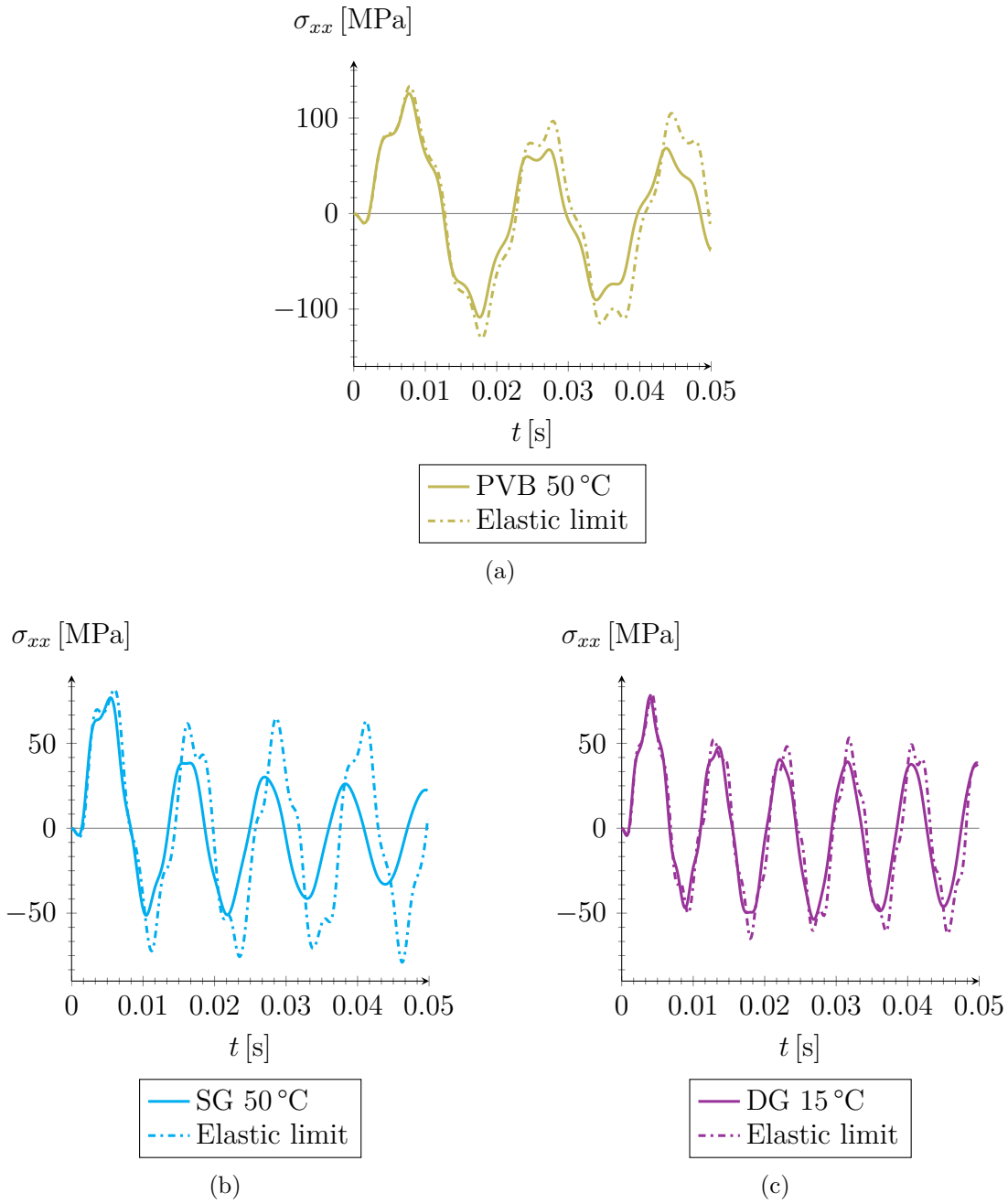

Figure 3.33. Viscoelastic interlayers and the corresponding elastic approximation. Stress components σ_{xx} at the center of the external surface of the second glass ply. (a) PVB at 50 °C. (b) SG at 50 °C. (c) DG at 15 °C.

In all the aforementioned cases, the dissipation of the back structure is interpreted

through a dashpot with a damping coefficient $c_r = 0.03 \cdot 2\sqrt{m_r k_r}$ (damping ratio of 3 %). We consider in detail only the case in which the interlayer is made of PVB at 50 °C, which is the most interesting one because the other materials provide results close to the monolithic limit.

The time history in terms of stress σ_{xx} and out-of-plane deflection w, evaluated at point D of Fig. 3.29(a), are represented in Fig. 3.34. It is clear that, as expected, a compliant back structure substantially contributes to reduce the stress and deflection. For a back structure formed by a simply supported beam, the solution is intermediate between those corresponding to the rigid support and the pre-tensioned cable. The condition of rigid support is clearly the worst of all; using a compliant cables approximately halves the stress in the glass.

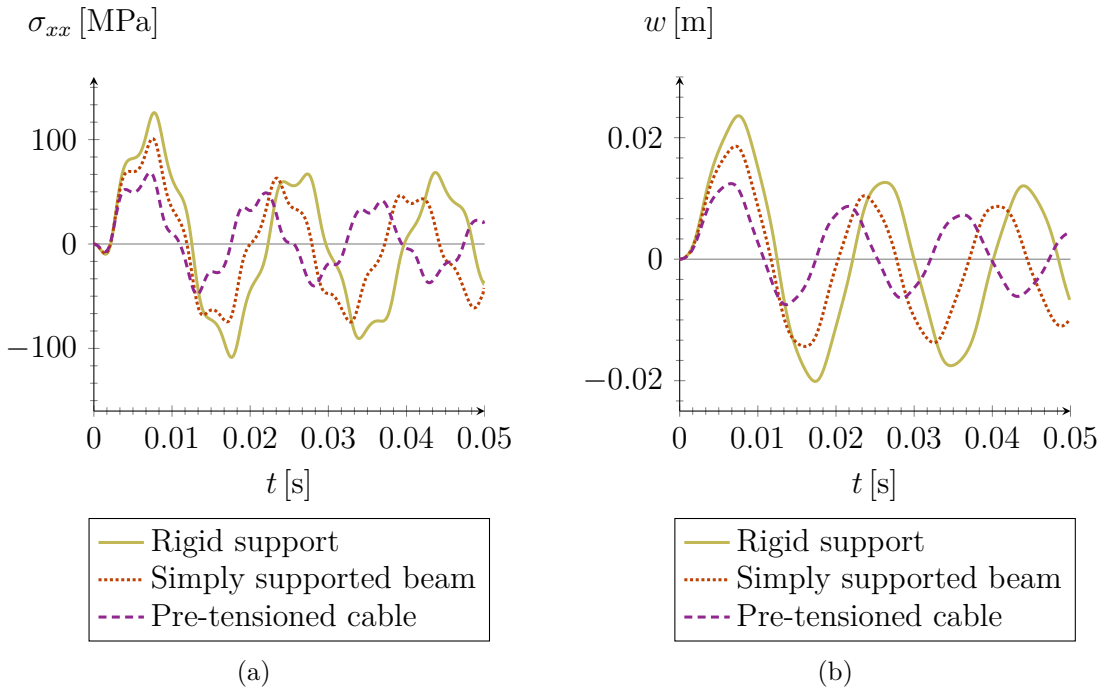

Figure 3.34. Comparison between different supporting structures for a laminated panel employing PVB at 50 °C. (a) Stress components σ_{xx} related to the 2$^{\text{nd}}$ ply, in correspondence of $(x, y, z) = (a/2, b/2, h/2)$. (b) Out-of-plane displacement w in correspondence of $(x, y) = (a/2, b/2)$.

The displacement of the back structure is plotted in Fig. 3.35 as a function of time for the two cases of simply supported beam and pre-tensioned cable. Since their fundamental period of vibration is much higher than the interval of observation, comparable with the characteristic duration of the blast wave, none of the graphs completes a period. The contribution from stiffness and inertia induces a slower

deformation in the simply supported beam than in the pre-tensioned cable. The more compliant is the load-bearing structure, the less is its resistance in terms of stiffness: the blast action is mainly equilibrated by the inertial contribution [21]. However, if on the one hand a compliant back structure may safeguard the glass integrity, on the other hand the resulting large displacements may be incompatible with the design serviceability limit states.

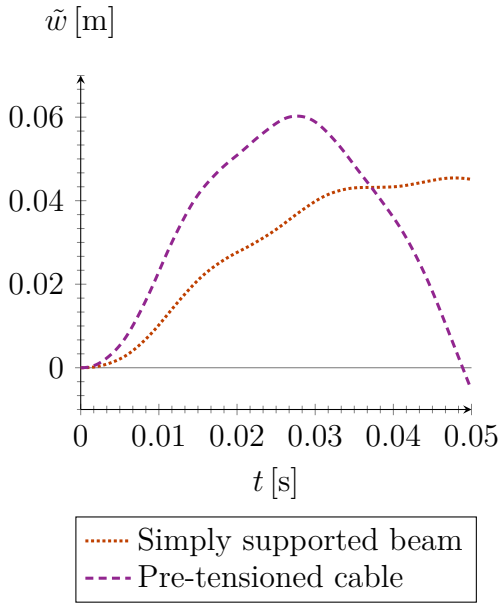

Figure 3.35. Time history of the displacement $\tilde{w}$ of the back structure, supporting a panel laminated with PVB at 50 °C as interlayer under the action of the blast wave. Comparison between simply supported beams and pre-tensioned cables.

Chapter 4

The advantages of dissipative supporting devices

The limited strength of glass and its intrinsic brittleness is such that only a low level of blast resistance can be achieved with conventional glass curtain walls [94]. Failure criteria are available to evaluate the strength of façades made of tempered monolithic glass panes [73]. Laminated glass is usually recommended because the viscous polymeric layers connecting the glass plies provide ductility in the post-breakage phase [16, 14, 67, 68, 13]. Anyway, from an engineering point of view, it is the entire façade subjected to the blast loading action, so that the performance requirements should be sought at the level of the assembly and not of the single glass panel. Therefore, it makes little sense to define blast-resistant *glass panes*: it would be more correct to refer to explosion-resistance *façade systems*.

As improvement, dissipative devices can be installed in order to absorb energy during a blast loading event. A viscous type of dissipation is usually proposed, probably because it is the kind most well known to engineers, whose mathematical modeling presents no difficulty via the definition of damping coefficients. For example, this mechanism is used by the spider connector designed by Amadio and Bedon [17], which is shown in Fig. 4.1.

However, this type of dissipation, for which the reaction force depends upon the displacement rate, does not seems to be suitable for structures stressed by short duration impulses transmitting sharp velocity jumps, inasmuch a viscous damper behaves like an almost rigid connector. Therefore, the attention is here concentrated on different-in-type dissipative devices based on material yielding, where the energy is absorbed through the plastic deformation of crushing components. An example in this direction is made by Wellershoff et al. [95], who proposed dissipative brackets for glazed façades for which the absorption of energy is provided by several crushing components (aluminium sleeves, dissipative crushable concrete, etc.). These devices are designed to be installed on stiff substructure such as a concrete frame, which is

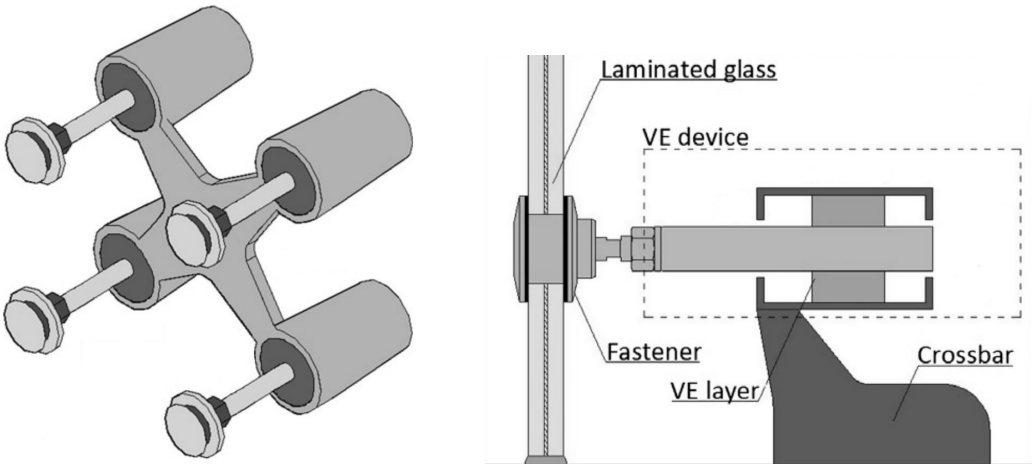

Figure 4.1. Viscoelastic (VE) spider connectors proposed by Amadio and Bedon [17]. Glass panels are linked to a spider connector through a piston, that slides inside a chamber in contact with a viscoelastic layer. (a) Assembled device and (b) schematic section.

in general too rigid to cooperate with glazing in absorbing the shock wave energy. Figs. 4.2(a)-4.2(b) report pictures of the device before and after a blast event. The working principle is shown in Fig. 4.2(c).

In order to analyze the possible advantages of inserting "sacrificial" components in a façade, we consider the paradigmatic model problem of a blast wave investing one glass pane, that is connected to an elastic load-bearing structure by the interposition of dissipative devices. The dynamic equilibrium under an impacting blast wave is studied by reducing the response of both the back structure and the pane to simple 1-DoF oscillators, through a simplification *à la* Rayleigh taking into account geometric second order effects. The glass plate can be considered monolithic, or laminated by using enhanced shear deformation theories [96] or effective bending properties in terms of stress and deflection [66]. The component is a two way device, schematized as a cylinder fixed on rear structure, which contains two dissipative elements, referred to as *shock absorbers*, activated by a mobile piston, which alternatively compresses one of them according to the direction of movement until their plastic collapse. Although the treatment is very general, being applicable to any kind of dissipative device, for the sake of illustration reference is made to shock absorbers made of an aluminium honeycomb as per Fig. 4.3, whose force-displacement constitutive relationships are approximately rigid-plastic, with tunable parameters. Analytical and numerical solutions are compared in order to validate the proposed model as well as the solver algorithm.

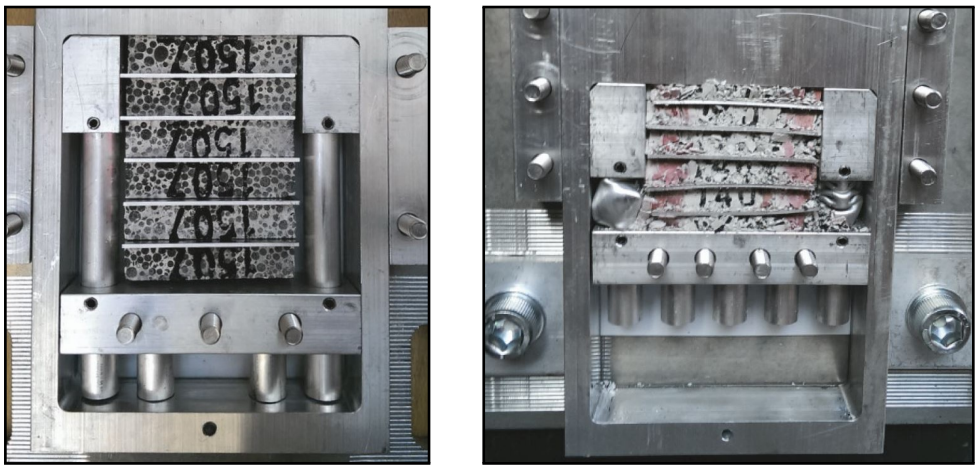

(a) (b)

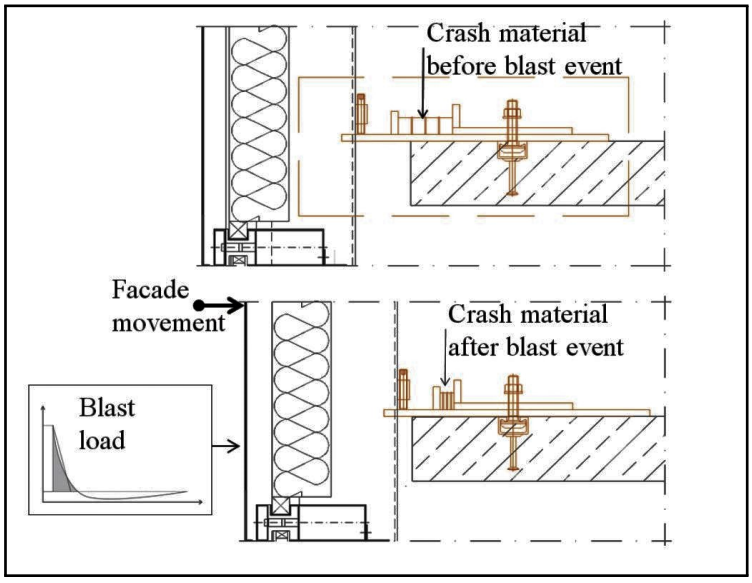

(c)

Figure 4.2. Dissipative façade bracket proposed in [95]. Crushing components are made by aluminium sleeves and crushable concrete. (a) Dissipative bracket in the non-activated state. (b) Dissipative bracket after inward testing. (c) Working principle.

There are theoretical aspects that have been very little investigated so far. Some studies consider the shock absorber as an equivalent viscoelastic dashpot. This approach is not accurate, since the response of a dashpot is governed by the velocity of deformation, whereas a shock absorber reacts in terms of applied forces. Another important phenomenon, generally neglected to the best of our knowledge, consists

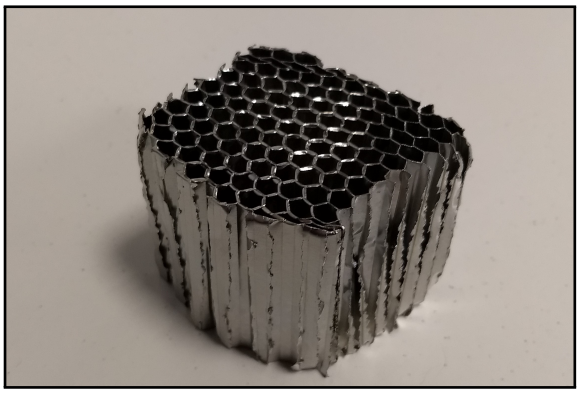

Figure 4.3. Example of a shock absorber made of an alumium honeycomb structure.

in the fact that, when a shock absorber is completely deformed (collapse of the honeycomb structure), it becomes suddenly rigid, so that the moving piston collides against it. It is during these impacts that the glass panes, as well as the load-bearing back structure, are the most stressed. The entity of the rebounds is related to the coefficient of restitution, which expresses the consequent energy loss in the proposed analytical model. Given the number of variables (properties of shock absorbers and back structure, inertia, coefficient of restitution), a parametric analyses is made to optimize the global dynamic response. The possibility of using a linear viscoelastic dissipator is also considered, for the sake of comparison. The following arguments have been discussed by Viviani and Royer-Carfagni [97].

4.1 Shock absorbers

For the case at hand , the model problem is represented in Fig. 4.4(a). It schematically reproduces a glass pane, contoured by a rigid frame, which is in turn connected to an elastic back structure via a dissipative device. The influence of the back structure is compared to that of a 1-DoF oscillator, while for the panel only the first mode of vibration is considered. The dissipative unit, as detailed in Fig. 4.4(b), is composed of two shock absorbers, hypothetically placed inside a cylinder, which plasticize when compressed above a critical value by the internally-sliding piston. This dynamic system is defined by six degrees of freedom, i.e. the displacements of

- the surfaces of the two shock absorbers potentially in contact with the piston, $Z_0^\ell(t)$ and $Z_0^r(t)$;
- the back structure, $Z_1(t)$;
- the centroid of the glass pane, $Z_2(t)$;

- the piston inside the cylinder, $Z_3(t)$;
- the frame contouring the glass pane, $Z_4(t)$.

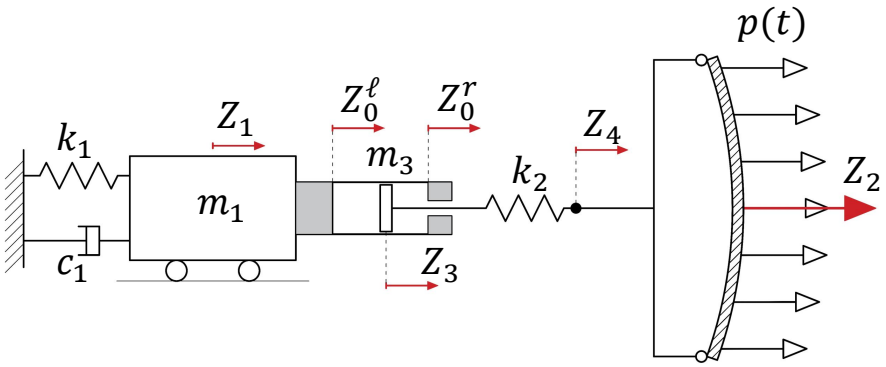

(a)

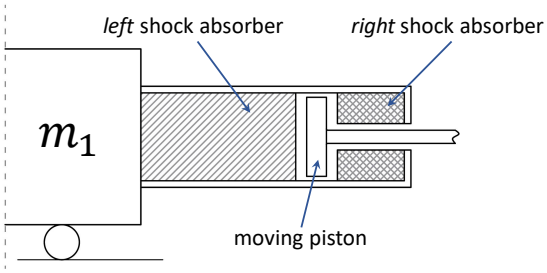

(b)

Figure 4.4. The model problem considered in the analysis. (a) Schematic representation and (b) detail of the dissipative unit composed of a moving piston, the right and the left shock absorbers.

Our interest is in calculating the system response, and in particular the stress in the glass pane, when this is subjected to the pressure time history $p(t)$ from a blast wave.

4.1.1 Blast action

The blast wave is supposed to provide an out-of-plane uniformly-distributed force per unit area $p(t)$ on the pane surface, which is interpreted via Friedlander equation [32] in the form

$$p(t) = -p_0\left(1 - \frac{t}{T_d}\right)e^{-\beta\frac{t}{T_d}}, \tag{4.1}$$

where $\beta = 1$ is the decay parameter, $T_d = 0.01\,\mathrm{s}$ is the time negative duration and $p_0 = 272\,\mathrm{kPa}$ is the initial pressure peak. These values, which can be obtained by an analytical or experimental procedures[1] [36, 98], approximately reproduce an explosion of a charge 100 kgTNT placed 15 m far from the glazing. The pressure calculated through (4.1) represents the net load acting on panel, and it implicitly accounts for other types of contributions, such as the increase of air pressure due to the thermal explosion and the dynamic pressure related to wind velocity and reflection phenomena[2].

The pressure-time graph, composed of a compression followed by a suction phase, is plotted in Fig. 4.5. It should be recalled, however, that a simplified expression is often used in the engineering practice, where the compression phase is approximated with a triangular law ad the subsequent suction phase is neglected, as indicated in the same figure.

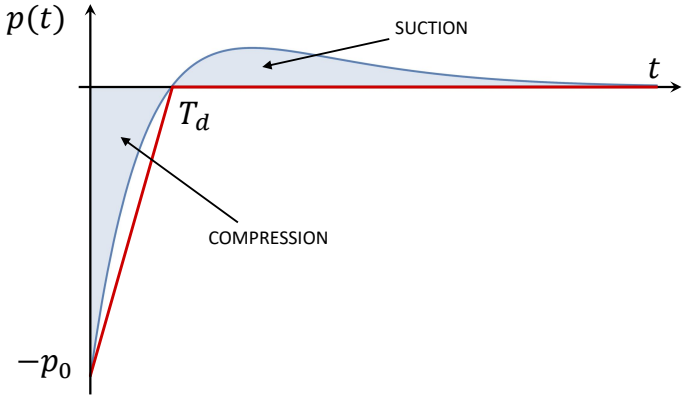

Figure 4.5. Force per unit area transmitted by the blast wave on the glass pane as a function of time: Friedlander equation (light blue) and simplified triangular model (red).

The triangular impulse is usually reputed to be conservatively on the safe side, as the suction phase should counteract the compression force. However, this is not always true [90, 44, 46], because the negative phase can activate the lower vibration modes of pane [47]. To illustrate, consider a simply supported rectangular glass plate, with size $a \times b \times s = 2.5 \times 2.5 \times 0.02\,\mathrm{m}^3$, Young's modulus and Poisson's ratio respectively

[1] The eventual experimental activity must be conducted according to the current standards and norms [3, 8, 9]. One can choose for an open arena blast test or alternatively for a controlled explosion inside a shock tube. In the last case a lower amount of explosive charge is required, but it is necessary to properly set-up and asses the performances of the shock tube [42].

[2] A detailed analysis of the various contributions from a blast wave can be found in [26, 38].

$E_g = 70 \cdot 10^9\,\mathrm{Pa}$ and $\nu = 0.22$ and mass per unit area $\mu = (2500 \cdot s)\,\mathrm{kg/m^2}$. The modal frequencies according Kirchhoff-Love plate theory [45] read

$$f_{mn} = \frac{\pi}{2}\left(\frac{m^2}{a^2} + \frac{n^2}{b^2}\right)\sqrt{\frac{E_g s^3}{12(1-\nu^2)\mu}}, \tag{4.2}$$

where m and n are the mode numbers. Fig. 4.6 represents the Fourier transforms of both Friedlander model, considering different decay coefficients β, and its triangular approximation. Observe that only a slight variation of the decay coefficient lead, the triangular approximation to be not on the safe side, inasmuch the magnitude of dynamic excitation in correspondence of the first fundamental frequency f_{11} may be much higher than for the case of the linearized compression phase only. For the specific case considered here, for which $\beta = 1$ has been set, the (blue) peak close to the frequency f_{11} is only slightly higher than the corresponding (red) value for the triangular law. However, we repute that the Friedlander model provides, in any case, a more precise indication of the actual conditions experienced by a façade during an explosion and, hence, it will be used in the sequel.

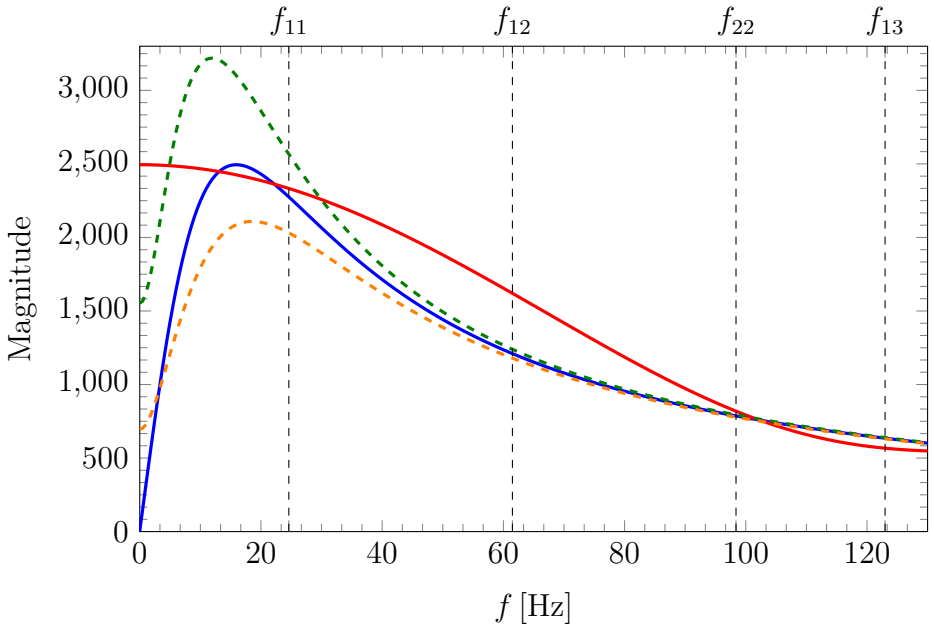

Figure 4.6. Magnitude–frequency diagram corresponding to the Fourier transforms of: Friedlander equation with $\beta = 0.1$ (blue) as previously defined, linearized compression phase (red), Friedlander equation with $\beta = 1.2$ (orange) and Firendlander equation with $\beta = 0.8$ (green).

4.1.2 Load-bearing back structure

The load-bearing back structure can be either massive or light-weight, since it can be made, e.g., either with *beams*, in the form of mullions, or with prestressed *cables*. Its dynamical properties can greatly affect the state of stress in the glass pane under blast loading conditions [21], but here only its first vibration mode is considered in the form of an equivalent harmonic oscillator of stiffness k_1, mass m_1 and damping coefficient c_1. In general, under the action of a triangular-shaped impulse of duration T_d, as for the simplified model of Fig.4.5, three different-in-type scenarios can be distinguished [38, 92]: the *impulsive* regime, the *dynamic* regime and the *quasi-static* regime. The impulsive regime takes place when the load duration is so small with respect to the fundamental vibration period of the structure, i.e., when $T_d\sqrt{k_1/m_1} < 0.4$, that its effect is to impart to the mass a momentum, letting it freely oscillate afterwards; the corresponding maximum displacement is of the order of $u_{\max} \simeq p_0 A/k_1$, where A is the invested area. On the opposite side, the quasi-static regime is for loads with longer duration, for which $T_d\sqrt{k_1/m_1} > 40$: now $u_{\max} \simeq 2p_0 A/k_1$, inasmuch the inertial forces do not contribute significantly. The dynamic regime is a trade-off between the aforementioned scenarios: in this case, $u_{\max}$ specifically depends on the load time history.

With reference to a back structure made either with beams or cables of length $L = 8\,\mathrm{m}$, the following three different cases are considered.

1. **Rigid structure.** This is the limit case $k_1 \to \infty$, representative of the quasi-static regime. Since no energy from the blast wave is absorbed by the back structure, this represents the most critical condition for the glass pane.

2. **Simply supported beam.** Mullions with cross-sectional inertia $I = 42\,930 \cdot 10^{-8}\,\mathrm{m}^4$ and mass per unit length $\bar{m}_b = 79.4\,\mathrm{kg/m}$ (standard profile IPE A 500 UNI 5398) are considered in order to keep the maximum deflection within the limit $L/30$, as verified a posteriori. Setting $E_s = 210\,\mathrm{GPa}$ for steel, the effective stiffness is $k_1 = 48E_sI/L^3 = 8.45184 \cdot 10^6\,\mathrm{N/m}$. By choosing the quadratic expression $\Upsilon(x) = 4(x/L)(x/L - 1)$ as the shape function for inflection, the lumped mass can be calculated as $m_1 = \bar{m}_b \int_0^L \Upsilon(x)^2\,dx \simeq 338.773\,\mathrm{kg}$.

3. **Pre-tensioned cable.** The impulsive regime is achieved for a back structure made with multiple cables, forming a net supporting several glass panes. In a 1-DOF schematization, we can set $N_0 = 300 \cdot 10^3\,\mathrm{N}$ as the effective tensile force in one equivalent cable, and obtain $k_1 = 2N_0/(L/2) = 150 \cdot 10^3\,\mathrm{N/m}$. In order to consider the weight of the fixing devices besides the self-weight of the cable, we set $m_1 = 100\,\mathrm{kg}$, even if ballast may be artfully added.

In all the aforementioned cases, the dissipation of the back structure is interpreted

by a dashpot, shown in Fig. 4.4(a), with a damping coefficient c_1 corresponding to a 3 % damping ratio, i.e., $c_1 = 0.03 \cdot 2\sqrt{m_1 k_1}$.

The considered load-bearing back structures are classified in Table 4.1 according to the loading-regime categories suggested in [92] and according to the parameter $T_d\sqrt{k_1/m_1}$. The characteristic load duration time, evidenced in Fig. 4.5, is set equal to $T_d = 0.01\,\mathrm{s}$.

Back Structure	**Loading Regime**	$T_d \cdot \sqrt{\frac{k_1}{m_1}}$
Rigid support	Quasi-static	∞
Simply supported beam	Dynamic	1.5795
Pretensioned cables	Impulsive	0.3872

Table 4.1. Rear supporting structures and correspondent loading regimes as per [92].

4.1.3 Glass pane

The glass pane is a monolithic plate[3] of size $a \times b \times s = 2.5 \times 2.5 \times 0.02\,\mathrm{m}^3$, with Young's modulus $E_g = 70\,\mathrm{GPa}$ and Poisson's ratio $\nu = 0.22$. The plate is simply supported by a contouring metallic frame, supposed rigid[4] in the model problem. Introduce a reference system (x, y) centered at one of plate corners and with axes parallel to the sides, so that the reference domain for the plate is $\{0 \le x \le a, 0 \le y \le b\}$. The out-of-plane displacement $w(x, y, t)$ is approximated as

$$w(x, y, t) = \Big[Z_2(t) - Z_4(t)\Big]\psi(x, y)\,, \tag{4.3}$$

where, consistently with the form of first vibration mode

$$\psi(x, y) = \sin\Big(\pi x/a\Big)\sin\Big(\pi y/b\Big)$$

[3]Laminated glass could be considered as a monolith with equivalent bending properties, using the definition of effective thickness [99, 100].

[4]This is a necessary simplifying assumption, because consideration of the elastic deformation of the frame would make the semi-analytical resolution of the problem impractical. However, it is probably on the safe side, because the compliance of the frame should absorb part of the energy from the blast wave and, hence, diminish its effect on the glass.

is the shape function, $Z_2(t) - Z_4(t)$ is the maximum deflection, i.e., the relative displacement between plate centroid and supported borders. Due to high pressures transmitted by the blast wave, it is necessary to take into account geometric-nonlinear effects by using von Kármán plate theory [101, 102, 63]. In order to approximate the in-plane stress function $\varphi(x, y, t)$, providing the membrane components of stress in the form

$$\bar{\sigma}_x(x, y, t) = \frac{\partial^2 \varphi(x, y, t)}{\partial y^2}, \tag{4.4a}$$

$$\bar{\sigma}_y(x, y, t) = \frac{\partial^2 \varphi(x, y, t)}{\partial x^2}, \tag{4.4b}$$

$$\bar{\tau}_{xy}(x, y, t) = -\frac{\partial^2 \varphi(x, y, t)}{\partial x \partial y}, \tag{4.4c}$$

we follow the procedure suggested by Levy [103]. The method is based on Fourier expansion; by keeping only the first two terms, one finds for a simply supported plate

$$\varphi(x, y, t) \simeq \left[Z_2(t) - Z_4(t)\right]^2 \cdot \left[\frac{E_g}{32(b^2/a^2)} \cos\left(\frac{2\pi x}{a}\right) + \frac{E_g}{32(a^2/b^2)} \cos\left(\frac{2\pi y}{b}\right)\right]. \tag{4.5}$$

From this, one calculates the membrane strains

$$\bar{\varepsilon}_x(x, y, t) = \frac{1}{E_g}\left(\frac{\partial^2 \varphi(x, y, t)}{\partial y^2} - \nu \frac{\partial^2 \varphi(x, y, t)}{\partial x^2}\right), \tag{4.6a}$$

$$\bar{\varepsilon}_y(x, y, t) = \frac{1}{E_g}\left(\frac{\partial^2 \varphi(x, y, t)}{\partial x^2} - \nu \frac{\partial^2 \varphi(x, y, t)}{\partial y^2}\right), \tag{4.6b}$$

$$\bar{\varepsilon}_{xy}(x, y, t) = -\frac{(1+\nu)}{E_g} \frac{\partial^2 \varphi(x, y, t)}{\partial x \partial y}. \tag{4.6c}$$

The component of curvatures can be approximated as

$$\chi_x(x, y, t) = -\frac{\partial^2 w(x, y, t)}{\partial x^2}, \tag{4.7a}$$

$$\chi_y(x, y, t) = -\frac{\partial^2 w(x, y, t)}{\partial y^2}, \tag{4.7b}$$

$$\chi_{xy}(x, y, t) = -\frac{\partial^2 w(x, y, t)}{\partial y \partial x}. \tag{4.7c}$$

In conclusion, the elastic energy of glass plate takes the form

$$\mathcal{U}^p = \frac{E_g s}{2(1-\nu^2)} \int_0^a \int_0^b (\bar{\varepsilon}_x + \bar{\varepsilon}_y)^2 - 2(1-\nu)(\bar{\varepsilon}_x \bar{\varepsilon}_y - \bar{\varepsilon}_{xy}^2)\, dxdy + \frac{E_g s^3}{24(1-\nu^2)} \int_0^a \int_0^b (\chi_x + \chi_y)^2 - 2(1-\nu)(\chi_x \chi_y - \chi_{xy}^2)\, dxdy, \quad (4.8)$$

where the contributions of membrane and bending strains are well separated in the sum.

4.1.4 Dissipative devices based on material yielding

As schematically indicated in Fig. 4.4(b), the dissipative device is composed of three parts: a cylinder, a mobile piston and two shock absorbers in unilateral contact with the piston. The cylinder, whose equivalent mass is $m_3 = 50\,\mathrm{kg}$, is interposed between the back structure and the framed glass panel. Their dissipation mechanism is based on the plastic capacity of the shock absorbers when compressed beyond the critical limit. There are different ways to achieve such a property by means of different materials and geometries, such as in the device proposed by Wellershoff et al. [95] which is formed by aluminium sleeves and dissipative concrete. Here, we consider honeycomb structures as in Fig. 4.3, whose constitute response under static compression [104, 105] is as schematically represented in Fig. 4.7(a). The graph shows a linear elastic branch followed by a plastic plateau at $F = F_{cr}$, until the maximum plastic displacement $\bar{\Delta}$ (end of stroke) is reached: this relationship may be supposed valid also in the dynamic case, modulo some approximations [106]. By neglecting the elastic phase, very limited if compared with the total plastic deformation, the out-put can be approximated by the rigid-plastic law of Fig. 4.7(b). Under this assumption, the response is completely characterized by the critical load F_{cr}, at which the plastic deformation occurs, and the maximum plastic shortening $\bar{\Delta}$. These parameters can be tailor-designed since they depend on the material and the structure of shock absorber [107, 108]. The upper bound for the absorbed energy $\mathcal{W}^d$ is clearly $\mathcal{W}^d \leq F_{cr}\bar{\Delta}$.

The shock absorbers are two because one is active during the compression phase and the other is needed for the subsequent suction phase. With reference to Fig. 4.4(a), the two units will be respectively distinguished with the labels "ℓ" (for *left*) and "r" (for *right*). Their properties should be specifically optimized according to their role. Since the contact between the piston and each one of the shock absorber is unilateral, the constitutive response of the whole unit, to be implemented in the solver algorithm, is represented in Fig. 4.8 for a cyclic response: the force F that the piston can equilibrate is a highly nonlinear function of the relative displacement

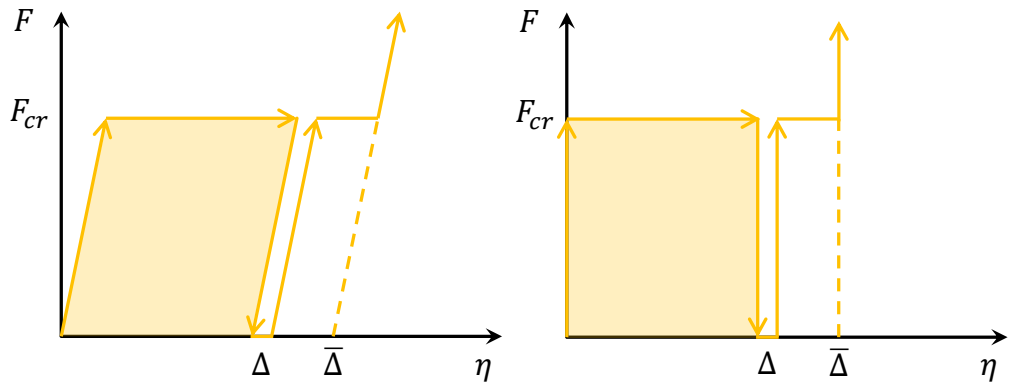

(a) Real experimental relation (b) Simplified experimental relation

Figure 4.7. Schematic force-displacement relationship for an aluminium honeycomb structure under static compression: (a) experimentally measured and (b) idealized response.

$Z_3 - Z_1$, as per Fig. 4.4(a). The first (third) quadrant of the graph is associated with the right (left) shock absorber.

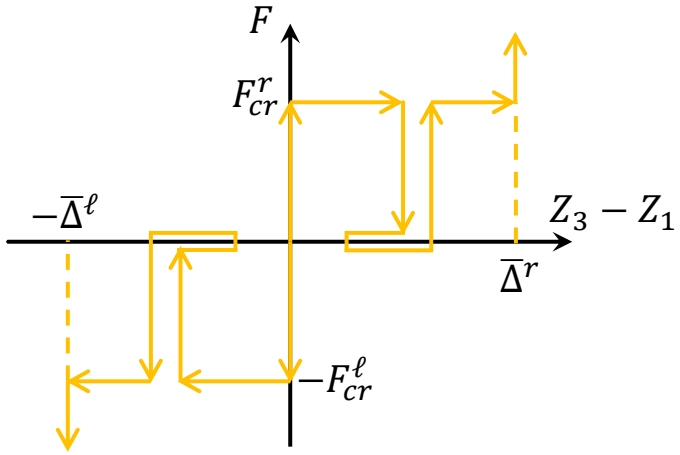

Figure 4.8. Constitutive relation for the whole dissipating unit under a non-monotone displacement of the piston. The force F that the piston can equilibrate is a nonlinear function of $Z_3 - Z_1$.

4.1.5 Dynamic equations

The solution of the dynamic system of Fig. 4.4(a) is governed by equations that change during the motion according to the type of contact between the piston and

the shock absorber. In particular, five distinct scenarios need to be considered, referred to as the *compression*, *compression-yielding*, *traction*, *traction-yielding*, and *uncoupled* phases. The transition from one phase to the other is determined by matching conditions in terms of displacements and velocities of the Lagrangian variables.

The blast wave acts on a system initially at rest in the reference, undistorted and un-yielded, in which $\Delta^\ell = \Delta^r = 0$.

- The **compression** phase occurs when the mobile piston gets in touch with the left shock absorber, no plasticization has yet taken place. Thus Δ^ℓ and Δ^r are constants over time because $k_2(Z_4 - Z_3) > -F^\ell_{cr}$. In order to avoid interpenetrations, the kinematic variable shall satisfy conditions

$$Z^\ell_0 = Z_1 - \Delta^\ell, \quad (4.9a) \qquad Z^r_0 = Z_1 + \Delta^r, \quad (4.9c) \qquad Z_1 = Z_3 + \Delta^\ell, \quad (4.9e)$$
$$\dot{Z}^\ell_0 = \dot{Z}_1, \quad (4.9b) \qquad \dot{Z}^r_0 = \dot{Z}_1, \quad (4.9d) \qquad \dot{Z}_1 = \dot{Z}_3. \quad (4.9f)$$

  In particular, the conditions (4.9e)-(4.9f) link the displacement of back structure with that of mobile piston, avoiding spurious velocity jumps between $\dot{Z}_3$ and $\dot{Z}^\ell_0$. Such discontinuities would imply the presence of unrealistic impulsive forces which cannot be transmitted by a shock absorber with a limited yielding strength, as indicated in Fig. 4.7(b).

- The **compression-yielding** phase starts when the mobile piston plasticizes the left shock absorber, so that $k_2(Z_4 - Z_3) = -F^\ell_{cr}$. The left dissipator absorbs energy as it shrinks, up to the limit $\Delta^\ell = \bar{\Delta}^\ell$ or, alternatively, when the transmitted force goes under the plastic threshold. The "crushing velocity" can be calculated as

$$\dot{\Delta}^\ell = \dot{Z}^\ell_0 - \dot{Z}_1 < 0\,, \tag{4.10}$$

  which provides the plastic displacement after integration. The initial conditions for the kinematic variables characterizing the beginning of this phase, read

$$Z^\ell_0 = Z_3, \quad (4.11a) \qquad Z^r_0 = Z_1 + \Delta^r, \quad (4.11c)$$
$$\dot{Z}^\ell_0 = \dot{Z}_3, \quad (4.11b) \qquad \dot{Z}^r_0 = \dot{Z}_1, \quad (4.11d)$$

  but this time there is not a "direct" relation between Z_1 and Z_3. When the total plastic deformation $\Delta^\ell = \bar{\Delta}^\ell$ is attained, the mobile piston impacts with the back structure, exchanging an impulsive force. We model this interaction as an impact problem, governed by balance of linear momentum and kinetic energy, as it will be soon explained.

- During the **traction** phase, the piston gets in touch with the right shock absorber, which is deputed to mitigate all the secondary suction effects of the blast wave. In analogy with the compression phase, as long as $k_2(Z_4 - Z_3) < F^r_{cr}$ there is no plasticization and, hence, Δ^ℓ and Δ^r remain constant. The conditions on the kinematic variables that characterize this phase now are

$$Z^\ell_0 = Z_1 - \Delta^\ell, \quad (4.12a) \qquad Z^r_0 = Z_1 + \Delta^r, \quad (4.12c) \qquad Z_1 = Z_3 - \Delta^r, \quad (4.12e)$$
$$\dot{Z}^\ell_0 = \dot{Z}_1, \quad (4.12b) \qquad \dot{Z}^r_0 = \dot{Z}_1, \quad (4.12d) \qquad \dot{Z}_1 = \dot{Z}_3. \quad (4.12f)$$

  As before, the expressions (4.12e)-(4.12f) couple the displacement of right shock absorber with that of mobile piston. Also at the beginning of this phase there are no velocity jumps between $\dot{Z}_3$ and $\dot{Z}^r_0$.

- The **traction-yielding** phase occurs when the mobile piston yields the right shock absorber, so that $k_2(Z_4 - Z_3) = F^r_{cr}$. The movement of the right shock absorber stops when $\Delta^r = \bar{\Delta}^r$ or $k_2(Z_4 - Z_3) < F^r_{cr}$. The "crushing velocity" is obtained as

$$\dot{\Delta}^r = \dot{Z}^r_0 - \dot{Z}_1 > 0\,. \quad (4.13)$$

  which provides the plastic displacement after time integration. The kinematic variable shall satisfy

$$Z^\ell_0 = Z_1 - \Delta^\ell, \quad (4.14a) \qquad Z^r_0 = Z_3, \quad (4.14c)$$
$$\dot{Z}^\ell_0 = \dot{Z}_1, \quad (4.14b) \qquad \dot{Z}^r_0 = \dot{Z}_3. \quad (4.14d)$$

  When the end stroke $\Delta^r = \bar{\Delta}^r$ is reached, the mobile piston and the back structure exchange an impulsive force, which is modelled as an impact.

- During the **uncoupled** phase, the load-bearing structure and the panel oscillate independently one another, since the piston is in contact with neither of the shock absorbers. The conditions for the kinematic variables are

$$Z^\ell_0 = Z_1 - \Delta^\ell, \quad (4.15a) \qquad Z^r_0 = Z_1 + \Delta^r, \quad (4.15c)$$
$$\dot{Z}^\ell_0 = \dot{Z}_1, \quad (4.15b) \qquad \dot{Z}^r_0 = \dot{Z}_1. \quad (4.15d)$$

  where Δ^ℓ and Δ^r are constants over time. The piston freely moves inside the cylinder. The uncoupled phase ends when the piston gets again in touch with one of the shock absorbers; impact occurs when this is a completely yielded unit, such that either $Z_3 = Z^\ell_0$ or $Z_3 = Z^r_0$.

As indicated above, an *impact* can occur between the mobile piston and the back structure. This condition cannot take place when the piston gets in touch with a shock absorber until this has reached the end stroke, otherwise, the contact force would be limited by the value F_{cr}. The solver algorithm accounts for impacts in two conditions: at the end of the *yielding* phases, and at the end stroke during the *uncoupled* phase, when the shock absorbers are fully yielded. The impulse cannot be transmitted to the glass pane because of the interposed spring k_2, indicated in Fig. 4.4(a) and here set equal to $k_2 = 3 \cdot 10^7\,\mathrm{N/m}$, which schematically interprets the compliance of the secondary elements of the façade, such as joints, supports, etc. Linear momentum must be conserved after the impact, but part of the kinetic energy can be lost. This loss is accounted for by the coefficient of restitution α, with $0 \leq \alpha \leq 1$, defined as the ratio between the differences in velocities. Therefore, denoting with $\dot{Z}_3^-$ and $\dot{Z}_1^-$ the velocities immediately before the impact, and with $\dot{Z}_3^+$ and $\dot{Z}_1^+$ the corresponding values just after the impact, the matching conditions are of the form

$$\begin{cases} m_1\dot{Z}_1^- + m_3\dot{Z}_3^- = m_1\dot{Z}_1^+ + m_3\dot{Z}_3^+ \\ \\ \alpha = \dfrac{\dot{Z}_3^+ - \dot{Z}_1^+}{-(\dot{Z}_1^- - \dot{Z}_3^-)}\,. \end{cases} \tag{4.16}$$

In addition we shall set $\dot{Z}_0^{r,+} = \dot{Z}_0^{\ell,+} = \dot{Z}_1^+$, $\dot{Z}_2^- = \dot{Z}_2^+$ and $\dot{Z}_4^- = \dot{Z}_4^+$.

For each one of the aforementioned scenarios, the governing equation can be found by Hamilton's principle in the form

$$\begin{cases} \dfrac{d}{dt}\left(\dfrac{\partial\mathcal{K}}{\partial\dot{Z}_0^j}\right) + \dfrac{\partial\mathcal{R}}{\partial\dot{Z}_0^j} + \dfrac{\partial\mathcal{U}}{\partial Z_0^j} = \dfrac{\delta\mathcal{W}}{\delta Z_0^j} \quad j = \ell, r \\ \\ \dfrac{d}{dt}\left(\dfrac{\partial\mathcal{K}}{\partial\dot{Z}_i}\right) + \dfrac{\partial\mathcal{R}}{\partial\dot{Z}_i} + \dfrac{\partial\mathcal{U}}{\partial Z_i} = \dfrac{\delta\mathcal{W}}{\delta Z_i} \quad i = 1,2,3,4 \end{cases} \tag{4.17}$$

where $\mathcal{K}$ is the kinetic energy, $\mathcal{R}$ is the dissipation function, $\mathcal{U}$ is the potential energy and $\mathcal{W}$ is the work performed by external forces.

The kinetic energy of system in Fig. 4.4(a) is

$$\mathcal{K} = \frac{1}{2}m_1\dot{Z}_1^2 + \frac{1}{2}m_3\dot{Z}_3^2 + \frac{1}{2}\rho s\int_0^a\int_0^b[(\dot{Z}_2 - \dot{Z}_4)\psi + \dot{Z}_4]^2\,dxdy. \tag{4.18}$$

The dissipation function, which accounts for the effects of the viscous damper of the back structure, reads

$$\mathcal{R} = \frac{1}{2}c_1\dot{Z}_1^2. \tag{4.19}$$

The potential energy results from the elastic deformation of the springs and the glass pane, so that it can be written in the form

$$\mathcal{U} = \frac{1}{2}k_1 Z_1^2 + \frac{1}{2}k_2(Z_4 - Z_3)^2 + \mathcal{U}^p\,, \tag{4.20}$$

where $\mathcal{U}^p$ is given by (5.11). The work of external forces is performed by the blast wave action and results to be

$$\mathcal{W} = p(t)\int_0^a \int_0^b [(Z_2 - Z_4)\psi + Z_4]\, dxdy. \tag{4.21}$$

Observe that during the yielding phases, also the dissipated energy $\mathcal{W}^d$ has to be added in the expression (5.14). For the yielding compression stage, one has $\mathcal{W}^d = -F_{cr}^{\ell}(Z_0^{\ell} - Z_1)$, while for the yielding traction stage, one finds $\mathcal{W}^d = F_{cr}^{r}(Z_0^{r} - Z_1)$. Note that the sign of F_{cr}^{ℓ} and F_{cr}^{r} are written according to the convention of Fig. 4.4(a).

For what concerns the uncoupled phase, Hamilton's principle is applied to each one of the two resulting decoupled systems. The motion of the panel is obtained by neglecting the contribution of the back structure inside the expressions (4.18)-(5.14); the load-bearing structure becomes a harmonic oscillator governed by the equation $m_1\ddot{Z}_1 + c_1\dot{Z}_1 + k_1 Z_1 = 0$.

The solver algorithm detects when the system alternatively enters each one of the five phases, accounting for the kinematic condition associated with that, as detailed above.

The model problem is solved with a mathematical algorithm which has to choose and solve the correct set of equilibrium equations, with the proper matching conditions, according to the five scenarios referred to in Section 4.1.5 as the *compression*, *compression-yielding*, *traction*, *traction-yielding* and *uncoupled* phases.

4.1.6 Validation with a finite element code

The algorithm is written in `Mathematica`, but in order to verify its soundness, it is useful to compare the theoretical solution with that provided by a commercial finite element (FE) software. The library of the commercial code `Straus7` does not contain elements that can specifically model impacts, but a contact with coefficient of restitution $\alpha = 1$ can be simulated with a very hard unilateral spring. Indeed, the impact phases, which are usually neglected in simulations of this kind, represent one of the most important aspects of the present model. In order to consider only the first vibration mode for the plate, the glazed pane is substituted with a lumped massive point and corresponding spring, calculated with Rayleigh's method. The resulting simplified lumped element model is shown in Fig. 4.9.

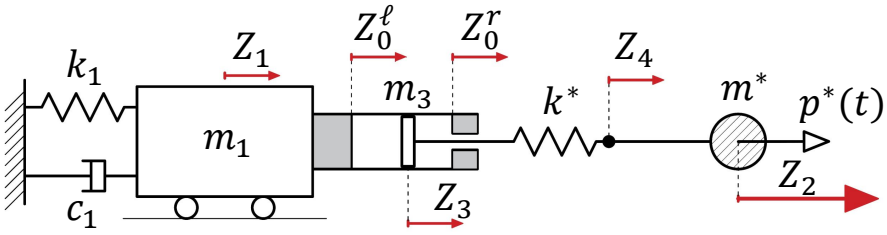

Figure 4.9. Schematic representation of the simplified lumped element model used for the algorithm validation with a commercial FE code.

Substituting the glass plate with a 1-DOF oscillator is certainly a drastic approximation, because the blast wave certainly activates higher modes. However, Fig. 4.6 indicates that the first mode is certainly the one that is excited the most. For what concerns the dynamics of plate, there is a substantial difference between the scheme of Fig. 4.4(a) and that of Fig. 4.9 because, in the former case, the frame supporting the plate moves with the piston, whereas the stiffness of the spring k^* has been calculated by assuming that the supports of the plate are fixed. However, this case just serves as confirmation of the solutions algorithm with reference to a commercial FE code.

The considered data have been set to amplify and highlight the presence of bounces. For what concerns the load-bearing structure, we maintain the mechanical properties of beam support indicated in Section 4.1.2, i.e., $k_1 = 8.45184 \cdot 10^6\,\mathrm{N/m}$ and $m_1 = 338.773\,\mathrm{kg}$; the damping coefficient c_1 corresponds to a 3 % damping ratio. The dissipative device is supposed to be constituted by two shock absorbers, whose properties are: $F_{cr}^\ell = 100\,\mathrm{kN}$ and $\bar{\Delta}^\ell = 0.03\,\mathrm{m}$; $F_{cr}^r = 50\,\mathrm{kN}$ and $\bar{\Delta}^r = 0.02\,\mathrm{m}$. The mass $m_3 = 50\,\mathrm{kg}$ represents the total inertia of the mobile piston. The properties of the oscillating massive point have been set by applying Rayleigh's method for a simply supported slab $a \times b \times s = 2.5 \times 2.5 \times 0.02\,\mathrm{m}^3$ made of glass, as already indicated in Section 4.1.3. By assuming $\psi(x,y) = \sin\left(\pi x/a\right)\sin\left(\pi y/b\right)$ as the shape function, one finds [70]

$$m^* = \rho s \int_0^a \int_0^b \psi^2 \, dxdy, \tag{4.22}$$

$$k^* = \frac{E_g s^3}{12(1-\nu^2)} \int_0^a \int_0^b \left(\frac{\partial^2\psi}{\partial x^2} + \frac{\partial^2\psi}{\partial y^2}\right)^2 - 2(1-\nu)\left[\frac{\partial^2\psi}{\partial x^2}\frac{\partial^2\psi}{\partial y^2} - \left(\frac{\partial^2\psi}{\partial x \partial y}\right)^2\right] dxdy. \tag{4.23}$$

The dynamic equations are derived as in Section 4.1.5. For the model problem of

Fig. 4.9 the kinetic energy (4.18), the potential energy (4.20) and the work made by the external forces (5.14) (modulo the plastic dissipation) have to be respectively rewritten as

$$\mathcal{K} = \frac{1}{2} m_1 \dot{Z}_1^2 + \frac{1}{2} m_3 \dot{Z}_3^2 + \frac{1}{2} m^* \dot{Z}_2^2, \tag{4.24}$$

$$\mathcal{U} = \frac{1}{2} k_1 Z_1^2 + \frac{1}{2} k^* (Z_2 - Z_3)^2, \tag{4.25}$$

$$\mathcal{W} = p^*(t) \cdot Z_2, \tag{4.26}$$

where $p^*(t) = p(t) \int_0^a \int_0^b \psi \, dxdy$.

The FE model implemented in `Straus7` is shown in Fig. 4.10. A `Spring-Damper` forms the back structure connecting the mass m_1 with a fixed point at one extremity, while the mass m^* is attached to the piston trough a `Spring` k^*. The masses m_1 and m^* are displayed as light blue spheres, which are constrained to move along the same direction of the force $p^*(t)$ (red arrow applied on the mass m^*). A detail of the model for the dissipative device, encapsulating the two shock absorbers, is shown in Fig. 4.11. The right shock absorber is connected by `Rigid links` to the mass m_1, while the mass m_3 is connected by `Rigid links` to the spring k^*, represented with blue bars. The mobile piston is constituted by a massive point m_3, which can get in contact with the shock absorbers through `Normal Contact` beams, colored in green. In practice, they are simple unilateral springs active in compression, whose stiffness is set equal to $1.5 \cdot 10^{11}$ N/m (higher values provide inaccurate numerical results). Observe that `Normal Contact` beams are associated in parallel with `Zero Gap` beams (colored in yellow) in order to avoid interpenetrations when the stroke end (completely yielded shock absorber) is reached. They provide a non-zero stiffness, set equal to $3 \cdot 10^{11}$ N/m, only when the gap is closed.

The time dependent solution is calculated by using the `Nonlinear Transient Dynamic` solver, implemented in the software. There are several parameters to be set: we choose the `Time step` $\Delta\tau = 10^{-5}$ s and `Newmark's beta` $\mathbf{B} = 0.5$. The results are reported for the time interval $0 \leq t \leq 0.1$ s, which is meaningful with respect to the the duration of the blast pressure. The graphs that describe the dynamic response in terms of the kinematic variables are represented in Figs. 4.12-4.14. They all demonstrate a perfect agreement between the theoretical and the FE solutions. In particular, the graph of $Z_3 - Z_1$ represented in Fig. 4.13, which corresponds to the relative displacement between the moving piston and the back structure, shows a perfect agreement with the solution provided by `Straus7`, in particular for what concerns the bounces produced by multiple impacts. This is

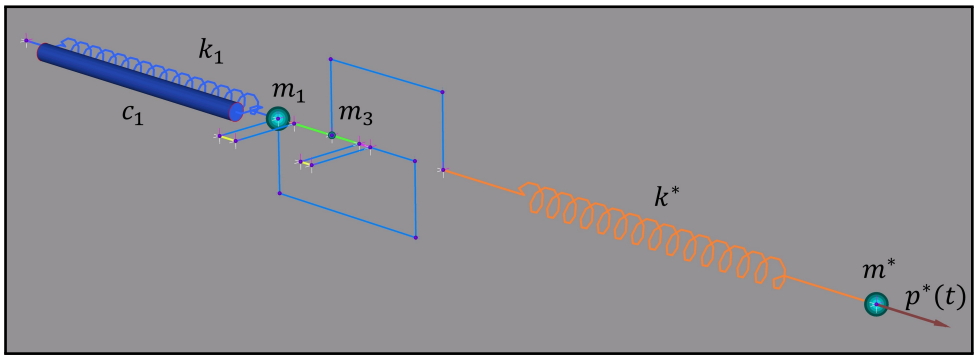

Figure 4.10. Simplified finite element model, implemented in `Straus7`.

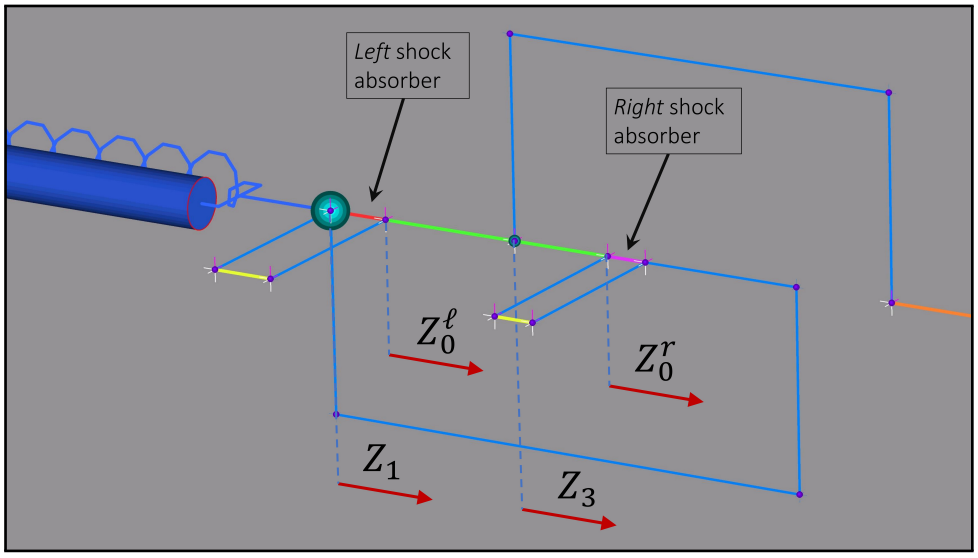

Figure 4.11. Detail of the dissipative device, implemented using the elements available in `Straus7` library. The indicated kinematic variables are those used in the theoretical problem.

indeed the most important result from the comparison. Unfortunately, `Straus7` cannot consider other aspects, such as the variability of the coefficient of restitution.

4.2 Optimization of dissipative device

Parametric analyses are now presented in order to optimize the dissipative system with respect to safeguarding the integrity of the glass pane.

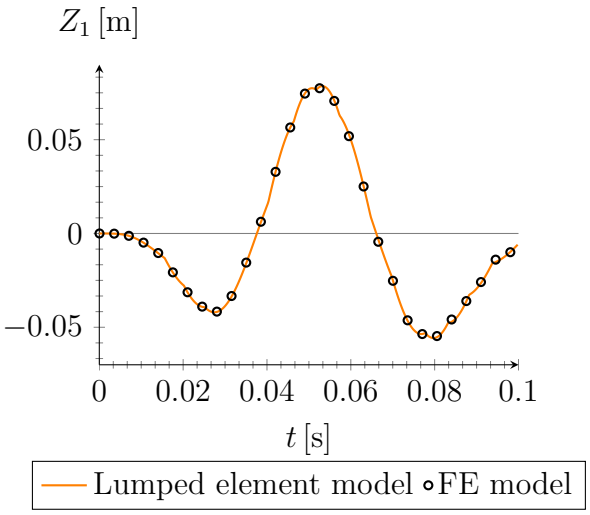

Figure 4.12. Comparison between theoretical and FE solutions: displacement Z_1 of the load-bearing back structure.

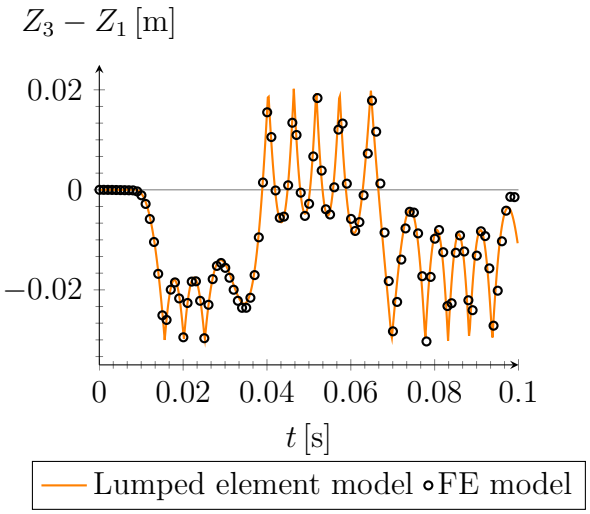

Figure 4.13. Comparison between theoretical and FE solutions: relative displacement $Z_3 - Z_1$ between the mobile piston and the load-bearing back structure.

4.2.1 Influence of the properties of the *left* shock absorber

The left shock absorber serves to mitigate the compression phase of the blast load according to Friedlander equation. Since the integrity of glass has to be preserved, the parameter of interest is the maximum (in absolute terms) out-of-plane displacement of pane, which is directly associated with the maximum stress caused by the compression phase. This is represented by $|Z_2 - Z_4|_{\max}$ in the scheme of Fig. 4.4(a),

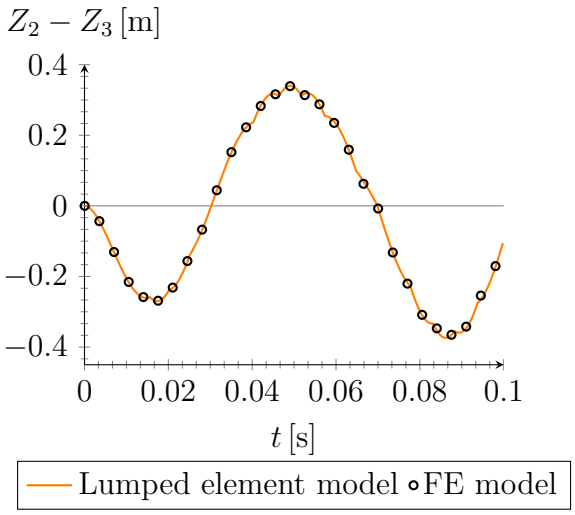

Figure 4.14. Comparison between theoretical and FE solutions: relative displacement $Z_2 - Z_3$ between the oscillating mass representative of the panel and the mobile piston.

and it clearly depends upon the parameter of the shock absorber, i.e., it is a function of F_{cr}^{ℓ} and $\bar{\Delta}^{\ell}$. Starting from the reference undistorted state $(Z_2 - Z_4) = 0$, we calculate the maximum first peak under the blast action as the aforementioned parameters are varied, whereas the properties of the right shock absorber have been fixed at $F_{cr}^{r} = 25\,000\,\mathrm{N}$ and $\bar{\Delta}^{r} = 0.1\,\mathrm{m}$. The back structure is supposed to be infinitely rigid ($k_1 \to \infty$), which represents the worst situation for the integrity of the glass pane. A further hypothesis is that there is no energy loss during the impacts of mobile piston, i.e., the coefficient of restitution is $\alpha = 1$.

Results are shown in Fig. 4.15, where the calculated points have been interpolated with a surface. There is well-recognizable "step", more marked for low values of F_{cr}^{ℓ}, which divides the surface into two regions: in words, $|Z_2 - Z_4|_{\max}$ rapidly jumps inside a small interval in terms of $\bar{\Delta}^{\ell}$. The location of the jump is correlated with time scale T_d characterizing the blast wave, which marks the transition from the compression to the suction phase. When the blast wave starts to exert a suction action, the mobile piston accelerates more rapidly than the panel because it presents a lower inertia; consequently, the mobile piston and the panel get closer because $\dot{Z}_3 > \dot{Z}_2$, increasing the relative displacement $|Z_2 - Z_4|$. During the compression phase, the peak value of $|Z_2 - Z_4|_{\max}$ is mitigated if the left shock absorber is not yet fully yielded when $t = T_d$, i.e., if the piston has not yet collided against the completely crushed left shock absorber at the end of its stroke, such as to avoid the impact. In this case, the inversion of the motion of the piston ($\dot{Z}_3 > 0$) due to the suction pressure is not emphasized by the rebound. This implies that the difference between $\dot{Z}_3$ and $\dot{Z}_2$ is reduced on average as well as the peak $|Z_2 - Z_4|_{\max}$.

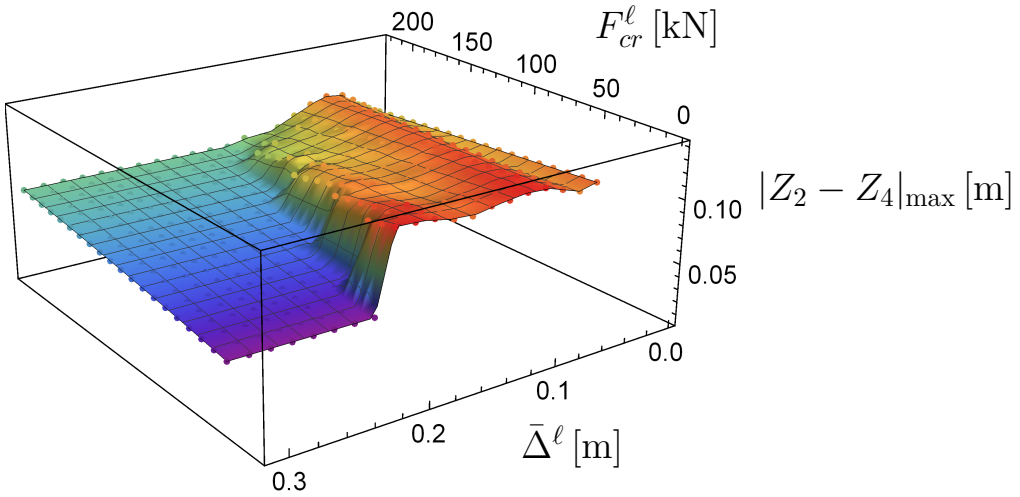

Figure 4.15. Maximum out-of-plane displacement of the glass pane $|Z_2 - Z_4|_{\max}$ during the compression phase, represented as a function of properties of the left shock absorber $\bar{\Delta}^{\ell}$ and F_{cr}^{ℓ}. Case of a rigid load-bearing back structure.

The graph suggests that an optimal condition is achieved in correspondence of the step in plotted surface. In particular, the right shock absorber should presents *i*) a noteworthy run $\bar{\Delta}^{\ell} \uparrow$, along which energy is dissipated and *ii*) a low activation force $F_{cr}^{\ell} \downarrow$ for plasticization, in order to minimize the action directly transmitted by the blast wave to the panel. In general, the impact of the piston with the fully-collapsed shock absorber has a negative effect.

In order to better appreciate the location of the jump, three graphs are presented in Fig. 4.16(a) which represents the intersection of the interpolation surface with planes $F_{cr}^{\ell} = \text{const}$. Observe that $|Z_2 - Z_4|_{\max}$ drops when $0.15 \leq \bar{\Delta}^{\ell} \leq 0.2\,\text{m}$. Before this sudden variation, the higher values of the activation force F_{cr}^{ℓ} provide a consistent, though limited, benefic effects, because the amount of energy absorbed is given by $F_{cr}^{\ell} \cdot \bar{\Delta}^{\ell}$. On the contrary, after the jump, lower values of the activation force F_{cr}^{ℓ} provide a better performance, because the glass pane is less constrained and, hence, it can accommodate the blast pressure with increased mobility; impacts are mitigated and energy is still dissipated thanks to the length of plasticization of the shock absorber. The jump is reduced by high values of F_{cr}^{ℓ} because there is a trade off among the aforementioned phenomena.

When no dissipative device is used ($F_{cr}^{\ell} \to \infty$ and $F_{cr}^{r} \to \infty$), the maximum out-of-plane displacement of the glass panes results to be $|Z_2 - Z_4|_{\max} \simeq 0.11\,\text{m}$, also plotted in Fig. 4.16(a). This is a limit case that serves as a benchmark to appreciate the advantage of shock absorbers, which is thwarted when their plastic run ($\bar{\Delta}^{\ell}$ or $\bar{\Delta}^{r}$) is too short. Likewise, if F_{cr}^{ℓ} represents a "barrier" too high to overcome, the shock absorber does not deform property and the advantage is null.

The panel deformation tends to be amplified during impacts, but the dissipative device allows to reduce this peak if correctly designed with an adequate plastic run.

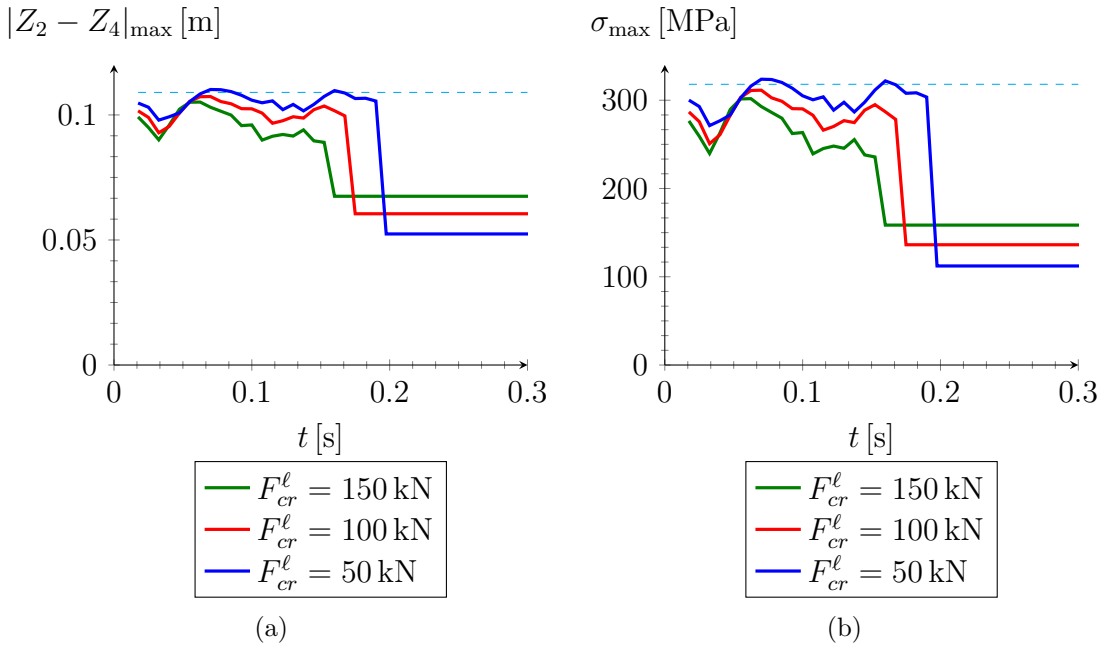

Figure 4.16. Case of a rigid load-bearing back structure. (a) Maximum out-of–plane displacement of the glass pane $|Z_2 - Z_4|_{\max}$ and (b) corresponding maximum stress, during the compression phase of the blast wave, represented as a function of $\bar{\Delta}^{\ell}$, for various values if F_{cr}^{ℓ}. The horizontal dashed line corresponds to the limit case with $F_{cr}^{\ell} \to \infty$ and $F_{cr}^{r} \to \infty$.

Due to second order geometric effects, the stress in the glass pane is not linearly proportional to the maximum out-of-plane displacement. Fig. 4.16(b) is the counterpart of Fig. 4.16(a) in terms of maximum stress, corresponding to the peak value of $|Z_2 - Z_4|_{\max}$, which is calculated according to the shape functions (5.6) and (5.8). The corresponding 3D plot is represented in Fig. 4.17. The nonlinear model, though approximate, indicates that doubling the out-of-plane displacement can triplicate the maximum stress. By assuming $\bar{\sigma} = 200\,\text{MPa}$ as the strength limit for glass under impulsive actions, one can notice that the glass pane is at risk of failure in a great portion of the plotted surface. The façade design should be oriented to choosing properties inside a safe domain, determined by the mechanical properties of the dissipative device.

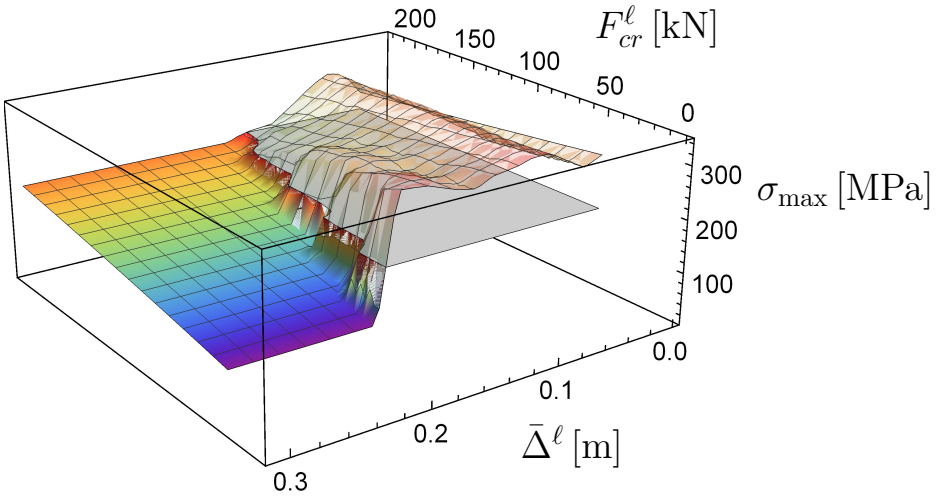

Figure 4.17. Case of a rigid load-bearing back structure. Maximum stress during the compression phase of the blast wave, represented as a function of $\bar{\Delta}^{\ell}$ and F_{cr}^{ℓ}. The gray horizontal plane indicates the assumed limit strength of glass under short-term loading.

4.2.2 Influence of the coefficient of restitution

The coefficient of restitution α expresses the energy loss during impacts, occurring when the mobile piston collides against the completely deformed shock absorbers. Although the value could be experimentally determined, our interest is for a parametric analysis indicating how this further source of dissipation can affect the final dynamic response. The mechanical parameters are the same of Section 4.2.1, with $k_1 \to \infty$; the left shock absorber is characterized by $\bar{\Delta}^{\ell} = 0.25\,\text{m}$ and $F_{cr}^{\ell} = 50\,\text{kN}$. The time dependent response of system is reported for $0 \leq t \leq 0.1\,\text{s}$.

The relative displacement $Z_3 - Z_1$ between the piston and the load-bearing back structure is plotted in Fig. 4.18. Whatever the coefficients of restitution, both the left and the right shock absorbers are completely deformed since $(Z_3 - Z_1)_{\min} = -\bar{\Delta}^{\ell} = -0.25\,\text{m}$ and $(Z_3 - Z_1)_{\max} = \bar{\Delta}^{r} = 0.1\,\text{m}$. This check is necessary to assure that impacts do occur. As expected, when the coefficient of restitution grows up $\alpha \uparrow$, the collisions are more frequent and the bounces are higher, because less energy is dissipated.

The out-of-plane displacement $Z_2 - Z_4$, shown in Fig. 4.19, is affected by the displacement of the mobile piston and, hence, by the coefficient of restitution. If collisions are frequent and bounces are high, the out-of-plane displacement tends to increase. Although the first peak is not affected, the influence of α becomes visible during the subsequent stages, where the peaks are higher. The proposed model does not consider friction forces and higher vibration modes for the glass pane, which certainly play a beneficial role. Therefore, we are probably considering the

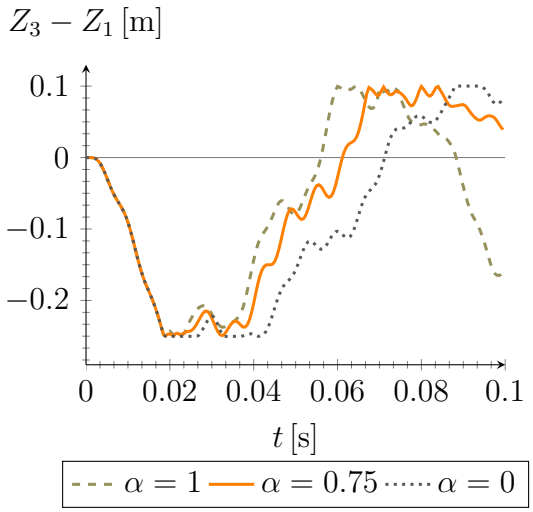

Figure 4.18. Relative displacement $Z_3 - Z_1$ of the piston with respect to the rigid load-bearing back structure. Influence of the coefficient of restitution α.

worst scenario, in which impacts can cause a catastrophic breakage of glass during free oscillations, despite a correct initial absorption. The coefficient of restitution plays a role in reducing the peaks since the lower it is, the higher is the dissipated energy. However, this effect is not of primary importance during the first impact.

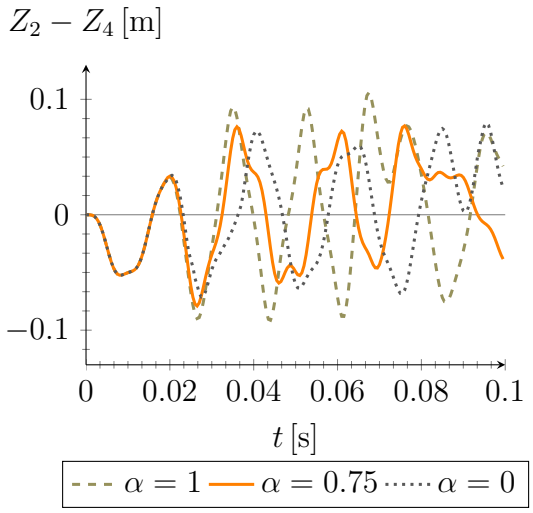

Figure 4.19. Out-of-plane displacement of panel $Z_2 - Z_4$. Influence of the coefficient of restitution α.

4.2.3 Influence of the load-bearing back structure

Several studies [20, 21, 109, 110, 111] have demonstrated that a compliant load-bearing back structure can limit the stress in the glass pane consequent to detonation waves. In the model problem, the role of the supporting system is interpreted by the stiffness k_1 and the mass m_1. In order to evaluate its influence, the time dependent response is calculated for $0 \leq t \leq 0.1\,\mathrm{s}$, for the following three different cases:

- *rigid support* $k_1 \to \infty$;
- *beam* support $k_1 = 8.45184 \cdot 10^6\,\mathrm{N/m}$ and $m_1 = 338.773\,\mathrm{kg}$;
- *cable* support $k_1 = 150 \cdot 10^3\,\mathrm{N/m}$ and $m_1 = 100\,\mathrm{kg}$.

We set $\bar{\Delta}^\ell = 0.25\,\mathrm{m}$, $F_{cr}^\ell = 50\,\mathrm{kN}$ and $\alpha = 1$; all the other material parameters are as before.

Fig. 4.20 shows the displacement Z_1 of the back structure, which is obviously null when this is rigid. A beam deflects much less than a cable, but the frequency of oscillation is higher, about twice. The time history of beam displacement presents a few angular points, corresponding to changes of the velocity $\dot{Z}_1$ due to the collision of the piston. The cable displacement is always smooth, meaning the effects of impacts are reduced.

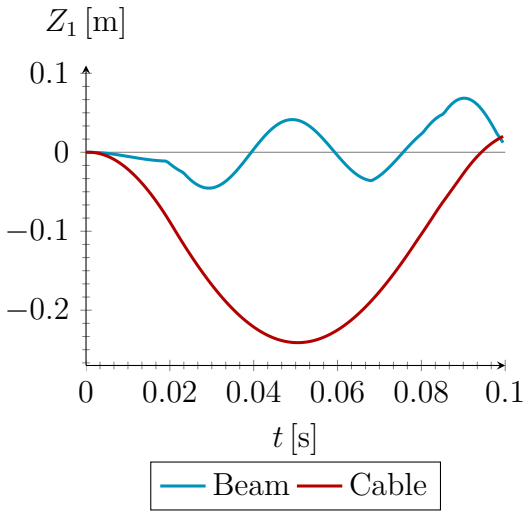

Figure 4.20. Influence of the load-bearing structure in terms of deflection Z_1.

The relative displacement $Z_3 - Z_1$ between the mobile piston and load-bearing structure is shown in Fig. 4.21. The solutions provided by the rigid and the beam

support are qualitatively analogous, in the sense that both of them attest the complete deformation of the shock absorbers in a comparable amount of time; furthermore the number of impacts, as well as their magnitude, are similar. The macroscopic difference between these two solutions consists in a little discrepancy between the trajectories: a rigid back structures anticipates the movement, i.e. the average velocity of the piston is higher. The solution for the cable totally differs from the others. The energy from the blast wave is largely absorbed by the deflection of the cable thanks to the lower stiffness k_1; consequently, the left shock absorber results unloaded. The right shock absorber is ineffective, because it does not even yield during the monitored time interval.

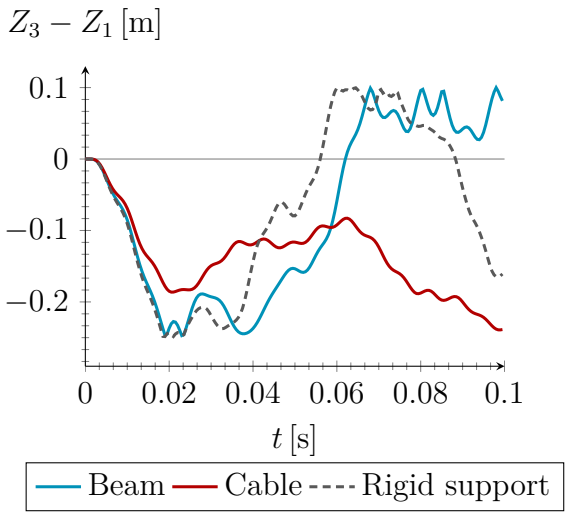

Figure 4.21. Influence of the load-bearing back structure for what concerns the relative displacement $Z_3 - Z_1$ between the piston and the structure itself.

The out-of-plane displacement $Z_2 - Z_4$ of the glass pane is visible in Fig. 4.22. The presence of the dissipative device in series with the spring k_2 produces similar results in all cases. For what concerns the first compression peak, all load-bearing structures are basically equivalent; potential advantages can only be achieved with dissipative devices. A similar conclusions holds for the subsequent suction peak, for which the trajectories are again very similar, except for the cable. Thanks to its high compliance, the cable can efficiently absorb the energy during the compression phase of a blast load, but since the piston does not activate the right shock absorber, the suction peak is not mitigated. In general, the rigid structure $k_1 \to \infty$ performs worse than the others, because it does not provide any contribution in absorbing the energy from the detonation wave. A cable structure excellently reduces the average deflection of panel during the dynamic response, but its inertia and stiffness should be optimized in order to reduce also the effects in suction phase. The beam provides

an intermediate effect, which is however very close to the case of rigid support.

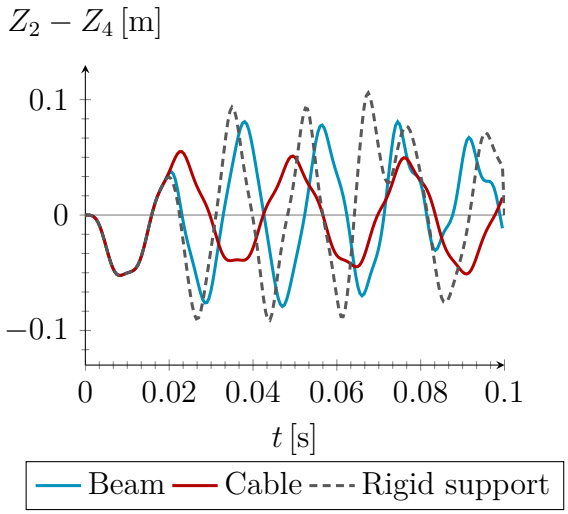

Figure 4.22. Influence of the load-bearing structure in terms of out-of-plane displacement of the glass panel $Z_2 - Z_4$.

4.3 The role of viscous dissipation

The capacity of devices based upon material yielding, considered in the previous Sections, is now compared to that of viscous dissipators, of the type proposed in [112] for structural applications in general, and more specifically to protect glazing curtain walls against explosions, as proposed in [113, 114].

4.3.1 Shock absorbers compared to viscous dampers

The mathematical description of the viscous dampers usually relies upon the definition of an *effective* damping coefficient, in order to collect all dissipative effects in a simple linear relationship between the viscous force and the relative velocity between two mobile elements. This is a simplified view of a complex phenomenon, which would require more sophisticated mathematical tools [115], but it is commonly accepted in the engineering practice. By following this description, consider the model problem of Fig. 4.23, where the lumped mass m_3 transmits, through a linear dashpot with damping coefficient c_2, the force $F_{31} = c_2(\dot{Z}_3 - \dot{Z}_1)$ to the load-bearing back structure of mass m_1. The mechanical properties of the glass plate remain as before; the supporting back structure is of the beam type, with the same values of m_1, k_1 and c_1 considered in Section 4.2.3. Equilibrium equations results

from Hamilton's principle, as in Section 4.1.5, but now the dissipation function to consider reads

$$\mathcal{R} = \frac{1}{2}c_1\dot{Z}_1^2 + \frac{1}{2}c_2(\dot{Z}_3 - \dot{Z}_1)^2. \tag{4.27}$$

Of course, in the expression (5.14) there is no contribution from the shock absorbers.

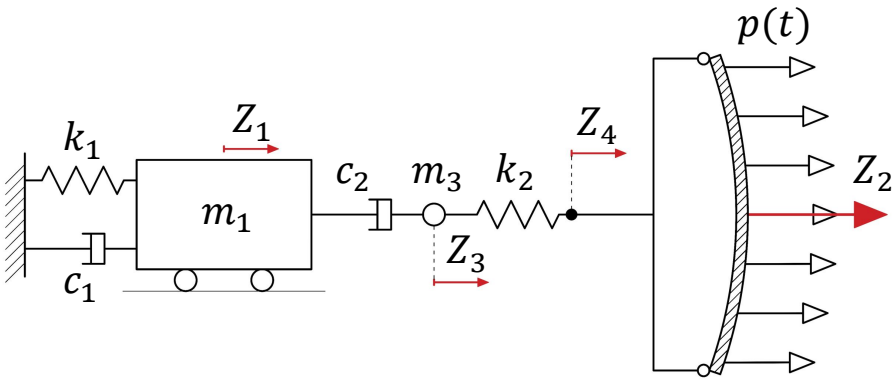

Figure 4.23. Schematic representation of the model problem where a linear viscous dashpot is used as the dissipative device.

The influence of the damping coefficient c_2 is evaluated with respect to the maximum stress $\sigma_{\max}$ in the glass pane and to the maximum relative displacement $Z_3 - Z_1$, representing the stroke of the dissipator, which are both subjected to technological limits. The first peaks of these quantities are recorded during the compression phase of blast action; note that, in general, they do not occur at the same instant. Fig. 4.24 shows the calculated values, respectively denoted with $\sigma_{\max}^{\text{v.d.}}$ and $|Z_3 - Z_1|_{\max}^{\text{v.d.}}$, as a function of c_2. As expected, $|Z_3 - Z_1|_{\max}^{\text{v.d.}}$ decreases with increasing c_2, because a high viscous resistance restrains the displacement under a short duration blast action. On the contrary, $\sigma_{\max}^{\text{v.d.}}$ increases, because most of the energy from the blast wave is absorbed by the plate deflection. Indeed, by increasing c_2, the response of the dashpot tends to that of a rigid link, represented by the limit $c_2 \to +\infty$ and providing asymptotically stationary values for $|Z_3 - Z_1|_{\max}^{\text{v.d.}}$ and $\sigma_{\max}^{\text{v.d.}}$, as can be guessed from the graphs of Fig. 4.24.

The time histories in terms of pane deflection $Z_2 - Z_4$ and related stress are compared with those obtainable with shock absorbers of the type previously considered (Fig. 4.4(a)), characterized by $\bar{\Delta}^{\ell} = 0.25\,\text{m}$, $F_{cr}^{\ell} = 50\,\text{kN}$ and $\bar{\Delta}^{r} = 0.1\,\text{m}$, $F_{cr}^{r} = 25\,\text{kN}$. In order to achieve comparable strokes for the dissipative devices, of the order of $|Z_3 - Z_1|_{\max} = 0.25\,\text{m}$, we set $c_2 = 10\,\text{kN·s/m}$, corresponding to a commercial motorbike damper. The corresponding graphs in terms of displacement and stress, are respectively juxtaposed in Figs. 4.25(a)-4.25(b) for the time interval

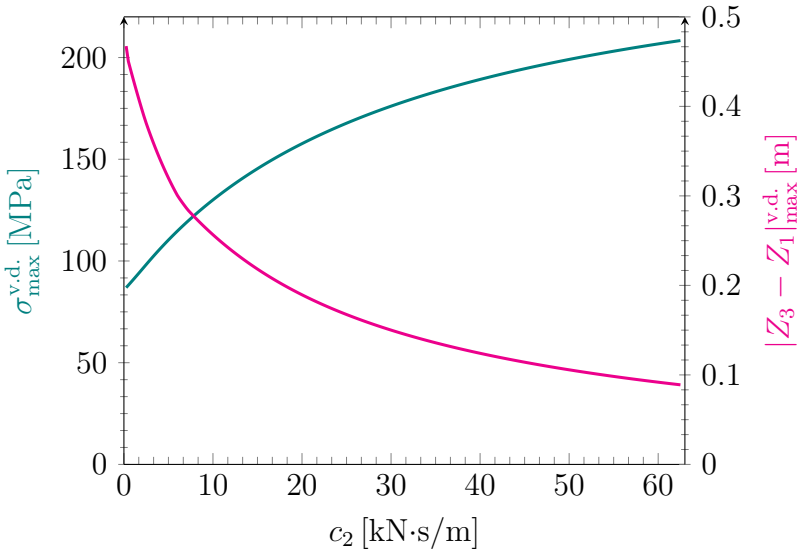

Figure 4.24. Effects of the viscous dissipative device. Peaks values of the stress in the glass pane $\sigma^{\text{v.d.}}_{\max}$, and of the dashpot stroke $|Z_3 - Z_1|^{\text{v.d.}}_{\max}$, obtained during the compression phase of the blast wave, plotted as functions of the damping coefficient c_2.

$0 \leq t \leq 0.05\,\text{s}$. Observe that shock absorbers are more efficient than viscous dampers in mitigating the effects of the explosion during the first compression phase, but the opposite is true for the subsequent free oscillations. In particular, the impacts between the moving piston and the shock absorbers at the stroke end produce the amplification of the panel deflection, especially when the coefficient of restitution is $\alpha = 1$. On the other hand, a viscous dampers dissipates energy, and consequently smoothen out the successive oscillations. In conclusion, both devices are effective, but their role is prominent in two distinct stages of the dynamic response.

4.3.2 A hybrid dissipation method

It is logical to conclude that the optimal compromise consists in coupling in parallel both a shock absorber and a viscous damper: the former mitigates the first blast impulse, while the latter can constraint the subsequent free oscillations, avoiding further peaks of stress. The model problem for such a hybrid dissipation device is represented in Fig. 4.26.

This integrated dissipation method should reduce the stress state in glass on average, and impart a more "regular" time-dependent response preventing amplification phenomena due to impacts. To illustrate, we assume a rigid back structure, a coefficient of restitution $\alpha = 1$ and we keep as constants the mechanical properties of the right shock absorber ($F^r_{cr} = 25\,\text{kN}$ and $\bar{\Delta}^r = 0.1$ m). Fig. 4.27(a) shows

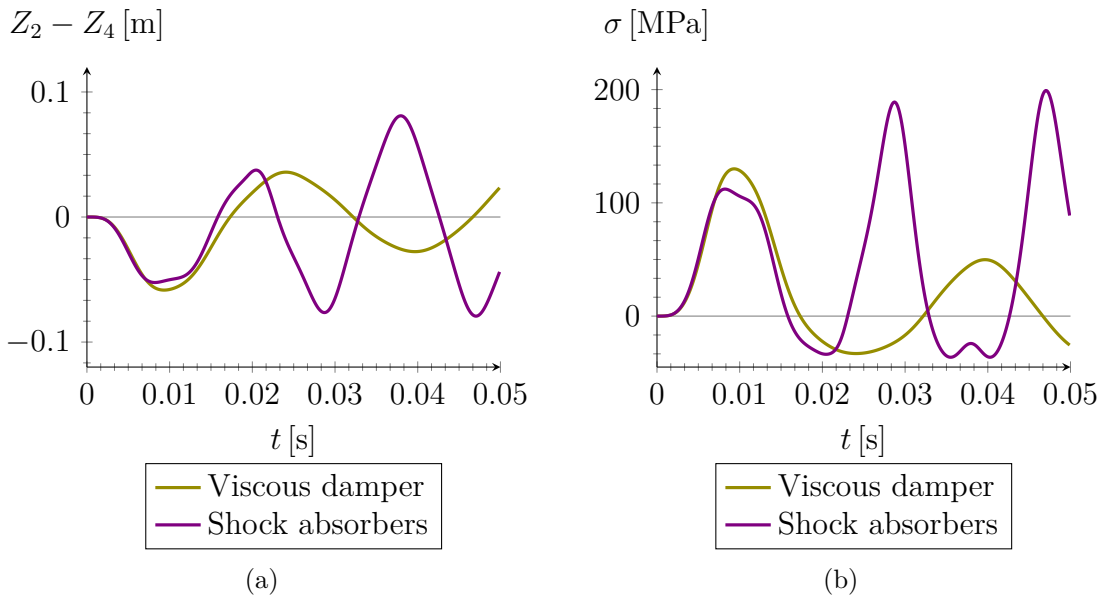

Figure 4.25. Comparison between viscous damper and shock absorbers. Time-histories in terms of (a) out-of-plane deflection $Z_2 - Z_4$ of the glass plate and (b) corresponding stress σ at its center.

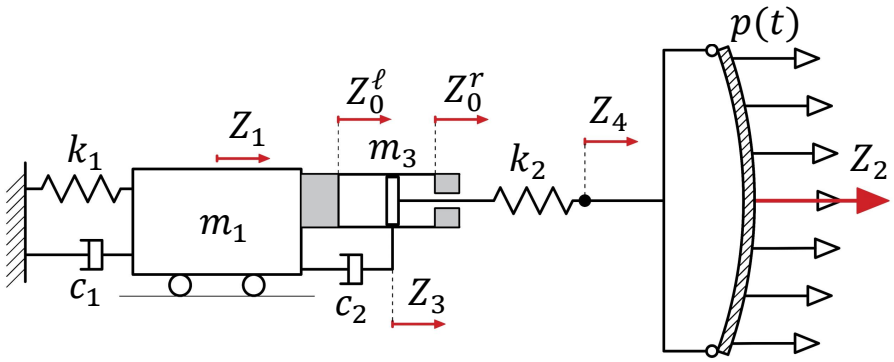

Figure 4.26. Schematic representation of the model problem employing a hybrid dissipative device, composed by a viscous damper coupled in parallel with shock absorbers.

the calculated first peak of the out-of plane displacement $|Z_2 - Z_4|_{\max}$, attained at the end of the compression phase of the blast wave, as function of F_{cr}^ℓ, $\bar{\Delta}^\ell$ and c_2: the three-dimensional volume is colored according to the value of $|Z_2 - Z_4|_{\max}$ reported in the legend. Most of the aspects already discussed for case of the sole shock absorber remain valid: a long stroke $\bar{\Delta}^\ell$ maximizes the absorption of energy when associated with a low yielding limit F_{cr}^ℓ, in order to let the panel accommodate

with its displacement the effect of the pushing blast wave. For what concerns the role of damping, the minimum deflection is obtained with $c_2 \to 0$ because, certainly, the damping refrains the movement of the glass pane. Indeed, the first deflection peak is always increased by the viscous forces, which represent an obstacle to the movement of the glass pane.

It should be remarked, however, that an increase of the damping coefficient reduces the demand in terms maximum stroke of the dissipative device. This is more clear in Fig. 4.27(b), which represents the intersection of the colored volume with planes $c_2 = const$. The step that, as indicated in Fig. 4.15, delimits the optimal domain for the properties of the shock absorber in the $F_{cr}^{\ell} - \bar{\Delta}^{\ell}$ plane, approaches lower values of $\bar{\Delta}^{\ell}$ when c_2 increases. This means that a viscous damper is very effective when there are design constraints that limit the size of the dissipative device, for example $\bar{\Delta}^{\ell} \leq 0.1\,\mathrm{m}$. If a design with $\bar{\Delta}^{\ell} \geq 0.2\,\mathrm{m}$ is allowed, the viscous damper has a very little effect in limiting the first peak of stress but, in any case, it controls the subsequent oscillations in which analogous (or bigger) values can be attained.

In order to appreciate the potential advantages of the various dissipation methods, we now compare the corresponding time-dependent responses when the supporting structure is of the beam type, as defined in Section 4.1.2. The following three types of dissipative devices are considered.

- **Integrated hybrid device**

  Dissipation is shared between a unit composed of two shock absorbers and one viscous damper, disposed in parallel as per Fig. 4.26. Mechanical parameters for the shock absorbers are $F_{cr}^{\ell} = 50\,\mathrm{kN}$, $\bar{\Delta}^{\ell} = 0.1\,\mathrm{m}$ and $F_{cr}^{r} = 25\,\mathrm{kN}$, $\bar{\Delta}^{r} = 0.05\,\mathrm{m}$, so as to limit the size of the device. The damping coefficient is $c_2 = 10\,\mathrm{kN{\cdot}s/m}$, as for a commercial motorcycle damper.

- **Shock absorbers**

  Energy is dissipated by the plastic yeilding of two shock absorbers, according to the scheme of Fig. 4.4(a). Mechanical properties are the same as before, i.e., $F_{cr}^{\ell} = 50\,\mathrm{kN}$, $\bar{\Delta}^{\ell} = 0.1\,\mathrm{m}$ and $F_{cr}^{r} = 25\,\mathrm{kN}$, $\bar{\Delta}^{r} = 0.05\,\mathrm{m}$.

- **Viscous damper**

  One viscous damper connects the load-bearing to the glass pane, as indicated in Fig. 4.23. The selected damping coefficient is $c_2 = 55\,\mathrm{kN{\cdot}s/m}$, in order to limit the relative displacement $|Z_3 - Z_1| \leq 0.1\,\mathrm{m}$ as in previous cases. This corresponds to approximately five motorcycle dampers disposed in parallel.

Results for the three aforementioned cases are collected in Fig. 4.28.

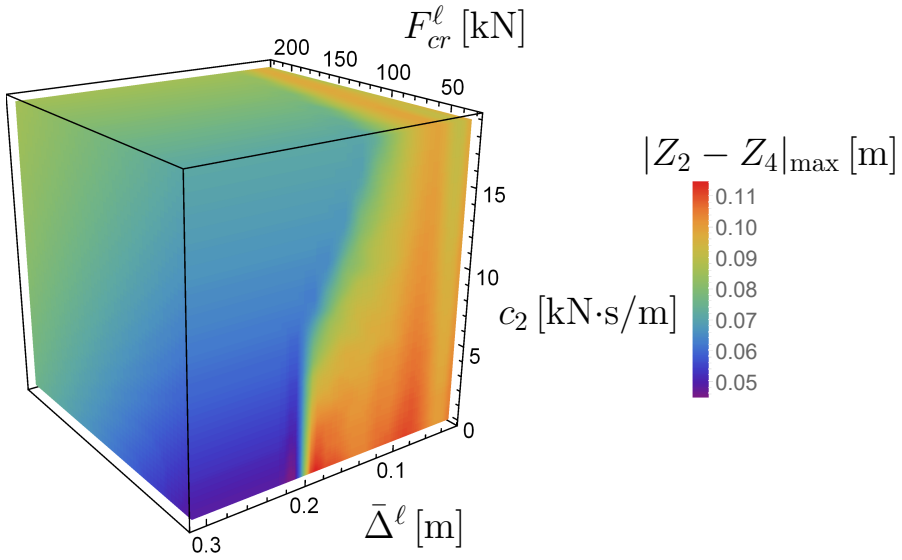

(a)

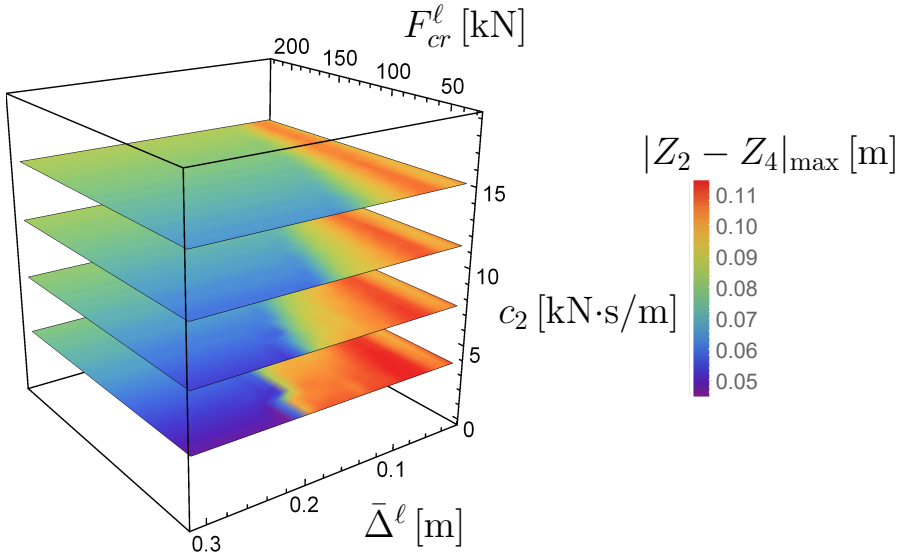

(b)

Figure 4.27. Maximum out-of-plane displacement of panel $|Z_2 - Z_4|_{\max}$ during the compression phase represented as a function of $\bar{\Delta}^{\ell}$, F_{cr}^{ℓ} and c_2, for a rigid load-bearing back structure. (a) Volume representation and (b) its intersection with planes $c_2 = \text{const}$.

Fig. 4.28(a) shows the displacement Z_1 of the back structure. The *hybrid device* is certainly the one that limits, better than the others, the deformation, and consequently, the bending stress in the supporting skeleton of the façade. Remarkably, this solution minimizes (in absolute terms) both the first and the subsequent peaks. The sole *viscous damper* limits the number of the oscillations, but the second peak is comparable to the first one. *Shock absorbers* alone provide the worst scenario, essentially because of the collisions of mobile piston that impart impulsive forces further deflecting the back structure.

These impacts are clearly recognizable in Fig. 4.28(b), which represents the relative displacement $Z_3 - Z_1$ between the piston and back structure, coinciding with the stroke of the piston within the dissipative unit. Of course, no collision occurs for a *viscous damper*, as evidenced by the graph that smoothly decays to zero. The *hybrid device* represents a compromise: both of shock absorbers reach the corresponding stroke ends, but the damper reduces the number and amplitude of the bounces.

The deflection of the glass pane $Z_2 - Z_4$ and the corresponding stress σ at its center are respectively shown in Figs. 4.28(c) and 4.28(d). The two representations are complementary to each other and can be discussed together. Observe that, in general, the successive peaks may be more dangerous than the first one, occurring at the end of the pressure phase of the blast action. The *hybrid device* is very effective in limiting all the peaks: the stress in glass never exceeds 150 MPa during the whole time history. A single *viscous damper* provides good results, but is less effective than shock absorbers in limiting the state of stress during the first peak, since the stress approaches the value $\sigma = 200\,\text{MPa}$.

For the case at hand *shock absorbers* alone do not perform well, essentially because their plastic capacity in terms of displacement is too small to avoid dangerous impacts. In particular, the left shock absorber crushes when $t \simeq T_d$, so that the suction phase of the blast wave increases the counter-deflection of the glass plate. The corresponding stress in glass (green line) overcomes the limit 200 MPa in proximity of the first and third impact. Indeed, in the presented simulation the parameter $\bar{\Delta}^\ell$ has been chosen to be very small in order to highlight the comparison with the hybrid device;it is too small to avoid collisions that can drastically amplify the plate deflection. In conclusion, it is of paramount importance to optimize the mechanical properties of shock absorbers, but the addition of a viscous damper adds an additional degree of freedom in the design process, which allows a much finer optimization of the dissipative device aimed at safeguarding the integrity of glass.

4.3.3 Concept design of a hybrid dissipative device

The previous analyses have shown that the combination of two dissipative methods can maximize the subtraction of energy from the system and safeguard the structural

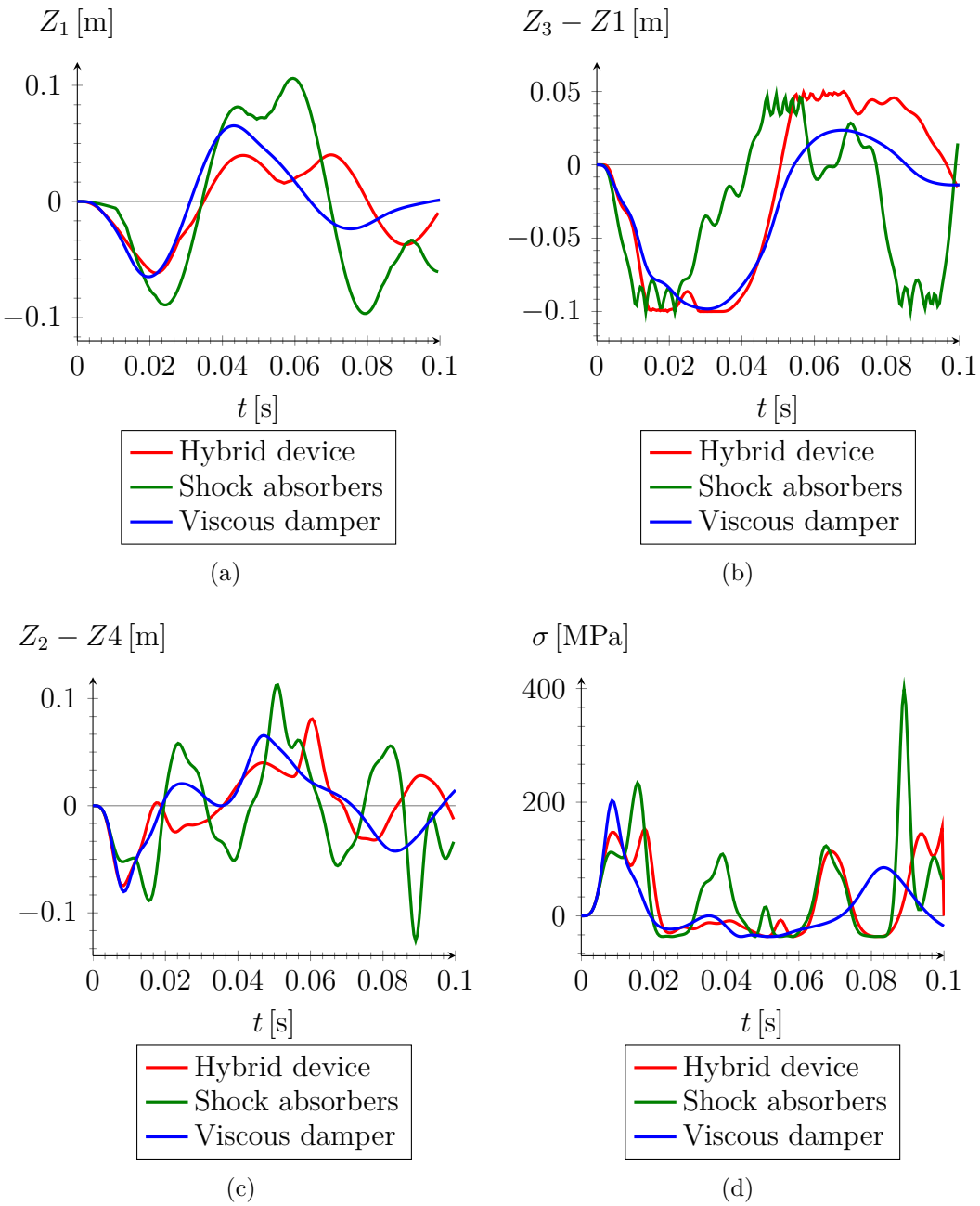

Figure 4.28. Comparison among three different types of dissipation devices: *integrated hybrid device*, *shock absorbers* and *viscous damper*. (a) Deflection Z_1 of the back structure; (b) stroke $Z_3 - Z_1$ of the dissipative unit; (c) out-of-plane displacement $Z_2 - Z_4$ of the glass pane; (d) maximum stress at the center of the glass pane.

integrity of glazing. Ideally one should employ crushing components in parallel with viscous dampers, in order to get the advantages of both mechanisms: yielding allows to limit the first stress peaks due to the impacting pressure wave; in a complementary way, viscous dampers are suitable to limit the subsequent free oscillations. Here, we illustrate a prototype for such a dissipative device. Of course there are innumerable alternative solutions.

Consider a mobile piston placed inside a cylinder, which goes in contact with two shock absorbers (made of aluminium honeycomb or aluminium foam); they collapse when the compression force exerted by the piston overpasses their yielding threshold. The empty volume inside the honeycomb cells is filled with oil or silicone fluid, which is spilled through a hole expressly prepared on the cylinder wall. When an impulsive load invests the panels, the mobile piston almost instantly compresses both shock absorbers and the presence of the fluid provides for a viscous resistance. In general, we believe that immersing the honeycombs into a fluid permits to maintain the device very compact; however, the global size should be set on the basis of project requirements. We emphasize the importance to design the correct type of seals, plugs, etc. to prevent the fluid leak and, at the same time, let the piston freely slide. The piston shall present orifices to let the fluid flow inside the whole cylinder when it is called to move. If a double-rod shaft is employed, it is not necessary the presence of any compensation chamber.

The dissipative device must be installed between the panels and the rear structure: on one side, the mobile piston is linked (for example by means of a threaded connection) to four adjacent panes; on the other side, two metal plates are welded to the back structure, in order to support the cylinder. There are several configurations that a glazed façade can assume. If we focus our attention on beam supported façades, it is possible to distinguish two main cases as shown in Fig. 4.29. On the left hand side, the panels are contoured by silicone (it does not offer any resistance) and the boundary constrains are punctually applied. In fact, the panels are linked together by a spider connector, constraining one corner of each panel through a rotule. On the right hand side, the panels are contoured by a rigid frame, which impedes any displacement (in the out-of-plane direction) along their perimeter. This is the case considered before, inasmuch the adopted shape function is null at the boundary of panel.

This prototype unifies two dissipation methods in one single device, whose purpose is to uncouple the relative motion between panels and rear structure, in order to dissipate energy during a bomb blast event. As a possible disadvantage, we recall its volumetric footprint (especially if not optimized) and the risk of oil leak. Nevertheless, we believe that such technical solution represents an optimal compromise among the existing dissipative technologies, employed in blast resisting façades.

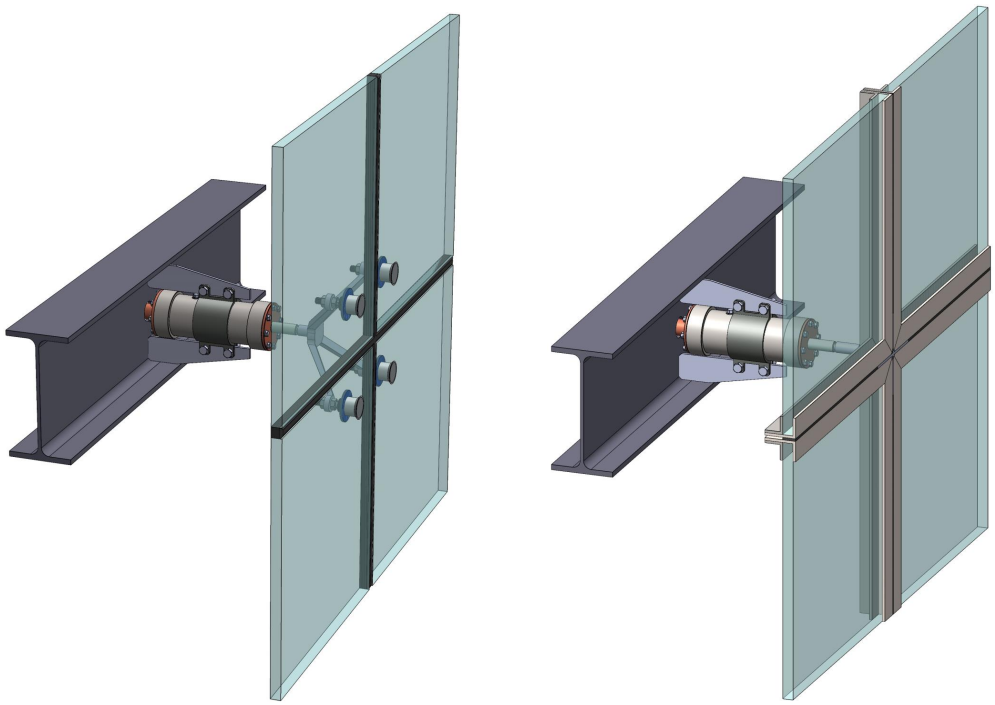

Figure 4.29. Hybrid dissipative device employed in different configurations.

Chapter 5

The role of the rear load-bearing structure

A proper design of the rear load-bearing structure can mitigate explosive actions and reduce the maximum stress to which panels are subjected. Preliminary investigations, relying upon an elementary linear elastic modelling [20], have shown that cable-supported façades perform much better than mullion and transom structures, because they are more compliant and, for this reason, they can absorb much of the energy from impulsive loads, as attested by J. Schlaich et al. [22]. In general, experimental activity does not allow to clearly highlight the role of several components, since most testing devices only assess the structural capacity of panes. For this reason, a lumped element model is proposed (geometric nonlinearities are taken into account) to provide a synthetic view of global dynamic response, addressed to optimize the back structure in terms of stiffness and inertia.

A paradigmatic case study models a cable-supported façcade; subsequently the analytical solution is compared with that obtained via finite element (FE) method. As a second step, parametric analyses are performed in order to furnish a general guide for the optimal design of bomb blast resisting façades. The rear supporting structure is oriented towards absorbing the energy released by the loading action, with the aim to safeguard the glass and limit the axial tensile force in the cable. The stiffness of the rear structure, possibly modified by a adding a spring element in series, is the key parameter to tune the global dynamic response. Moreover, the supporting cable may be ballasted to achieve the optimal inertia. Of course, this solution shall respect all technological requirements under design actions (e.g., wind), especially in terms of deformability. Further comparisons with the results from linearized analysis highlight advantages and drawbacks of such simplified approach [21].

5.1 Lumped element model of a cable-supported façade

5.1.1 Case study

Consider a façade composed of horizontal rows of rectangular glass panels, connected to vertical supporting elements. The façade is supposed very wide, so that one can consider only one glazed column linked to a vertical element, as represented in Fig. 5.1. Each glass panel is supposed to be contoured by a secondary frame, assumed to be rigid, which is in turn connected to the rear load-bearing structure. Although the frames should be fixed to the vertical structure at corner points, a fictitious one point connection is considered in correspondence of the center, further supposing that also the mass of vertical rear structure is lumped at such fixation points.

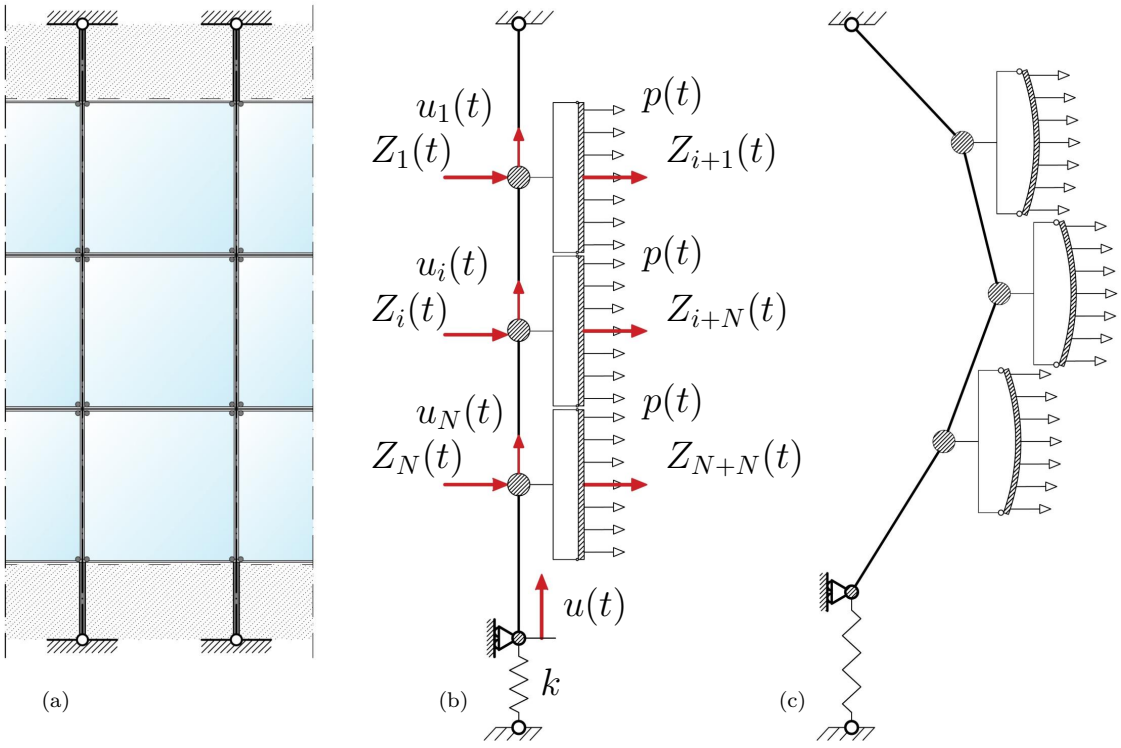

Figure 5.1. Case study: (a) façade composed of N horizontal rows of glass panels; (b) the (undeformed) simplified $(2N + 1)$ DoF model; (c) deformed configuration of the model.

The blast load is supposed to develop an out-of-plane uniformly distributed force per unit area $p(t)$ on the panels surface. This is described through Friedlander relation in the form

$$p(t) = -p_r\left(1 - \frac{t}{T_d}\right)e^{-\frac{\beta}{T_d}t}, \tag{5.1}$$

where, for the case at hand, $\beta = 0.82$ is the decay parameter, the time positive duration is $T_d = 0.025\,\mathrm{s}$ and the initial pressure peak is $p_r = 50\,\mathrm{kPa}$. These values can be obtained by an analytical or experimental procedure, as indicated in [36, 98]; our choice is such that they are very similar to those used in the experimental campaign of Larcher et al. [116]. Friedlander equation prescribes compression (negative force per unit area), followed by suction pressure (positive force per unit area) when $t \geq T_d$, as represented in Fig. 5.2 with light blue line.

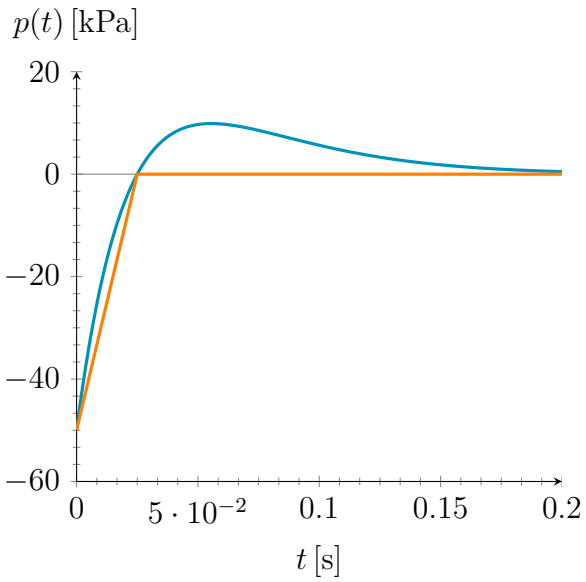

Figure 5.2. Time dependent force per unit area $p(t)$ consequent to a reflected blast wave: Friedlander equation (light blue line) and its linearized form (orange line).

The Friedlander equation is commonly adopted to describe blast loading on a plane surface [14, 116, 10], but sometimes it is simplified in the engineering applications, by just considering the compression phase and neglecting the subsequent suction phase. Moreover, the negative part of the exponential form is often linearized within the interval $(0, T_d)$ by maintaining as constant the value of the peak pressure[1], so to obtain the bi-linear graph represented in orange color in Fig. 5.2. In the engineering practice, the suction pressure phase is somehow reputable capable of "mitigating"

[1]Sometimes the linearization is done by maintaining as constant also the compression impulse. Here, we do not change the duration T_d, therefore the compression impulse is slightly reduced.

the pressure peak, because of the difference in sign. However, this simplification may be not on the safe side.

More precisely, it is useful to calculate the Fourier transform of the pressure time history. Fig. 5.3 presents three curves that correspond to the magnitude-frequency diagrams corresponding to: (*i*) the complete Friedlander equation (2.1), (*ii*) the linearized compression phase and (*iii*) the compression phase only of Friedlander equation, i.e. $p(t) = 0$ for $t > T_d$. Observe that the complete expression (2.1) exhibits, with respect to the others, a higher peak between 15 Hz and 40 Hz. This is due to the fact that the sequence of the negative and positive phases may be associated with a "complete cycle", whose frequency is of the same order of $1/T_d$. On the other hand, the curves overlap in practice for the higher frequencies, even if the linear approximation (*iii*) slightly overestimates the response between 15 Hz and 40 Hz. Since part of the structure may have a resonant response at the lowest frequencies, we consider correct to consider, in our simulations, the complete blast wave, thus not neglecting the suction pressure phase. This is in accordance with Teich et al. [46], which highlights how the failure might occur in opposition with the principal design load direction (e.g., wind), because the suction phase sometimes affects the structural integrity of façade.

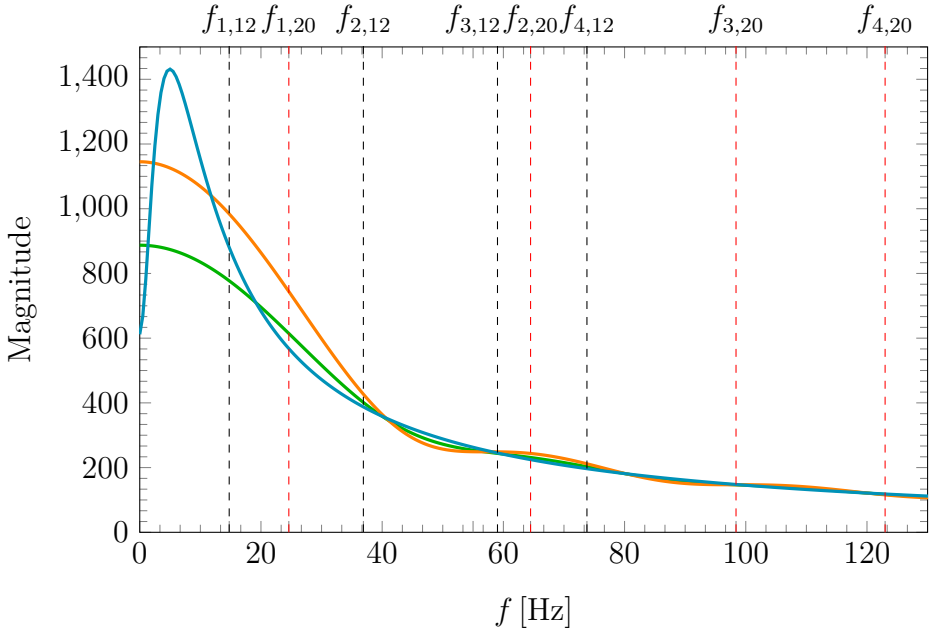

Figure 5.3. Magnitude-frequency diagram corresponding to the Fourier transform of: Friedlander equation (light blue); the linearized compression phase (orange); only the compression phase ($0 \leq t \leq T_d$) in Friedlander equation (green).

We anticipate that each glass panel is a vibrating plate, which will be reduced to

a nonlinear 1-DoF (Degrees of Freedom) oscillator by assuming, as per Rayleigh's method [70], a proper shape function for the deflection. This will be selected according to the first vibration mode of the corresponding plate, by considering the noteworthy geometric nonlinearities that induce membrane stresses. However, a rough first-order estimate of the interaction with the blast wave can be obtained by considering the linearized model for the vibrating glass panels.

Consider then a monolithic[2] glass panel with dimensions $a \times b \times s$, where s is the thickness, supposed simply supported at the borders. Its natural frequencies are denoted with $f_{j,s}$, where $j = 1,2,\dots$ is the mode number and s is the thickness of panel (expressed in millimeters). We calculate $f_{j,s}$ with the classic relationship for Kirchhoff-Love plate theory [45], which reads

$$f_{j,s} = \frac{\pi}{2}\left(\frac{m^2}{a^2} + \frac{n^2}{b^2}\right)\sqrt{\frac{E_g s^3}{12(1-\nu^2)\mu}}, \tag{5.2}$$

where m and n are integers that determine the mode number, E_g and ν are the Young's modulus and Poisson's ratio for glass, respectively, and μ is the mass per unit area of panel. Setting $E_g = 70 \cdot 10^9$ Pa, $\nu = 0.22$, $\mu = 2500\,\mathrm{kg/m^3} \cdot s$, $a = b = 2$ m, $s = 12$ mm or $s = 20$ mm, in agreement with the simulations of the forthcoming Sections, representative values of $f_{j,s}$ are evidenced with vertical lines in Fig. 5.3.

The first and fourth modes are the ones that are prone to be excited, probably because their geometrical shape is such to maximize the work from the action. The graphs of Fig. 5.3 suggest that the first mode of vibration is dominant in response to the blast wave, whereas the frequencies for the fourth modes are located on the right hand side of the abscissae. The more the panel is thick, the more the fourth mode is negligible with respect to the first mode, with a quantitative estimation that is expressed by the intersections of the Fourier's graphs with the vertical lines $f = f_{j,s}$, $j = 1,4$. These considerations justify, albeit tentatively at this stage, our choice to model the panel with a 1 DoF oscillator associated with the first mode: the approximation is the more accurate, the thicker the panel is.

The rear load-bearing structure is a cable, whose stiffness is determined by three factors: the tensile axial force in the rest position, its cross section, and the Young's modulus of the material. Moreover, as represented in Fig. 5.1, the cable is connected in series with a spring, which can be tuned to modify its stiffness if needed. This possibility will be investigated in the following Sections.

The Lagrangian variables of the model are also indicated in Fig. 5.1. Any configuration is defined by $3N + 1$ scalar functions of time, i.e.

[2]The case of laminated glass panels may be handled in a similar way by considering the deflection effective thickness [117, 118], i.e. the thickness of a monolith with equivalent bending properties in terms of deflection.

- the horizontal displacements $Z_i(t)$, with $i = 1, \dots, N$ of the points of the rear structure, to which the glass panels are ideally connected;
- the horizontal displacements $Z_{i+N}(t)$, with $i = 1, \dots, N$ of the centroids of the panels, which completely define, through the assumed shape function, the out-of-plane displacement of the other points.
- the vertical displacements $u_i(t)$ with $i = 1, \dots, N$ of the centroids of the glass panels, which coincide with the displacements of the points where the panels are connected to the cable.
- the elongation of the spring $u(t)$.

The equations of motion can be derived from Hamilton's principle once the kinetic energy, the potential energy and the work performed by the external forces are determined.

5.1.2 Nonlinear model of rear structure and panels

In the vertical reference configuration of Fig. 5.1(b), the length of cable L, supporting N identical panels, is supposed to be $L = (N + 1)h$, where h is the distance between two consecutive lumped mass. Observe that L slightly exceeds the total measure of the panels to take into account the clearance for the anchoring devices. The panels are of size $2 \times 2\,\mathrm{m}^2$ and $h = 2.05\,\mathrm{m}$ to take into account the gap for the silicone gaskets. We consider the cases $N = 3$ with $L = 8.2\,\mathrm{m}$, and $N = 6$ with $L = 14.35\,\mathrm{m}$. The cable is a steel rope (Young's modulus $E_c = 160 \cdot 10^9\,\mathrm{Pa}$) with diameter $d = 25\,\mathrm{mm}$. The lumped masses for the rear structure, denoted by m_i for $i = 1, \dots, N$, are calculated by assuming that the mass of cable comprised between two nodes is equally distributed between the nodes themselves: if the mass per unit length of the cable is $m_c = 3\,\mathrm{kg/m}$, then $m_i = m_c \cdot h$. However, we leave the possibility open that the cable can be ballasted to achieve an optimized inertia, i.e. m_i may also incorporate the artificially added extra weight .

The axial tensile force of cable, which determines its stiffness, may change during the motion because of cable elongation and spring deformation. The actual length of cable L_f depends upon the displacement of nodes, represented in Fig. 5.4, and it reads

$$L_f = \sqrt{Z_1^2 + (h - u_1)^2} + \sum_{i=2}^{N} \sqrt{(Z_i - Z_{i-1})^2 + (h + u_{i-1} - u_i)^2} + \sqrt{Z_N^2 + (h - u)^2}. \quad (5.3)$$

In general, we assume that $u_i(t) \ll Z_i(t)$ and that $\dot{u}_i(t) \ll \dot{Z}_i(t)$. This means that in the expression of kinetic energy the contribution due to the vertical movement of nodes is negligible. Moreover, in order to reduce the degrees of freedom, it seems reasonable to assume that the vertical elongation of the spring $u(t)$ is linearly distributed along the cable, thus

$$u_i = \frac{i}{N+1}\, u(t), \qquad \text{with } i = 1, \ldots, N. \tag{5.4}$$

This hypothesis is a constraint that slightly increases the stiffness of vibrating system, but the forthcoming comparison with a FE model will confirm that this error is limited.

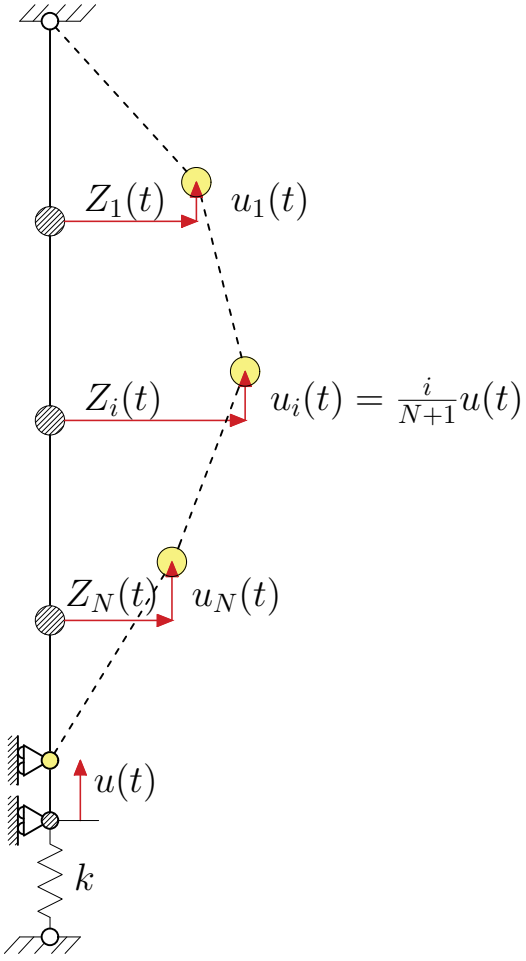

Figure 5.4. Lagrangian variables for the deformation of the cable.

The elastic energy of cable reads

$$\mathcal{U}^R = T_0(L_f - L) + \frac{1}{2}\frac{E_c A}{L}(L_f - L)^2 + T_0 u + \frac{1}{2}ku^2, \tag{5.5}$$

where T_0 is the initial pretension, $A = \pi d^2/4$ is the cross sectional area and k is the constant of spring.

For the i^{th} glass panel, with $i = 1, \ldots, N$, consider a reference system (x_i, y_i) with origin at one of its four corners and axes parallel to the borders, so that the reference domain for the panel is $0 \leq x_i \leq a$ and $0 \leq y_i \leq b$. We reduce its dynamic behavior to a single DoF oscillator by calculating the out-of-plane displacement field $w_i(x, y, t)$ through the approximation

$$w_i(x, y, t) \simeq \Big(Z_{i+N}(t) - Z_i(t)\Big)\psi(x, y) \quad \text{with } i = 1, \ldots N, \tag{5.6}$$

where, consistently to the form of the first vibration mode, $\psi(x, y) = \sin\Big(\pi x/a\Big)\sin\Big(\pi y/b\Big)$ is the shape function and $Z_{i+N}(t) - Z_i(t)$ is the time dependent relative displacement between the generic lumped mass on the cable, coinciding with the fixation point, and the displacement of the panel centroid, which represents the maximum deflection.

Due to the great amount of energy transmitted by the blast-wave, we expect that $Z_{i+N}(t) - Z_i(t)$ is large in comparison with plate thickness. As a consequence, it is necessary to consider membrane effects, by using the von Kármán plate theory [101, 63]. This requires to find the in-plane stress function $\varphi_i(x, y, t)$ for the i^{th} panel. With respect to the aforementioned reference system, the membrane stresses read

$$\bar{\sigma}_x = \frac{\partial^2 \varphi_i(x, y, t)}{\partial y^2}, \tag{5.7a}$$

$$\bar{\sigma}_y = \frac{\partial^2 \varphi_i(x, y, t)}{\partial x^2}, \tag{5.7b}$$

$$\bar{\tau}_{xy} = -\frac{\partial^2 \varphi_i(x, y, t)}{\partial x \partial y}. \tag{5.7c}$$

We follow the approximate procedure described in [103] based on Fourier expansion, to analytically calculate the stress function. By using for φ_i the first two terms of the series, we obtain the second order function

$$\varphi_i(x, y, t) \simeq \Big(Z_{i+N}(t) - Z_i(t)\Big)^2 \cdot \left[\frac{E_g}{32(b^2/a^2)}\cos\left(\frac{2\pi x}{a}\right) + \frac{E_g}{32(a^2/b^2)}\cos\left(\frac{2\pi y}{b}\right)\right], \tag{5.8}$$

where $Z_{i+N}(t) - Z_i(t)$ provides the time dependence. By using (5.8), one readily obtains

$$\bar{\varepsilon}_x = \frac{1}{E}\left(\frac{\partial^2\varphi_i(x,y,t)}{\partial y^2} - \nu\frac{\partial^2\varphi_i(x,y,t)}{\partial x^2}\right), \tag{5.9a}$$

$$\bar{\varepsilon}_y = \frac{1}{E}\left(\frac{\partial^2\varphi_i(x,y,t)}{\partial x^2} - \nu\frac{\partial^2\varphi_i(x,y,t)}{\partial y^2}\right), \tag{5.9b}$$

$$\bar{\varepsilon}_{xy} = -\frac{2(1+\nu)}{E}\frac{\partial^2\varphi_i(x,y,t)}{\partial x\partial y}. \tag{5.9c}$$

The curvatures of plate depend upon the out-of-plane displacement field and they may be approximated as

$$\chi_x = -\frac{\partial^2 w_i(x,y,t)}{\partial x^2}, \tag{5.10a}$$

$$\chi_y = -\frac{\partial^2 w_i(x,y,t)}{\partial y^2}, \tag{5.10b}$$

$$\chi_{xy} = -\frac{\partial^2 w_i(x,y,t)}{\partial y\partial x}. \tag{5.10c}$$

Therefore, from (5.9) and (5.10), the elastic energy of the i^{th} glazed panel reads

$$\begin{aligned}\mathcal{U}_i^P = &\frac{E_g s}{2(1-\nu^2)}\int_0^a\int_0^b (\bar{\varepsilon}_x+\bar{\varepsilon}_y)^2 - 2(1-\nu)(\bar{\varepsilon}_x\bar{\varepsilon}_y - \bar{\varepsilon}_{xy}^2)\,dxdy \\ &+ \frac{E_g s^3}{24(1-\nu^2)}\int_0^a\int_0^b (\chi_x+\chi_y)^2 - 2(1-\nu)(\chi_x\chi_y - \chi_{xy}^2)\,dxdy,\end{aligned} \tag{5.11}$$

where the contributions of membrane and bending strains are well separated in the sum. Damping phenomena are not considered, on the safe side, since we are interested in the peak strains in glass during the first (compression) phase of blast loading. We can demonstrate that, under the aforementioned assumptions, the response of a panel coincides with that of a quasi-linear oscillator of the Duffing type, where the nonlinear (cubic) term results from the membrane deformation.

The potential energy of the whole system is associated with the elastic deformation of both rear structure and glass panels, i.e.

$$\mathcal{U} = \mathcal{U}^R + \sum_{i=1}^{N}\mathcal{U}_i^P. \tag{5.12}$$

The kinetic energy for the system is written by taking into account the effective mass of panels through the shape function $\psi(x, y)$, in the form

$$\mathcal{K} = \sum_{i=1}^{N} \frac{1}{2}\rho s \cdot \int_0^a \int_0^b \left[(\dot{Z}_{i+N} - \dot{Z}_i) \sin\left(\frac{\pi x}{a}\right) \sin\left(\frac{\pi y}{b}\right) + \dot{Z}_i \right]^2 dxdy + \frac{1}{2} m_i \dot{Z}_i^2 \,, \quad (5.13)$$

where, as stated before, the contribution of the vertical displacement of the nodes has been neglected.

The work performed by the blast load $p(t)$, whose time dependence is expressed by (2.1), is calculated by multiplying this force per unit area for the out-of-plane displacement of panel, and it reads

$$\mathcal{W} = \sum_{i=1}^{N} p \int_0^a \int_0^b \left[(Z_{i+N} - Z_i) \sin\left(\frac{\pi x}{a}\right) \sin\left(\frac{\pi y}{b}\right) + Z_i \right] dxdy. \quad (5.14)$$

The equilibrium equations, which govern the nonlinear dynamic response of the façade, are obtained via Hamilton's principle in the form

$$\begin{cases} \dfrac{\mathrm{d}}{\mathrm{d}t}\left(\dfrac{\partial \mathcal{K}}{\partial \dot{Z}_i}\right) + \dfrac{\partial \mathcal{U}}{\partial Z_i} = \dfrac{\delta \mathcal{W}}{\delta Z_i} \,, \\ \\ \dfrac{\partial \mathcal{U}}{\partial u} = 0 \,, \end{cases} \quad (5.15)$$

with $i = 1, \ldots, 2N$. This is a nonlinear system of $2N$ differential equations and 1 algebraic equation, associated with the presence of the spring.

The system (5.15) is numerically solved with the finite difference method under the initial conditions

$$Z_i(0) = 0, \quad u(0) = 0, \quad (5.16a)$$
$$\dot{Z}_i(0) = 0, \quad \dot{u}(0) = 0 \,. \quad (5.16b)$$

These indicate that the façade is at rest before being invested by the blast load.

5.2 Dynamic response

With the purpose to validate the model proposed, we compare the analytical solution with that obtained with `Straus7` (a commercial FE software).

5.2.1 Isolated panel

Firstly we focus our attention on an isolated panel, with all the edges constrained in the out-of-plane direction, but free to move in-plane. The panel is monolithic, of size $a \times b \times s = 2 \times 2 \times 0.020 \quad \mathrm{m}^3$, whose mechanical properties correspond to that of float glass (Young's modulus $E_g = 70\,\mathrm{GPa}$, Poisson's ratio $\nu = 0.22$, density $\rho = 2500\,\mathrm{kg/m}^3$). Its thickness has been selected in order to keep the maximum stress below the glass strength, of the order $100 \div 150\,\mathrm{MPa}$ for very short-duration loads. As example, Larcher et al. [119] assume $35 \div 85\,\mathrm{MPa}$ for annealed glass and 196 MPa for tempered glass.

The numerical FE model considers each panel formed by 100 `Plate` elements, in particular they are `Quad4` type (4 nodes per element). The out-of-plane force per unit area is uniformly distributed on panels surface, and it is imposed through the command `Global pressure` which does not change the direction of force vectors during calculation (so the pressure is not acting at right angle to the deformed shape).

Now the time dependent variable is the displacement of panel centroid, here generically indicated as $Z(t)$. If we are based on (5.6), the out-of-plane displacement field results $w(x, y, t) = Z(t)\psi(x, y)$, while the stress function $\varphi(x, y, t)$ takes the same expression of (5.8) by setting $Z(t)$ in place of $Z_{i+N}(t) - Z_i(t)$. The effective inertia is defined by equivalent mass m^P

$$m^P = \rho s \int_0^a \int_0^b \psi(x, y)^2 dxdy\,. \tag{5.17}$$

The effective time dependent load $f(t)$, associated with the work of external forces, reads

$$f(t) = p(t) \int_0^a \int_0^b \psi(x, y)\, dxdy\,. \tag{5.18}$$

The effective stiffness is derived from the elastic strain energy of one single panel $\mathcal{U}^P$, which has the same form of (5.11) by substituting $Z(t)$ in place of $Z_{i+N}(t) - Z_i(t)$. In particular we write

$$\frac{\partial \mathcal{U}^P}{\partial Z(t)} = \alpha\, Z(t) + \beta\, Z(t)^3\,, \tag{5.19}$$

where the coefficients α and β, whose expression is not recorded for brevity, are related to the bending strains and median-fiber strains, respectively. Therefore, the nonlinear second order differential equation (of Duffing type) is obtained

$$m^P \ddot{Z}(t) + \alpha\, Z(t) + \beta\, Z(t)^3 = f(t)\,. \tag{5.20}$$

Observe that the use of the linear Kirchhoff-Love plate theory, instead of the von Kármán theory, is equivalent to the linearization of this expression when $\beta = 0$. This limit case is also considered for the sake of comparison.

The graph of Fig. 5.5(a) reports, for $0 \leq t \leq 0.15\,\mathrm{s}$, the centroid displacement $Z(t)$, obtained from the FE model and analytical model *à la* von Kármán as per (5.20), or the Kirchhoff-Love plate theory, with $\beta = 0$. Observe that, with respect to the FE solution, the linear Kirchhoff-Love theory highly overestimates the plate deflection and underestimates the frequency of oscillations. The von Kármán model provides a much better accuracy, especially in terms of maximum deflection (errors in defect less than 10%). The frequency is now slightly overestimated, as a consequence of the fact that the vibrating plate is artificially "constrained" when it is reduced to a 1-DoF oscillator.

The comparison in terms of maximum stress in glass is illustrated in Fig. 5.5(b). With respect to the FE results, the Kirchhoff-Love theory overestimates the stress of about 50%, while the von Kármán approach provides a very good agreement in terms of peak stress. It should be noticed, however, that numerical simulations show high frequency secondary oscillations that superimpose onto the main trend, which agrees with the predictions from the model *à la* von Kármán. This may be due to the reduction of the response of glass pane to that of a 1-DoF oscillator assuming the shape function associated with the first vibration mode only. It is evident that also higher modes of vibration can be excited by the blast wave, but these is not considered in the simplified approach. In any case we will show the effects of the higher modes are mitigated when the response of the whole façade is taken into account, as shown next.

The difference between the Kirchhoff-Love and the von Kármán models can be better appreciated in the phase portrait of Fig. 5.6. It is obtained from the solution of the homogeneous equations associated with (5.20), with either $\beta = 0$ or $\beta \neq 0$, under the initial conditions $Z(0) = 0$ and $m^P \dot{Z}(0) = \int_0^\infty f(t)\,dt$ (the blast wave is considered as an impulsive load). The ellipse for the von Kármán case indicates a much lower deflection for the same boundary conditions, if compared with the trajectory for Kirchhoff-Love. In general, the difference diminishes if the impulse decreases and/or the thickness of panel increases, and vice-versa.

In conclusion, the linear Kirchhoff-Love plate theory does not seem suitable to model a plate under an impulsive bomb blast action. On the other hand, the simplified approach relying upon von Kármán plate theory can estimate, with a limited error, the maximum deflection and peak stress, which indeed are the most important quantities for design.

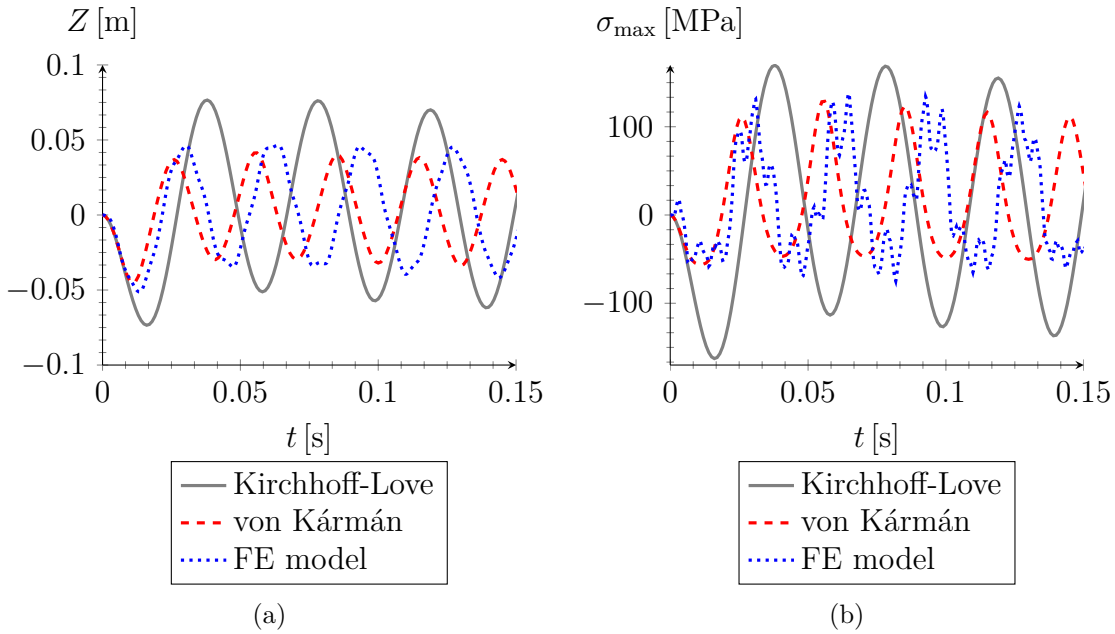

Figure 5.5. Dynamic response of the sole panel: (a) centroid displacement $Z(t)$ and (b) maximum stress $\sigma_{\max}$. Comparison among the simplified models *à la* Kirchhoff-Love or von Kármán, and the FE numerical solution.

5.2.2 Global dynamic response of the façade

Now we consider the lumped element model of the whole façade, with the glass plates characterized according von Kármán theory. Comparisons will be made with a FE model of the glazed façade, implemented in the software `Straus7`. For the case of $N = 3$ panels, the FE model is represented in Fig. 5.7, both in the reference and the deformed configurations. The deformed configuration is subsequent to the blast wave action previously introduced. It is needed to give a qualitative idea of what we obtain at the end of FE analysis, executed with `Straus7`, in terms of displacements. In particular, it is a frame representing the deformed façade at the instant $t = 0.1\,\text{s}$.

In the lumped element model of Fig. 5.4, the diameter of cable has been chosen by considering an initial tensile force (before the arrival of the blast wave) $T_0 = 150\,\text{kN}$, so that the resulting stress is less than the design value at rest $\sigma_d = 300\,\text{MPa}$. The prestress force T_0 is sufficiently high to maintain the maximum deflection of the cable within the limit $L/50$ under wind load, conventionally set equal to $1.5\,\text{kPa}$, in the case of rigid spring ($k \to \infty$). For what concerns the FE model, the rear structure is formed by two identical cables. They are both connected in series to springs at their lower ends, whose mechanical properties (stiffness, inertia, prestress) are one half of those used in the lumped element model because only one column of glass

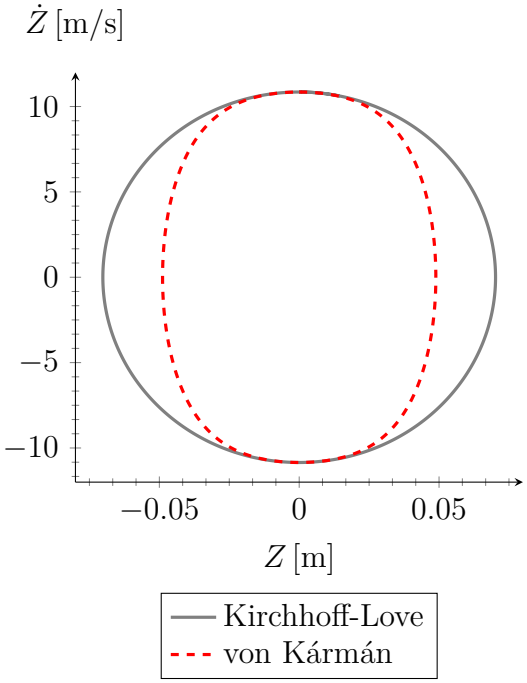

Figure 5.6. Phase portrait. Comparison between Kirchhoff-Love and von Kármán plate theories.

panes is considered. Every cable is made by $N+1$ `Truss` elements with null density, because the inertia is concentrated at the nodes (their masses are represented with light blue spheres in Fig. 5.7).

The glass panels are square monoliths of size $a \times b = 2 \times 2\,\mathrm{m}^2$ and thickness either $s = 12\,\mathrm{mm}$ or $s = 20\,\mathrm{mm}$. The mechanical properties and the type of finite elements in the mesh are the same used before. We use `Rigid links` to connect the panels to the cables. The `links` are useful to constrain the translations of the plate borders to the rear structure and schematically reproduce the role of mechanical connectors. The applied pressure follows the Friedlander's wave form (2.1), maintaining fixed the direction of force vectors (command `Global pressure` in `Straus7`). The solution is calculated with the `Nonlinear transient dynamic solver` directly implemented in the software. There are several parameters that shall be set as input data: we choose the `Time step` $\Delta\tau = 0.0005\,\mathrm{s}$ and `Newmark's beta` $\beta = 0.5$. The results are reported for $0 \leq t \leq 0.3\,\mathrm{s}$, which is sufficiently large with respect to the effective duration of the blast wave. For higher values of t, we expect that the viscous damping would play an important role, but this is not considered here.

For façade with either $N = 3$ or $N = 6$ panels, results are presented in terms relevant for structural design.

For a value of spring constant $k = 2 \times 10^6$ N/m, the time dependent spring

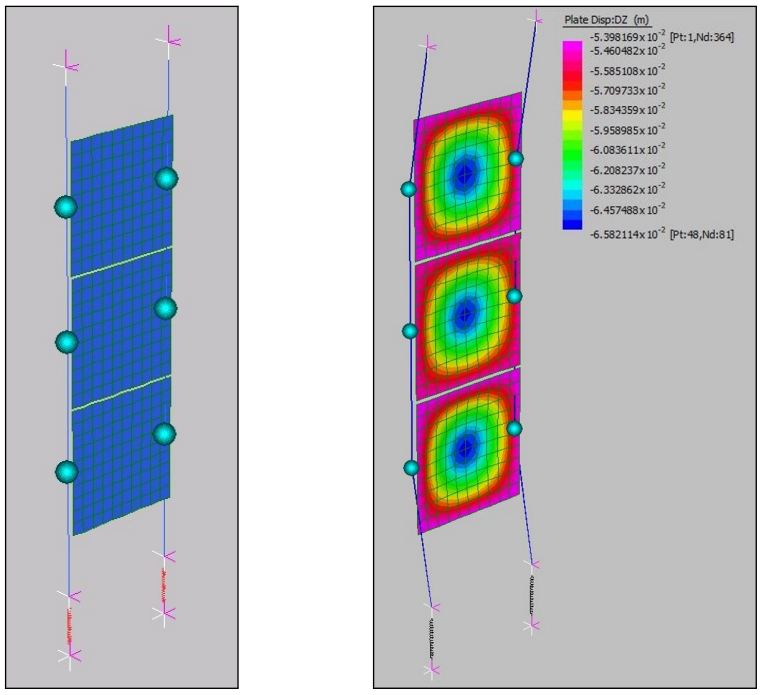

(a) Reference configuration

(b) Deformed configuration

Figure 5.7. FE model of the façade, as implemented in the software `Straus7`. (a) Reference and (b) deformed configurations.

elongation $u(t)$, calculated with either the lumped element model or the FE model, is shown in Fig. 5.8. This case refers to a glass plate thickness $s = 12\,\text{mm}$, but results are almost identical for $s = 20\,\text{mm}$. For both $N = 3$ and $N = 6$, the lumped element model correctly estimates the peak values and the wave form. The maximum value of the spring elongation does not exceed the reasonable technological limit $u_{\max} \leq 0.20 \div 0.25\,\text{m}$. The graph for $N = 6$ excellently reproduces the results of FE model, but the solution for $N = 3$ presents a difference for $t \geq 0.2\,\text{s}$. This is due to a higher stiffness of the lumped element model in comparison with the FE model, possibly due to the hypothesis (5.4), which implies the observed increase in terms of frequency, especially when the cable is short. However, the deviation is not important because the structural design requires an accurate estimation of the maximum peak, which is precisely caught by the simplified model.

The corresponding deflection of the cable, made non-dimensional with respect to its length L, is represented in Fig. 5.9. In both the cases $N = 3$ and $N = 6$, the maximum displacement approximately results $L/10$, which is reasonable from a technological point of view. As in the previous graphs, the solution for the lumped

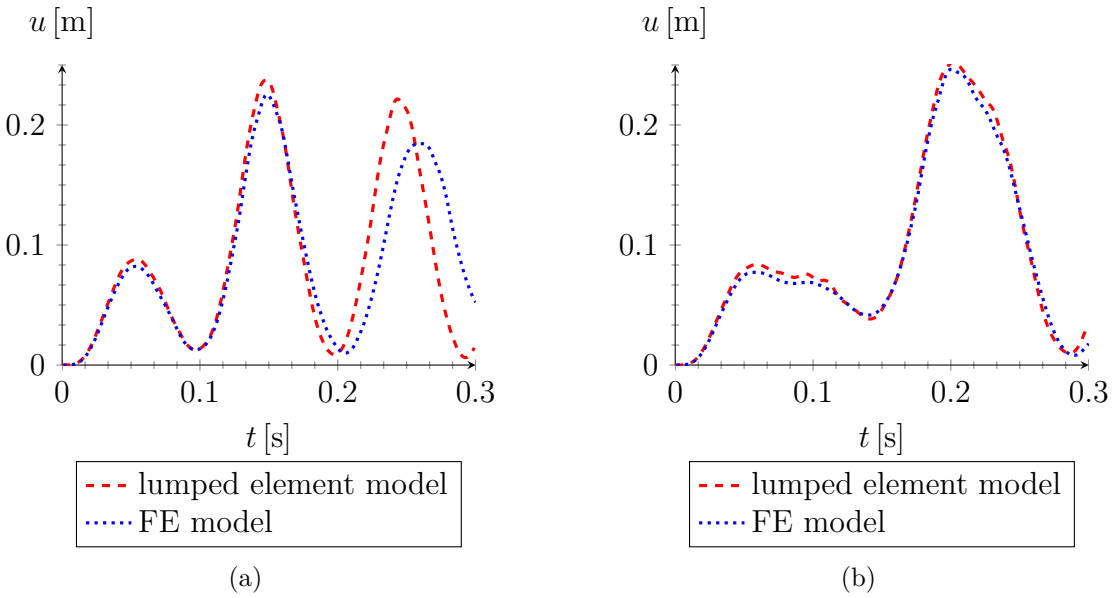

Figure 5.8. Dynamic response: elongation of the spring $u(t)$ for $k = 2 \times 10^6$ N/m. Comparison between lumped element and FE models for (a) $N = 3$ and (b) $N = 6$.

element model better agrees with the FE results when $N = 6$.

The stress in the cable depends upon the tensile force $T(t)$ to which it is subjected during the blast action: this is represented in Fig. 5.10. The maximum value, in practice the same for both $N = 3$ and $N = 6$, is $T_{\max} \simeq 620\,\text{kN}$, about four times the initial value $T_0 = 150\,\text{kN}$. This will exceed the design stress in the cable, which will consequently yield. As it will be shown, in order to maintain the cable within the elastic limit it is necessary to change the spring stiffness, but the purpose here is simply to compare the results from the analytical and the FE model from a purely theoretical point of view. The result is very good, especially for $N = 6$.

The weakest elements of the façade are certainly represented by glazed panels. The most stressed point is expected to correspond to the centroid of central panel, when $N = 3$, or of the third and fourth panels, when $N = 6$. The corresponding graphs are shown in Fig. 5.11 for $s = 12\,\text{mm}$, and Fig. 5.12 for $s = 20\,\text{mm}$. The results are in excellent agreement for $s = 20\,\text{mm}$, but for $s = 12\,\text{mm}$ we notice additional high frequency oscillations, especially for $N = 3$ and $t \geq 0.2\,\text{s}$. Nevertheless, the peak values are well estimated, with a percentage error of the order of 10%. As already observed for the case of the sole panel, this is due the reduction of each glass panel to a 1-DoF oscillator, assuming as a shape function that associated with the first vibration mode. Recall from the discussion of Fig. 5.3 that such an approximation is the more accurate the thicker the panel is. When the thickness is $s = 12\,\text{mm}$, higher modes are presumably activated, and this is the reason for the

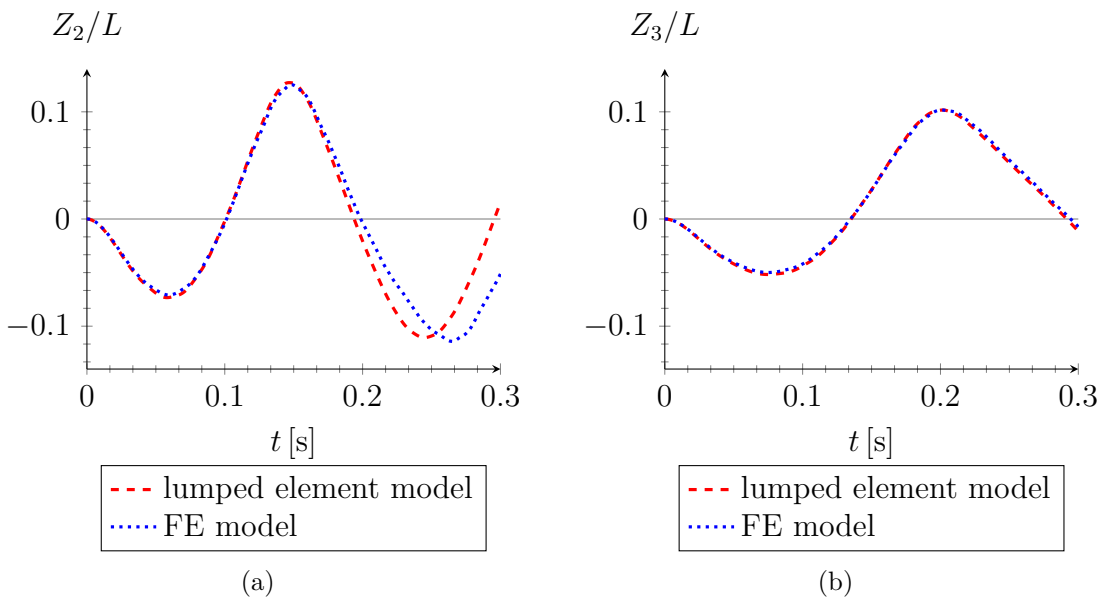

Figure 5.9. Dynamic response: non-dimensional maximum deflection of the cable represented by (a) $Z_2(t)/L$ for $N = 3$ and $L = 8.2\,\mathrm{m}$; (b) $Z_3(t)/L = Z_4(t)/L$ for $N = 6$ and $L = 14.35\,\mathrm{m}$.

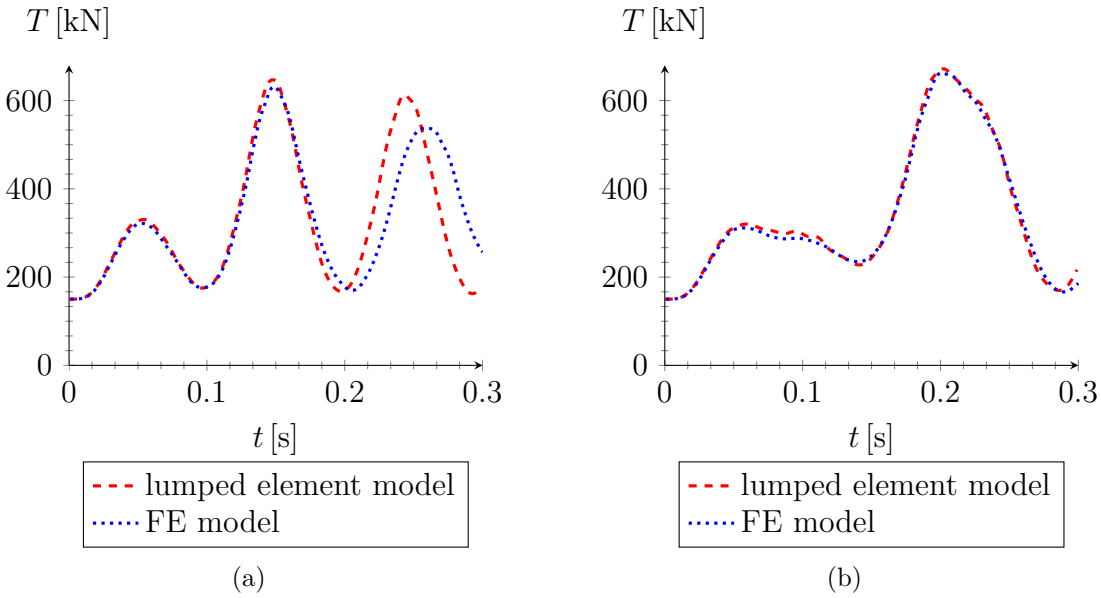

Figure 5.10. Dynamic response: axial tensile force in the cable. Comparison between lumped element and FE models for (a) $N = 3$ and (b)$N = 6$.

secondary oscillations at higher frequencies in the FE model that are observed in Fig. 5.11.

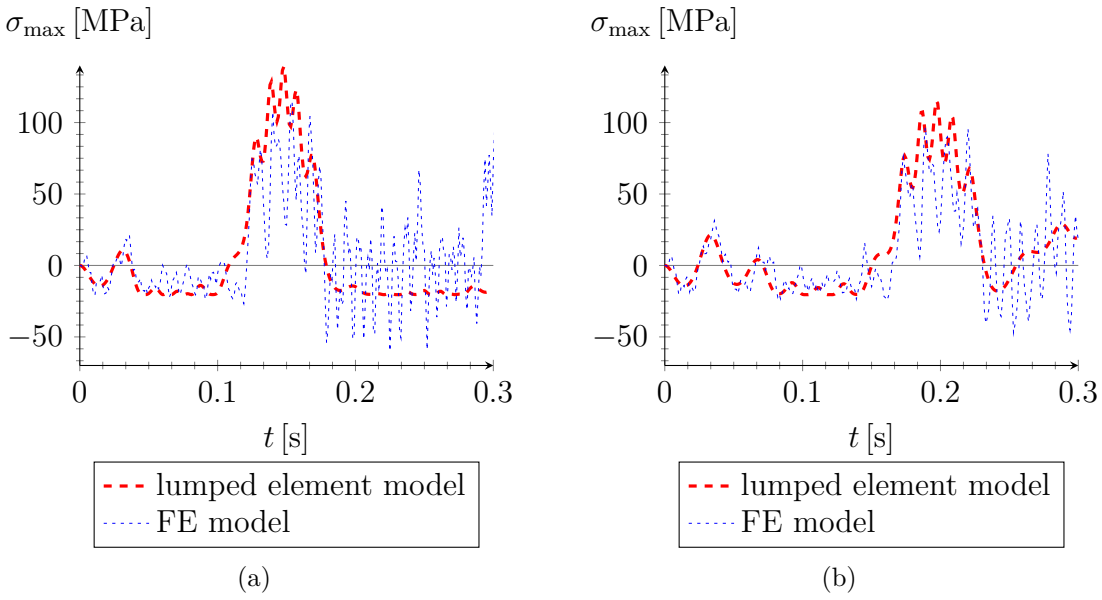

Figure 5.11. Dynamic response, case $s = 12\,\text{mm}$: stress at the centroid of central panel, for (a) $N = 3$, and of the fourth panel for (b) $N = 6$.

In any case, it is of paramount important to observe that the peak stress in the glass panel of thickness $s = 20\,\text{mm}$ is of the order of 80 MPa, for both $N = 3$ and $N = 6$. When an identical glass panel is rigidly constrained along the boundary, the graphs of Fig. 5.5(b) in Section 5.2.1 indicate a maximum stress about 50% higher, of the order of 120 MPa. Indeed, also the secondary high-frequency oscillations, not captured by the 1-DoF oscillator, which are well evident for the case of the sole panel, tend to be mitigated when there is a supporting cable. These findings confirm the benefic effect of a compliant rear structure, which can absorb most of the energy from the blast action while preserving the integrity of panels.

5.3 Parametric analyses

Despite its simplicity, the lumped element model is sufficiently accurate in estimating key quantities, such as the maximum stress in the glass and the maximum tensile force/deflection in the cable. Based on this, we investigate how the spring stiffness and the inertia of cable can be tuned in order to safe-guard the integrity of glass, supposed of thickness $s = 12\,\text{mm}$ in all the numerical experiments. Comparisons will be made with a much simpler approach, referred to as the *linear model* since it

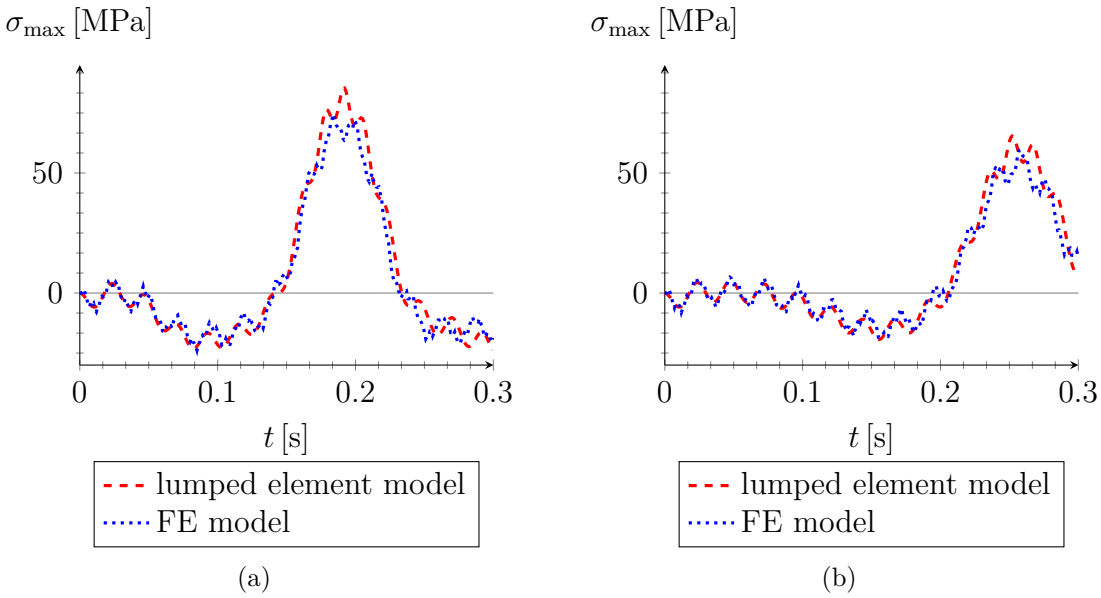

Figure 5.12. Dynamic response, case $s = 20\,\text{mm}$: stress at the centroid of central panel, for (a) $N = 3$, and of the fourth panel for (b) $N = 6$.

is characterized by: *i*) the absence of the spring ($k \to \infty$), *ii*) the time independence of the axial tensile force in the cable ($T(t) = T_0$) and *iii*) the linear modeling *à la* Kirchhoff-Love of the glass panels (membrane stresses are neglected). We wonder: what kind of information can be obtained from the linear model to a problem that presents strong geometric nonlinearities?

5.3.1 Influence of the spring stiffness

The deflection of cable is represented by $Z_2(t)$, for the case $N = 3$, or $Z_3(t)$, for $N = 6$. These are normalized by the length L of the cable and shown in Fig. 5.13 for various values of the spring elastic constant k. As expected, the magnitude increases as k decrease, because the rear structure becomes more compliant. The linear model overestimates the deflection also when compared with the case $k \to \infty$, because it neglects that the cable is strained by the transverse displacement and its tensile force increases. The differences between the cases $N = 3$ and $N = 6$ are not relevant. Although, for the best of our knowledge, international standards do not prescribe a precise limit for the cable deflection, a reasonable value, dictated by technological requirements, is the order of $L/10$ under the extreme condition of an explosion.

It is evident from Fig. 5.14 that if the spring stiffness k is diminished, also the maximum value of the tensile force in the cable is reduced. However, the decrease of

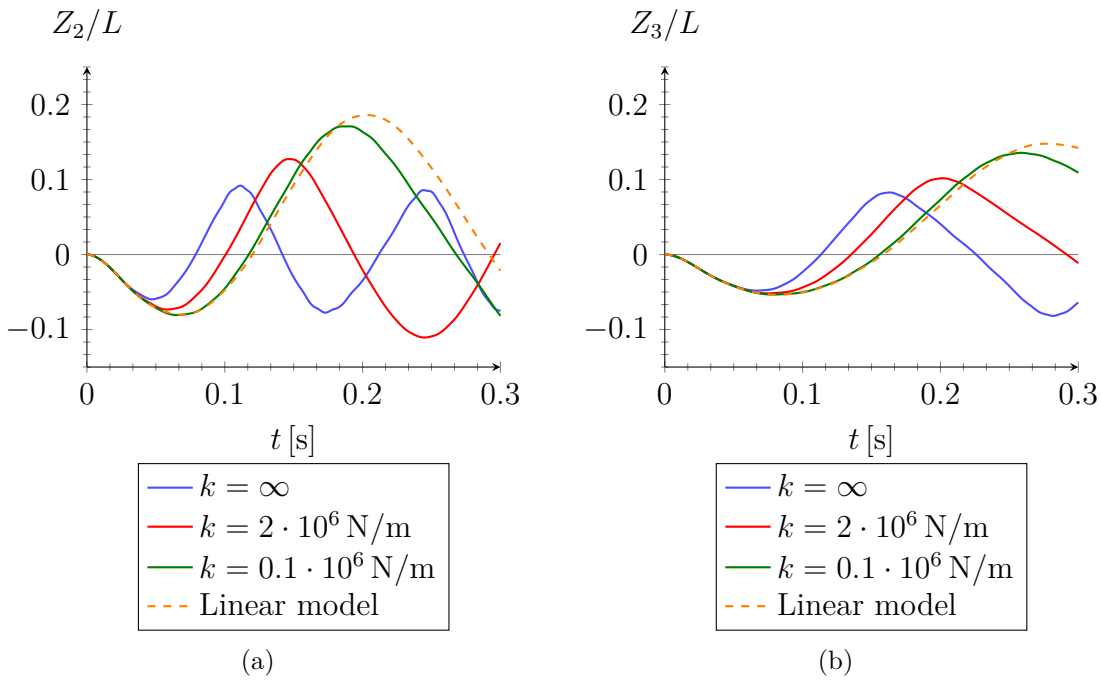

Figure 5.13. Parametric analysis: maximum deflection of the cable as a function of the elastic constant k of the spring. Cases (a) $N = 3$ and (b) $N = 6$.

k collides with the technological constraint that imposes an upper bound for cable deflection: a compromise is thus required. By hypothesis, the linear model does not account for any variations of the tensile force, so it is not useful, not even in a preliminary design. In general, the façade with $N = 6$ panels substantially performs in the same way of that with $N = 3$ panels. The peaks stress for $k \to \infty$ are substantially the same and the same is true when the spring stiffness is varied.

The stress in the glass panes of thickness $s = 12\,\text{mm}$ is represented in Fig. 5.15. If we decrease the spring elastic constant, the cable becomes more compliant and the state of stress inside the panels diminishes. This confirms that a compliant rear structure is able to absorb the largest part of energy from the blast wave, preserving the glass panels. To this respect, the benefic effect is slightly less relevant if compared with the tensile force drop in the cable. Observe as well that the linear model does not consider the positive contribution of the membrane strains and, consequently, it tends to overestimate the stress in glass. Moreover, the nonlinear analysis evidences that the peak stress is maintained for a shorter time with respect to the linear model. This is important, because the phenomenon of subcritical crack growth [120] renders the strength of glass dependent upon the duration of the load: the shorter the duration, the higher the strength. Observe that a long cable ($N = 6$) performs much better than a short cable ($N = 3$). In fact, the deflection increases

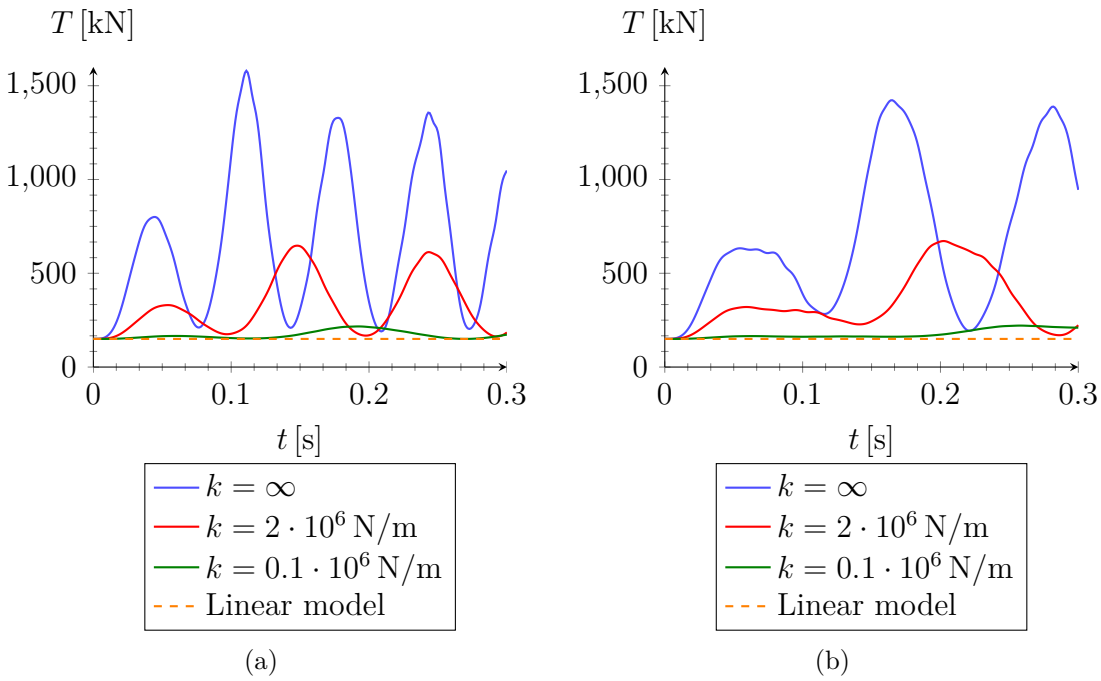

Figure 5.14. Parametric analysis: axial tensile force in the cable depending on the spring stiffness k. Cases (a) $N = 3$ and (b) $N = 6$.

with the length of cable and the rear structure becomes more compliant.

5.3.2 Influence of the cable mass

We now keep fixed the spring stiffness to $k = 2 \times 10^6\,\mathrm{N/m}$ and we vary the linear distributed mass on the cable in order to evaluate its influence on the dynamic response of the façade.

The nondimensional deflection of the cable (maximum sag divided by length) tends to decreases by increasing the mass. This is evident from Fig. 5.16, which reports various graphs corresponding to different values of the mass *per* unit length of the cable (recall that the mass of the bare cable is approximately 3 kg/m). In the lumped element model, the masses are concentrated at the nodal points: therefore, this analysis also corresponds to the case in which the cable is ballasted by additional masses, appositely placed at the fixation points. Indeed, a high inertia can counterbalance the impulse from the blast wave, especially during the initial compression phase. The frequency of the oscillations consequently decreases, but the benefits becomes less relevant in terms of maximum displacement. This moderately diminishes when the mass *per* unit length passes from 3 kg/m to 100 kg/m, although the peak is reached in a longer time. Recall that the model does not account for

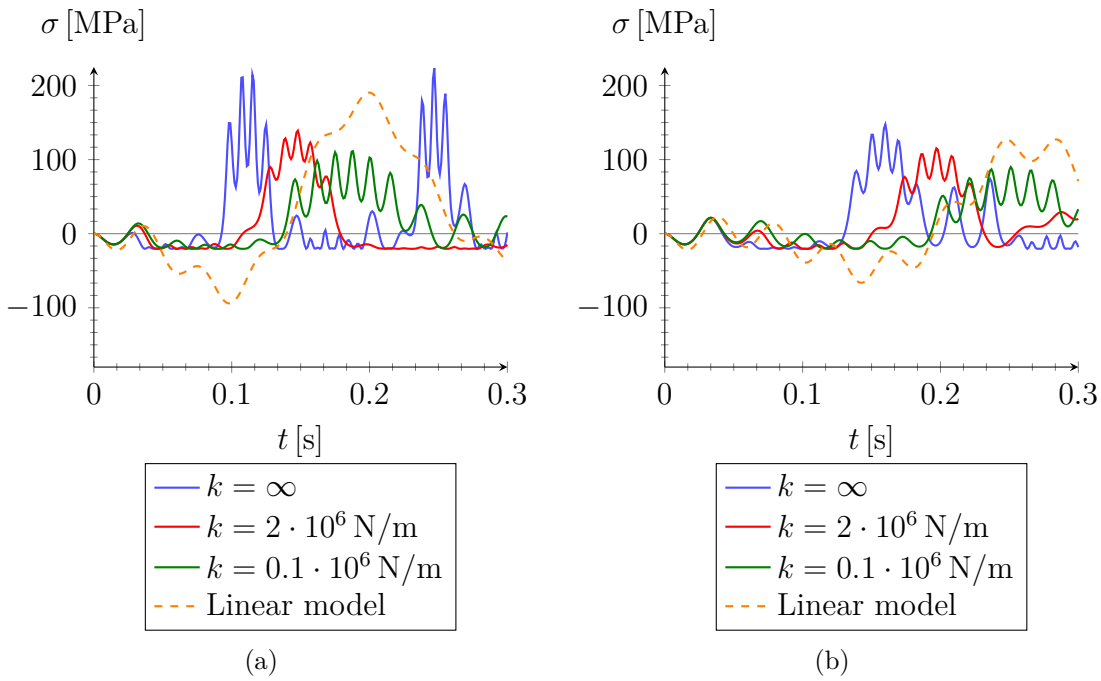

Figure 5.15. Parametric analysis: stress in glass of thickness $s = 12\,\text{mm}$ for varying stiffness k of the spring for (a) $N = 3$ (central panel) and (b) $N = 6$ (third or fourth panel).

the damping of the structure, but the damping should certainly limit the maximum deflection in the case in which the peak is reached later, since the viscous capacity has the time to dissipate energy. Increasing the number of panes limits as well the maximum deflection, but the effect is not remarkable.

The tensile force in the cable varies in accordance with its maximum deflection, as represented in Fig. 5.17. If the cable is artificially ballasted, its oscillations are retarded and reduced; consequently, the increase of its axial tensile force is reduced. There is not a substantial difference between a façade with $N = 3$ and $N = 6$ in terms of peak value, but there is a noteworthy effect in terms of frequency.

The influence of the mass on the stress in glass is shown in Fig. 5.18. The graphs suggest that increasing the mass greatly affects the frequency, confirming that the state of stress in the glass panels depends upon the oscillations of supporting structure. However, the peak stress remains approximately at the same level ($\sigma_{\max} \simeq 120\,\text{MPa}$), even if it is reached in different times. Indeed, there is a complicated interaction between the vibrations of the rear structure and the vibrations of the panels. If the cable is very heavy, the inertial forces refrain the movement of panel supports, so that it behaves as rigidly fixed. However, the movement of cable may drag the panel and increase the stress in glass.

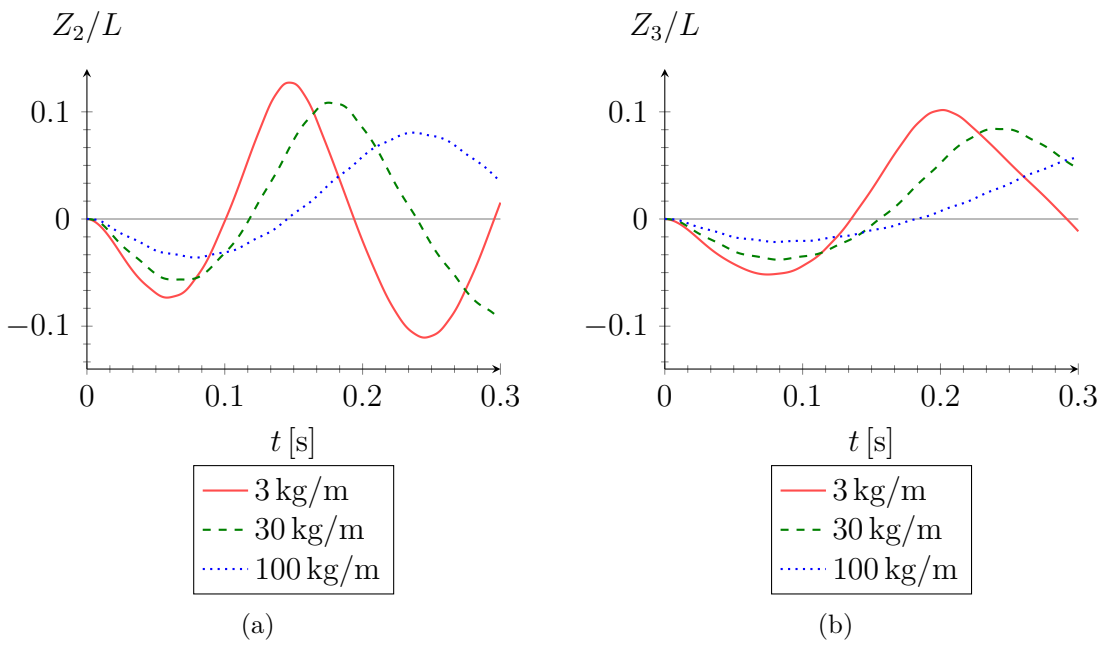

Figure 5.16. Parametric analysis: deflection of cable for various values of its mass per unit length. Cases (a) $N = 3$ and (b) $N = 6$.

5.3.3 Comparison with the linear model

A full nonlinear analysis is computationally expensive and it presents a number of variables (cable diameter, spring stiffness) that complicate the preliminary design. Therefore, it is interesting to discuss what are the conclusions that can be obtained with a simple linear model. Although we have already demonstrated that a linear approach is in general unreliable, nevertheless some indications can be obtained, albeit at the qualitative level, for what concerns the choice of the optimal spring stiffness and the optimal value of ballast. The procedure implies two steps:

- consider first the linear model in order to determine the *optimal* values of the distributed mass and the initial tensile force in the cable that, while respecting technological limits, minimize the displacement of cable;
- successively, using a nonlinear analysis, calculate the cable diameter and tune the spring stiffness to limit the stress in both cable and glass.

The first step considers the mechanical properties of cable in terms of tangential stiffness, associated with its initial prestressing force (T_0), and inertia (mass m_c per unit length). The linear model certainly overestimates the deflection of the cable and underestimates its tensile force during the movement. Also the stress in glass

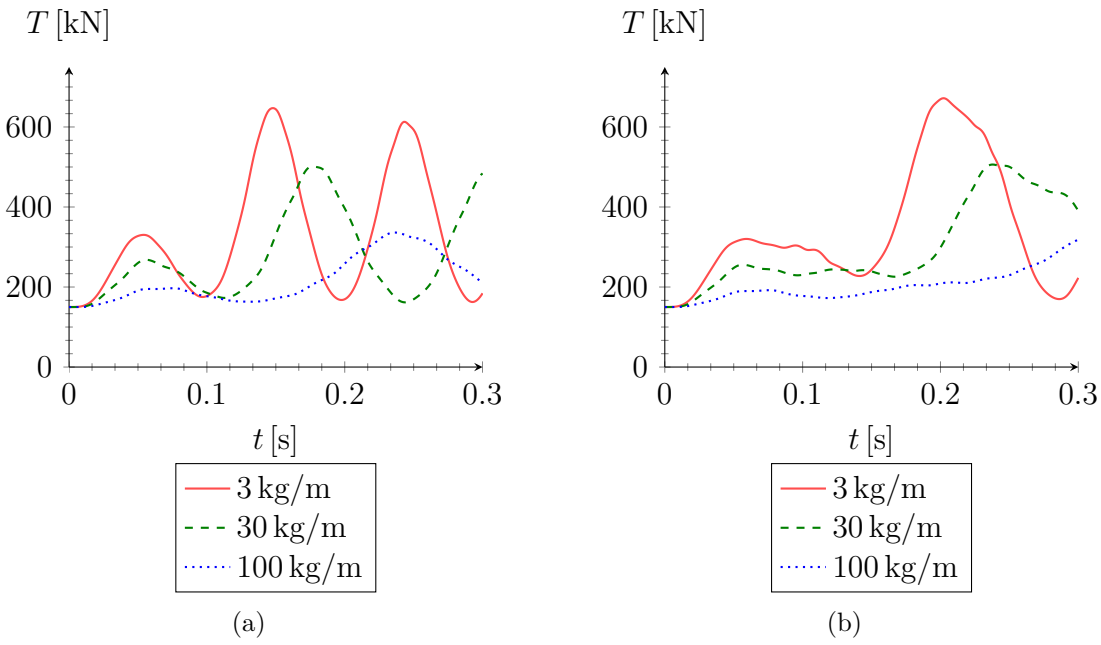

Figure 5.17. Parametric analysis: axial tensile force in the cable for various values of its mass per unit length. Cases (a) $N = 3$ and (b) $N = 6$.

may be very different if compared with the results from a nonlinear analyses, but the peak value is in general mitigated by the nonlinear membrane effect. These considerations suggest to apply the nonlinear model a posteriori, to precisely determine the diameter of cable according to the material strength. Adding a spring in series with the cable provides another parameter in the design phase. By decreasing its stiffness, the deflection of cable slightly increases (see Fig. 5.13), while the stress in the glass considerably diminishes (see Fig. 5.15). Indeed, it is the spring that permits to improve the global capacity of façade by limiting the maximum stress in glass.

To illustrate, the aforementioned procedure is applied to the case $N = 3$.

We start by calculating the maximum absolute value $Z_{2,\max}$ in the deflection history $Z_2(t)$ according to the linear model. This quantity is represented in Fig. 5.19 as a function of the initial tensile force T_0 and the distributed mass of cable m_c. The set of points that respect the deflection limit $L/10 = 820\,\text{mm}$ ($L = 8.2\,\text{m}$) is bounded by the red curve.

The maximum stress in glass according to the linear analysis, again plotted as a function of T_0 and m_c, is shown in Fig. 5.20. All the dark-marked points respect the deflection limit just imposed, while the red point with coordinates $\{\bar{m}_c = 35\,\text{kg/m};\ \bar{T}_0 = 460\,\text{kN};\ \bar{\sigma}_{\max} = 350\,\text{MPa}\}$ minimizes the stress inside this

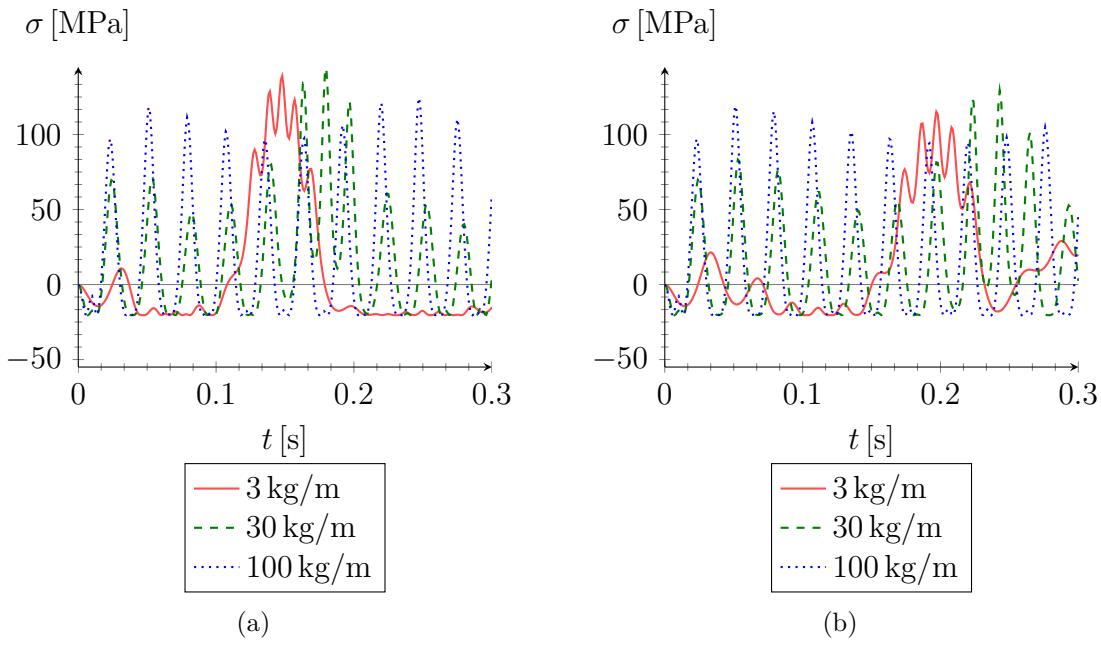

Figure 5.18. Parametric analysis: dependence of the stress in glass of thickness $s = 12\,\text{mm}$ on the mass of cable per unit length for (a) $N = 3$ (central panel) and (b) $N = 6$ (third or fourth panel).

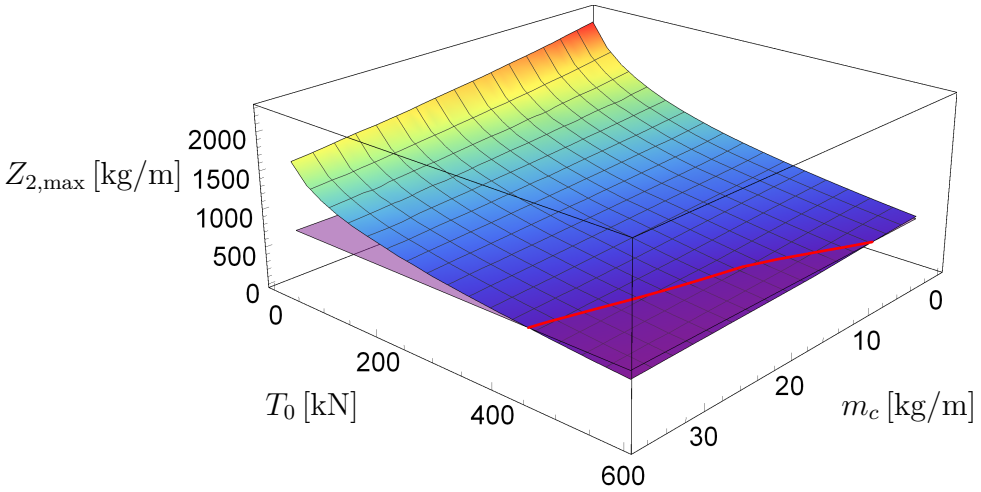

Figure 5.19. Maximum absolute displacement $Z_{2,\max}$ as a function of the initial tensile force T_0 in the cable and its mass per unit length m_c. The red curve delimits the region $Z_{2,\max} \leq L/10$.

subdomain. One may assume that under short duration impulsive loads, the glass can withstand, at most, a tensile stress of the order of 200 MPa, which is represented

by a horizontal plane in the same reference system. It is evident that, according to the linear analysis, the red point does not respect the stress limit. Nevertheless, by maintaining constant the coordinates $\bar{m}_c$ and $\bar{T}_0$, we can attempt to reduce the stress by adding a spring. The spring stiffness is optimized by following a nonlinear analysis. We first set the diameter of cable starting from the value $\bar{T}_0$: by considering a maximum tensile stress of 300 MPa one obtains $d \geq 45$mm. By choosing $k = 2 \times 10^6$ N/m, we evaluate the maximum stress in the glass according to the nonlinear model. The result is represented by the blue point in Fig. 5.19, whose coordinates are $\{\bar{m}_c = 35\,\text{kg/m};\ \bar{T}_0 = 460\,\text{kN};\ \bar{\sigma}_{\max} = 138\,\text{MPa}\}$. Now, the structural integrity of glass is guaranteed. Also the resistance of cable should be checked with the nonlinear model: the maximum tensile stress reached during the time-history is $\sigma_{\text{cable,max}} \simeq 450$ MPa according to the nonlinear analysis, which is within the tolerable limits for high-strength steel.

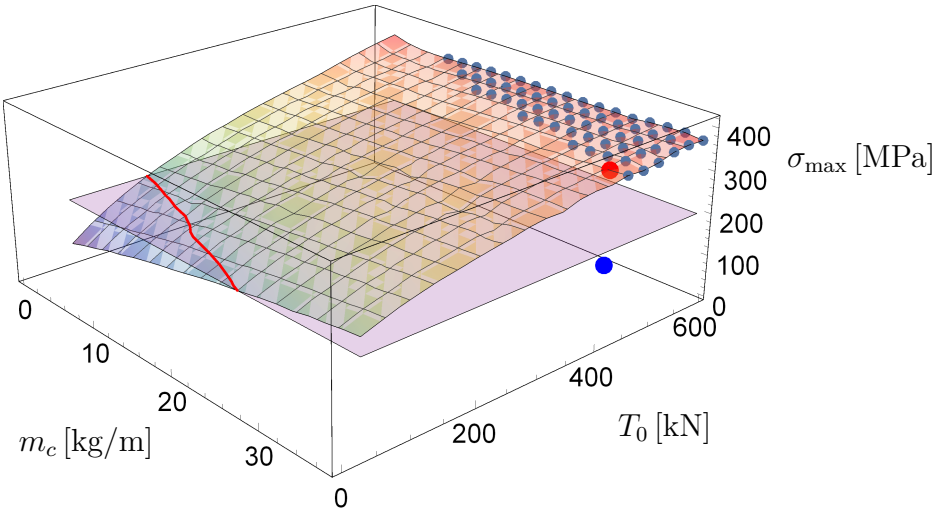

Figure 5.20. Maximum stress in the glass as a function of the initial tensile force T_0 in the cable and its mass per unit length m_c. The dark marked points respect the deflection limit. The blue point is obtained from nonlinear analysis.

One may also consider a complementary approach, which now starts from the graph of the maximum stress in glass, represented in Fig. 5.21 still as a function of T_0 and m_c. The points of the surface that respect the restriction $\sigma_{\max} \leq 200$ MPa are confined by the red curve and correspond to the lower values of mass and tensile force.

Consider then the maximum deflection of cable as a function of the same project variables as per Fig. 5.22. All the dark-marked points respect the stress limit just imposed and the red point with coordinates $\{\bar{m}_c = 9\,\text{kg/m};\ \bar{T}_0 = 150\,\text{kN};\ \bar{Z}_{2,\max} = 1510\,\text{mm}\}$ minimizes the maximum deflection inside the subdomain. Now we perform a nonlinear analysis by setting $k = \infty$, because it is not necessary to further

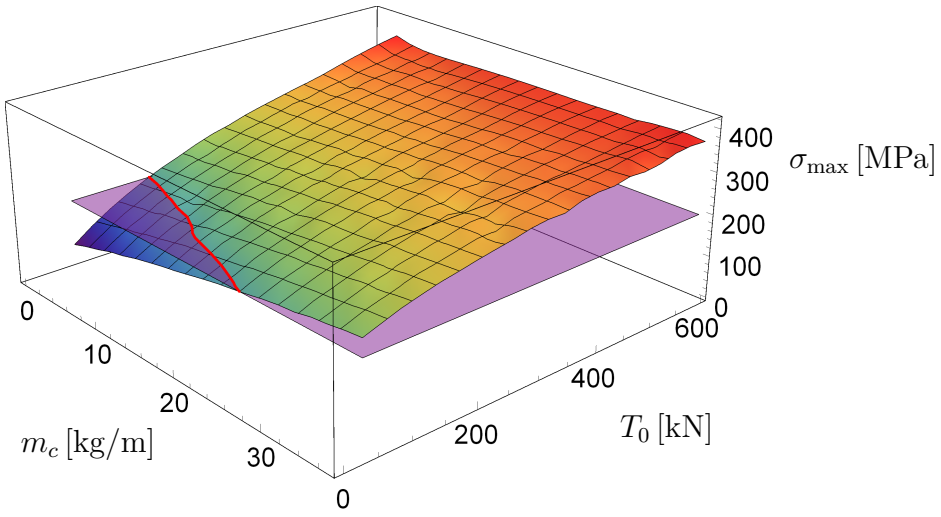

Figure 5.21. Maximum stress in the glass as a function of the initial tensile force T_0 in the cable and its mass per unit length m_c. The red curve delimits the region $\sigma_{\max} \leq 200$ MPa.

reduce the stress in glass, but rather the cable deflection and, to this respect, the best choice is not to add the spring. We want to check if the cable deflection, overestimated in the linear approach, effectively overcomes the limit $L/10$, represented as a horizontal plane in the same plot.

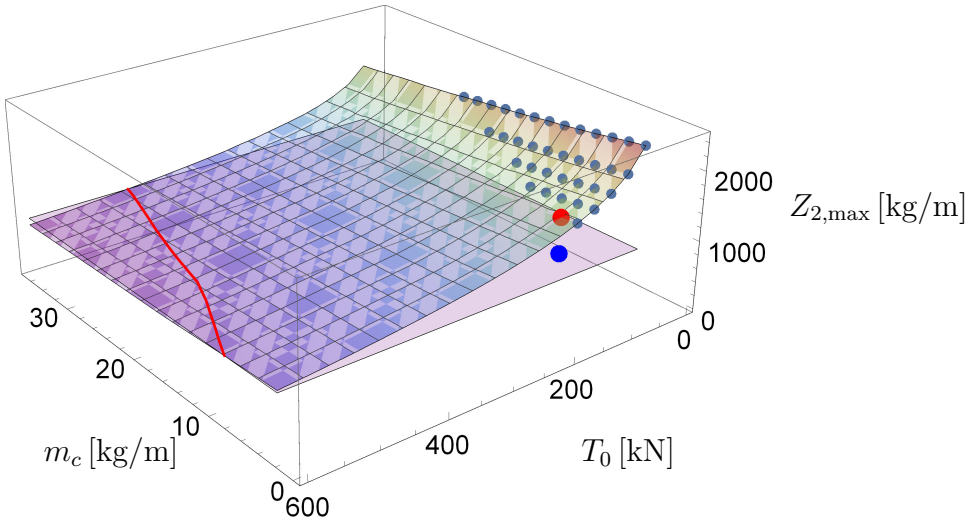

Figure 5.22. Maximum absolute displacement as a function of the initial tensile force T_0 in the cable and its mass per unit length m_c. The dark marked points respect the stress limit. The blue point is obtained from nonlinear analysis for $k = \infty$.

From the nonlinear analysis one obtains the blue point represented in Fig. 5.22, which still does not respect the deflection limit. It is evident that in this second approach, the stiffness k of the additional spring is not considered. In other words, one looses the possibility of introducing in the design an additional parameter, represented by the spring stiffness, that instead plays a role of paramount importance.

Chapter 6

Conclusions

Several aspects concerning the dynamic behavior of blast resistant glazed façades, have been investigated from a theoretical point of view. Although the attention has been focused on pressure waves from explosions, the same methods of analysis could be used, more in general, for loads of impulsive nature, such as those corresponding to soft bodies impacting the glazed surface. The problem can be approached at different levels, as discussed in this thesis. The conclusions are divided according to the content of the chapters and they follow the order of the exposed arguments.

The modeling of impulsive actions

The mathematical modeling of impulsive actions on glazed surfaces regards explosions and impacts.

An explosive load can be analytically interpreted via Friedlander equation, i.e., a semi-empirical formula for which the time history of pressure follows an exponential wave form. All the parameters involved (such as pressure peak, duration, decay coefficient, etc.) strictly depend on the mass of charge and the distance from the target. By knowing these data, it is possible to calculate the blast parameters by means of experimental relations recorded in the technical literature, thus obtaining the complete pressure curve. When the shock wave hits a target, there are also further phenomena to consider. One of the most important is certainly the reflection, that increases the initial pressure through a multiplicative factor. If the charge is not suspended in air, also the reflection with the ground has to be accounted for. The experimental testing procedures are useful to asses the bearing capacity of panels during the pre- and post-breakage phases. They are ruled by international recommendations within two main categories: full scale arena blast tests and shock tube loading tests. Both of them predispose specific criteria to classify the loading conditions, thanks to which the resistance of glass windows can be rated. In the engineering practice, only the first part of the blast impulse is commonly considered

as the most important, while the suction phase is often neglected. However, this could lead to incorrect results, because the complete loading curve can excite the fundamental modes of vibration characterizing the glass plate.

As a related problem concerning impulsive loads, the standardized soft-body impact test on glazed panels has been theoretically analyzed. This is a free-boundary value problem, because the imprint of the impinging mass, made with a twin pneumatic tyre, changes with the resultant of the contact force. The panel has been reduced to a simple linear oscillator by using Rayleigh's method and the interaction with the impacting tyres has been obtained through a linear spring and dashpot in unilateral contact, to consider multiple bounces if needed. Comparison with experiments recorded in the technical literature has evidenced the good agreement that can be obtained with this method, despite its simplicity, in terms of acceleration and displacement, evidencing the important role of the damping. Moreover, I have observed that, in cases of practical interest, the panel inertia can be neglected on the safe side and, in addition, the displacement of the panel, both in the linear and in the (geometric) nonlinear regime, is almost independent of the size of the contact imprint of the tyres. Therefore, by considering the panel as an equivalent nonlinear spring, a simple energetic balance allows to calculate the effective equivalent static force consequent to the impact, which can be used to determine a posteriori the stress and strain in the glass. In any case, we have shown in representative examples that this method can only be applied when the inertia forces are negligible. Therefore, one should preliminary check, e.g. by using Rayleigh's method, that the participating mass of the panel is substantially less than the mass of the impactor, otherwise the approximation, though conservative, is not accurate.

In order to obtain an engineered finite element tool to be used in a commercial software for structural analysis, we have defined a contact model formed by nonlinear beam elements, which can reproduce a constant pressure on an elliptical area, homothetically varying with the resultant of the contact forces. This tool, referred to as "contact-box", can be added to the complete model of a real structure to calculate the consequence of the impact in complex conditions. This represents an improvement with respect to a dedicated software like `SJ Mepla`, which only allows to consider one panel with elastic constraints, which not always can accurately reproduce the actual stiffness of the rear supporting structure and its inertia. Moreover, the proposed approach allows to insert damping to follow the motion until complete dissipation, and it can consider multiple rebounds if required. The model, implemented in `Straus7`, shows results in good agreement with `SJ Mepla`, both in the linear and in the nonlinear case, for the problems that this software can handle. Results also agree with those obtained with numerical models using the kinematic contact formulation implemented in `ABAQUS`. However, left aside the difficulty in meshing, the same problem requires a computation time of the order of a few minutes with the contact box tool implemented in `Straus7`, which becomes

of the order of a few days for the kinematic contact formulation in ABAQUS, when using the same processor. The potentialities of the proposed approach are even more evident for the paradigmatic case study of a full façade supported by cables, where geometric nonlinearities are of paramount importance and the inertia of the whole system participates in the motion. For this case, any analysis with SJ Mepla that considers an isolated panel cannot produce accurate results, whereas a full 3D model with ABAQUS would require much more time, both for meshing and computation.

This study has been limited to the case of monolithic glass, but using the concept of the effective thickness, it could be readily extended to the case of laminated glass. Experimental tests to corroborate the proposed approach will be the subject of future work.

Laminated glass modeled via fractional calculus

Laminated glass is formed by a series of glass plies, bonded together by interposed polymeric interlayers. Under impulsive loads (such as those deriving from explosions), the dynamic behavior of laminated glass is strongly affected by the viscoelastic properties of interlayers. For durations comparable with that of a blast load, the dynamic response of polymers is correctly interpreted by relaxation functions showing a power law dependence on time. Consequently, the approach via fractional calculus appears natural, inasmuch only two experimental parameters are needed to characterize the viscoelasticity. Note that the most used approach, which expands the relaxation function in Prony series according to a Weichert arrangement of spring-dashpot Maxwell elements, requires at least 20-30 parameters to achieve an adequate fit.

On the basis of an accurate kinematic description [121], the dynamic problem for a simply supported sandwich beam has been developed and solved *à la* Galerkin. The equilibrium equations have been integrated by means of Grünwald-Letnikov method, which does not present additional difficulties with respect to a classical step-by-step method for ordinary integral/differential equations. In this specific case, the major difficulty consists in treating the pressure time history, because it exhibits a strong jump when the wave hits the surface. Therefore, the load has been decomposed into its jump part and the remaining continuous part, so that a regularized form is obtained. Then, the governing equations have been preliminary integrated: since the jump function can be tackled analytically, the Grünwald-Letnikov numerical procedure can be used only for the second part. The convergence analysis has highlighted the advantages obtainable with this approach, when compared to the direct numerical integration of the irregular datum.

Several numerical experiments have been performed by considering sandwich beams of various sizes, laminated with different types of commercial polymeric interlayers. These can be mechanically characterized by means of static relaxation

tests on laminated glass specimens, which are preferable to dynamic tests because the polymer is processed in the autoclave as in real conditions. The calibration of fractional viscoelastic parameters can be done graphically, by interpolating with a straight line the relaxation curve in the bi-logarithmic stress-time plane. A parametric analysis has allowed a direct geometric evaluation of the effects of fractional viscoelastic parameters describing the relaxation curve. The comparison with the traditional approach, based on Prony series, has highlighted the following advantages related to the fractional approach: the calibration of the mechanical response of the polymer is much simpler; the numerical solution is more straightforward; the convergence is faster.

The model has been extended to laminated glass *plates*. The equilibrium equations have been deduced from Hamilton's principle and solved *à la* Galerkin. Further numerical experiments have been conducted under impulsive loading conditions, by applying the Grünwald-Letnikov integration method without regularizing the pressure time history, as detailed above. The mechanical response of a simply supported plate has showed the importance of the first mode of vibration. The state of stress depends on the used polymer: if the interlayer is stiff, a low level of deformation/bending stress is reached. Also the case of a panel supported by a deformable rear structure has been modeled, with the purpose of concisely demonstrating that when the rear structure is compliant, the panel tends to be less stressed.

As a further development, it could be useful to consider the geometric nonlinearities and the consequent development of membrane stresses in the glass plies. The experimental validation of the model could be made by testing laminated glass panels in a shock tube apparatus. Of course, also the post-glass-breakage response is of paramount importance, but this certainly requires an ad hoc treatment. In any case, despite its simplicity, the problem addressed demonstrates the great potential of the fractional viscoelastic approach in interpreting the response of laminated glass to blast loads and, more generally, to loads of short duration, as in the case of bodies impacting on the glazing.

The advantages of dissipative supporting devices

Since laminated glass presents a limited ductility, I have evaluated the potential advantages with respect to blast loads of interposing dissipative devices between the glazed façades and the supporting back structures. The considered case study represents a paradigmatic situation: one panel connected to an elastic back structure by means of an equivalent dissipative device. Simplifying assumptions have been made for the glass pane and the load-bearing back structure. The blast loads have been modeled again via Friedlander equation. The dissipative device consists of a mobile piston in unilateral contact, on the two opposite sides, with shock absorbers capable of plastic dissipation. The dynamic equations involve various scenarios,

which are recognized and solved by a customized algorithm. A finite element model implemented in a commercial software has confirmed the results obtained with a simplified problem, but the proposed approach is much more complete, since it allows to consider more precisely the possible impacts of the piston with the load-bearing structure (possible energy loss have been taken into account through an appropriate coefficient or restitution). This is perhaps the major novelty, as it seems that, so far, very little attention has been paid at the rebounds resulting from impacts, which can overload the glass and compromise its structural integrity.

Parametric analyses have been made to determine the role of the shock absorbers and optimize their properties. The results can be summarized as follows.

- An optimal shock absorber should present a long stroke, in order to maximize energy dissipation, and a low yielding limit, in order not to refrain the movement of the glass pane when it is invested by the blast load. It is of paramount importance to design the stroke in relation to the duration of the compression phase from the blast load. The stress in the glass pane can be substantially reduced if the shock absorber is not yet fully deformed when this phase ends, so that the impact with the back structure does not occur when the suction phase begins; otherwise the counter-inflection of the pane would be increased. Indeed, the stroke end should be reached after the start of the suction phase.

- Although the role played by the coefficient of restitution (energy loss during impact) is not of primary importance, it limits the pane oscillations in subsequent instants, when the blast load is almost exhausted.

- The compliance of the back structure has a limited effect during the first compression phase of the blast load; however, a flexible supporting structure greatly reduces the stress in glass during the subsequent oscillations. The stroke and activation force of the shock absorbers shall be calibrated according to the inertia and stiffness of the back structures. For example, a shock absorber, which is effective for a transom and mullion façade, may malfunction when the glazing is supported by pre-tensioned cables.

The effects of shock absorbers have been compared with those obtainable by replacing them with more conventional viscous dampers. The stress level in the glass under the first compression phase increases proportionally with the damping coefficient. In fact, by recalling that the reaction force depends on the relative speed of the coupled components, since an impulsive load produces a strong velocity gradient in the invested panel, a damper may respond like a rigid link. On the other hand, the damping coefficient cannot be arbitrarily reduced, otherwise the displacements would become too large. In any case, viscous dampers are strongly effective in limiting the subsequent oscillations of the system, after the passage

of the pressure wave. It thus appears natural to propose a hybrid device, where viscous dampers and shock absorbers are integrated in parallel: the shock absorbers can strongly reduce the stress in glass during the first compression phase, whereas the damper comes into play in the subsequent oscillations, contributing as well to mitigate the effects of impacts when the shock absorbers reach the stroke end. This technical solution seems to represent the best compromise, because it reduces the deflection of glass panel and minimizes the displacement of back structure. However, more studies are needed to engineer the device.

Because of the large number of variables, a limitation of the work consists in having taken into account just one representative example. Therefore, it will be necessary to extend this analysis to other façade configurations in future developments [97].

The role of rear load-bearing structure

Since the structural design is oriented to the assessment of the whole glazing system, a lumped element model has been proposed to analyze the dynamic response of a cable-supported façade under blast loading conditions. The load is a time dependent force per unit area following Friedlander equation. Again, the equilibrium equations have been deduced from Hamilton's principle. The nonlinear behavior of supporting cable (axial force depending on transverse deflection) and glass panels (membrane stresses) have been considered. In order to tune the compliance of the load-bearing structure, a spring element can be added in series with the cable. The model has been validated by comparison with numerical solutions obtained via the finite element software `Straus7`. This indicates that the lumped element model well estimates the peak values of tensile force and the deflection of cable, as well as the maximum stress in the glass panels.

Parametric analyses have been performed for varying stiffness and inertia of the rear structure, obtained by changing the spring elastic constant and the mass of the cable, respectively. The general conclusion is that the more compliant is the rear structure, the lower is the stress in both cable and glass. Remarkably, this is in contrast with the somehow intuitive belief that the structural design of a bomb blast resisting façade should be oriented to the increase of stiffness and resistance properties. Ballasting the cable diminishes its tensile force and deflection, but increases the stress in glass. However, there are technological limits in terms of deflection under service and extreme load scenarios. Therefore, in order to best guarantee the integrity of façade, one shall optimize the design parameters. These are the initial tensile force and the diameter of supporting cable, its mass which can be varied by ballasting, the stiffness of the in-series spring and the thickness of the glass. The goal is to tune the rear load-bearing structure in order to absorb most of the energy released by the explosion and thus safeguard the integrity of glass.

Since there are many design variables, we have suggested to consider first a simplified approach, referred to as the *linear model*, where the tensile force in a cable is supposed to remain constant, the in-series spring is rigid and the membrane stress in glass are negligible. From this, one can rapidly derive optimal values of the stiffness and inertia related to the back structure. The nonlinear approach is used a posteriori, in order to tune the spring stiffness and the diameter of cable to respect the technological limits. Indeed, although the linear model cannot capture the real state of stress in cable and glass, nevertheless it can provide a first indication in terms of optimal values of some design parameter, which may be refined and complemented through a subsequent nonlinear analysis.

This study is restricted to the case of cable-supported façades, a system that is highly recommended because of its intrinsic compliance. In general, mullion/transom façades appear to be too stiff to absorb the energy from the load and safeguard the glass [21].

Appendix A

Fractional calculus in viscoelasticity

Experiments [122] have provided a wealth of evidence that materials like rubber, polymers, steel, under an assigned stress history $\tau(t) = \tau_0\,\mathcal{H}(t)$, being $\mathcal{H}(t)$ the unit Heaviside step function and $\tau_0 = 1\,\text{Pa}$ the reference unitary shear stress, exhibit a strain response $J(t)$, which can be expressed as

$$J(t) = \frac{t^\alpha}{C_\alpha\,\Gamma(1+\alpha)}\,,\quad (0 \leq \alpha \leq 1)\,. \tag{A.1}$$

Here α, with $0 \leq \alpha \leq 1$, is a number, $\Gamma(\cdot)$ is the Euler's Gamma Function, t $[s]$ is the time and C_α [Pa s^α] is a dimensional coefficient. Both α and C_α can be obtained from best fitting with experimental data. The function $J(t)$ is referred to as the *creep function*.

There are two limit cases. When $\alpha = 0$, then $J(t) = \text{const}$ and the response is linear elastic. Since $\Gamma(1) = 1$, one finds that the elastic modulus is equal to C_0 [Pa]. On the other hand, when $\alpha = 1$, one has that $J(t)$ is a linear function of t, which corresponds to the case of the classical Newton-Petroff viscous model, with constant of viscosity C_1 [Pa $\cdot$ s] because, again, $\Gamma(2) = 1$. Hence, the coefficient α continuously tunes the response from the pure elastic ($\alpha = 0$) to the pure viscous ($\alpha = 1$) cases.

Once $J(t)$ is known, the Boltzmann superposition principle allows us to define the strain history $\gamma(t)$ associated with an assigned stress history $\tau(t)$, in the form

$$\gamma(t) = \frac{1}{C_\alpha\Gamma(1+\alpha)}\int_0^t (t-\bar{t})^\alpha\,\dot{\tau}(\bar{t})\,d\bar{t}\,. \tag{A.2}$$

This expression is valid when the system is quiescent at $t = 0$, i.e., $\gamma(0) = 0$ and $\tau(0) = 0$. In the case that $\tau(0) \neq 0$, an extra term $G(t)\,\tau(0)$ has to be added on the

right hand side of (A.2). Integration by parts of (A.2) provides the constitutive law for the viscoelastic material that reads

$$\gamma(t) = \frac{1}{C_\alpha}\, {}_0\mathcal{I}_t^\alpha[\tau(\cdot)](t)\,, \tag{A.3}$$

where ${}_0\mathcal{I}_t^\alpha$ is the *Riemann-Liouville* (R-L) fractional integral of order α operating on any generic function $f(\cdot)$ according to

$${}_0\mathcal{I}_t^\alpha[f(\cdot)](t) = \frac{1}{\Gamma(\alpha)} \int_0^t (t-\bar{t})^{\alpha-1}\, f(\bar{t})\, d\bar{t}\,. \tag{A.4}$$

If one supposes that the strain history is assigned in the form $\gamma(t) = \mathcal{U}(t)$, since $\gamma(t)$ remains constant for $t > 0$, the corresponding stress history will decay in time according to the *relaxation function*, referred to as $R(t)$ in the sequel. Using again the Boltzmann superposition principle, the stress history corresponding to an assigned strain history will be given by

$$\tau(t) = \int_0^t R(t-\bar{t})\dot{\gamma}(\bar{t})\, d\bar{t}\,. \tag{A.5}$$

The relaxation function $R(t)$ is strictly related to the creep function $G(t)$ by the fundamental law of viscoelasticity

$$\widehat{J}(s)\, \widehat{R}(s) = s^{-2}\,, \tag{A.6}$$

where $\widehat{J}(s)$ and $\widehat{R}(s)$ are the Laplace transform of $J(t)$ and $R(t)$ respectively, while s is the complex variable of the Laplace transform. After some calculations, one obtains that if $J(t)$ is of the form (A.1), the corresponding $R(t)$ is given by

$$R(t) = \frac{C_\alpha}{\Gamma(1-\alpha)} t^{-\alpha}\,. \tag{A.7}$$

Hence, inserting this expression in (A.5), one obtains

$$\tau(t) = C_\alpha\, {}_0\mathcal{D}_t^\alpha[\gamma(\cdot)](t)\,, \tag{A.8}$$

where ${}_0^C\mathcal{D}_t^\alpha$ is the Caputo's fractional derivative of order α, which is an operator transforming any function $f(\cdot)$ in

$${}_0\mathcal{D}_t^\alpha[f(\cdot)](t) = \frac{1}{\Gamma(1-\alpha)} \int_0^t (t-\bar{t})^{-\alpha}\, \dot{f}(\bar{t})\, d\bar{t}\,, \tag{A.9}$$

Also in this case, the provided expression is valid when $\gamma(0) = 0$, otherwise the extra term $\gamma(0)R(t)$ should be added on the right hand side of (A.8). It is clear, as it can be directly verified through integration by parts, that if the system is at rest for $t \leq 0$, then the integral and differential operators commute, i.e.,

$$ {}_0\mathcal{I}_t^{\alpha}[{}_0\mathcal{D}_t^{\alpha}[\gamma(\cdot)]](t) = \gamma(t), \text{ or, formally, } \; {}_0\mathcal{I}_t^{\alpha}[\gamma(\cdot)](t) = {}_0\mathcal{D}_t^{-\alpha}[\gamma(\cdot)](t)\,. \tag{A.10} $$

In conclusion, equations (A.3) and (A.8) represent the constitutive laws of fractional viscoelasticity. The main properties of the fractional viscoelastic characterization are the following.

i) As $\alpha = 0$, the linear elastic constitutive law is recovered; for $\alpha = 1$, the Newton-Petrof law for a purely viscous material is obtained. It follows that the intermediate value $0 < \alpha < 1$ provides and intermediate condition between the two aforementioned extreme (ideal) cases.

ii) For a quiescent system at $t \leq 0$, the R-L and the Caputo operators are the inverse one of the other.

iii) The operators (A.3) and (A.8) are linear and, hence, the main properties of the classical derivatives and integral of integer order (linearity, semigroup properties) are still valid, even if integration by parts and Leibniz rule in general do not hold true [123, 124].

iv) In the Laplace domain, they exactly behave as the classical derivatives and integrals; for example

$$ \mathcal{L}\left\{\frac{d^n f}{dt^n}, s\right\} = (s)^n \hat{f}(s)\,, \;\; \mathcal{L}\left\{ {}_0^C\mathcal{D}_t^{\alpha}[f], s\right\} = (s)^{\alpha}\widehat{f}(s)\,, \tag{A.11} $$

provided that the values of $f(t)$ and its derivatives up to $n-1$ are null at $t = 0$.

In the engineering practice, it is often necessary to use alternative formulations of the fractional integral (A.4) and the fractional derivative (A.9). Assume to subdivide a time interval of interest $[0, T]$ in s subintervals whose amplitude is $\Delta t = t_j - t_{j-1}$. Then, take a generic continuous function denoted as $f(t)$, so that $f(t_j) = f_j$ and $\mathbf{f}_s^T = [f(t_1)\ f(t_2)\ \ldots\ f(t_s)]$. The fractional integral and the fractional derivative of order α at the point t_j can be numerically approximated through Grünwald-Letnikov operators defined as

$$ {}_0\mathcal{I}_t^{\alpha}[f(\cdot)](t) \simeq (\nabla^{-\alpha} f)(t_j) = \Delta t^{\alpha} \sum_{r=0}^{j-1} \frac{\Gamma(r+\alpha)}{\Gamma(r+1)\Gamma(\alpha)} f(t_j - r\Delta t)\,, \tag{A.12} $$

$$ {}_0\mathcal{D}_t^{\alpha}[f(\cdot)](t) \simeq (\nabla^{\alpha} f)(t_j) = \Delta t^{-\alpha} \sum_{r=0}^{j-1} \frac{\Gamma(r-\alpha)}{\Gamma(r+1)\Gamma(-\alpha)} f(t_j - r\Delta t)\,. \tag{A.13} $$

These can be expressed in compact matrix form. The approximation of the fractional derivative is

$$\nabla^{\alpha}\mathbf{f}_s = \mathbf{A}_s^{(\alpha)}\mathbf{f}_s, \tag{A.14}$$

where $\mathbf{A}_s^{(\alpha)}$ is a $s \times s$ lower band strip matrix

$$\mathbf{A}_s^{(\alpha)} = \frac{1}{\Delta t^{\alpha}} \begin{bmatrix} \omega_1(\alpha) & & & \\ \omega_2(\alpha) & \omega_1(\alpha) & & \\ \vdots & \ddots & \ddots & \\ \omega_s(\alpha) & \dots & \omega_2(\alpha) & \omega_1(\alpha) \end{bmatrix}, \tag{A.15}$$

with $\omega_1 = 1$, $\omega_2 = -\alpha$, $\dots$, $\omega_{j+1} = \dfrac{j-\alpha-1}{j}\omega_j(\alpha)$. Obviously, by setting $\mathbf{B}_s^{(\alpha)} = \mathbf{A}_s^{(-\alpha)}$, the matrix form of the fractional integral reads

$$\nabla^{-\alpha}\mathbf{f}_s = \mathbf{B}_s^{(\alpha)}\mathbf{f}_s. \tag{A.16}$$

Using this discretization, an integral/differential fractional equation can be directly solved step-by-step. Of course the time step Δt has to be accurately chosen, depending on the regularity of the datum.

Bibliography

[1] Department of the Army - United States. *Structures to resist the effects of accidental explosions*, volume 88. Departments of the Army, Navy, and Air Force, 1991.

[2] European Committee for Standardization CEN. Glass in building. pendulum test-impact test method and classification for flat glass. 2002.

[3] GSA (General Services Administration). Standard test method for glazing and window systems subject to dynamic overpressure loadings, 2003.

[4] EN 13123-1. *Windows, doors and shutters-explosion resistance - requirements and classification - Part 1: shock tube*. 2001-10.

[5] EN 13123-2. *Windows, doors and shutters-explosion resistance - requirements and classification - Part 2: range test*. 2004-05.

[6] EN 13124-1. *Windows, doors and shutters-explosion resistance - test method - Part 1: shock tube*. 2001-10.

[7] EN 13124-2. *Windows, doors and shutters-explosion resistance - test method - Part 2: range test*. 2004-05.

[8] International Organization for Standardization (ISO 16933:2007). Glass in building—explosion-resistant security glazing—test and classification for arena air-blast loading. 2007.

[9] International Organization for Standardization (ISO 16934:2007). Glass in building — explosion-resistant security glazing — test and classification by shock-tube loading. 2007.

[10] X. Zhang and C. Bendon. Vulnerability and protection of glass windows under blast: experiments, methods and current trends. *International Journal of Structural Glass and Advanced Materials Research*, 1(2):10–23, 2017.

[11] C. Bedon, X. Zhang, F. Santos, D. Honfi, M. Kozłowski, M. Arrigoni, L. Figuli, and D. Lange. Performance of structural glass facades under extreme loads–design methods, existing research, current issues and trends. *Construction and Building Materials*, 163:921–937, 2018.

[12] I. V. Ivanov. Analysis, modelling, and optimization of laminated glasses as plane beam. *International Journal of Solids and Structures*, 43(22-23):6887–6907, 2006.

[13] L. Galuppi and G. Royer-Carfagni. The post-breakage response of laminated heat-treated glass under in plane and out of plane loading. *Composites Part B: Engineering*, 147:227–239, 2018.

[14] J. Pelfrene, J. Kuntsche, S. V. Dam, W. V. Paepegem, and J. Schneider. Critical assessment of the post-breakage performance of blast loaded laminated glazing: experiments and simulations. *International Journal of Impact Engineering*, 88:61–71, 2016.

[15] DIN EN 13541:2012. *Glass in building-security glazing-testing and classification of resistance against explosion pressure*. 2012.

[16] P. A. Hooper, R. A. M. Sukhram, B. R. K. Blackman, and J. P. Dear. On the blast resistance of laminated glass. *International Journal of Solids and Structures*, 49(6):899–918, 2012.

[17] C. Amadio and C. Bedon. Viscoelastic spider connectors for the mitigation of cable-supported façades subjected to air blast loading. *Engineering Structures*, 42:190–200, 2012.

[18] C. Amadio and C. Bedon. Blast analysis of laminated glass curtain walls equipped by viscoelastic dissipative devices. *Buildings*, 2(3):359–383, 2012.

[19] C. Amadio and C. Bedon. Elastoplastic dissipative devices for the mitigation of blast resisting cable-supported glazing façades. *Engineering Structures*, 39:103–115, 2012.

[20] M. Maffeis, G. Royer-Carfagni, and L. Viviani. An engineering approach for the basic design of glazed surfaces under blast waves. In *All Eyes on Smarter Glass. Glass Performance Days (GPD) 2019*, pages 2–7. Glaston Finland Oy, June 2019.

[21] G. Royer-Carfagni and L. Viviani. Basic design of cable-supported glazed surfaces under blast waves. *International Journal of Non-Linear Mechanics*, 123:103489, 2020.

[22] J. Schlaich and T. Schober, H.and Moschner. Prestressed cable-net façades. *Structural engineering international*, 15(1):36–36, 2005.

[23] W. Sobek, S. Feierabend, L. Blandini, and F. Tarazi. Cable-stayed glass façades-15 years of innovation at the cutting edge. In *Challenging Glass Conference Proceedings*, volume 2, pages 599–608, 2010.

[24] F. A. dos Santos, C. Cismasiu, and C. Bedon. Smart glazed cable facade subjected to a blast loading. *Proceedings of the Institution of Civil Engineers-Structures and Buildings*, 169(3):223–232, 2016.

[25] P. A. Thompson. *Compressible-Fluid Dynamics*. McGraw-Hill, 1972.

[26] G. F. Kinney and K. J. Graham. *Explosive shocks in air*. Springer Science & Business Media, 2013.

[27] L. I. Sedov. *Similarity and dimensional methods in mechanics*. CRC press, 1993.

[28] G. I. Taylor. The formation of a blast wave by a very intense explosion I. Theoretical discussion. *Proceedings of the Royal Society of London. Series A. Mathematical and Physical Sciences*, 201(1065):159–174, 1950.

[29] G. I. Taylor. The formation of a blast wave by a very intense explosion II. The atomic explosion of 1945. *Proceedings of the Royal Society of London. Series A. Mathematical and Physical Sciences*, 201(1065):175–186, 1950.

[30] T. Ngo, P. Mendis, A. Gupta, and J. Ramsay. Blast loading and blast effects on structures–an overview. *Electronic Journal of Structural Engineering*, 7(S1):76–91, 2007.

[31] F. G. Friedlander. Note on the diffraction of blast waves by a wall. *UK Home Office Dept, RC (A)*, 1939.

[32] P. S. Bulson. *Explosive loading of engineering structures*. CRC Press, 1997.

[33] H. L. Brode. Numerical solutions of spherical blast waves. *Journal of Applied physics*, 26(6):766–775, 1955.

[34] C. N. Kingery and G. Bulmash. Technical report arbrl-tr-02555: air blast parameters from tnt spherical air burst and hemispherical burst. *AD-B082*, 713, 1984.

[35] V. Karlos, G. Solomos, and M. Larcher. Analysis of the blast wave decay coefficient using the kingery–bulmash data. *International Journal of Protective Structures*, 7(3):409–429, 2016.

[36] M. D. Goel, V. A. Matsagar, A. K. Gupta, and S. Marburg. An abridged review of blast wave parameters. *Defence Science Journal*, 62(5):300–306, 2012.

[37] M. Teich and N. Gebbeken. The influence of the underpressure phase on the dynamic response of structures subjected to blast loads. *International Journal of Protective Structures*, 1(2):219–233, 2010.

[38] T. Krauthammer. *Modern protective structures*, volume 22. CRC Press, 2008.

[39] N. M. Newmark and R. J. Hansen. Design of blast resistant structures. *Shock and vibration handbook*, 3, 1961.

[40] Joint Research Centre - Institute for the Protection and Security of the Citizen. *Calculation of blast loads for application to structural components*. 2013.

[41] Joint Research Centre - Institute for the Protection and Security of the Citizen. *Resistance of structures to explosion effects: Review report of testing methods*. Publications Office of the European Union, 2013.

[42] R. Andreotti, M. Colombo, A. Guardone, P. Martinelli, G. Riganti, and M. Di Prisco. Performance of a shock tube facility for impact response of structures. *International Journal of Non-Linear Mechanics*, 72:53–66, 2015.

[43] Joint Research Centre - Institute for the Protection and Security of the Citizen. *A comparison of existing standards for testing blast resistant glazing and windows*. Publications Office of the European Union, 2014.

[44] J. Wei and L. R. Dharani. Response of laminated architectural glazing subjected to blast loading. *International Journal of Impact Engineering*, 32(12):2032–2047, 2005.

[45] G. Krall. *Meccanica tecnica delle vibrazioni*. Istituto matematico dell'Università di Roma, 1940.

[46] M. Teich, P. Warnstedt, and N. Gebbeken. Influence of negative phase loading on cable net facade response. *Journal of architectural engineering*, 18(4):276–284, 2012.

[47] S. E. Rigby, A. Tyas, T. Bennett, S. D. Clarke, and S. D. Fay. The negative phase of the blast load. *International Journal of Protective Structures*, 5(1):1–19, 2014.

[48] Deutsches Institut für Bautechnik, Mitteilungen DIBt 2/2003, S. 58 bis 68. Technical regulation for the use of glazing crash-secure (TRAV). 2003.

[49] CEN/TC 250-SC11. prCEN/TS xxxx-1:2019: Design of glass structures – part 1: Basis of design and materials. in progress.

[50] J. Schneider and J. Wörmer. Impact loading on glass panes by soft body impact–theoretical analysis and experimental verification. *Proceedings Glass Processing Days. (June 2001)*, 2001.

[51] J. Schneider, A. Burmeister, and S. Schula. Two mechanical design concepts for simulating the soft body impact at glazings - part 1: Numerical, transient finite element simulation and simplified concept with equivalent static loads. *Stahlbau*, 80(S1):81–87, 2011.

[52] I. Mohagheghian, Y. Wang, J. Zhou, X. Guo, M. Charalambides, Y. Yan, and J. P. Dear. Soft impact response of laminated glass plates. In *ICCM 20-20th International Conference on Composite Materials*. International Committee on Composite Materials (ICCM), 2015.

[53] J. Schneider and S. Schula. Simulating soft body impact on glass structures. *Proceedings of the Institution of Civil Engineers: Structures and Buildings*, 169(6):416–431, 2016.

[54] J. Alonso, J.A. Parra, A. Pacios, and M.C. Huerta. Similarity index: A procedure for comparing impact time histories validated with soft impact test. *Engineering Structures*, 198(109513), 2019.

[55] M. Peroni, G. Solomos, V. Pizzinato, and M. Larcher. Experimental investigation of high strain-rate behaviour of glass. In *Applied Mechanics and Materials*, volume 82, pages 63–68, 2011.

[56] W. Goldsmith. *Impact: The theory and physical behavior of colliding solids*. Edward Arnold, 1960.

[57] K. H. Hunt and F. R. E. Crossley. Coefficient of restitution interpreted as damping in vibroimpact. *Journal of Applied Mechanics*, 1975.

[58] Y. Zhang and I. Sharf. Validation of nonlinear viscoelastic contact force models for low speed impact. *Journal of Applied Mechanics*, 76(5):051002, 2009.

[59] M. Timmel, S. Kolling, P. Osterrieder, and P. A. Du Bois. A finite element model for impact simulation with laminated glass. *International Journal of Impact Engineering*, 34(8):1465–1478, 2007.

[60] M. Fröling, K. Persson, and P. E. Austrell. A reduced model for the design of glass structures subjected to dynamic impulse load. *Engineering Structures*, 80:53–60, 2014.

[61] J. A. Parra, J. Alonso, A. Pacios, and M. C. Huerta. Effective energy applied to a glass plate during an impact test. *International Journal of Impact Engineering*, 130:11–18, 2019.

[62] C. E Anderson, C. E. Weiss, and S. Chocron. Impact experiments into borosilicate glass at three scale sizes. *Journal of Applied Mechanics*, 78(5):051011, 2011.

[63] M. Amabili. *Nonlinear mechanics of shells and plates in composite, soft and biological materials*. Cambridge University Press, 2018.

[64] I. D. Bohmann. *Sj Mepla Manual Theory, Version 3.5*. SJ Software GmbH, Aachen, 2012.

[65] A. Pacios, S. Postigo, and C. Huerta. Relationship between characteristic parameters of impact test for safety glasses. *Stahlbau*, 80(S1):61–66, 2011.

[66] L. Galuppi, G. Manara, and G. Royer-Carfagni. Practical expressions for the design of laminated glass. *Composites Part B: Engineering*, 45(1):1677–1688, 2013.

[67] L. Galuppi and G. Royer-Carfagni. A homogenized model for the post-breakage tensile behavior of laminated glass. *Composite Structures*, 154:600–615, 2016.

[68] L. Galuppi and G. Royer-Carfagni. A homogenized analysis *à la* Hashin for cracked laminates under equi-biaxial stress. Applications to laminated glass. *Composites Part B: Engineering*, 111:332–347, 2017.

[69] L. Viviani, A. Consolaro, M. Maffeis, and G. Royer-Carfagni. Engineered modelling of the soft-body impact test on glazed surfaces. *Engineering Structures*, 226:111315, 2021.

[70] R. W. Clough and J. Penzien. *Dynamics of Structures*. Computers & Structures, Inc., 1995.

[71] S. P. Timoshenko and S. Woinowsky-Krieger. *Theory of plates and shells*. McGraw-hill, 1959.

[72] X. Zhang, H. Hao, and G. Ma. Laboratory test and numerical simulation of laminated glass window vulnerability to debris impact. *International Journal of Impact Engineering*, 55:49–62, 2013.

[73] X. Zhang, H. Hao, and Z. Wang. Experimental study of laminated glass window responses under impulsive and blast loading. *International Journal of Impact Engineering*, 78:1–19, 2015.

[74] M. Amabili. Nonlinear damping in large-amplitude vibrations: modelling and experiments. *Nonlinear Dynamics*, 93(1):5–18, 2018.

[75] M. Amabili. Nonlinear damping in nonlinear vibrations of rectangular plates: derivation from viscoelasticity and experimental validation. *Journal of the Mechanics and Physics of Solids*, 118:275–292, 2018.

[76] M. Amabili. Derivation of nonlinear damping from viscoelasticity in case of nonlinear vibrations. *Nonlinear Dynamics*, 97(3):1785–1797, 2019.

[77] E. J. Yoder and M. W. Witczak. *Principles of pavement design*. John Wiley & Sons, 1991.

[78] DIN 18008-4:. *Glass in building-design and construction rules-part 4: additional requirements for barruer glazing*. Deutsches Institut für Normung, Berlin, Germany.

[79] A. Aguiar, R. Fosdick, and J. Sánchez. A study of penalty formulations used in the numerical approximation of a radially symmetric elasticity problem. *Journal of Mechanics of Materials and Structures*, 3(8):1403–1427, 2008.

[80] J. Pelfrene, S. Van Dam, J. Kuntsche, and W. Van Paepegem. Numerical simulation of the EN 12600 pendulum test for structural glass. In *Challenging Glass Conference Proceedings*, volume 5, pages 429–438, 2016.

[81] J. Schneider and S. Schula. Simulating soft body impact on glass structures. *Proceedings of the Institution of Civil Engineers-Structures and Buildings*, 169(6):416–431, 2016.

[82] G. Royer-Carfagni and M. Silvestri. Fail-safe point fixing of structural glass. New advances. *Engineering structures*, 31(8):1661–1676, 2009.

[83] F. Freddi, G. Royer-Carfagni, and M. Silvestri. Full-scale experiments for point-fixing frameless laminated glass. *International Journal of Applied Glass Science*, 1(3):257–272, 2010.

[84] G. Royer-Carfagni and M. Silvestri. An innovative point-fixing device for architectural glazing. From concept to realization. *Glass Technology International*, 20:84–88, 2009.

[85] M. Di Paola, L. Galuppi, and G. Royer Carfagni. Fractional viscoelastic characterization of laminated glass beams under time-varying loading. *International Journal of Mechanical Sciences*, 196:106274, 2021.

[86] M. López-Aenlle, A. Noriega, and F. Pelayo. Mechanical characterization of polyvinil butyral from static and modal tests on laminated glass beams. *Composites Part B: Engineering*, 169:9–18, 2019.

[87] X. Centelles, F. Pelayo, M. J. Lamela-Rey, A. I. Fernández, R. Salgado-Pizarro, J. R. Castro, and L. F. Cabeza. Viscoelastic characterization of seven laminated glass interlayer materials from static tests. *Construction and Building Materials*, 279:122503, 2021.

[88] M. L. Williams, R. F. Landel, and J. D. Ferry. The temperature dependence of relaxation mechanisms in amorphous polymers and other glass-forming liquids. *Journal of the American Chemical society*, 77(14):3701–3707, 1955.

[89] L. Biolzi, S. Cattaneo, M. Orlando, L. Ruggero Piscitelli, and P. Spinelli. Constitutive relationships of different interlayer materials for laminated glass. *Composite Structures*, 244:112221, 2020.

[90] T. Krauthammer and A. Altenberg. Negative phase blast effects on glass panels. *International Journal of Impact Engineering*, 24(1):1–17, 2000.

[91] X. Chen, S. Chen, , and Li G.-Q. Experimental investigation on the blast resistance of framed pvb-laminated glass. *International Journal of Impact Engineering*, 149:103788, 2021.

[92] W. E. Baker, P. A. Cox, J. J. Kulesz, R. A. Strehlow, and P. S. Westine. *Explosion Hazards and Evaluation*. Elsevier, 1983.

[93] L. Galuppi and G. Royer-Carfagni. Laminated beams with viscoelastic interlayer. *International Journal of Solids and Structures*, 49(18):2637–2645, 2012.

[94] D. C. Weggel, B. J Zapata, and M. J. Kiefer. Properties and dynamic behavior of glass curtain walls with split screw spline mullions. *Journal of Structural Engineering*, 133(10):1415–1425, 2007.

[95] F. Wellershoff, M. Förch, G. Lori, M. Zobec, D. Casucci, and P. Grosser. Façade brackets for blast enhancement. *ce/papers*, 2(5-6):351–367, 2018.

[96] M. Amabili, P. Balasubramanian, R. Garziera, and G. Royer-Carfagni. Blast loads and nonlinear vibrations of laminated glass plates in an enhanced shear deformation theory. *Composite Structures*, 252, 2020.

[97] L. Viviani and G. Royer-Carfagni. How dissipative devices could enhance the capacity of glazed surfaces under impacting blast waves. *International Journal of Non-Linear Mechanics*, 137:103813, 2021.

[98] V. Karlos and G. Solomos. *Calculation of blast loads for application to structural components*, volume 26456. Ispra: European Commission-Joint Research Centre, 2013.

[99] L. Galuppi and G. F. Royer-Carfagni. Effective thickness of laminated glass beams: new expression via a variational approach. *Engineering Structures*, 38:53–67, 2012.

[100] L. Galuppi and G. Royer-Carfagni. The effective thickness of laminated glass plates. *Journal of Mechanics of Materials and Structures*, 7(4):375–400, 2012.

[101] M. Amabili. Nonlinear vibrations of rectangular plates with different boundary conditions: theory and experiments. *Computers & structures*, 82(31-32):2587–2605, 2004.

[102] F. Alijani and M. Amabili. Non-linear vibrations of shells: A literature review from 2003 to 2013. *International journal of Non-Linear mechanics*, 58:233–257, 2014.

[103] S. Levy. Bending of rectangular plates with large deformations. *National advisory committee for aeronautics, Technical notes*, 846, 1942.

[104] R. K. Mc Farland Jr. The development of metal honeycomb energy-absorbing elements. *Jet Propulsion Laboratory, California Institute of Technology, Technical Report No. 32-639*, 1964.

[105] H. Zhao and G. Gary. Crushing behaviour of aluminium honeycombs under impact loading. *International Journal of Impact Engineering*, 21(10):827–836, 1998.

[106] Z. Zou, S. R. Reid, P. J. Tan, S. Li, and J. J. Harrigan. Dynamic crushing of honeycombs and features of shock fronts. *International Journal of Impact Engineering*, 36(1):165–176, 2009.

[107] T. Wierzbicki and W. Abramowicz. On the crushing mechanics of thin-walled structures. *Transactions of the ASME*, 1983.

[108] W. Chen and T. Wierzbicki. Relative merits of single-cell, multi-cell and foam-filled thin-walled structures in energy absorption. *Thin-Walled Structures*, 39(4):287–306, 2001.

[109] C. J. Field, J. A. Godinho, and S. R. Wopschall. Blast performance of cable-supported curtain walls. In *Structures Congress 2012*, pages 322–332, 2012.

[110] C. Bedon and C. Amadio. Exploratory numerical analysis of two-way straight cable-net façades subjected to air blast loads. *Engineering Structures*, 79:276–289, 2014.

[111] R. R. C. Piyasena, D. P. Thambiratnam, T. H. T. Chan, and N. J. Perera. Comparative analysis of blast response of cable truss and cable net façades. *Engineering Failure Analysis*, 104:740–757, 2019.

[112] F. Hejazi, A. Zabihi, and M. S. Jaafar. Development of elasto-plastic viscous damper finite element model for reinforced concrete frames. *Soil Dynamics and Earthquake Engineering*, 65:284–293, 2014.

[113] C. Bedon and C. Amadio. Passive control systems for the blast enhancement of glazing curtain walls under explosive loads. *The Open Civil Engineering Journal*, 11(1), 2017.

[114] G. Lori, C. Morison, M. Larcher, and J. Belis. Sustainable facade design for glazed buildings in a blast resilient urban environment. *Glass Structures & Engineering*, 4(2):145–173, 2019.

[115] M. Di Paola, L. Galuppi, and G. Royer-Carfagni. Fractional viscoelastic characterization of laminated glass beams under time-varying loading. *International Journal of Mechanical Sciences*, 196:106274, 2021.

[116] M. Larcher, G. Solomos, F. Casadei, and N. Gebbeken. Experimental and numerical investigations of laminated glass subjected to blast loading. *International Journal of Impact Engineering*, 39(1):42–50, 2012.

[117] L. Galuppi and G. Royer-Carfagni. Effective thickness of laminated glass beams: new expression via a variational approach. *Engineering Structures*, 38:53–67, 2012.

[118] L. Galuppi and G. Royer-Carfagni. The effective thickness of laminated glass plates. *Journal of Mechanics of Materials and Structures*, 7(4):375–400, 2012.

[119] M. Larcher, M. Arrigoni, C. Bedon, J. C. A. M. Van Doormaal, C. Haberacker, G. Hüsken, O. Millon, A. Saarenheimo, G. Solomos, L. Thamie, A. Williams, and A. Stolz. Design of blast-loaded glazing windows and facades: a review of essential requirements towards standardization. *Advances in Civil Engineering*, 2016.

[120] S. Wiederhorn and L. Bolz. Stress corrosion and static fatigue of glass. *Journal of the American Ceramic Society*, 53(10):543–548, 1970.

[121] L. Galuppi and G. Royer-Carfagni. Laminated beams with viscoelastic interlayer. *International Journal of Solids and Structures*, 49(18):2637–2645, 2012.

[122] P. G. Nutting. A new general law of deformation. *Journal of the Franklin Institute*, 191(5):679–685, 1921.

[123] V. E. Tarasov. No violation of the leibniz rule. no fractional derivative. *Communications in Nonlinear Science and Numerical Simulation*, 18(11):2945–2948, 2013.

[124] V. E. Tarasov. Leibniz rule and fractional derivatives of power functions. *Journal of Computational and Nonlinear Dynamics*, 11(3):art. n. 031014, 2016.

Acknowledgments

I would like to express my sincere gratitude to Maffeis Engineering S.p.A. for financial and technical support during the lasts three years.

A special thank goes to Prof. Gianni Royer-Carfagni for solving all my doubts and for his helpful guidance.

Thank to my family and Lucia for the endless emotional support.